

INVESTIGATING PHENOMENA IN  
VORTEX-INDUCED VIBRATION OF A CYLINDER  
USING CONTROLLED VIBRATION

A Dissertation

Presented to the Faculty of the Graduate School

of Cornell University

in Partial Fulfillment of the Requirements for the Degree of

Doctor of Philosophy

by

Timothy Lester Morse

January 2009

© 2009 Timothy Lester Morse

ALL RIGHTS RESERVED

# INVESTIGATING PHENOMENA IN VORTEX-INDUCED VIBRATION OF A CYLINDER USING CONTROLLED VIBRATION

Timothy Lester Morse, Ph.D.

Cornell University 2009

In this study, we use controlled vibration, where we oscillate a rigid cylinder with a prescribed motion, in a fluid flow, in order to provide insight into aspects of vortex-induced vibration. We make extensive measurements of the fluid forces on a cylinder that oscillates sinusoidally, transverse to a free stream, at both  $Re = 4,000$  and  $Re = 12,000$ , and generate high resolution contour plots of various fluid forcing quantities in the plane of normalized amplitude and wavelength. With such resolution, we are able to discover discontinuities in the force and phase contours, which enable us to clearly identify boundaries separating different fluid forcing regimes. These boundaries appear remarkably similar to boundaries separating different vortex formation modes in the Williamson & Roshko (1988) map of regimes. Wake vorticity measurements (using DPIV) exhibit the 2S, 2P, and P+S modes, as well as a regime where the vortex formation is not synchronized with the cylinder oscillation. A further new discovery is the existence of a region where two vortex formation regimes overlap. Associated with this overlap region, we identify a distinct mode of vortex formation where two pairs of vortices are shed per cycle of oscillation (similar to the 2P mode) but the secondary vortex is much weaker, which we have termed '2P<sub>OVERLAP</sub>', or simply the '2P<sub>O</sub>' mode. This '2P<sub>O</sub>' mode is of particular importance, as it is responsible for generating the peak resonant response of the body.

By examining the energy transfer from fluid to body motion we predict the

response of an elastically mounted cylinder that agrees remarkably well with measured free vibration responses. We introduce the concept of an “energy portrait”, which allows us to identify stable and unstable amplitude response solutions and thus to predict clearly the hysteretic and intermittent switching mode transitions, both of which correspond with such phenomena measured from free vibration. In addition to predicting steady state (sinusoidal) behavior, we develop a quasi-steady model which allows us to predict the dynamics of a freely oscillating cylinder having transient or unsteady behavior. Using this model, we find a regime of normalized flow velocity where steady state vortex-induced vibrations cannot occur, and the cylinder can only oscillate with unsteady motion.

Further studies include the effect of Reynolds number on the critical mass for an oscillating body, below which a structure will vibrate up to infinite normalized velocity. Finally, we measure the effect of spanwise end conditions on a free vibration response.

## **BIOGRAPHICAL SKETCH**

Timothy Morse was born in Corning, NY on May 29, 1981. He grew up in Camillus, NY where he attended West Genesee High School, graduating as the salutatorian in May 1999. In August 1999 he began his undergraduate education at the Cooper Union for the Advancement of Science and Art in Manhattan, NY. He graduated at the top of his class in May 2003 with a Bachelor of Engineering degree in mechanical engineering. He started his graduate research at Cornell University in the Sibley School of Mechanical & Aerospace Engineering in August 2003, completing a Masters of Science in January 2007.

Dedicated to my wife Melissa,  
for her unending love and support

## ACKNOWLEDGEMENTS

I would like to thank my advisor, Professor Charles H. K. Williamson, for his wisdom and guidance throughout my graduate work at Cornell and for our many stimulating discussions.

This work would not have been possible without the incredible support and generosity of time of the entire Fluid Dynamics Research Laboratories team. Thanks to Scott Nolan & James Buscher for their help with getting the experiments started; thanks to Paolo Luzzatto-Fegiz for his expertise on all things mathematical; thanks to Raghu Govardhan for his guidance and collaboration; and most importantly, thanks to Matt Horowitz for all his advice and assistance.

I also greatly appreciate the advice of my special committee members, Professor Lance Collins and Professor Todd Cowen. Special thanks are also due to Prof. Cowen and his research student, Evan Variano for their assistance in diagnosing Laser problems.

On a personal note, I am grateful to my wife, Melissa for all her patience and support, which were essential to all my achievements. I would also like to thank my parents and family for all their encouragement over the years.

Finally I would like to recognize the funding support of The Ocean Engineering Division of the Office of Naval Research, monitored by Dr. Tom Swain (ONR Contract No. N00014-04-1-0031 and N00014-07-1-0303). I was also supported through a National Science Foundation Graduate Research Fellowship and a National Defense Science and Engineering Graduate Fellowship.

## TABLE OF CONTENTS

Biographical Sketch . . . . .	iii
Dedication . . . . .	iv
Acknowledgements . . . . .	v
Table of Contents . . . . .	vi
List of Tables . . . . .	ix
List of Figures . . . . .	x
<b>1 Introduction</b>	<b>1</b>
<b>2 Employing controlled vibrations to predict fluid forces on a cylinder undergoing vortex-induced vibration</b>	<b>4</b>
2.1 Introduction . . . . .	5
2.2 Experimental Details . . . . .	7
2.3 Direct comparison to free vibration . . . . .	8
2.4 Controlled vibration at constant amplitude . . . . .	11
2.5 Conclusions . . . . .	13
<b>3 Fluid forcing, wake modes, and transitions for a cylinder undergoing controlled oscillations</b>	<b>16</b>
3.1 Introduction . . . . .	17
3.2 Experimental Details . . . . .	23
3.3 Fluid forcing contours and vortex formation modes . . . . .	25
3.4 Characterizing wake mode boundaries and transitions . . . . .	31
3.4.1 Mode boundaries with abrupt jumps in fluid forcing . . . . .	31
3.4.2 Regimes of overlapping wake modes . . . . .	34
3.4.3 Wake modes with non-synchronized fluid forcing . . . . .	37
3.5 Conclusions . . . . .	40
<b>4 Prediction of vortex-induced vibration response by employing controlled motion</b>	<b>43</b>
4.1 Introduction . . . . .	44
4.2 Experimental details . . . . .	54
4.3 Regimes of fluid forcing and vortex formation modes . . . . .	57
4.4 Contours of fluid excitation and effective added mass . . . . .	61
4.5 Prediction of a free vibration response . . . . .	68
4.6 Introducing “energy portraits” to understand mode transitions . . . . .	72
4.6.1 Introduction of the concept of an “energy portrait” . . . . .	72
4.6.2 Hysteresis between the Initial $\leftrightarrow$ Upper branches . . . . .	79
4.6.3 Intermittent switching between Upper $\leftrightarrow$ Lower branches . . . . .	82
4.7 Defining the regime where free vibration is possible . . . . .	84
4.8 Conclusions . . . . .	86

<b>5</b>	<b>Steady, unsteady, and transient vortex-induced vibration predicted using controlled motion data</b>	<b>89</b>
5.1	Introduction . . . . .	90
5.2	Experimental Details . . . . .	97
5.3	Equations of motion and introduction of a quasi-steady model . .	98
5.3.1	Steady state equations of motion for free vibration . . . . .	99
5.3.2	Contours of fluid forcing . . . . .	101
5.3.3	Quasi-steady model for free vibration response . . . . .	104
5.4	Transient behavior for moderate and high mass ratio systems . .	106
5.4.1	Approaching a lower branch equilibrium . . . . .	107
5.4.2	Intermittent switching between upper and lower branch equilibria . . . . .	107
5.5	Unsteady behavior for very low mass ratio systems . . . . .	111
5.5.1	The effect of reducing mass ratio on the upper branch to lower branch transition . . . . .	111
5.5.2	Regime of unsteady response solutions in the $A^* - U^*$ plane	116
5.5.3	Frequency response at very low mass ratio . . . . .	119
5.6	Conclusions . . . . .	122
<b>6</b>	<b>The effect of Reynolds number on the critical mass phenomenon in vortex-induced vibration</b>	<b>125</b>
6.1	Introduction . . . . .	126
6.2	Experimental Details . . . . .	132
6.3	Vortex-induced vibration at infinite normalized velocity . . . . .	133
6.4	Influence of Reynolds number on prediction of critical mass . . .	136
6.5	Conclusions . . . . .	141
<b>7</b>	<b>The effect of end conditions on the vortex-induced vibration of cylinders</b>	<b>144</b>
7.1	Introduction . . . . .	145
7.2	Experimental details . . . . .	151
7.3	Effect of end conditions on free vibration response . . . . .	155
7.3.1	Comparison between unattached endplate and no endplate	155
7.3.2	Comparison between unattached endplate and attached endplate . . . . .	159
7.4	Study of end conditions through controlled vibration . . . . .	161
7.5	Comparison with previous investigations employing different end conditions . . . . .	165
7.6	Conclusions . . . . .	168
<b>A</b>	<b>Additional fluid forcing contours</b>	<b>170</b>
<b>B</b>	<b>The effect of Reynolds number on fluid force contours and prediction of the modified "Griffin plot"</b>	<b>173</b>

<b>C</b>	<b>Complete vorticity fields for each major vortex formation mode</b>	<b>177</b>
<b>D</b>	<b>The effect of fluid forcing at frequencies above the fundamental oscillation frequency</b>	<b>184</b>
<b>E</b>	<b>Publications from this work</b>	<b>191</b>
E.1	Journal Publications . . . . .	191
E.2	Conference Publications . . . . .	192

## LIST OF TABLES

3.1	Non-dimensional parameters for controlled vibration contours . . . . .	18
4.1	Non-dimensional parameters for free vibration prediction . . . . .	47
5.1	Non-dimensional parameters for quasi-steady model . . . . .	100
7.1	Non-dimensional parameters for end condition study . . . . .	154

## LIST OF FIGURES

2.1	Direct comparison of forces between free and controlled vibration	9
2.2	Comparison of force time traces between free and controlled vibration in the lower branch . . . . .	10
2.3	Comparison of force time traces between free and controlled vibration in the intermittent switching region . . . . .	12
2.4	Force measurements along an amplitude cut of $A^* = 0.5$ . . . . .	14
3.1	Grid resolution of controlled vibration measurements . . . . .	23
3.2	Schematic diagram of the experimental arrangement for controlled vibration . . . . .	24
3.3	Map of vortex shedding regimes . . . . .	27
3.4	Vorticity fields for each of the main vortex shedding modes {P+S, 2S, 2P, 2P <sub>O</sub> } . . . . .	29
3.5	Contours of the force in phase with velocity, $C_Y \sin \phi$ , and the force in phase with acceleration, $C_Y \cos \phi$ , at $Re = 4,000$ . . . . .	30
3.6	Time trace locations in the normalized amplitude-wavelength plane . . . . .	32
3.7	Typical force time traces for the transition from the 2S mode to 2P mode of vortex formation . . . . .	34
3.8	Typical force time traces and spectra for the transition from the P+S mode to the 2P mode of vortex formation . . . . .	35
3.9	Typical force time trace in the 2S–2P <sub>O</sub> region . . . . .	36
3.10	Typical force time trace in the 2P <sub>O</sub> –2P region . . . . .	37
3.11	The coalescing 2S mode of vortex formation: typical time traces, force spectra, and vorticity field . . . . .	39
3.12	Typical time traces, force spectra, and vorticity field in the desynchronized region . . . . .	40
4.1	Grid resolution of controlled vibration measurements . . . . .	53
4.2	Matched experimental arrangement for free vibration and controlled vibration . . . . .	55
4.3	Map of vortex shedding regimes . . . . .	58
4.4	Vorticity fields for each of the main vortex shedding modes {P+S, 2S, 2P, 2P <sub>O</sub> } . . . . .	60
4.5	Contours of the force in phase with velocity, $C_Y \sin \phi$ (normalized “fluid excitation”), for $Re = 4,000$ . . . . .	63
4.6	Contours of the effective added mass, $C_{EA}$ , for $Re = 4,000$ . . . . .	64
4.7	Cuts of constant normalized velocity, $U^*$ , for $Re = 4,000$ and $m^* = 10.0$ . . . . .	65
4.8	Force and energy transfer time traces in the 2P <sub>O</sub> –2P overlap region	66
4.9	Vorticity fields and decomposed force time traces in the 2P <sub>O</sub> –2P overlap region . . . . .	67

4.10	Vorticity fields for decreasing amplitude in the 2P region ( $\lambda^* = 8.0$ )	69
4.11	Prediction of a free vibration response at high and low mass-damping . . . . .	70
4.12	Schematic plots of an “energy portrait” . . . . .	74
4.13	Energy portrait for $m^* = 10, U^* = 7.0$ (lower branch) . . . . .	76
4.14	Energy portrait for $m^* = 10, U^* = 5.1$ (initial and upper branch) . . . . .	77
4.15	Energy portrait for $m^* = 10, U^* = 5.1$ , showing distinct values of fluid excitation ( $E_{IN}^*$ ) for the 2S and 2P <sub>O</sub> vortex formation modes . . . . .	78
4.16	Energy portraits and amplitude response for the hysteresis mode transition . . . . .	80
4.17	Energy portrait for $m^* = 10, U^* = 6.3$ (upper and lower branches) . . . . .	82
4.18	Map of where free vibration can occur in the amplitude-wavelength plane . . . . .	85
5.1	Comparison between steady state predicted response and directly measured free vibration response ( $m^* = 10.49, \zeta = 0$ ) . . . . .	92
5.2	Representation of each of the main vortex formation modes: {2S, 2P, P+S, 2P <sub>O</sub> } . . . . .	94
5.3	Contours of $C_Y \sin \phi$ and $C_{EA}$ at $Re = 4,000$ . . . . .	102
5.4	Prediction of transient behavior for an equilibrium solution in the lower branch, $m^* = 10, \zeta = 0.001, U^* = 8.0$ . . . . .	108
5.5	Prediction of intermittent switching transient behavior, $m^* = 10, \zeta = 0.001, U^* = 6.3$ . . . . .	109
5.6	Phase switching and vortex formation modes in the 2P–2P <sub>O</sub> overlap regime . . . . .	112
5.7	Predicted amplitude response for moderate mass ratio systems . . . . .	113
5.8	Predicted amplitude response for a very low mass ratio system, $m^* = 1.0$ . . . . .	114
5.9	Comparison between measured free vibration amplitude and frequency response at $m^* = 1.19$ , and predictions from controlled vibration at $m^* = 1.0$ . . . . .	117
5.10	Map of steady and unsteady solutions in the $A^*–U^*$ plane for $m^* = 1.0$ . . . . .	118
5.11	Schematic plot showing how a void with no steady state solution occurs . . . . .	119
5.12	Predicted frequency response at different values of mass ratio . . . . .	120
6.1	Amplitude of vibration ( $A^*$ ) for varying mass ratio ( $m^*$ ) at infinite normalized velocity . . . . .	134
6.2	Locations of the operating point in the normalized amplitude-velocity plane for $Re = 12,000$ . . . . .	135
6.3	Streamlines and vorticity contours for the 2P vortex formation mode and for a desynchronized wake . . . . .	137

6.4	Schematic diagram showing how the operating point is determined . . . . .	138
6.5	Critical mass as a function of Re . . . . .	140
6.6	The regime of normalized velocity ( $U^*$ ) for a synchronized response . . . . .	141
7.1	Effect of gap size on transverse force measurements . . . . .	147
7.2	Schematic diagram of typical end conditions . . . . .	150
7.3	Free vibration response for the unattached endplate case and the no endplate case . . . . .	156
7.4	Free vibration response ( $A^*$ vs. $(U^*/f^*)S$ ) for the unattached endplate case and the no endplate case . . . . .	157
7.5	Comparison of displacement time traces between a cylinder with an unattached endplate ( $g^* = 0.04$ ), and a cylinder with no endplate . . . . .	159
7.6	Free vibration response for the unattached endplate case and the attached endplate case . . . . .	160
7.7	Time traces of transverse force ( $C_Y$ ) for an unattached endplate ( $g^* = 0.04$ ), and for no endplate in the initial and upper branches of response . . . . .	162
7.8	Time traces of transverse force ( $C_Y$ ) and phase angle ( $\phi$ ) for an unattached endplate ( $g^* = 0.04$ ), and for no endplate in the lower branch . . . . .	163
7.9	The effect of endplate gap ( $g^*$ ) on the fluid excitation ( $C_Y \sin \phi$ ) for a cylinder with an unattached endplate . . . . .	164
7.10	A summary of the amplitude responses for several different end conditions . . . . .	166
7.11	Comparison of the amplitude response among several previous vortex-induced vibration studies . . . . .	167
A.1	Contours of the magnitude of the total force ( $C_Y$ ) and the vortex force ( $C_V$ ), at Re = 4,000 . . . . .	171
A.2	Contours of the total phase ( $\phi$ ) and the vortex phase ( $\phi_V$ ) at Re = 4,000 . . . . .	172
B.1	Contours of $C_Y \sin \phi$ at Re = 12,000 . . . . .	174
B.2	The effect of mass-damping and Re on peak amplitude of response	175
C.1	Vorticity fields for the 2S mode of vortex formation ( $A^* = 0.5, \lambda^* = 5.0$ ) . . . . .	178
C.2	Vorticity fields for the P+S mode of vortex formation ( $A^* = 1.2, \lambda^* = 4.0$ ) . . . . .	179
C.3	Vorticity fields for the 2P <sub>0</sub> mode of vortex formation ( $A^* = 0.8, \lambda^* = 5.6$ ) . . . . .	180

C.4	Vorticity fields for the 2P mode of vortex formation ( $A^* = 0.8, \lambda^* = 5.6$ ) . . . . .	181
C.5	Vorticity fields for the 2P mode of vortex formation ( $A^* = 0.6, \lambda^* = 6.4$ ) . . . . .	182
C.6	Vorticity fields for the 2P mode of vortex formation ( $A^* = 1.2, \lambda^* = 8.0$ ) . . . . .	183
D.1	Force time trace and spectrum for a controlled vibration run in the desynchronized wake regime, ( $A^* = 0.3, \lambda^* = 9.4$ ) . . . . .	185
D.2	Displacement time trace, force time traces, and spectra for a free vibration run in the desynchronized wake regime, ( $U^* = 10.54$ ) .	186
D.3	Predicted cylinder motion in the desynchronized regime for $m^* = 10$ . . . . .	189
D.4	Predicted cylinder motion in the desynchronized regime for $m^* = 0.5$ . . . . .	189

## CHAPTER 1

# Introduction

When a bluff body such as a circular cylinder is placed in a fluid flow, a series of alternately signed vortices may form in the wake, called a Von Kármán vortex street, which will yield a periodic force on the body. If the body is part of an elastic structure, the oscillating forces may induce vibration of the structure in a phenomenon known as vortex-induced vibration. This vibration is a significant problem in many fields of engineering, leading to fatigue and eventually failure of various structures such as oil riser tubes, heat exchanger tubes, bridges, and chimneys. The wide range of problems involving vortex-induced vibration has led to a large number of experimental and computational studies on the subject, including several review articles such as Sarpkaya (1979), Bearman (1984), Parkinson (1989), and more recently Williamson & Govardhan (2004); as well as several books such as Blevins (1990), Naudascher & Rockwell (1994), and Sumer & Fredsoe (1997).

In this study, we focus on the most conceptually simple instance of vortex-induced vibration: the case of a circular cylinder constrained to move only transverse to a uniform incoming flow. Such a system is often used as a paradigm for understanding more complicated cases, such as multiple degrees of freedom, pivoted cylinders, or flexible cables. Our approach is to use controlled vibration, where we prescribe the motion of the cylinder, and measure the fluid forcing and the wake vortex dynamics over a wide range of oscillating amplitudes and frequencies. From this data, we can make predictions about the response of a freely vibrating, elastically mounted cylinder (free vibration

case), as well as provide deeper insight into various vortex-induced vibration phenomena.

This controlled vibration approach has been employed by several prior studies, for example: Mercier (1973), Sarpkaya (1977), Staubli (1983), Gopalkrishnan (1993), Hover, Techet & Triantafyllou (1998), Carberry, Sheridan & Rockwell (2001), Carberry, Sheridan & Rockwell (2005). In this study, we conduct a new set of controlled vibration force measurements with two main goals: (1) to carefully match the experimental conditions between free vibration and controlled vibration and (2) to obtain much higher resolution of the force data (in terms of amplitude and frequency of vibration) than in any prior study.

In this dissertation, each chapter forms a self-contained study, and therefore includes its own detailed Introduction section and Conclusions section. However, we have found it convenient to place all the references together at the end of the dissertation.

In Chapter 2, we examine the relationship between controlled vibration and free vibration by directly comparing force measurements between the two cases. We show that if the cylinder dynamics as well as all aspects of the experimental arrangement are carefully matched, controlled vibration can yield fluid forcing in close agreement with measurements from free vibration.

In Chapter 3, we make extensive measurements of the fluid forcing for a cylinder undergoing controlled vibration over a wide range of normalized amplitude and wavelength at  $Re = 4,000$ . These measurements are used to generate very high resolution contours of various fluid forcing quantities. From these contours, we identify different fluid forcing regimes and characterize the wake

dynamics in each of these regimes using PIV measurements of the wake vorticity.

These very high resolution force contours are used to make predictions regarding the response of a freely vibrating cylinder in Chapter 4. We also introduce the concept of an “energy portrait”, which is a plot of the energy transfer into the body motion, and the energy dissipated by damping, as a function of normalized amplitude. These energy portraits allow us to predict the existence of stable and unstable equilibrium solutions, and to show how the vibration system may exhibit a hysteretic mode transition, or intermittent switching, both of which correspond with such phenomena measured from free vibration.

We extend our force contours to predict unsteady and transient cylinder dynamics in Chapter 5 by introducing a quasi-steady model, which assumes that our measurements of force for a sinusoidally oscillating cylinder can be applied to the case where the amplitude or frequency of oscillation is varying.

In Chapter 6, we use our force contours to predict the critical mass phenomena in vortex-induced vibration. As found by Govardhan & Williamson (2002), if the mass of the oscillating structure falls below a certain critical value, resonant vibration can persist up to infinite normalized velocity. Using our controlled vibration data as well as some new measurements of the dynamics of a cylinder oscillating with no restoring force, we determine the effect of  $Re$  on the critical mass ratio.

Finally, in Chapter 7 we explore the effect of spanwise end conditions on vortex-induced vibrations, both for free vibration and controlled vibration.

## CHAPTER 2

# **Employing controlled vibrations to predict fluid forces on a cylinder undergoing vortex-induced vibration**

MORSE, T. L. & WILLIAMSON, C. H. K. (2006)

Published in *Journal of Fluids and Structures* **22**, 877-884.

In the present study, we measure the fluid forces on a vertical cylinder that is forced to vibrate transversely to a water channel flow, and compare directly to the forces encountered by freely vibrating cylinders, under conditions where we carefully match the amplitude, frequency, and Reynolds number ( $Re$ ) of the two cases. A key point is that we use precisely the same cylinder and submerged flow configuration for both the free and controlled cases. Where the free vibration exhibits closely sinusoidal motion, the controlled sinusoidal motion yields forces in close agreement with the free vibration case. Although this result might be expected, previous comparisons have not been uniformly close, which highlights the importance of matching the experimental conditions precisely, and of accurately measuring the phase between the force and body motion. For a lightly damped system, which is perhaps the most significant case to analyze, one typically finds that the maximum response amplitude is quite unsteady. One might conventionally expect prediction of forces to be difficult in such cases. However, it is of practical significance that even in this case, a quasi-steady approximation is effective. This is a significant point because it suggests that controlled vibration measurements for constant amplitude motion might

remain applicable to free vibration systems undergoing even transient or intermittent motions.

## 2.1 Introduction

The problem of vortex-induced vibration is of interest to many fields of engineering. It affects, for example, the dynamics of riser tubes bringing oil from the seabed to the surface, the flow around heat exchanger tubes, and the design of civil engineering structures such as bridges and chimneys. An overview of recent phenomena in vortex-induced vibration can be found in the review by Williamson & Govardhan (2004).

The case of an elastically mounted rigid cylinder that is confined to move transversely to the flow is often used as a paradigm for understanding the problem of vortex-induced vibration in general. Such a system, for low mass and damping, has been shown to have three branches of response as the normalized velocity is increased: an initial branch, upper branch, and lower branch, with a hysteresis between the initial and upper branches, and intermittent switching between the upper and lower branches (Khalak & Williamson, 1999). A central question in the study of vortex-induced vibration of an elastically mounted (free vibration) cylinder is to what extent can results from controlled vibration experiments, where the cylinder is prescribed to have a sinusoidal motion, be applied to the case where the cylinder oscillates freely under vortex-induced motion.

There have been many studies of controlled vibrations of cylinders. For example, Mercier (1973), Sarpkaya (1977), and Carberry *et al.* (2001, 2005) measured the forces on a cylinder that is controlled to oscillate with constant ampli-

tude, over a range of frequencies. Carberry *et al.* also used DPIV (digital particle image velocimetry) to examine the wake vortex dynamics. Staubli (1983) and Gopalkrishnan (1993) made force measurements over a range of amplitudes and frequencies. However, very few past investigations have focused on direct comparisons of fluid forces between the two cases of controlled vibration and free vibration, *using precisely the same experimental arrangements* for the submerged cylinder, except for the recent works of Triantafyllou, Hover and co-workers at MIT using their Virtual Cable Testing Apparatus in a towing tank Hover *et al.* (1998). In the present study, we have carefully matched the experimental arrangement between free and controlled vibration cases, which appears to be important if one wants to accurately compare predicted and measured responses for freely vibrating systems.

For an elastically mounted cylinder, when the body oscillation frequency is synchronized with the periodic vortex mode, the force,  $F(t)$ , and the response displacement,  $y(t)$ , are often approximated by the following representations:

$$F(t) = F_0 \sin(2\pi ft + \phi) \quad (2.1)$$

$$y(t) = A \sin(2\pi ft) \quad (2.2)$$

The phase angle,  $\phi$ , between the fluid force and the body displacement is crucial in determining the energy transfer from the fluid to the body, which in this simplified case, is given by:

$$E = \pi A F_0 \sin \phi \quad (2.3)$$

This energy input is balanced by the energy dissipated due to the structural damping. Therefore, for free vibration to occur, the phase angle must lie in the range  $\phi = 0^\circ - 180^\circ$ . For very low mass-damping, (which leads to the highest

peak amplitude), the energy dissipated is very low, and thus the phase is close to  $0^\circ$ , or close to  $180^\circ$ . This presents a difficulty in accurately predicting free vibration at low mass-damping with controlled vibration experiments, because a small difference in phase angle of just 2-4 degrees can cause the system to change from positive to negative excitation.

## 2.2 Experimental Details

The present experiments were conducted in the Cornell-ONR Water Channel, which has a cross-section of 38.1 cm x 50.8 cm. The turbulence level in the test section of the water channel was less than 0.9% over the range of velocities (5-30 cm/s) used in this study. A cylinder of diameter 3.81 cm and length 38.1 cm was suspended vertically in the water channel and forced to oscillate transverse to the flow using a computer controlled motor attached to a transverse lead screw. A fixed end plate was placed 2 mm below the bottom of the cylinder (but not in contact with the cylinder) to encourage two-dimensional vortex shedding, following the study of Khalak & Williamson (1996). The range of  $Re$  in this study was 2400 - 6800.

A two-axis force balance utilizing LVDTs (linear variable distance transducers) was used to measure the lift and drag forces on the cylinder. The transverse displacement of the cylinder was measured using a non-contact (magnetostrictive) position transducer. The measured force signals were filtered using a low-pass filter at 5Hz. The small phase lag due to filtering (typically  $3^\circ - 4^\circ$ ) was carefully measured, and the force signals were systematically adjusted to account for it. Also, the inertial forces in the transverse direction were subtracted

from the total measured force. Instantaneous phase information was obtained through use of the Hilbert transform, where we follow closely the details described in Khalak & Williamson (1996).

### 2.3 Direct comparison to free vibration

In our experiments, we chose to directly match the values of  $A^*$ ,  $U^*/f^*$ , and  $Re$  at several points in the initial, upper, and lower amplitude branches of the free vibration response of Govardhan & Williamson (2000), shown in Figure 2.1. (In this study,  $A^* = A/D = \text{amplitude/diameter}$ ;  $U^*/f^* = U/fD$ , where  $U = \text{free stream velocity}$ ,  $f = \text{oscillation frequency}$ .) The measured transverse force coefficient for controlled vibrations agrees very well with the free vibration data in all three response branches. The phase angle also agrees well in all three branches, but is very close to  $0^\circ$  in the initial and upper branches, and very close to  $180^\circ$  in the lower branch. This illustrates the sensitive nature of measuring the phase angle to predict the correct sign of energy transfer.

We might expect good agreement between sinusoidal controlled vibration and free vibration in the lower branch, where the free vibration response is close to sinusoidal. We show, in Figure 2.2, time traces of position, force, and phase, from free vibration in the lower branch, and the corresponding time traces from a controlled vibration experiment at the same amplitude and frequency. The free vibration motion is so periodic that it is difficult to tell which time trace is controlled and which is free. However, one might ask how successful is controlled vibration in regions of intermittent switching, where the response is known to jump between the upper branch and the lower branch (Khalak &

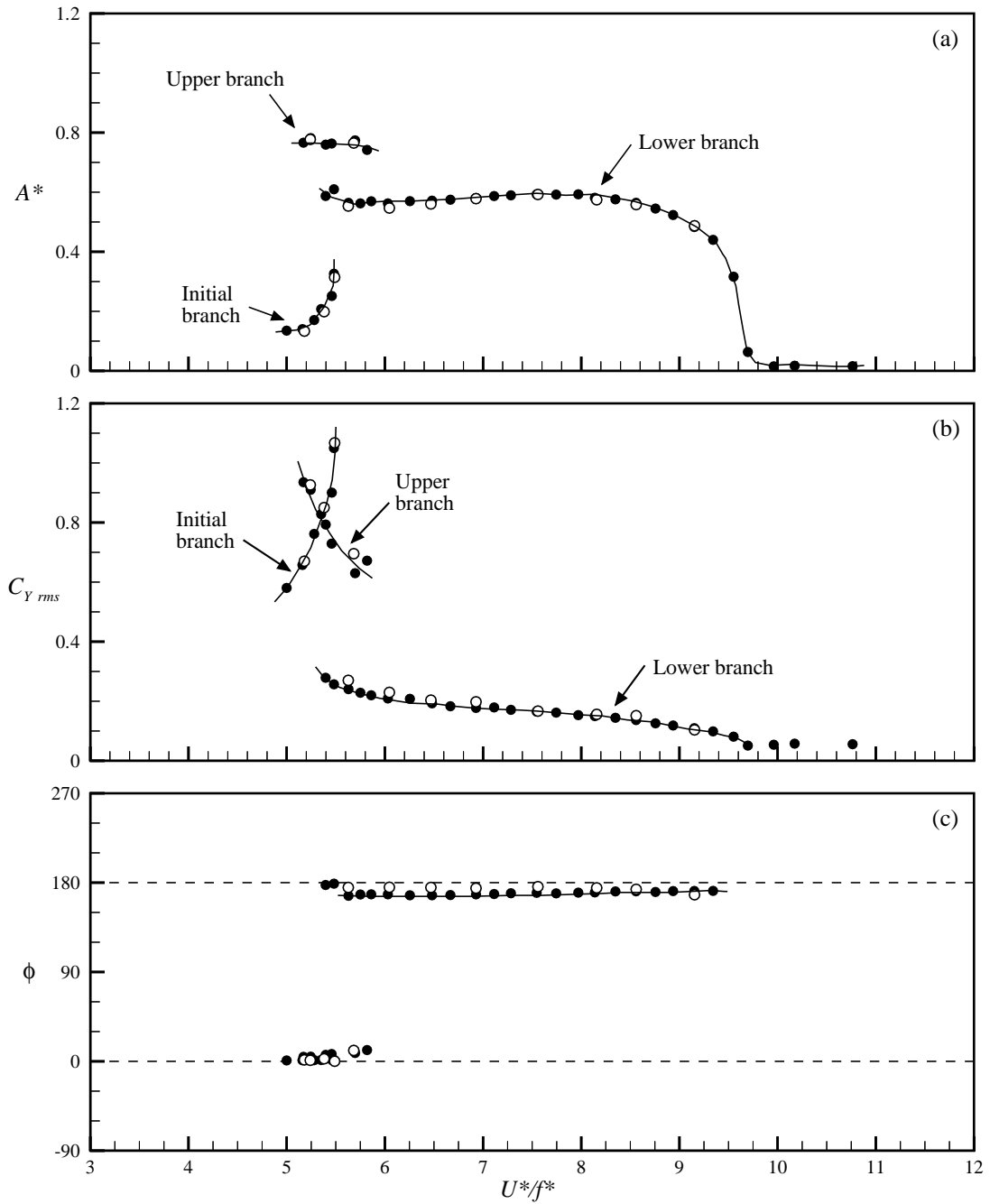


Figure 2.1: Direct comparison of controlled and free vibration at the matched values of  $\{A^*, U^*/f^*, Re\}$ . • Free vibration,  $m^* = 8.6$ ,  $\zeta = 0.0016$  (Govardhan & Williamson, 2000). ◦ Sinusoidal controlled vibration (present results).  $Re = 2400 - 6800$ .

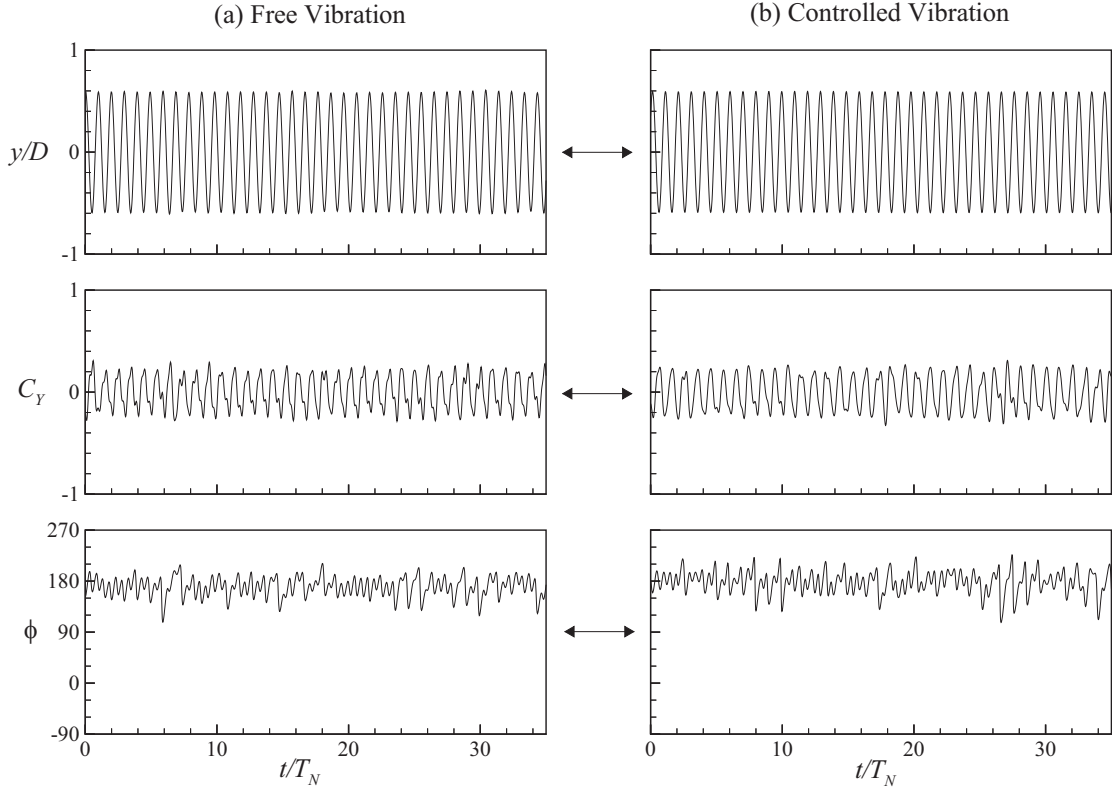


Figure 2.2: Comparison of the position, force coefficient, and phase time traces in the lower branch,  $U^*/f^* = 7.55$ , for both free vibration (a) and controlled vibration (b).

Williamson, 1999). This is an important question if we want to be able to accurately predict peak amplitudes (which are especially of interest to practicing engineers) since the peak amplitude in free vibration occurs where there can exist intermittent mode switching, for systems of low mass and damping.

We focus on the regime of intermittent switching in Figure 2.3. Our approach here is to treat the motion as quasi-steady. We matched the amplitude and frequency of the upper branch, and separately matched the amplitude and frequency of the lower branch, using sinusoidal controlled vibrations. The intriguing result is that even in regions of intermittent switching, where the cylinder is jumping between modes, sinusoidal controlled vibration reasonably represents

the force and phase angle of free vibration during periods when the system resides in one state or the other. This suggests that one might use controlled vibration results to accurately predict the peak amplitude of a freely vibrating body, even in the presence of unsteady vibrations.

## 2.4 Controlled vibration at constant amplitude

In addition to comparing with free vibration results, we also performed controlled vibration experiments to compare directly with the controlled vibration results of Carberry *et al.* (2005) for constant values of amplitude. We matched  $A^* = 0.5 = \text{constant}$ ,  $\text{Re} = 4,400$  and varied  $(U^*/f^*)$ , as in their study. In order to relate such a constant amplitude controlled vibration experiment to free vibration, we plot our chosen amplitude conditions in Figure 2.4 and compare with a typical free vibration response plot. We find a phase angle below  $180^\circ$  for controlled vibration over the regime of  $(U^*/f^*) = 5.5 - 9.5$ , corresponding to the lower branch, yielding positive energy transfer, which is consistent with the fact that the free vibration response exists in this regime. It is particularly interesting that the phase exceeds  $180^\circ$  at  $(U^*/f^*) = 9.5$ , suggesting a switch from positive to negative excitation, at a point which is roughly where the free vibration becomes desynchronized and where the amplitude,  $A^*$ , falls below 0.5. We also see a jump in the force and phase at  $(U^*/f^*) = 5.6$  which corresponds to where a mode transition is seen in the free vibration response. The sudden switch to negative energy transfer at this point would suggest that free vibration would not exist for  $(U^*/f^*) < 5.6$ , which is what one finds for elastically mounted bodies at this level of amplitude,  $A^* = 0.5$ .

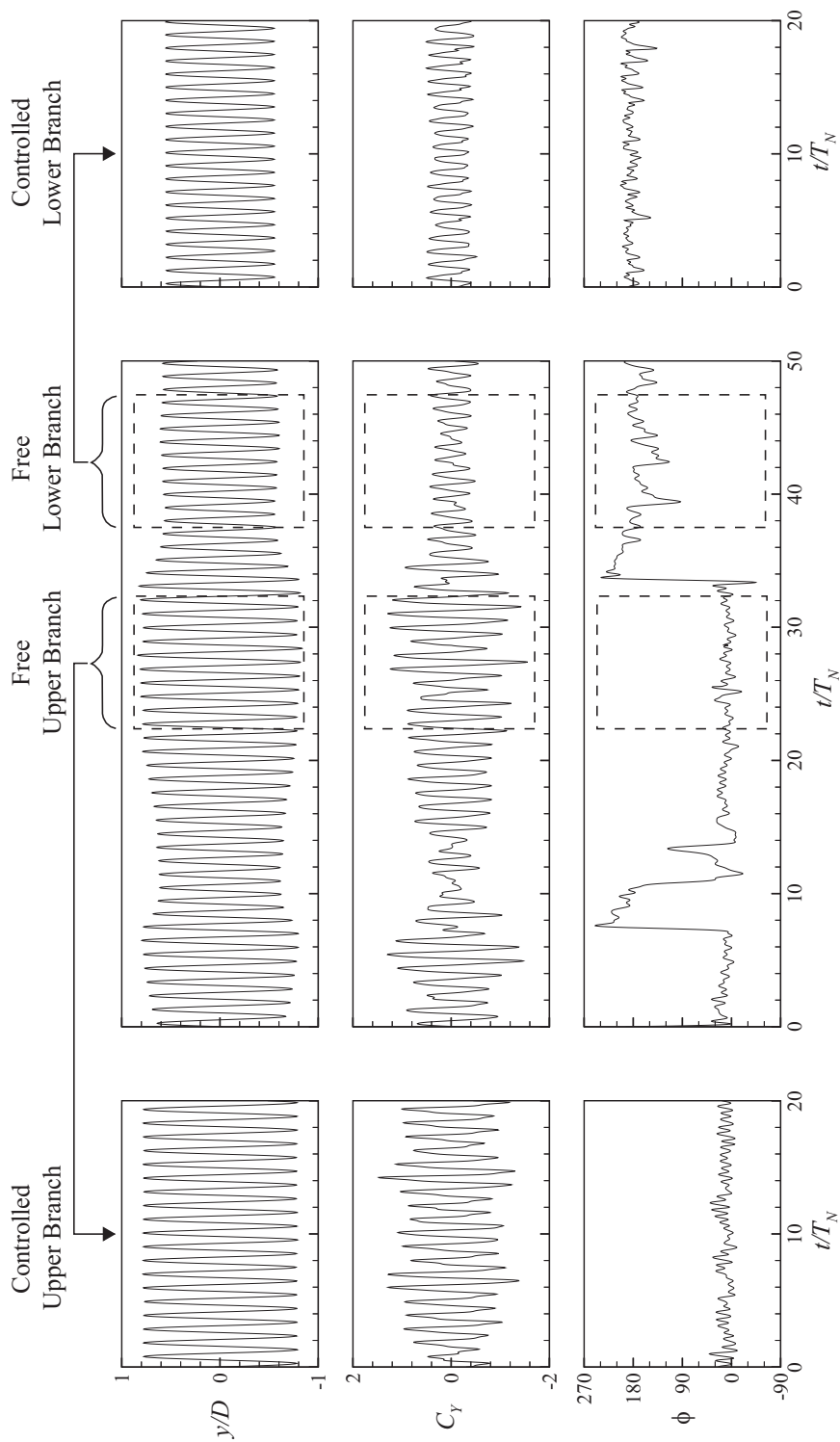


Figure 2.3: The position, force coefficient, and phase angle time traces in the intermittent switching region of the free vibration response,  $U^*/f^* = 5.6$ . By matching the upper branch free response conditions with sinusoidal controlled vibration, we find reasonable agreement of the force and phase angle. Separate matching for the lower branch yields similarly good agreement of force and phase.

We find excellent agreement in the measurement of the force coefficient between our data and those of Carberry *et al.* (2005), in the lower branch of response. The fact that Carberry *et al.* find negative energy transfer over part of this lower branch regime, where free vibrations are found in previous studies, could perhaps be related to quite different experimental arrangements. While in our setup the cylinder was suspended vertically in the water channel and oscillated above a fixed end plate, Carberry *et al.* supported the cylinder horizontally with end plates that moved with the cylinder. It is possible that differences in experimental arrangements would influence the measurement of force and phase.

## 2.5 Conclusions

Our controlled vibrations of a cylinder are arranged to carefully match the amplitude, frequency, and Reynolds number of an elastically mounted cylinder at low mass and damping. Despite the fact that one might naturally expect good agreement between the forces if the free and controlled vibrations are both close to sinusoidal, since the body effectively follows almost the same path through the fluid, previous comparisons have not necessarily been close. We may conclude that it is important to carefully match the experimental conditions between free and controlled vibration, such as in the present study, or in the experiments of Hover *et al.* (1998), to accurately predict forces applicable to free vibration. At low mass and damping, the excitation needed to balance the energy dissipation is small, and so the phase of the fluid force is also small, thus the precise measurement of phase is very important.

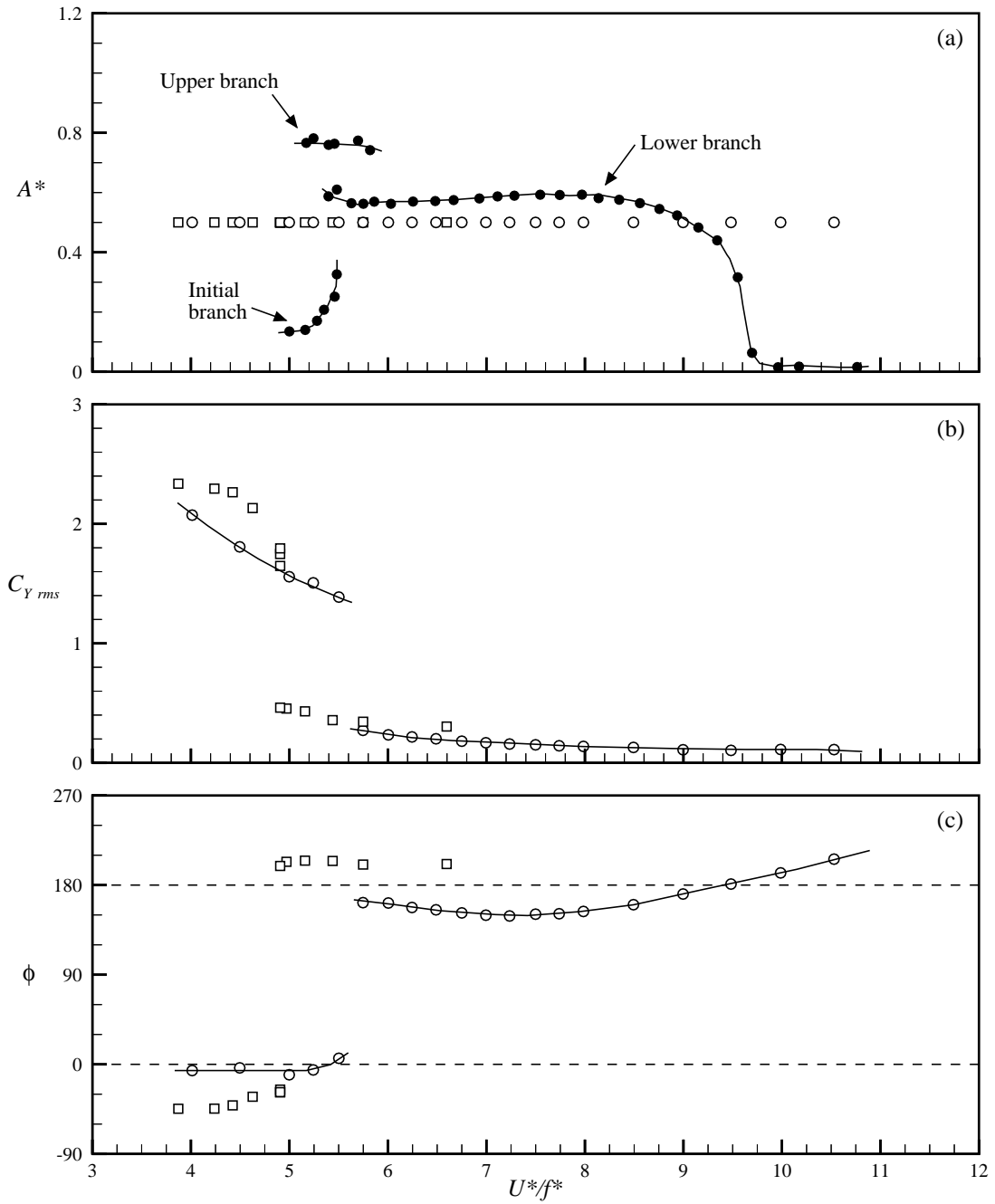


Figure 2.4: Controlled sinusoidal vibrations at constant  $A^* = 0.5$ ,  $Re = 4,400$ . ● Free vibration response plot,  $m^* = 8.6$ ,  $\zeta = 0.0016$  (Govardhan & Williamson, 2000). ○ Sinusoidal controlled vibration (present results). □ Sinusoidal controlled vibration from Carberry *et al.* (2005).

In cases of very low mass and damping, the peak amplitude response of a lightly-damped body is quite unsteady; the cylinder is subject to an intermittent switching between an upper and a lower response amplitude branch, where close comparison with forced vibration results is more difficult. However, it is of practical significance that even in this case, a quasi-steady approximation is effective. For example, if one vibrates the body in a controlled steady state oscillation corresponding to the upper branch conditions, the forces compare well with such measurements taken over intermittent time periods when the free system resides in the upper response branch. The same is true of the lower branch response conditions. This is an important point because it suggests that controlled vibration measurements for constant amplitude motion might remain applicable, in a *quasi-steady manner*, to free vibration systems undergoing even transient motions with unsteady amplitudes. In our further work, it also appears that this quasi-steady approach will yield insight into the mode jumps that occur as the freely vibrating system transitions between different response amplitude branches.

A subject of recent debate has been the relevance of controlled vibration to accurately predicting free vibration. The present results, with precise matching of experimental conditions, suggest that controlled vibration, even with strictly sinusoidal motion, can indeed reasonably predict free vibration responses, at least over the parameter space so far investigated.

## CHAPTER 3

# Fluid forcing, wake modes, and transitions for a cylinder undergoing controlled oscillations

MORSE, T. L. & WILLIAMSON, C. H. K. (2009)

To appear in *Journal of Fluids and Structures*.

In this study, we make extensive measurements of the fluid forces on a cylinder that is controlled to oscillate transverse to a free stream at  $Re = 4,000$ . These measurements are used to create very high resolution contour plots (considerably higher than in any previous study) of the magnitude of fluid forcing, and its phase relative to the cylinder motion (as well as other fluid forcing quantities) in the plane of normalized amplitude and wavelength. Previous contours of force have been assumed to be continuous in the amplitude-wavelength plane, despite the fact that jumps in the fluid forcing and vortex formation modes were known to occur in other studies, including free vibration. In this investigation, we find clear discontinuities in the force contours, and we are thus able to identify boundaries separating different fluid forcing regimes. These appear remarkably similar to boundaries separating different vortex shedding modes in the Williamson & Roshko (1988) map of regimes. Measurements of vorticity fields confirm the modes of vortex formation in each regime; we find the 2S, 2P, and P+S modes, as well as a regime where the vortex formation is not synchronized with the cylinder oscillation. A new characteristic, which is only observable with very high-resolution data, is the existence of a region where two vortex formation regimes overlap. In the overlap region, we identify a distinct mode of vortex formation where two pairs of vortices are shed per cycle of

oscillation (similar to the 2P mode) but the secondary vortex is much weaker, which we have termed '2P<sub>OVERLAP</sub>', or simply the '2P<sub>O</sub>' mode. The wake can switch intermittently between the 2P and 2P<sub>O</sub> modes, even as the cylinder is oscillating with constant amplitude and frequency. The highest amplitude yielding positive fluid excitation lies inside the overlap region, therefore a study of the vortex dynamics in this region is essential to understanding the behavior of a free vibration system at peak amplitude response.

### 3.1 Introduction

Much of the interest in the flow around a cylindrical body oscillating transversely to a free stream is due to its relevance to vortex-induced vibration, which occurs when a body is placed in a flow and the fluctuating lift force due to the asymmetric formation of vortices in the wake causes the body to vibrate. Vortex-induced vibration is an important problem in many fields of engineering, affecting the dynamics of riser tubes bringing oil from the seabed to the surface, as well as civil engineering structures such as bridges, chimneys, and buildings, among other applications. The range of problems caused by vortex-induced vibration has led to a large number of experimental and computational studies on the subject, including several review articles, for example: Sarpkaya (1979), Griffin & Ramberg (1982), Bearman (1984), Parkinson (1989), Williamson & Govardhan (2004).

In the present study, we are interested in the fluid forcing and wake modes that arise from controlled vibration, where a cylinder is prescribed to move with a sinusoidal motion transverse to a free stream. For such a motion, the relevant

Table 3.1: Non-dimensional groups. In the groups below,  $U$  is the free-stream velocity,  $\lambda$  is the oscillation wavelength,  $f$  is the oscillation frequency,  $D$  is the cylinder diameter,  $L$  is the submerged cylinder length,  $\nu$  is the fluid kinematic viscosity,  $\rho$  is the fluid density, and  $F_Y$  is the transverse fluid force.

Normalized wavelength	$\lambda^*$	$\frac{\lambda}{D} = \frac{U}{fD}$
Normalized amplitude	$A^*$	$\frac{A}{D}$
Transverse force coefficient	$C_Y$	$\frac{F_Y}{\frac{1}{2}\rho U^2 DL}$
Reynolds number	$Re$	$\frac{\rho U D}{\mu}$

parameters, in addition to Reynolds number ( $Re$ ), are the oscillation amplitude ( $A$ ), and the oscillation wavelength ( $\lambda$ ), or the oscillation frequency ( $f$ ), which in this study we non-dimensionalize as shown in Table 3.1. The normalized wavelength,  $\lambda^* = \lambda/D = U/fD$  is equivalent to the ratio  $U^*/f^*$  used in free vibration studies such as Govardhan & Williamson (2000) where  $U^* = U/f_N D$ ,  $f^* = f/f_N$  with  $f_N$  being the natural frequency of the structure. The normalized wavelength may also be multiplied by the Strouhal number ( $S$ ) to obtain the ratio of the stationary cylinder shedding frequency ( $f_{vo}$ ) to the actual oscillation frequency ( $f$ ), i.e.  $\lambda^* S = f_{vo}/f$ . In the present study, the Strouhal number was found to be 0.207.

The measured transverse force is often approximated by a sinusoidal function, thus the motion and force is often represented by:

$$y(t) = A \sin(\omega t) \quad (3.1)$$

$$F(t) = F_{Y0} \sin(\omega t + \phi) \quad (3.2)$$

For certain regions of the parameter space, the fluid forcing exhibits somewhat non-sinusoidal behavior. However, in general, we shall present the component of forcing that occurs at the fundamental (body oscillation) frequency, based on a Fourier series analysis. This is the most relevant component, because other frequency components will not yield a net contribution to the energy transfer between the fluid and the body. The transverse force coefficient (at the fundamental) can be decomposed into two components, one in phase with velocity,  $C_Y \sin \phi$  (which yields the “fluid excitation”), and one in phase with acceleration,  $C_Y \cos \phi$  (which yields the “effective added mass”). The phase,  $\phi$ , between the fluid forcing and cylinder motion is an extremely important parameter as it determines whether the fluid adds or removes energy from the system and thus whether free vibration is possible.

There are several existing classical studies on fluid forcing for a cylinder undergoing controlled vibration. In a pioneering study, Bishop & Hassan (1964) showed that as the frequency of cylinder oscillation increases, there is a simultaneous jump in the magnitude of the fluid force ( $C_Y$ ) and its phase ( $\phi$ ), which occurs at an oscillation frequency close to the frequency of vortex shedding for a stationary cylinder. Subsequent controlled vibration studies, such as the measurements of force for particular broadly spaced values of amplitude (which we shall call “amplitude cuts”) by Mercier (1973), and Sarpkaya (1977) have also found sharp jumps in the fluid forcing near the natural vortex shedding frequency for a stationary cylinder. In the present work, one of our objectives is to identify precisely the location of this jump, and other such force jumps, *throughout the normalized amplitude-wavelength plane* using our extremely high-resolution force data.

In order to make predictions of the response of an elastically mounted cylinder, Staubli (1983) generated contour plots of the lift force magnitude and phase angle from his controlled vibration force measurements. He compared his predictions to the free vibration measurements of Feng (1968), and found some regions of the response where the comparison is successful, and other regions where the comparison is not close. The most extensive force measurements to date come from Gopalkrishnan (1993), and Hover *et al.* (1998) who generated complete contour plots of the fluid forcing over a wide range of normalized amplitude and wavelength. The zero fluid excitation curve ( $C_Y \sin \phi = 0$ ) obtained from these contours was shown in Hover *et al.* (1998) to have generally good agreement with a free vibration response at very low mass-damping (as one might expect), however some portions of the response lay in regions where the force data from controlled vibration predicted negative excitation.

One important question for these controlled vibration studies is to what extent can their results be applied to the case of a freely vibrating, elastically mounted cylinder. As mentioned above, and pointed out by Williamson & Govardhan (2004), as well as Carberry *et al.* (2004), several past controlled vibration studies have found negative fluid excitation for values of normalized amplitude and wavelength at which free vibration is known to occur, suggesting that controlled vibration results may not necessarily be used to predict accurately the free vibration case. However, in Chapter 2 (Morse & Williamson, 2006) we make direct comparisons between free and controlled vibration and show that *if the experimental conditions are carefully matched*, controlled vibration can yield fluid forces which are in very close agreement with results from free vibration, over an entire response plot.

In addition to these force measurements, there have been several studies focusing on the wake of an oscillating cylinder. Ongoren & Rockwell (1988a) examined the near wake of an oscillating circular cylinder as well as several other body geometries and found that there is a switch in timing of the vortex formation across the phase jump found by Bishop & Hassan (1964). Williamson & Roshko (1988) conducted an extensive study of the different vortex shedding modes that exist for an oscillating cylinder, which they defined, for example, as a '2S' mode indicating two single vortices formed per cycle, a '2P' mode meaning two pair of vortices formed per cycle, and an asymmetric 'P+S' mode comprising a pair of vortices and a single vortex per cycle. They mapped out where these modes occur in the plane of normalized amplitude and wavelength as may be seen later in Figure 3.3(b). Ongoren & Rockwell (1988b) observed patterns similar to the 2S, 2P, and P+S modes for the case of a cylinder oscillating in-line with the flow.

Carberry *et al.* (2001) made simultaneous force and wake vorticity measurements in controlled vibration. They showed that the well-known jump in fluid forcing described above was due to a change in vortex formation pattern from the 2P to the 2S mode, which is consistent with the free vibration results of Govardhan & Williamson (2000). This transition was further characterized with various chosen "amplitude cuts" and Reynolds numbers in Carberry *et al.* (2005). They found that at frequencies ( $f$ ) near the (stationary cylinder) shedding frequency ( $f_{vo}$ ), the vortex shedding mode depended on the initial conditions and in fact, for a certain band of frequencies, the wake could make a one-time transition from one mode to the other, even while the frequency was held constant. Pottebaum (2003) conducted experiments on heated cylinders oscillating in a flow and found that, in certain regimes, the wake could switch in-

termittently between the 2S and 2P modes. He concluded that this phenomenon was likely due to temperature induced variations in the fluid viscosity. In the present study, we will show regions where the wake switches intermittently between vortex formation modes, in the absence of any temperature variations.

In this work, we conduct controlled vibration experiments over an extensive range of normalized amplitude and wavelength with very high resolution, much higher than in any previous data set, as shown in Figure 3.1, amounting to 5,680 experimental runs, each of which comprises 100 cycles of oscillation. One of the original motivations for the force data presented here was to obtain very high resolution force contours using precisely the same flow facility and experimental arrangement as in Govardhan & Williamson (2000, 2006), in order to make accurate predictions of the free vibration response. Comprehensive analysis and further extensive measurements linking controlled vibration with free vibration response is presented in Chapter 4 (Morse & Williamson, 2009c). In the present study, we focus on defining the regimes of vortex shedding and especially on the transitions between these regimes.

Following a description of the experimental details in §3.2, we show contours of fluid forcing obtained from our high resolution data in §3.3. Boundaries between vortex shedding modes are determined by looking for abrupt jumps in the character of the fluid forcing. We also present DPIV measurements of the vorticity for these different modes. In §3.4 we characterize the mode boundaries by looking more closely at time traces of the fluid forcing. This is followed by the conclusions in §3.5.

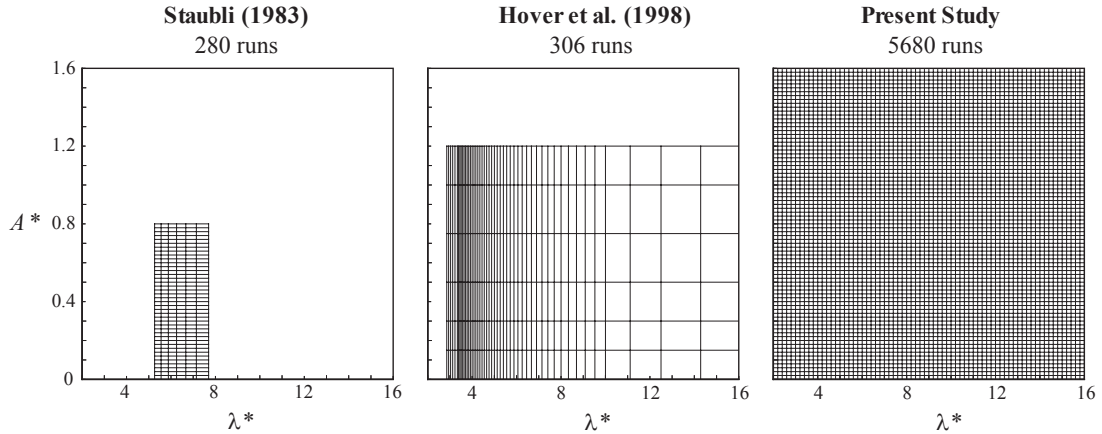


Figure 3.1: Grid resolution of controlled vibration measurements from previous studies and in the present study. We are able to obtain a very high resolution, as well as a wide range of the parameters.

## 3.2 Experimental Details

The present experiments are conducted in the Cornell-ONR Water Channel, which has a cross-section of 38.1 cm x 50.8 cm. The turbulence level in the test section of the water channel is less than 0.9%. A cylinder of diameter 3.81 cm and length 38.1 cm is suspended vertically in the water channel and forced to oscillate transverse to the flow using a computer-controlled motor attached to a transverse lead screw, as shown schematically in Figure 3.2. The flow speed is kept constant to give  $Re = 4,000$ . A fixed end plate is placed 2 mm below the bottom of the cylinder (but not in contact with the cylinder) to encourage two-dimensional vortex shedding, following the study of Khalak & Williamson (1996). A total of 5,680 runs, each for 100 cycles of oscillation, are conducted for approximately 500 hours worth of data. Normalized amplitude, ( $A^*$ ) is varied from 0.02 to 1.6 with a resolution of 0.02. Normalized wavelength, ( $\lambda^*$ ) is varied from 2 to 16 with a resolution of 0.2. Such an extensive data set is only possible because the experiment is conducted in a continuously flowing water channel

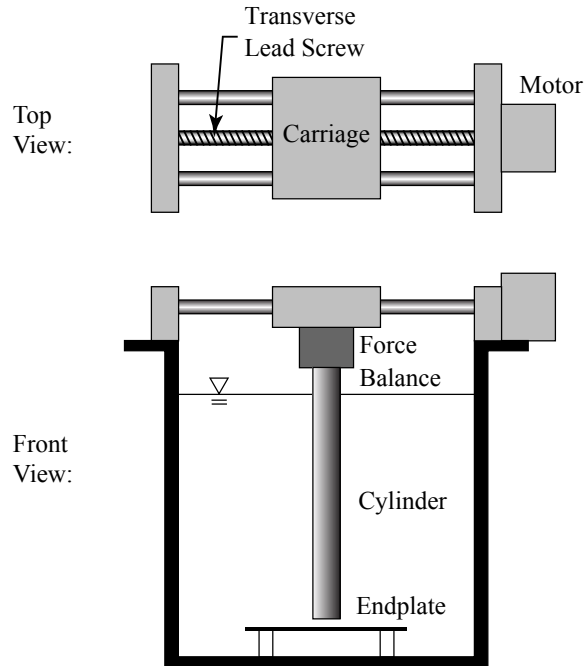


Figure 3.2: Schematic diagram of the experimental arrangement. The cylinder is suspended vertically in a water channel and is oscillated transverse to the flow (into the page) using a computer controlled motor and lead screw.

facility, and thus can be automated to run unattended for a large number of experimental runs.

A two-axis force balance utilizing LVDTs (linear variable distance transducers) is used to measure the lift and drag forces on the cylinder. The transverse displacement of the cylinder is measured using a non-contact (magnetostrictive) position transducer. For each run, the fluid force magnitude and phase angle (relative to the body motion) at the fundamental (body oscillation) frequency is calculated using a Fourier series analysis. In most cases, the fluid forcing is quite sinusoidal and thus the component at the fundamental frequency represents essentially all of the force signal content. In some cases, which are discussed in §3.4.3 (for example, in the desynchronized regime), the fluid forcing is less sinusoidal, and the component at the fundamental may represent only a small

portion of the total force signal content.

In addition to the extensive force measurements described above, we also use Digital Particle Image Velocimetry (DPIV) to examine the cylinder wake. The flow is seeded with 14-micron silver coated glass spheres, which are illuminated by a sheet of laser light from a 50 mJ Nd:Yag pulsed laser. Pairs of particle images are acquired using a Jai CV-M2CL CCD camera (1600 x 1200 pixels), and analyzed using cross-correlation of sub-images. We use a two-step windowing process (with window shifting) to obtain particle displacements between image pairs. The viewing area is 26 cm x 34 cm corresponding to 6.75 by 9 diameters. The time between images is adjusted to vary between 10 and 20 ms depending on the cylinder oscillation parameters. Vorticity fields calculated from the image pairs are phase averaged over approximately 10 to 20 cycles to remove the smaller weak structures resulting from intermittent small-scale three-dimensionality in the flow and thus obtain a clear picture of the dynamics of the principal spanwise vorticity.

### **3.3 Fluid forcing contours and vortex formation modes**

Upon examining our controlled vibration data, we notice that the fluid forcing shows qualitative abrupt jumps in certain regions as amplitude or frequency is varied. By following these jumps throughout the normalized amplitude-wavelength plane, we are able to identify clear boundaries separating regions of distinct fluid forcing, indicated by the colored regimes in Figure 3.3(a). When these boundaries are compared to the boundaries separating different vortex formation modes in the Williamson & Roshko (1988) map in (b), we see a re-

markable similarity. Thus we expect that the regions we identify, based solely on the fluid forcing, will correspond with different modes of vortex formation, similar to those of Williamson & Roshko.

One of the most interesting features of the map of regimes in Figure 3.3 is the existence of regions where two modes overlap. In these overlap regions, the fluid forcing switches intermittently between two distinct modes even as the cylinder is oscillating with constant amplitude and frequency. This phenomenon appears in two places: as an overlap between the 2P region and the region where the wake is desynchronized (right hand edge of the yellow 2P region in Figure 3.3), and more importantly, in a region that lies in between the 2P and 2S modes and overlaps them both, which we label '2P<sub>OVERLAP</sub>' or more simply '2P<sub>O</sub>'. This overlap phenomenon is different from the one-time switch in forcing found by Carberry *et al.* (2005) which is related to the hysteresis found by Bishop & Hassan (1964). It is similar to the switching behavior Pottebaum (2003) found for his heated cylinders, although in this case no temperature variation is required. We emphasize here that the discovery of these overlapping regions is only possible because of the high resolution used in this study.

We now wish to study which vortex formation modes exist in the different regimes of Figure 3.3(a). In Figure 3.4 we confirm the existence of the P+S, 2S, and 2P modes in the regions we expect them. We were initially curious to see what mode of vortex formation exists in the overlap region, lying between the 2P and 2S modes. Would it resemble one mode or the other, or something in between? What we find is a variation of the 2P mode, namely the '2P<sub>O</sub>' mode, where, although there are two pairs of vortices shed per cycle, the secondary vortex is much weaker and decays rapidly as the vortex pair moves

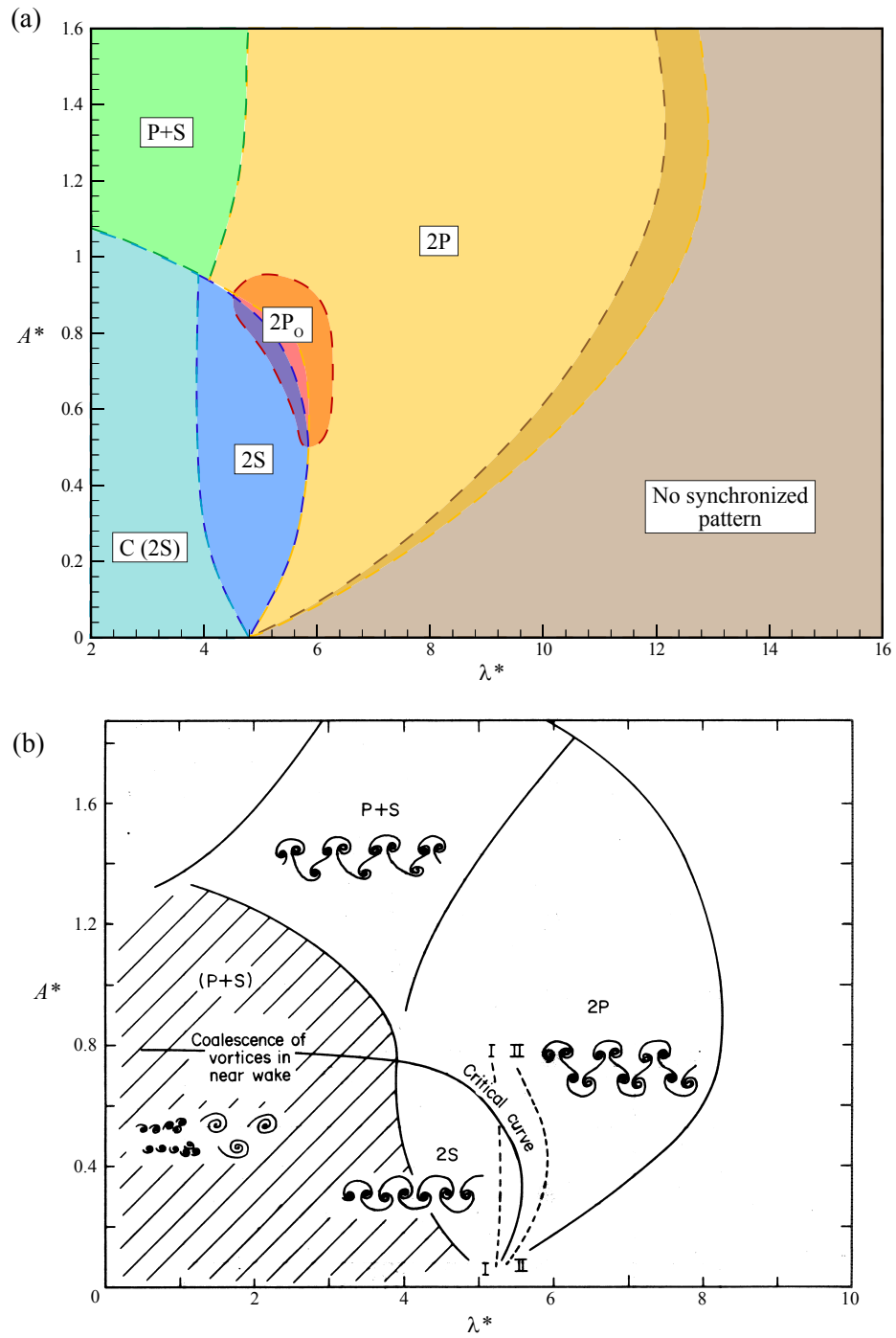


Figure 3.3: Map of vortex shedding regimes. There is a remarkable similarity between the mode boundaries we identify in the present study from force measurements in (a) and the boundaries identified by Williamson & Roshko (1988) from flow visualization in (b). Overlapping colors indicate regions where two vortex shedding modes overlap.

downstream, as shown in Figure 3.4(b). This  $2P_O$  vortex formation mode is equivalent to the “intermediate wake state” identified by Carberry, Sheridan & Rockwell (2003) in one of their “amplitude cuts”, existing for a narrow band of frequencies. It is also equivalent to the ‘ $2P_{UPPER}$ ’ mode found by Govardhan & Williamson (2000) in the same region of the normalized amplitude-wavelength plane, in their case for the “upper branch” of a free vibration response at very low mass-damping. (Their ‘ $2P_{LOWER}$ ’ mode found in the “lower branch” of free vibration is equivalent to the pure 2P mode described here.)

We note that the identification of a distinct  $2P_O$  mode would not be possible from free vibration experiments since the change in strength of the secondary vortex is accompanied by a change in amplitude of vibration, and we would thus interpret the two different modes as simply an amplitude effect changing the character of only one mode. Here we show that even for constant amplitude and frequency both the 2P and  $2P_O$  modes can exist. From the vorticity field in Figure 3.4(b) we see that one could easily mistake the  $2P_O$  mode for a 2S mode depending on how well one resolved the small secondary vortex.

Now that we have defined the different regions of vortex formation, we plot precise, high-resolution contours of key fluid forcing parameters. Here we show contours of the force in phase with velocity,  $C_Y \sin \phi$ , and contours of the force in phase with acceleration,  $C_Y \cos \phi$ , shown in Figure 3.5. Further contours of force and phase are included in Appendix A. It is not possible to plot *continuous* contours across our complete parameter space (as presented in some previous studies), due to the existence of overlapping modes and discontinuities, made evident from the resolution of the present data.

The force in phase with velocity,  $C_Y \sin \phi$ , represents a normalized “fluid ex-

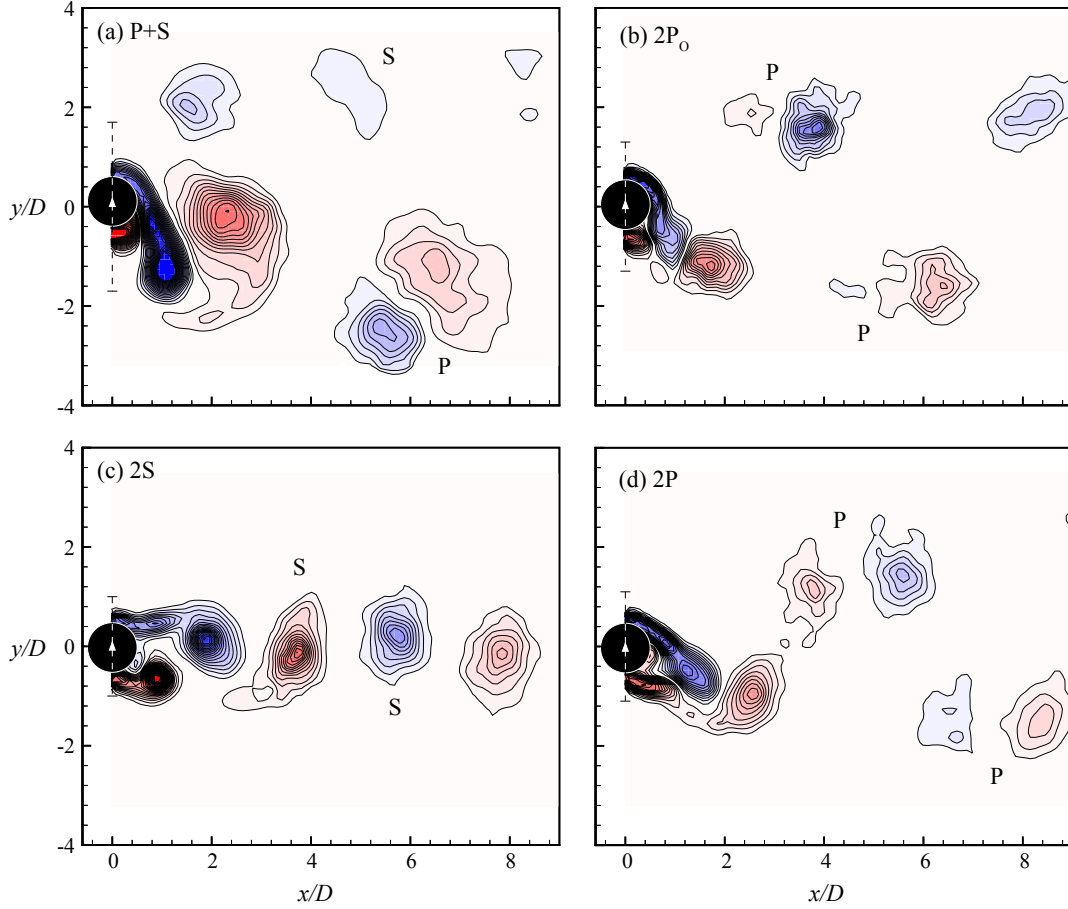


Figure 3.4: Vorticity fields for each of the main vortex shedding modes  $\{P+S, 2S, 2P, 2P_0\}$ . We observe a switch in timing of the initially shed vortex from the 2S mode to the 2P mode. In all cases the vorticity field is phase-averaged over 20 cycles of oscillation. Contour levels shown are:  $\omega D/U = \pm 0.4, \pm 0.8, \pm 1.2, \dots$  Measurement locations are as follows: P+S mode: ( $A^* = 1.2, \lambda^* = 4.0$ );  $2P_0$  mode: ( $A^* = 0.8, \lambda^* = 5.6$ ); 2S mode: ( $A^* = 0.5, \lambda^* = 5.0$ ); 2P mode: ( $A^* = 0.6, \lambda^* = 6.4$ ).

citation”, and thus determines in what regions free vibration may occur. From Figure 3.5 we can see there exist positive excitation regions within the 2S, 2P, and desynchronized regimes. The P+S regime shows strongly negative fluid excitation, so we would not expect to see such a mode for a freely vibrating cylinder at this  $Re$ , and indeed no such free vibration response modes have been experimentally observed. The highest amplitude for which there is positive fluid

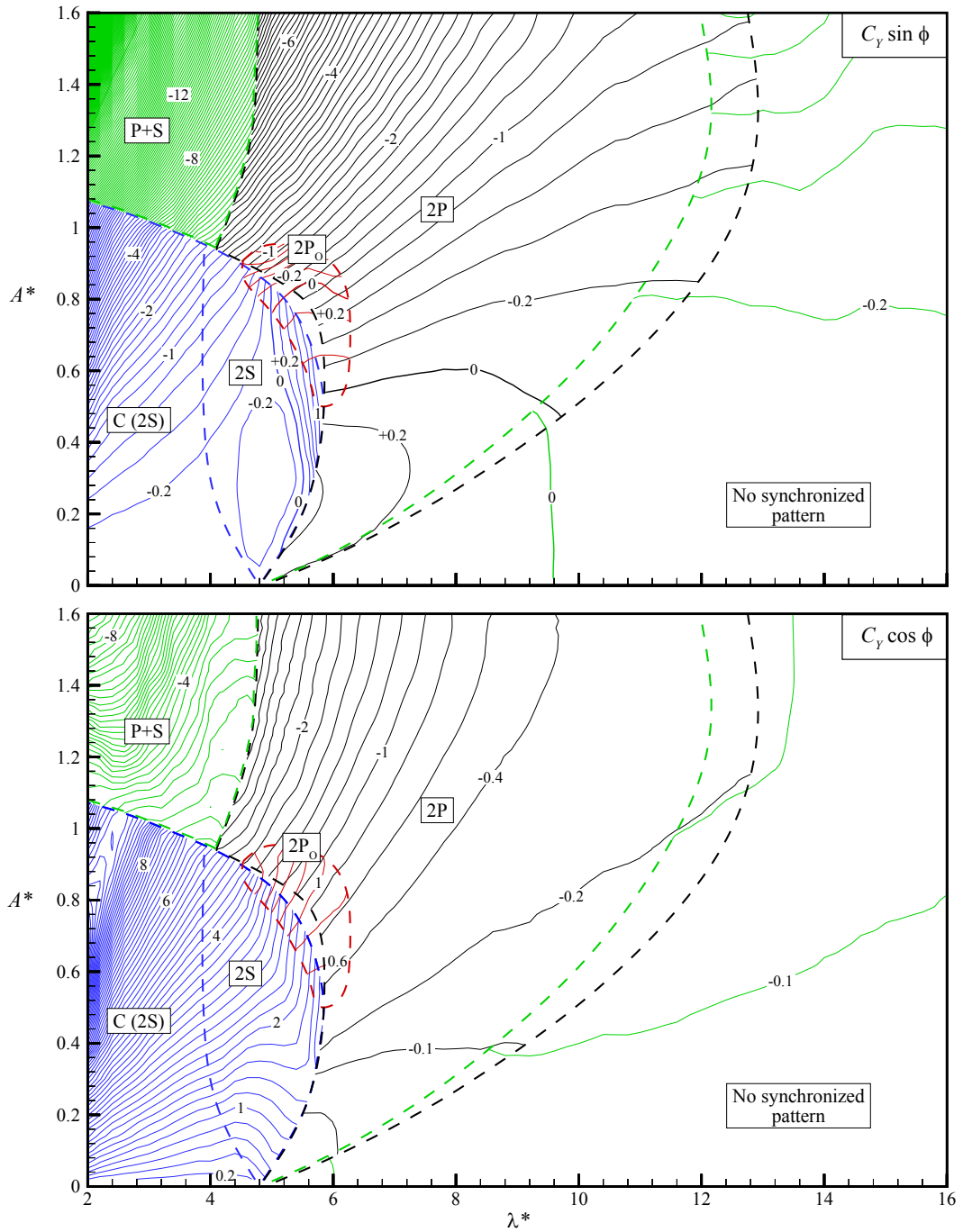


Figure 3.5: Contours of the force in phase with velocity,  $C_Y \sin \phi$  (normalized “fluid excitation”), and the force in phase with acceleration,  $C_Y \cos \phi$ , at  $Re = 4,000$ . Boundaries between modes are indicated by dashed lines. Note that contours overlap in regions where multiple vortex shedding modes are possible. Contour interval in both cases is 0.2 with an additional contour at  $C_Y \cos \phi = -0.1$  for increased clarity.

excitation is inside the  $2P_O$  region, thus a study of the fluid forcing and vortex dynamics in this region is key to understanding the dynamics of the cylinder at its peak amplitude of free vibration.

### 3.4 Characterizing wake mode boundaries and transitions

In the previous section, we identified different regimes of vortex formation in the normalized amplitude-wavelength plane. Although we used DPIV measurements of vorticity to verify the mode of vortex formation, the *boundaries defining these regimes were determined solely from the fluid forcing*. In this section we focus on time traces of the fluid forcing across these boundaries, to characterize the nature of the transitions. The parameters defining these time traces are shown in Figure 3.6, distinguished by the encircled numbers.

#### 3.4.1 Mode boundaries with abrupt jumps in fluid forcing

In order to fully characterize the transition from the 2S to the 2P mode, it is necessary at this point to introduce the concept of the “vortex force”. Following the analysis of Govardhan & Williamson (2000), we decompose the total transverse fluid force coefficient ( $C_{TOT}$ ) into a “potential force” component ( $C_{POT}$ ) given by the potential added mass force, and a “vortex force” component ( $C_{VORT}$ ), due to the dynamics of vorticity. For sinusoidal body motion, the potential force coefficient can be calculated to be:

$$C_{POT}(t) = 2\pi^3 \frac{y(t)/D}{(U^*/f^*)^2} \quad (3.3)$$

Thus we see that the instantaneous potential added mass force,  $C_{POT}$ , is al-

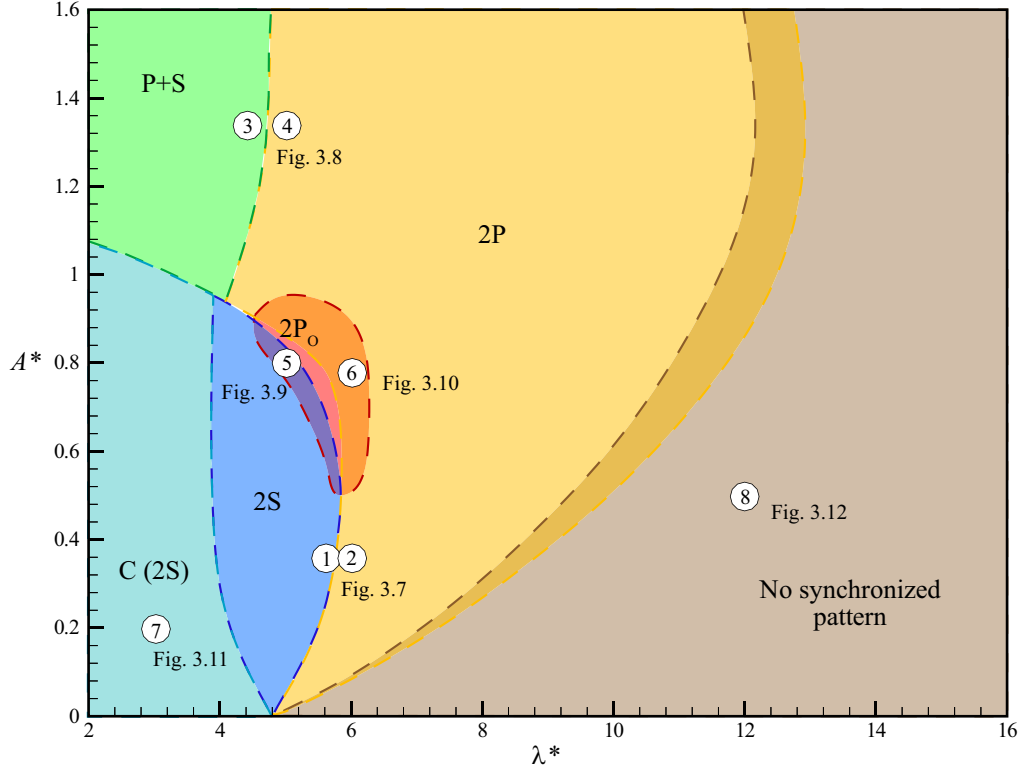


Figure 3.6: Locations in the normalized amplitude-wavelength plane for which force time traces are shown in Figures 3.7-3.12 (indicated by the encircled numbers).

ways in phase with the cylinder motion,  $y(t)$ , as one might expect. The vortex force coefficient can then be found by subtracting the potential force coefficient from the total force coefficient:

$$C_{VORT}(t) = C_{TOT}(t) - C_{POT}(t) \quad (3.4)$$

As a simplification of the nomenclature, we shall continue to use  $C_Y$  and  $\phi$  to denote the magnitude and phase of the total force, and use  $C_V$  and  $\phi_V$  to denote the magnitude and phase of the vortex force.

The use of the concept of vortex force is useful to understand the transitions between the 2S and 2P modes because its variation more directly reflects

changes in the vortex formation. The use of vortex force will be necessary to identify the  $2P_0$  regime as described below.

The transition from the 2S to 2P mode of vortex formation at low amplitudes has been studied before. In the present work, we characterize the transition (see points 1 and 2 in Figure 3.6) by looking at force time traces at similar values of normalized amplitude and wavelength on either side of the boundary, shown in Figure 3.7. The magnitude of the vortex force is quite similar for both the 2S and 2P modes, however the vortex phase shows almost a  $180^\circ$  difference. This is due to the  $180^\circ$  switch in timing of the vortex formation as shown by the vorticity fields in Figure 3.4 and identified by several previous investigations (for example Gu *et al.*, 1994; Govardhan & Williamson, 2000). When the potential force, which has a phase of  $0^\circ$ , is added to the vortex force, the magnitude of the total force for the 2S mode becomes about four times greater than for the 2P mode, with a considerable phase jump also remaining.

In contrast to the 2S to 2P transition, for the P+S to 2P mode transition (points 3 and 4 in Figure 3.6), neither the vortex force nor the total force show dramatic changes in magnitude or phase (although there is a small jump that may be seen in the contours of Figure A.1 and A.2). Instead, the boundary between these modes is found by examining the shape of the fluid forcing time trace as in Figure 3.8. For the P+S mode, the fluid forcing shows a clear asymmetry which can be further identified in the force spectra with a strong peak at two times the oscillation frequency ( $f_{\text{FORCE}}/f = 2.0$ ). With a small change in the normalized wavelength, the peak at  $2f$  essentially vanishes, indicating a switch to the symmetric 2P mode of vortex formation (see Figure 3.8). This change is abrupt, yielding a well defined boundary.

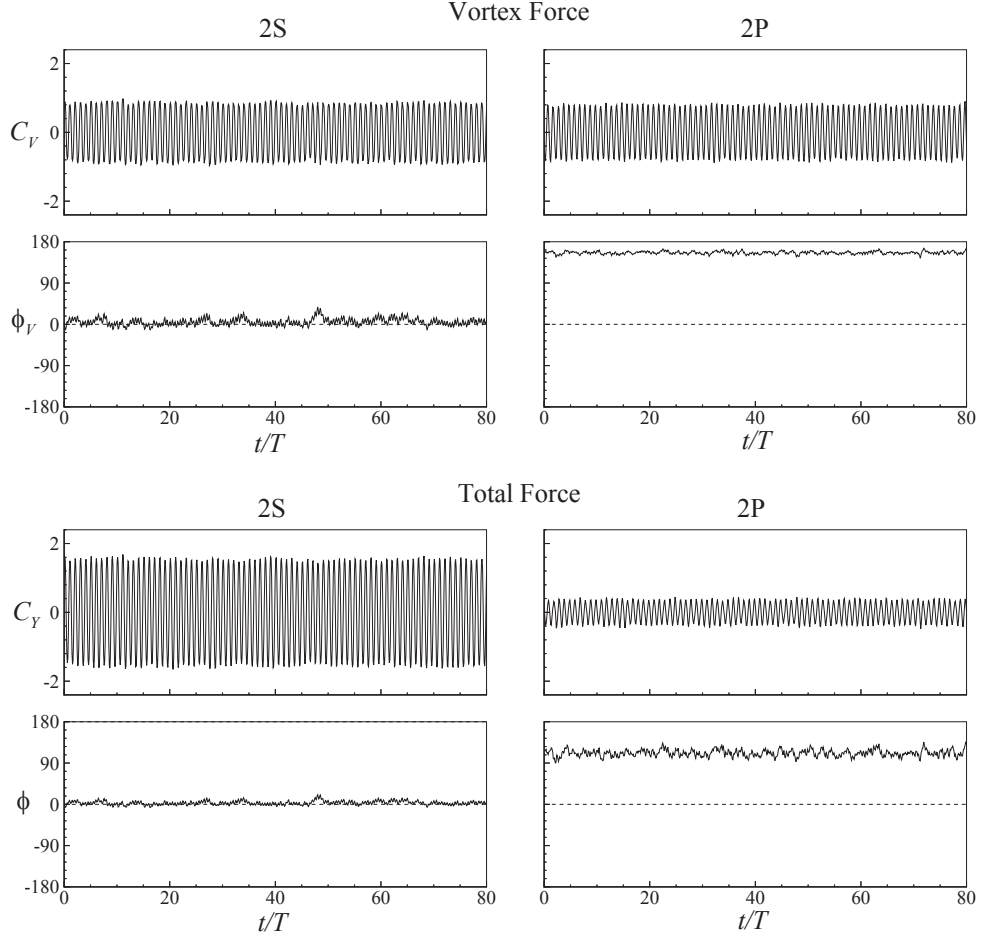


Figure 3.7: Typical force time traces for the transition from the 2S mode to 2P mode of vortex formation. The magnitude of the vortex force is nearly equal in both cases, however there is a large jump in the vortex phase, due to a change in the timing of vortex shedding. This difference in phase leads to a large difference in the magnitude of the total force. Time trace locations are points (1) and (2) in Figure 3.6, 2S mode: ( $A^* = 0.36$ ,  $\lambda^* = 5.6$ ); 2P mode: ( $A^* = 0.36$ ,  $\lambda^* = 6.0$ ).

### 3.4.2 Regimes of overlapping wake modes

For the boundaries described above, the transitions are abrupt with one clear vortex formation mode on either side of the boundary. We also find several regions where two distinct vortex formation modes can exist at a particular point in the  $(A^*, \lambda^*)$  plane. At these points, the forcing time trace reveals an intermit-

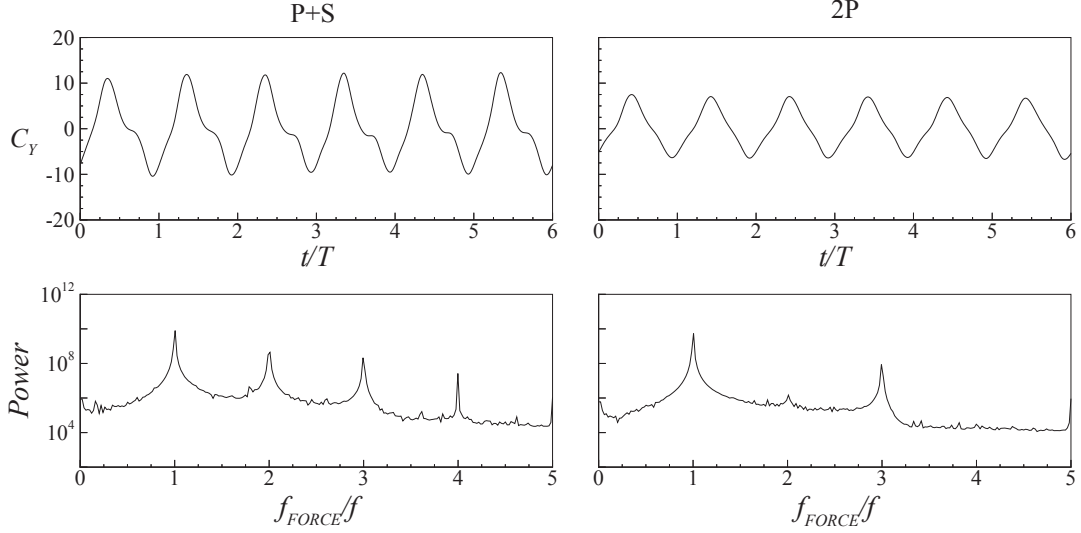


Figure 3.8: Typical force time traces and spectra for the transition from the P+S mode to the 2P mode of vortex formation. The large peak at twice the oscillation frequency for the P+S mode is not found for the 2P mode. Locations are points (3) and (4) in Figure 3.6, P+S mode: ( $A^* = 1.34, \lambda^* = 4.4$ ); 2P mode: ( $A^* = 1.34, \lambda^* = 5.0$ ).

tent switching in time between two distinct modes. For the case where the  $2P_O$  mode overlaps with the 2S mode (point 5 in Figure 3.6), this switching is most readily apparent in the vortex phase, as shown in Figure 3.9. The vortex phase switches between a value near  $0^\circ$  and a value near  $180^\circ$ , corresponding with a switch in timing of the vortex formation as the wake transitions from the 2S mode to the  $2P_O$  mode. In order to obtain the contours of the fluid forcing, in Figure 3.5, the force signals were analyzed separately for each mode. We also point out that *if one were to look only at the total force, the different vortex formation modes could not be identified*, highlighting here the importance of using the vortex force formulation.

As we move through the  $2P_O$  region we find a small sliver in the  $(A^*, \lambda^*)$  plane for which the  $2P_O$  mode exists by itself (see Figure 3.3). At slightly higher wavelength (point 6 in Figure 3.6) there exists an overlap of the  $2P_O$  mode and

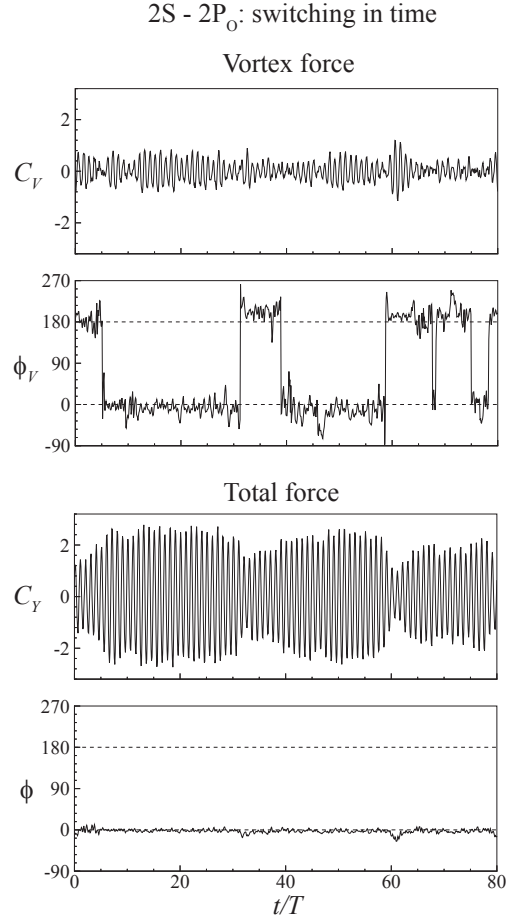


Figure 3.9: Typical force time trace in the 2S–2P<sub>O</sub> region. The intermittent switching of the vortex formation mode is most apparent in the vortex phase, which jumps between a value close to 0°, corresponding to the 2S mode, and a value close to 180°, corresponding to the 2P<sub>O</sub> mode. Location is point (5) in Figure 3.6: ( $A^* = 0.8$ ,  $\lambda^* = 5.0$ ).

the standard 2P mode. Time traces of the fluid forcing, in Figure 3.10, show that the vortex phase is near 180° for all times, indicating no significant change in the timing of shed vortices. The switching becomes apparent when we look at the phase of the total force. When the wake is shedding vortices in the 2P<sub>O</sub> mode, the magnitude of the vortex force is much smaller as compared to the pure 2P mode. Thus when the potential force (which always has a phase of 0°) is added back in, the total phase for the 2P<sub>O</sub> becomes near 0°. Note that the

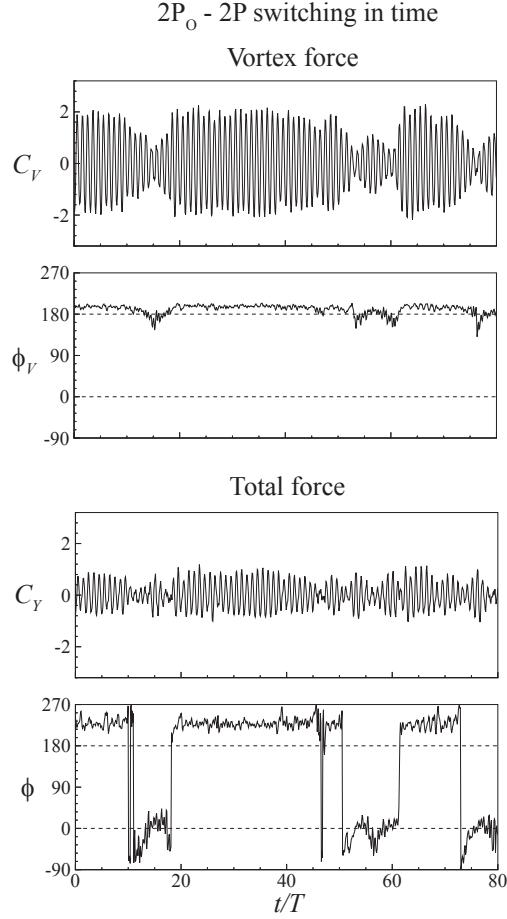


Figure 3.10: Typical force time trace in the 2P<sub>O</sub>–2P region. There is no dramatic change in vortex phase, however the total phase reveals an intermittent switching between the two modes. For the pure 2P mode the phase is above 180° yielding negative excitation. For the 2P<sub>O</sub> mode, the phase is near 0°. Location is point (6) in Figure 3.6: ( $A^* = 0.78$ ,  $\lambda^* = 6$ ).

inclusion of the potential force has no bearing on the sign of energy transfer, because  $(C_Y \sin \phi)$  is exactly equivalent to  $(C_V \sin \phi_V)$ .

### 3.4.3 Wake modes with non-synchronized fluid forcing

In the above sections, we have focused on regions for which the vortex formation is synchronized with the body motion. We shall now discuss two regimes

where much of the fluid force is not synchronized with the body vibration. In one case, we have short wavelength ( $\lambda^*$  is small), causing a synchronized 2S mode, but the small vortices coalesce in the near wake, forming large scale structures: the C(2S) mode in Figure 3.3. In the second case, we have a long wavelength ( $\lambda^*$  is large), such that several vortices form in each half cycle of vibration: the desynchronized vortex formation mode in Figure 3.3.

For short wavelength,  $\lambda^* < 4$ , and for amplitudes,  $A^* < 1$ , the cylinder sheds alternately signed small vortices as it oscillates (i.e. the 2S mode), but these small vortices coalesce into larger-scale structures further downstream. For this coalescing 2S mode, or ‘C(2S)’ mode in Figure 3.3, we find a significant component to the fluid forcing at a frequency below the oscillation frequency as shown in Figure 3.11(a). Since the coalescence does not occur with the same timing for each cycle of vibration, the phase averaged vorticity field in (b) shows only weak structures downstream. Williamson & Roshko (1988), using flow visualization, showed that far downstream this coalescence could, under some conditions, lead to a vortex street of immense size, much larger than the scale of the oscillating body.

The boundary separating the C(2S) mode from the pure 2S mode is less distinct than any other boundary we identified. As the wavelength is increased, the low frequency forcing becomes smaller and smaller. We define the boundary in Figure 3.3 as the point where the low frequency peak in the force spectra is no longer discernable.

At the high-wavelength end of the parameter space, beyond the 2P mode boundary in Figure 3.3, we find a region where the transverse force time traces and spectra show forcing at a frequency ( $f_{\text{FORCE}}$ ) higher than the oscillation

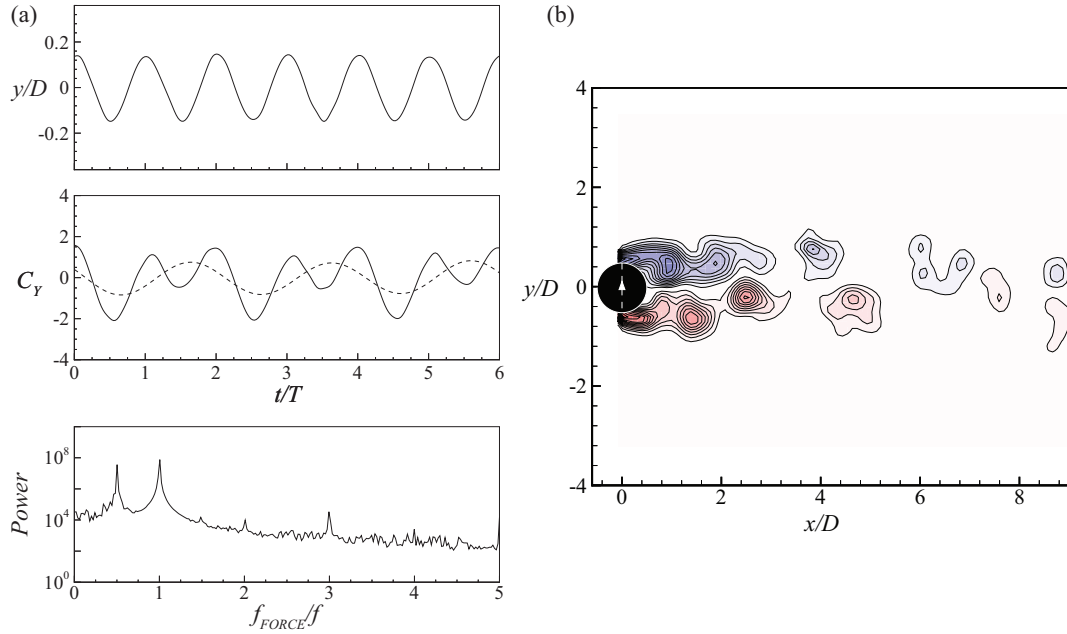


Figure 3.11: The coalescing 2S mode of vortex formation: typical time traces, force spectra, and phase-averaged vorticity field. The dashed line in the force time trace shows only the component at the lower frequency which appears due to the coalescence of vortices downstream (the solid line shows the entire force signal). Contour levels shown for the vorticity field are:  $\omega D/U = \pm 0.4, \pm 0.8, \pm 1.2, \dots$  Location is point (7) in Figure 3.6: ( $A^* = 0.2, \lambda^* = 3$ ).

frequency ( $f$ ), as shown in the time traces of Figure 3.12(a). In this case, we can think of the cylinder as moving through the fluid along an extended wavelength, shedding several vortices per half cycle. These vortices will not be synchronized with the motion, thus in the phase-averaged vorticity field of Figure 3.12(b), no strong vorticity is found beyond a few diameters downstream. Note that even though the vortex shedding is desynchronized, there remains a distinct component to the fluid forcing at the oscillation frequency which, interestingly, would give rise to free vibration. Finally, for the narrow band of overlap between the 2P region and the desynchronized region, the fluid forcing switches intermittently in time between a synchronized single frequency forcing, and the type of desynchronized forcing shown in Figure 3.12.

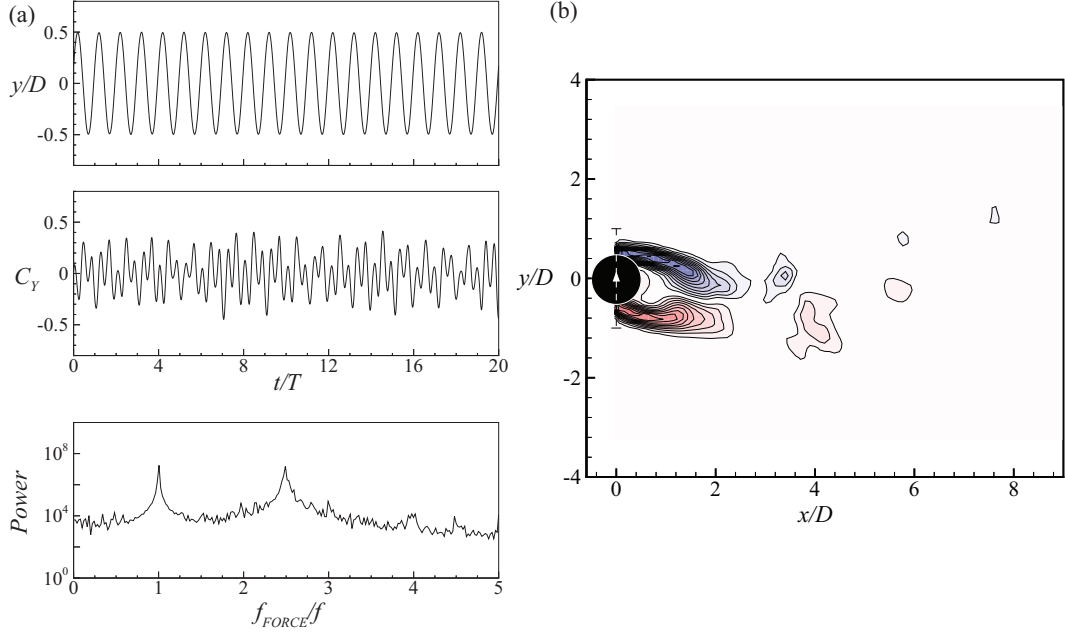


Figure 3.12: Typical time traces, force spectra, and phase-averaged vorticity field in the desynchronized region. The fluid forcing is not synchronized with the cylinder motion, having a significant component near the natural vortex shedding frequency. Contour levels shown for the vorticity field are:  $\omega D/U = \pm 0.4, \pm 0.8, \pm 1.2, \dots$ . Location is point (8) in Figure 3.6: ( $A^* = 0.5, \lambda^* = 12$ ).

### 3.5 Conclusions

In this study, we present new measurements of fluid force on a cylinder, whose controlled vibration is transverse to a flow, in the form of very high-resolution contour plots within the plane of normalized amplitude and wavelength ( $A^*, \lambda^*$ ). Our principal contour diagrams comprise the force in phase with velocity ( $C_Y \sin \phi$ ), which is also a normalized fluid excitation, and the force in phase with acceleration ( $C_Y \cos \phi$ ), related to a normalized effective added mass. We include further contour plots of magnitude and phase of the total force ( $C_Y, \phi$ ) and of the vortex force ( $C_V, \phi_V$ ) in Appendix A.

In some previous studies, contour plots of fluid excitation in the plane of

amplitude-wavelength have been assumed to be continuous, even though, on the basis of free vibration studies, as well as “amplitude cuts” from controlled vibration studies, we expect that there must exist boundaries where vortex formation, and hence fluid force, would jump. However, our high resolution fluid excitation contours have made it possible to accurately determine several distinct boundaries, and to identify regimes in the plane of amplitude-wavelength, based solely on the force measurements. The contours are clearly *not continuous* across the whole range of amplitude-wavelength. Indeed, we find a remarkable agreement between the shapes of the regimes evaluated from force measurements, and the regimes of vortex formation modes identified from flow visualization found in the Williamson-Roshko (1988) map of regimes. By analyzing vortex modes in the present controlled vibration study using DPIV, we find the modes one would expect from comparison with the Williamson-Roshko map, namely the 2S and 2P modes, as well as the asymmetric P+S mode, which has been measured for the first time using DPIV in experiment.

The high resolution contour plots have further enabled us discover a new high-amplitude regime which overlaps the boundary between the 2S and 2P regimes. Vorticity measurements identify the new vortex formation mode to be one quite similar to the 2P mode, but where the second vortex of each pair is much weaker than the first vortex, in what we define as the ‘2P<sub>OVERLAP</sub>’ or ‘2P<sub>O</sub>’ mode. During an experiment, the vortex formation mode and fluid force switches intermittently between the 2P<sub>O</sub> and 2P modes (or between the 2P<sub>O</sub> and 2S modes), even when the amplitude and frequency are fixed. Our prior understanding of such 2P<sub>O</sub> and 2P modes, which resemble (respectively) the 2P mode in the upper branch of free response (Govardhan & Williamson, 2000), and the 2P mode of the lower response branch, was that these patterns of vortex for-

mation were simply the same 2P mode exhibiting somewhat different character in different parts of the 2P mode regime in the Williamson-Roshko map. However, it is significant that the 2P and  $2P_O$  modes are distinct, both occurring at the same values of amplitude and wavelength. It was not possible to deduce this fact, based only on free vibration, because the higher fluid excitation ( $C_Y \sin \phi$ ) of the  $2P_O$  mode would necessarily push the vibration to higher amplitudes than the 2P mode. An understanding of this overlap regime is significant because it represents a region of positive fluid excitation that has the highest amplitude, and is responsible for exhibiting the peak amplitudes possible in free vibration.

In this study, we also characterize the transitions across boundaries of the flow regimes within the amplitude-wavelength plane, illustrating the sometimes large changes in fluid force or vortex dynamics that can occur for small increments of amplitude or frequency of the controlled motion. Finally, we find that even in the desynchronized regime, where the vortex formation frequency becomes uncoupled to the body vibration frequency, the body *may be able to vibrate* due to the existence of a component of fluid forcing at the body vibration frequency, yielding positive fluid excitation. This is interesting, as most of the fluid force is associated with the uncoupled (and higher) vortex formation frequency, yet the wake is sufficiently organized by the body motion in a manner to yield at least some positive fluid excitation. One might perhaps expect free vibration to exhibit a quasi-periodic response under these conditions.

## CHAPTER 4

# Prediction of vortex-induced vibration response by employing controlled motion

MORSE, T. L. & WILLIAMSON, C. H. K. (2009)

Submitted to *Journal of Fluid Mechanics*

In order to predict response and wake modes for elastically mounted cylinders in a fluid flow, we employ controlled vibration experiments, comprising prescribed transverse vibration of a cylinder in the flow, over a wide regime of amplitude and frequency. A key to this study is the compilation of high resolution contour plots of fluid force, in the plane of normalized amplitude and wavelength. With such resolution, we are able to discover discontinuities in the force and phase contours, which enable us to clearly identify boundaries separating different fluid forcing regimes. These appear remarkably similar to boundaries separating different vortex formation modes in the Williamson & Roshko (1988) map of regimes. Vorticity measurements exhibit the 2S, 2P, and P+S vortex modes, as well as a regime where the vortex formation is not synchronized with the body vibration. By employing such fine resolution data, we discover a high-amplitude regime where two vortex formation modes overlap. Associated with this overlap regime, we identify a new distinct mode of vortex formation comprising two pairs of vortices formed per cycle, where the secondary vortex in each pair is much weaker than the primary vortex. This vortex mode, which we define as the  $2P_{\text{OVERLAP}}$  mode ( $2P_{\text{O}}$ ), is significant because it is responsible for generating the peak resonant response of the body. We find that

the wake can switch intermittently between the  $2P$  and  $2P_0$  modes, even as the cylinder is vibrating with constant amplitude and frequency. By examining the energy transfer from fluid to body motion, we predict a free vibration response which agrees closely with measurements for an elastically mounted cylinder. In this work, we introduce the concept of an “energy portrait”, which is a plot of the energy transfer into the body motion, and the energy dissipated by damping, as a function of normalized amplitude. Such a plot allows us to identify stable and unstable amplitude response solutions, dependant on the rate of change of net energy transfer with amplitude (the sign of  $dE^*/dA^*$ ). Our energy portraits show how the vibration system may exhibit a hysteretic mode transition, or intermittent mode switching, both of which correspond with such phenomena measured from free vibration. Finally, we define the complete regime in the amplitude-wavelength plane where free vibration may exist, which requires not only a periodic component of positive excitation, but also stability of the equilibrium solutions.

## 4.1 Introduction

Vortex-induced vibration is an important problem in many fields of engineering. It affects the dynamics of riser tubes bringing oil from the seabed to the surface, as well as civil engineering structures such as bridges, chimneys, and buildings, and is cause for concern in many other practical applications. The range of problems caused by vortex-induced vibration has led to a large number of experimental and computational studies on the subject, including several review articles, for example: Sarpkaya (1979), Griffin & Ramberg (1982), Bearman (1984), Parkinson (1989), and more recently Williamson & Govardhan (2004).

We focus on one of the most conceptually simple instances of vortex-induced vibration: the case of an elastically mounted rigid cylinder, constrained to move transverse to an incoming flow, which is often used as a paradigm for understanding more diverse experimental arrangements. For such an arrangement, previous studies (such as Khalak & Williamson, 1999) have shown that for systems of low combined mass-damping there exist three branches of response as the normalized velocity is increased, namely the initial branch, upper branch, and lower branch. The transition between the initial and upper branch exhibits a hysteresis, while the transition from the upper to the lower branch shows an intermittent switching. For systems of high mass-damping, only the initial and lower branches exist, with a hysteretic mode transition between them (Feng, 1968). Examples of the two-branch and three-branch response may be found later in this work (see Figure 4.11).

In the present study, we employ controlled vibration of a body in a water channel flow, where the cylinder is effectively translated with a prescribed sinusoidal trajectory relative to the fluid, to provide a deeper understanding of vortex-induced vibration phenomena for freely vibrating bodies. Initially, we set out to investigate a number of questions; for example, what is the cause of the hysteresis between the initial branch and upper branch of response? What causes intermittent switching between the upper and lower branches? What is the relationship between the modes of vortex formation and the fluid excitation? What modes of vortex formation can cause vortex-induced vibration? To what extent can controlled vibration be used to accurately predict the behavior of a freely vibrating cylinder? We address all of these questions in the present work, as well as expand upon the new results which will be presented.

Before addressing the above questions, we shall briefly introduce an equation of motion generally used to represent the vortex-induced vibration of a cylinder oscillating in the transverse  $y$ -direction (perpendicular to the free stream) as follows:

$$m\ddot{y} + c\dot{y} + ky = F(t), \quad (4.1)$$

where  $m$  is the total oscillating structural mass,  $c$  is the structural damping, and  $k$  is the spring constant. When the body motion is synchronized with the vortex formation, the cylinder motion,  $y(t)$  and fluid forcing,  $F(t)$  are typically well approximated by sinusoidal functions (of course, in controlled vibration, the motion is precisely sinusoidal):

$$y(t) = A \sin(2\pi ft), \quad (4.2)$$

$$F(t) = F_1 \sin(2\pi ft + \phi), \quad (4.3)$$

where  $f$  is the oscillation frequency. The phase angle,  $\phi$ , between the fluid force and the body displacement is an important quantity, influencing the energy transfer from fluid to body motion, and thereby also the response of the body. In this problem, we select a set of relevant non-dimensional parameters, which are presented in Table 4.1. In particular, the principal parameters defining the body motion are the normalised amplitude ( $A^*$ ), and the frequency ratio ( $f^*$ ), in a flow with normalised velocity  $U^*$ .

Equations defining the steady state response amplitude and frequency may be derived as follows, following the approach of Khalak & Williamson (1999):

$$A^* = \frac{1}{4\pi^3} \frac{C_Y \sin \phi}{(m^* + C_A) \zeta} \left( \frac{U^*}{f^*} \right)^2 f^*, \quad (4.4)$$

$$f^* = \sqrt{\frac{m^* + C_A}{m^* + C_{EA}}}. \quad (4.5)$$

Table 4.1: Non-dimensional groups. In the groups below,  $U$  is the free-stream velocity,  $\lambda$  is the oscillation wavelength,  $f$  is the oscillation frequency,  $f_N$  is the natural frequency in water,  $D$  is the cylinder diameter,  $L$  is the submerged cylinder length,  $\nu$  is the fluid kinematic viscosity,  $\rho$  is the fluid density, and  $F$  is the transverse fluid force. The added mass,  $m_A$ , is given by  $m_A = C_A m_d$ , where  $m_d$  is the displaced fluid mass and  $C_A$  is the potential added-mass coefficient ( $C_A = 1.0$  for a circular cylinder).

Mass ratio	$m^*$	$\frac{m}{\pi\rho D^2 L/4}$
Damping ratio	$\zeta$	$\frac{c}{2\sqrt{k(m+m_A)}}$
Normalized velocity	$U^*$	$\frac{U}{f_N D}$
Normalized wavelength	$\lambda^*$	$\frac{\lambda}{D} = \frac{U}{fD}$
Normalized amplitude	$A^*$	$\frac{A}{D}$
Frequency ratio	$f^*$	$\frac{f}{f_N}$
Transverse force coefficient	$C_Y$	$\frac{F}{\frac{1}{2}\rho U^2 D L}$
Reynolds number	$Re$	$\frac{\rho U D}{\mu}$

where  $C_A$  is the potential added mass coefficient ( $C_A = 1.0$  for a circular cylinder), and  $C_{EA}$  is an “effective” added mass coefficient due to the transverse force in phase with the body acceleration:

$$C_{EA} = \frac{1}{2\pi^3} \frac{C_Y \cos \phi}{A^*} \left( \frac{U^*}{f^*} \right)^2, \quad (4.6)$$

We refer to equations (4.4) and (4.5) as the “amplitude equation” and the “frequency equation”.

We may also discuss the response equations above in the context of energy

considerations. The energy transferred from the fluid to the cylinder motion, over one cycle of oscillation, is given by:

$$E_{IN} = \pi A F_1 \sin \phi. \quad (4.7)$$

Thus, the phase angle,  $\phi$ , must be between  $0^\circ$  and  $180^\circ$  to yield positive excitation, and this is a required condition for free vibration to occur. We may note that for a cylinder with prescribed sinusoidal motion, the fluid forcing may be close to (but not precisely) sinusoidal. If we represent the fluid forcing as  $F(t) = \{F_1 \sin(\omega t + \phi) + F_2 \sin(2\omega t + \phi_2) + \dots\}$  then the force component we present in this study is the one corresponding to the fundamental frequency ( $\omega$ ) given by the magnitude ( $F_1$ ) and the phase ( $\phi$ ). Only this component will make a net contribution to the energy transfer from fluid to body motion. In essence, equation (4.7) is valid even for non-sinusoidal forcing. The energy dissipated by the structural damping is given by:

$$E_{OUT} = 4\pi^3 c A f^2. \quad (4.8)$$

If the system is oscillating with a constant amplitude and frequency, the energy into the system must exactly balance the energy out of the system, over one cycle, which yields:

$$\underbrace{C_Y \sin \phi}_{E_{IN}^*} = \frac{4\pi^3 A^* (m^* + C_A) \zeta}{\left(\frac{U^*}{f^*}\right)^2 f^*} \underbrace{f^*}_{E_{OUT}^*}, \quad (4.9)$$

which is equivalent to a simple manipulation of the amplitude equation (4.4) above. The term  $C_Y \sin \phi$  is the force coefficient in phase with velocity, which we define as the “fluid excitation”, and this represents a normalized energy into the system,  $E_{IN}^*$ , over a cycle. For a free vibration system oscillating at steady state this must be balanced by the normalized energy out of the system,  $E_{OUT}^*$ ,

related to the combined mass-damping of the system, and is given by the right-hand side of equation (4.9). The combined mass-damping,  $(m^* + C_A)\zeta$ , is a key parameter in vortex-induced vibration, as indicated by its appearance in the amplitude equation (4.4).

Our approach, in this study, is to prescribe the *relative* trajectory of the cylinder through the fluid to be a sine wave, and to measure the fluid forces over a wide range of normalized amplitude ( $A^*$ ) and normalized wavelength ( $\lambda^*$ ). One may note that normalized wavelength is equivalent to the parameter  $U^*/f^* = U/fD$ , which is the flow velocity normalized with the actual oscillation frequency ( $f$ ), rather than the natural frequency ( $f_N$ ). We shall use these force measurements, along with equation (4.9), to make response predictions for a freely vibrating cylinder.

In the case of a controlled body, which is translated along a sinusoidal trajectory, Williamson & Roshko (1988) observed a set of different vortex formation modes, existing within certain regimes in a plot of normalised amplitude and wavelength of the body motion. Among the vortex formation modes they found were a '2S' mode representing two single vortices formed per cycle, a '2P' mode meaning two pair of vortices formed per cycle, and an asymmetric 'P+S' mode comprising a pair of vortices and a single vortex, in each cycle. The Williamson-Roshko map of regimes is shown, for example, in Figure 4.3(b) later. Ongoren & Rockwell (1988*b*) observed some comparable vortex formation modes, in the case of a body oscillating in-line with the flow.

In the case of free vibration at high mass-damping, Brika & Laneville (1993) found a two-branch response, observing the 2S mode in their initial branch and a 2P mode in their lower branch, which corresponded well with the Williamson-

Roshko map of mode regimes. At low mass-damping, Khalak & Williamson (1999) were able to superpose their free vibration response branches onto the map of wake modes, deducing that the initial branch lies in the 2S region, while the upper and lower branches both lie in the 2P region. These modes were confirmed in free vibration by Govardhan & Williamson (2000), employing simultaneous force and wake vorticity measurements. However, they found that the 2P mode in the upper branch exhibits a secondary vortex in each vortex pair that is much weaker than the primary vortex. This is significant to the discovery, in the present work, of the '2P<sub>O</sub>' mode.

Several previous controlled vibration studies exist in the literature. Bishop & Hassan (1964), Mercier (1973), Sarpkaya (1977), and Carberry *et al.* (2001, 2005) measured the fluid forcing on a vibrating cylinder, over a range of frequencies, and at selected fixed values of amplitude (which we shall call "amplitude cuts"). A significant result from these prior studies (see in particular the early work of Bishop & Hassan, 1964) is the existence of a distinct jump in the phase and magnitude of the lift force as the frequency is increased through the natural vortex shedding frequency for a stationary cylinder. In their controlled vibration studies, Carberry *et al.* (2001, 2005) show that this jump is associated with a change from a "low frequency wake state" (equivalent to the 2P mode) to a "high frequency wake state" (equivalent to the 2S mode). This confirms the earlier suggestion of Williamson & Roshko (1988), and the free vibration studies of Brika & Laneville (1993) and Govardhan & Williamson (2000) that these jumps correspond to a change from the 2P to 2S mode, or vice versa. Carberry, Sheridan & Rockwell (2003) also identify an "intermediate wake state", equivalent to the upper branch 2P mode found by Govardhan & Williamson (2000).

Contour plots of lift force have been generated by Staubli (1983), from his controlled vibration experiments, and he used these contours to make predictions of the response of a free vibration system which he compared with the free vibration measurements of Feng (1968), at high mass-damping. The prediction was reasonable for lower values of normalized velocity (in what we call the initial branch), but such comparison was not close for higher  $U^*$  (the lower branch). The most extensive previous force contour measurements come from experiments conducted in the MIT Towing Tank Facility; presented in Gopalkrishnan (1993), and in Hover *et al.* (1998). They compiled force coefficients in phase with velocity ( $C_Y \sin \phi$ ), and in phase with acceleration ( $C_Y \cos \phi$ ), over a wide range of normalized amplitude and wavelength. Hover *et al.* (1998) were also able to run ingenious virtual free vibration experiments in the same facility, using their “Virtual Cable Testing Apparatus”. Their zero fluid excitation contour ( $C_Y \sin \phi = 0$ ) yielded reasonable agreement with one of their (virtual) free vibration responses, at very low mass-damping. However, some portions of the free vibration response were situated in regions where the force contours from controlled vibration predicted negative excitation.

One important question, mentioned earlier, is to what extent can measurements from controlled vibration be applied to the case of a freely vibrating, elastically mounted cylinder? Carberry *et al.* (2004), using constant amplitude experiments, compared forces and wake modes found for controlled vibration, and for free vibration, finding some similar wake modes and jumps in the force and its phase. However, they also measured regimes of negative excitation from controlled vibration (suggesting that free vibration should not occur) under conditions where free vibration has been readily found. They concluded that sinusoidal controlled motion “does not simulate all the key components of the

flow-induced motion.” This seems reasonable based on the results that were available at the time from different facilities or groups. However, in Chapter 2 (Morse & Williamson, 2006) we made direct comparisons between free and controlled vibration and showed that, *if the experimental conditions are matched*, controlled vibration can yield fluid forces which are in very close agreement with results from free vibration, over an entire response plot. It is possible that this careful matching of conditions is a key point in these studies. In preset work, we shall present further amplitude response predictions, using our controlled vibration force contours, which are in close agreement with measured free vibration response, at both high and low mass-damping. This indicates that the use of controlled vibration is indeed quite reasonable to predict free vibration response.

In this work, we measure the fluid forcing for a cylinder oscillating under controlled vibration over an extensive range of normalized amplitude and wavelength, with much higher resolution than in previous data sets, as indicated by Figure 4.1. The use of almost 6,000 runs leads to sufficiently fine resolution to allow a study of distinct fluid forcing regimes, some of which overlap, and lead to phenomena we shall discuss later in §4.6. Over this wide regime of amplitude-wavelength, we present selected examples of the vorticity dynamics associated with certain vortex modes in the wake, using DPIV measurements. The force measurements are used to predict the behavior of a freely vibrating cylinder, and to explain the mode transitions which occur between different branches of response.

Following a description of the experimental details in §4.2, we introduce of a set of regimes of vortex formation in §4.3, that we have been able to identify

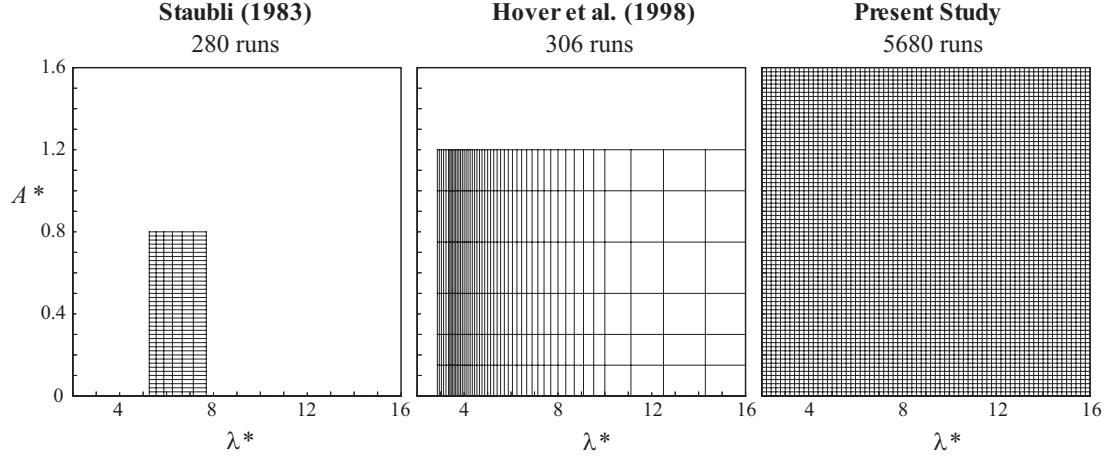


Figure 4.1: Grid resolution of controlled vibration measurements from previous studies and in the present study. We are able to obtain a very high resolution, as well as a wide range of the parameters.

from the fluid forcing measurements. In particular, in this section, we present the overlap regime associated with the  $2P_O$  vortex formation mode, which is significant because this mode is responsible for yielding a positive excitation at the highest amplitude, and so would be associated with the peak amplitude response in free vibration. In §4.4, we present contours of fluid forcing obtained from our high resolution data, and explore the relationship between fluid excitation and vortex formation mode, particularly for our comparison between the  $2P_O$  and  $2P$  modes. In Chapter 3 (Morse & Williamson, 2009b), we have presented selected force contour plots, as found here, but we included several other such plots in a more complete set, for reference  $\{C_Y, \phi, C_Y \sin \phi, C_Y \cos \phi, C_{VORT}, \phi_{VORT}\}$ . The last two parameters refer to “vortex force” magnitude and phase. Also, in this earlier publication, we have studied the force time traces, and force spectra, as one moves across various boundaries of the fluid force regimes, to further characterize such regimes.

In §4.5, we use our force contours to accurately predict the response of a

freely vibrating cylinder, demonstrating good agreement between prediction and direct free vibration measurements. The introduction of “energy portraits” in §4.6, illustrating the excitation energy and energy dissipated by damping, as a function of amplitude, enable us to further understand the existence of hysteresis between modes of vibration, as well as intermittent switching between modes. The energy portraits enable us to clearly illustrate the stability and instability of equilibrium amplitude solutions, predicted from the force contour data. In §4.7, employing the finely resolved force contours, we have been able to identify the regime within the amplitude-wavelength plane for which free vibration is possible, taking into account stability of the possible vibration solutions. This is followed by our conclusions in §4.8.

## 4.2 Experimental details

The present experiments are conducted in the Cornell-ONR Water Channel, which has a cross-section of 38.1 cm × 50.8 cm. The turbulence level in the test section of the water channel is less than 0.9%. We match very closely the experimental arrangement used in the free vibration study of Govardhan & Williamson (2000) with our controlled vibration arrangement here. In both cases a circular cylinder is suspended vertically in the water channel, and oscillated transverse to an incoming flow, as shown schematically in Figure 4.2. The only difference is that in the free vibration case, the cylinder is attached to a spring-mounted carriage running on air bearings, which oscillates freely, transverse to the flow, due to vortex-induced motion. In the controlled vibration case, the cylinder is mounted on a transverse lead screw attached to a computer-controlled motor and it oscillates with a prescribed sinusoidal motion.

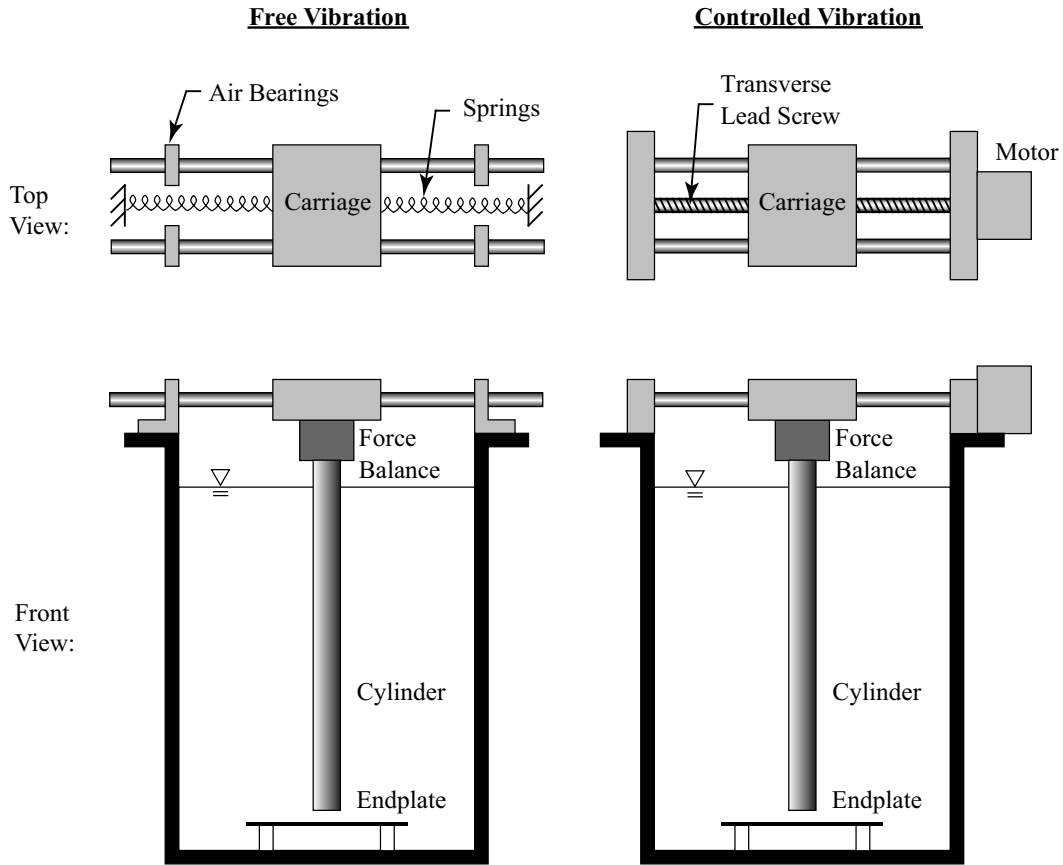


Figure 4.2: Schematic diagram of the experimental arrangement which is closely matched to the arrangement for free vibration. In both cases the cylinder is suspended vertically in a water channel and oscillates transverse to the flow (into the page). For the controlled vibration case we prescribe the motion using a computer controlled motor and lead screw.

We use a test cylinder of diameter 3.81 cm and length 38.1 cm with the flow speed kept constant to give a Reynolds number:  $Re = 4,000$ . In Appendix B, we also show results for  $Re = 12,000$ , obtained using a larger cylinder of diameter 6 cm and length 42 cm with a higher flow velocity. A fixed end plate is placed 2 mm below the bottom of the cylinder (but not in contact with the cylinder) to encourage two-dimensional vortex shedding, following the study of Khalak & Williamson (1996). For each Reynolds number, we carry out a total of 5,680 runs, each for 100 cycles of oscillation, to yield a total of approximately 1000

hours worth of data. Normalized amplitude, ( $A^*$ ) is varied from 0.02 to 1.6, with a resolution of 0.02. Normalized wavelength, ( $\lambda^*$ ) is varied from 2 to 16, with a resolution of 0.2. Such an extensive data set is only possible because the experiment is conducted in a continuously flowing water channel facility, rather than a towing tank facility, and thus can be automated to run unattended for a large number of experimental runs, often overnight.

A two-axis force balance utilizing LVDTs (linear variable differential transducers) is used to measure the lift and drag forces on the cylinder. The transverse displacement of the cylinder is measured using a non-contact (magnetostrictive) position transducer. For each run, the fluid force magnitude ( $F_1$ ) and phase angle ( $\phi$ ) at the fundamental (body oscillation) frequency is calculated using a Fourier series analysis. Relevant fluid forcing quantities, such as  $C_Y \sin \phi$  and  $C_{EA}$ , are obtained using just the force component at the body oscillation frequency. In most cases, the fluid forcing is quite sinusoidal and thus this component represents essentially all of the force signal content.

In addition to the extensive force measurements described above, we use Digital Particle Image Velocimetry (DPIV) to measure vorticity in the wake of the vibrating cylinder, for the case of  $Re = 4,000$ . The flow is seeded with 14-micron silver coated glass spheres, which are illuminated by a sheet of laser light from a 50 mJ Nd:Yag pulsed laser. Pairs of particle images are acquired using a Jai CV-M2CL CCD camera (1600  $\times$  1200 pixels), and analyzed using cross-correlation of sub-images. We use a two-step windowing process (with window shifting) to obtain particle displacements between image pairs. Further details on our DPIV processing may be found in Govardhan & Williamson (2000). The viewing area is 26 cm  $\times$  34 cm, corresponding to 6.75 by 9 diameters. The time

between images is adjusted to vary between 10 and 20 ms depending on the cylinder oscillation parameters. Vorticity fields calculated from the image pairs are phase averaged over approximately 10 to 20 cycles to remove the small weak vorticity structures generated by intermittent small-scale three-dimensionality in the flow, and thus obtain a clear picture of the dynamics of the principal spanwise vorticity.

### 4.3 Regimes of fluid forcing and vortex formation modes

Employing our controlled vibration data, we are able to identify conditions where the fluid forcing shows qualitative abrupt jumps, as amplitude or frequency is varied, similar to the jumps found in the “amplitude cuts” of previous controlled vibration studies. We follow these jumps throughout the normalized amplitude-wavelength plane, and are able to identify clear boundaries separating regions of distinct fluid forcing, indicated by the colored regimes in Figure 4.3(a). These boundaries show a remarkable similarity to the boundaries separating different vortex formation modes in the Williamson & Roshko (1988) map, shown in Figure 4.3(b), and which were identified by (fine resolution) flow visualization observation of the flow patterns. We naturally expect that the regions found here, based solely on the fluid forcing, will correspond with similar modes of vortex formation found by Williamson & Roshko (1988).

By measuring the wake vorticity at certain locations in the amplitude-wavelength plane, we confirm the existence of certain modes of vortex formation, that are labelled for each fluid forcing regime in Figure 4.3. The P+S, 2S and 2P modes are presented in Figure 4.4(a), (b) and (c). The 2S and 2P modes

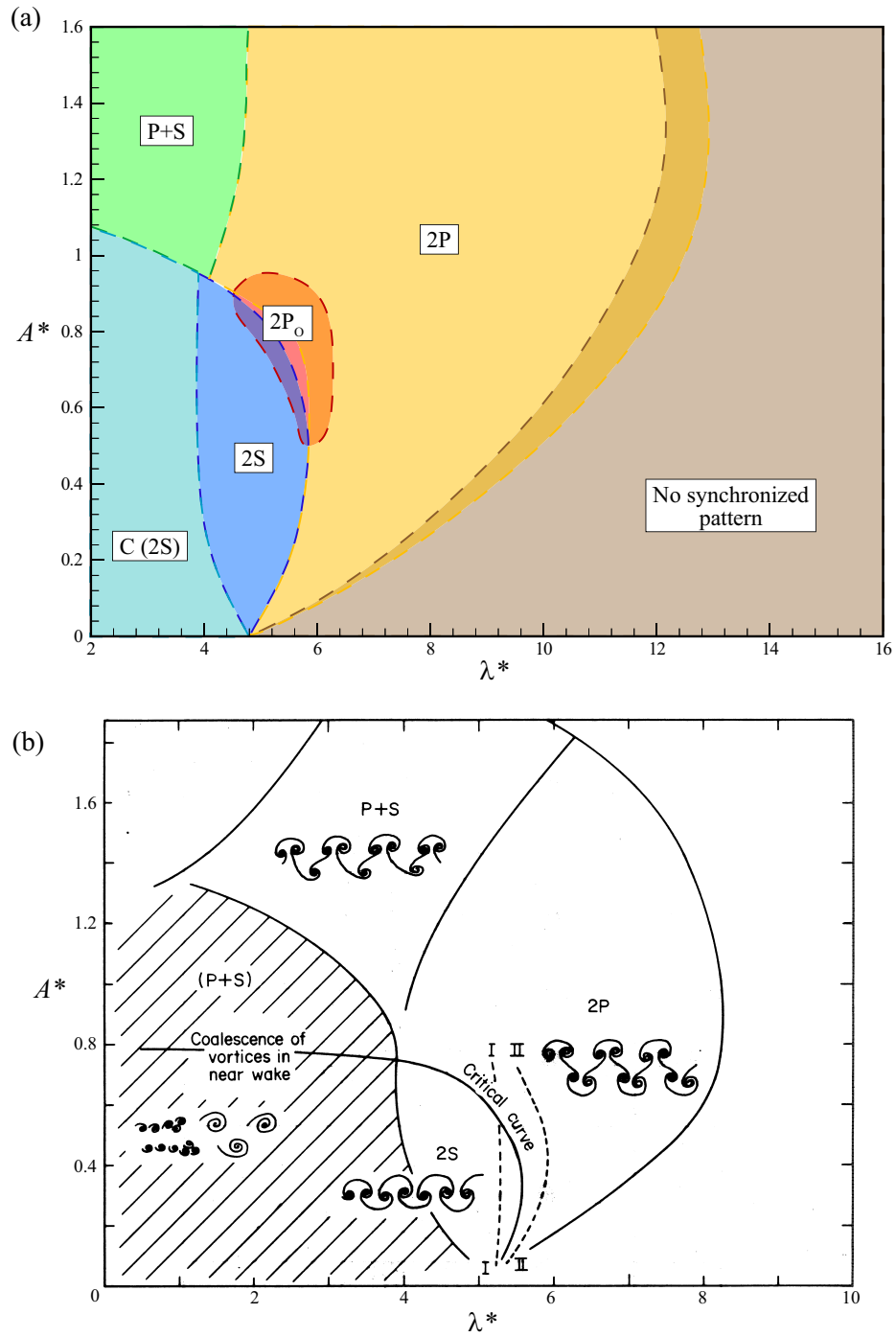


Figure 4.3: Map of vortex shedding regimes. There is a remarkable similarity between the mode boundaries we identify in the present study from force measurements in (a) and the boundaries identified by Williamson & Roshko (1988) from flow visualization in (b). Overlapping colors indicate regions where two vortex shedding modes overlap.

may be compared with such vortex modes from free vibration in Govardhan & Williamson (2000). Added to these classical modes, we have been able to identify a distinct new mode of vortex formation ( $2P_O$  mode), existing in its own clearly defined region of the amplitude-wavelength plane, overlapping the boundary between 2S and 2P regions. Vorticity measurements of this mode reveal that, although there are two pairs of vortices shed per cycle of vibration, the secondary vortex in each pair is much weaker than the primary vortex, and decays rapidly as the vortex pair moves downstream, as shown in (d). This is in contrast with the classical 2P mode in (c), where the primary and secondary vortex in a vortex pair have roughly equal strength (Govardhan & Williamson, 2000). We label this new mode as ' $2P_{\text{OVERLAP}}$ ' or simply ' $2P_O$ '. We find significant overlapping regimes, in Figure 4.3, where the wake can switch intermittently between the  $2P_O$  and 2P modes (or between the  $2P_O$  and 2S modes), *even if the cylinder is vibrating with steady amplitude and frequency.*

The identification of this distinct  $2P_O$  mode allows us to clarify the vortex formation mode for the upper and lower branches in a free vibration response. Our initial interpretation of the results of Govardhan & Williamson (2000) was that the 2P mode they found for the upper branch of response, which exhibited a much smaller secondary vortex (as for the  $2P_O$  mode), was the same mode essentially as the 2P mode in the lower amplitude branch, but was simply affected in its configuration by an increase in amplitude. The present work clearly shows that the existence of the  $2P_O$  mode is not simply an amplitude effect, but instead it is a mode that is quite distinct from the 2P mode, existing at the same amplitude and wavelength. The concept of an overlap region could not be discovered from free vibration, because the 2P and  $2P_O$  modes yield different values of fluid excitation and thus cannot sustain free vibration at the same amplitude

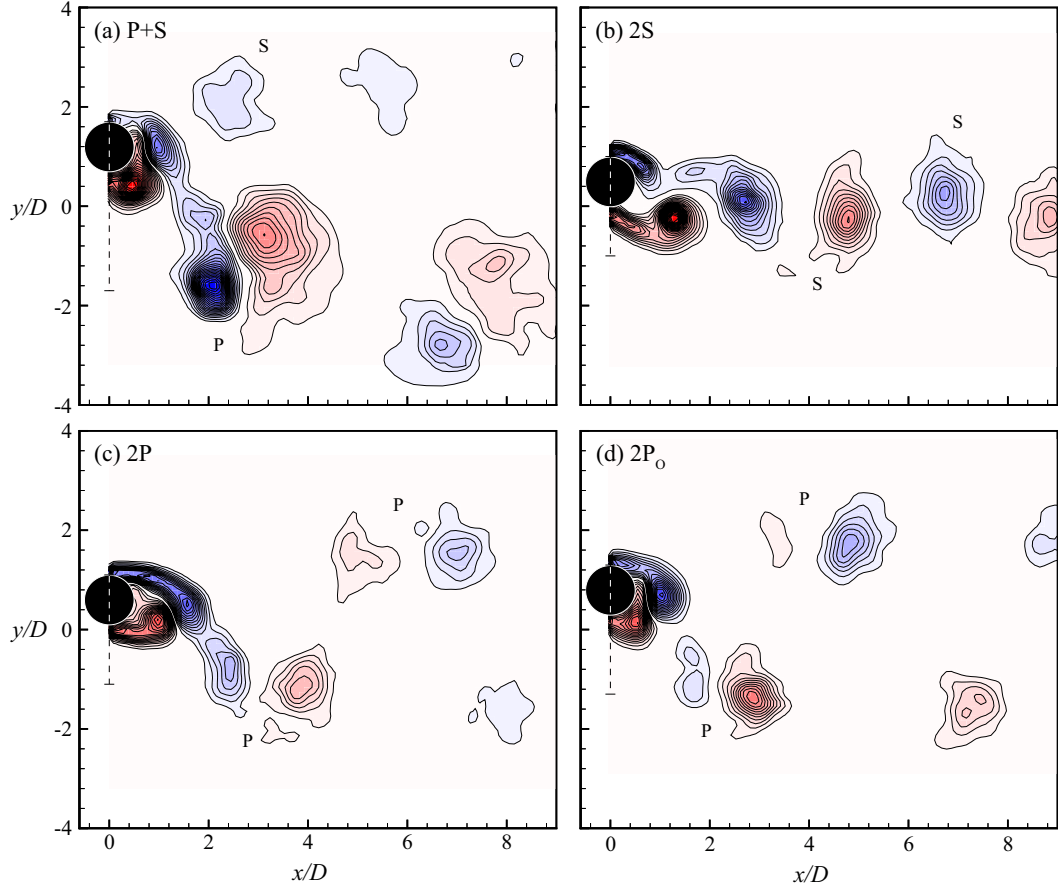


Figure 4.4: Vorticity fields for each of the main vortex shedding modes  $\{P+S, 2S, 2P, 2P_0\}$ . We observe a switch in timing of the initially shed vortex from the 2S mode to the 2P mode. In all cases the vorticity field is phase-averaged over 20 cycles of oscillation, contour levels shown are:  $\omega D/U = \pm 0.4, \pm 0.8, \pm 1.2, \dots$  Measurement locations in the amplitude-wavelength plane are as follows: P+S mode:  $(A^* = 1.2, \lambda^* = 4.0)$ ; 2S mode:  $(A^* = 0.5, \lambda^* = 5.0)$ ; 2P mode:  $(A^* = 0.6, \lambda^* = 6.4)$ ;  $2P_0$  mode:  $(A^* = 0.8, \lambda^* = 5.6)$ .

level. This is further discussed later in §4.6.

In addition to the principal four modes of vortex formation shown in Figure 4.4, namely the set  $\{2S, 2P, 2P_0, P+S\}$ , we also find a region where the wake is not synchronized with the cylinder oscillation, at high normalized wavelength (the brown shaded region in Figure 4.3); and a region where a 2S mode initially forms behind the cylinder, but the vortices coalesce downstream, at low normal-

ized wavelength, called the coalescing 2S mode, or C(2S) in Figure 4.3. Finally, there is a small band where the desynchronized wake region overlaps with the 2P mode, in which the wake will switch intermittently between these two conditions. The desynchronized wake mode, and the C(2S) mode, are characterized using detailed force time traces and spectra in Chapter 3 (Morse & Williamson, 2009b).

In this study, the existence of an overlapping mode is significant, because it is associated with the maximum amplitude where one experiences positive excitation. It will thus be the mode yielding the peak resonant amplitude in free vibration. We shall also see that, as a result of the fact that the  $2P_O$  mode overlaps other regimes, the possible mode jumps and interplay between the modes, can become quite complex, and this will be investigated in §4.6.

#### 4.4 Contours of fluid excitation and effective added mass

Although we may present several useful fluid forcing quantities in a set of contour plots, we choose in this study to focus on the two most relevant quantities for the prediction of free vibration responses, namely the fluid excitation ( $C_Y \sin \phi$ ) shown in Figure 4.5, and the effective added mass coefficient ( $C_{EA}$ ) shown in Figure 4.6. The fluid excitation primarily affects the amplitude of vibration ( $A^*$ ), as shown in the amplitude equation (4.4) above. On the other hand, the effective added mass ( $C_{EA}$ ) affects primarily the frequency of vibration ( $f^*$ ), as shown in the frequency equation (4.5), and will be of use in predicting response in §4.5. We also include here a related plot in Figure 4.7, in the plane of amplitude-wavelength, of lines for which the normalised velocity ( $U^*$ ) is a

constant. We shall use this plot extensively in §4.6 to show how the energy transfer into the body motion varies as a function of amplitude, for fixed values of normalised velocity,  $U^*$ .

The regions of positive fluid excitation (which is necessary for free vibration to occur), exist within the 2S, 2P,  $2P_O$ , and desynchronized regimes, that are shown in Figure 4.5. In fact, it is significant that the highest amplitude for which there is positive fluid excitation lies in a  $2P_O$  overlap region. In this region, the wake may intermittently switch between a  $2P_O$  mode of vortex shedding, which will yield a net positive excitation, and a 2P mode of vortex shedding, yielding net negative excitation, as shown in the time trace of the instantaneous rate of energy transfer (i.e. power) in Figure 4.8. This means that, for the conditions shown in Figure 4.8 ( $A^* = 0.8$ ,  $\lambda^* = 5.4$ ), free vibration could occur only if the mode of vortex formation is  $2P_O$ . If the mode of vortex formation were to switch to the 2P mode, the fluid excitation would become negative, and the amplitude would drop until the fluid excitation becomes positive for this 2P mode ( $A^*$  below about 0.56), or until the vortex formation possibly switches back to the  $2P_O$  mode. This switching of vortex formation modes is what leads to the intermittent switching between the upper branches and lower branches of a free vibration response, as explained in more detail in §4.6.

In order to more fully understand the difference between the  $2P_O$  and 2P vortex formation modes, we shall briefly introduce the concept of a “vortex force”. Following the analysis of Lighthill (1986) and Govardhan & Williamson (2000), we decompose the total transverse fluid force coefficient ( $C_{TOT}$ ) into a “potential force” component ( $C_{POT}$ ) given by the potential added mass force, and a “vortex force” component ( $C_{VORT}$ ), due to the dynamics of vorticity. For sinu-

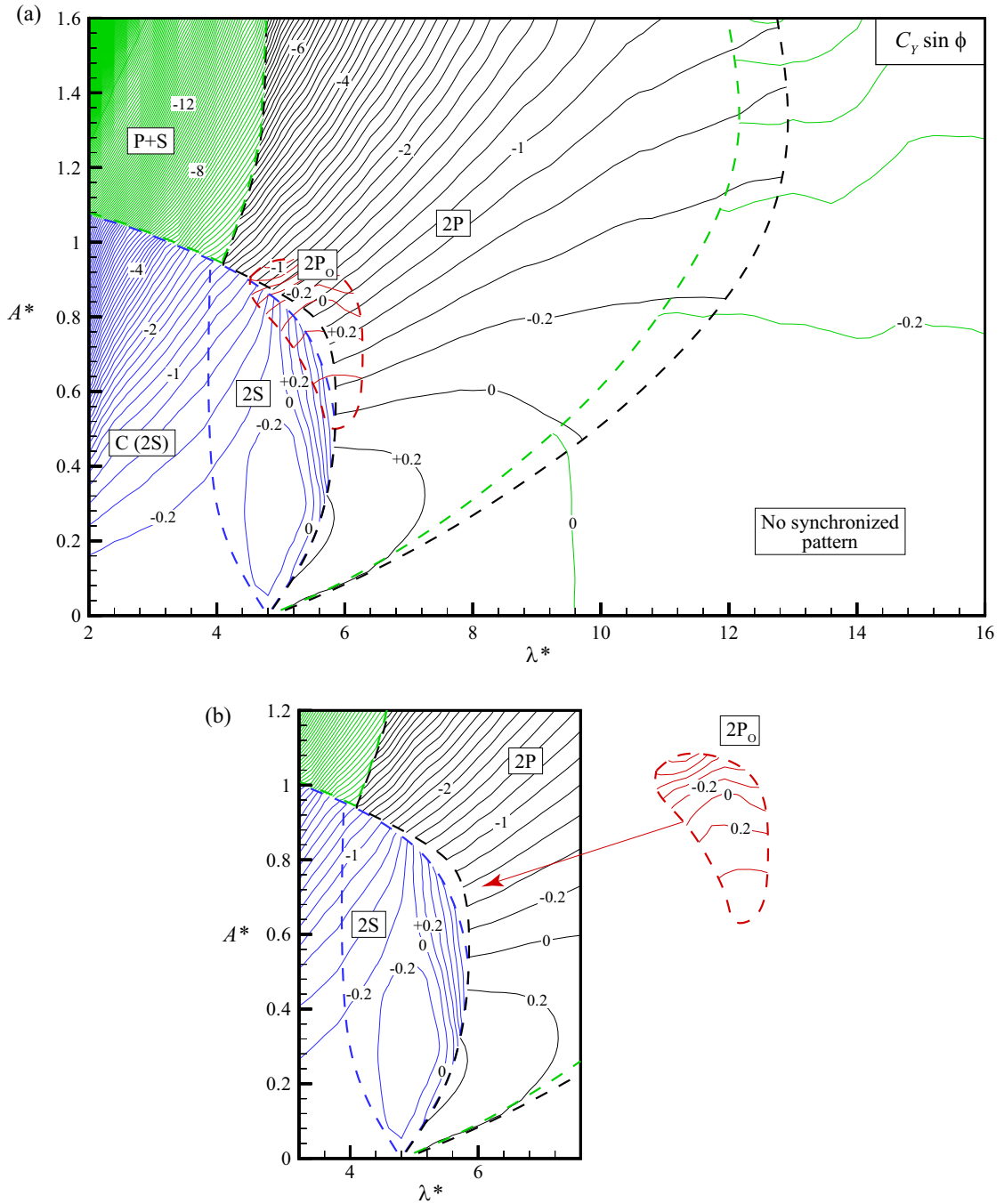


Figure 4.5: Contours of the force in phase with velocity,  $C_Y \sin \phi$  (normalized “fluid excitation”), for  $Re = 4,000$ . Boundaries between modes are indicated by dashed lines. Note that contours overlap in regions where multiple vortex shedding modes are possible. In (b) we pull away the  $2P_0$  mode to more clearly show the 2P and 2S mode regions underneath. Contour interval is 0.2.

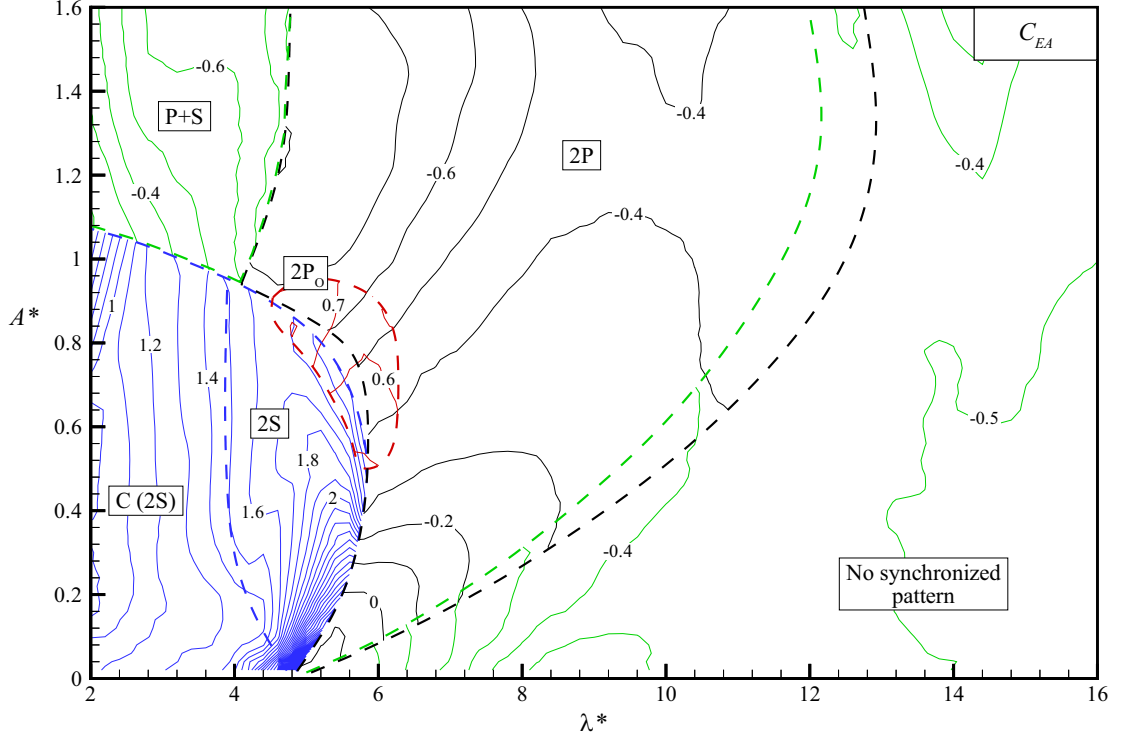


Figure 4.6: Contours of the effective added mass,  $C_{EA}$ , for  $Re = 4,000$ . Boundaries between modes are indicated by dashed lines. Note that contours overlap in regions where multiple vortex shedding modes are possible. Contour interval is 0.1.

soidal body motion, the potential force coefficient can be calculated to be:

$$C_{POT}(t) = 2\pi^3 \frac{y(t)/D}{(U^*/f^*)^2} \quad (4.10)$$

Thus we see that the instantaneous potential added mass force  $C_{POT}$  is always in phase with the cylinder motion,  $y(t)$ , as one might expect. The vortex force coefficient can then be found by subtracting the potential force coefficient from the total force coefficient:

$$C_{VORT}(t) = C_{TOT}(t) - C_{POT}(t) \quad (4.11)$$

So that we may further illustrate the difference between the  $2P_0$  and  $2P$  vortex modes, we show force time traces and wake vorticity fields for each mode,

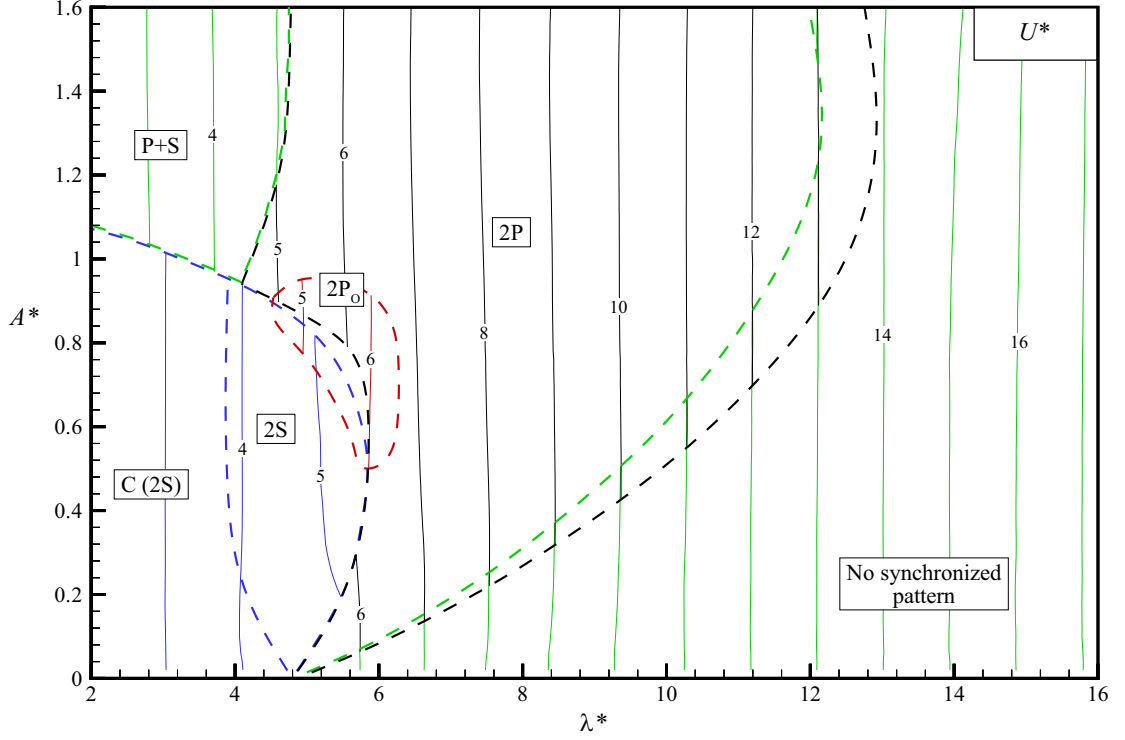


Figure 4.7: Cuts of constant normalized velocity ( $U^*$ ) for  $Re = 4,000$  and  $m^* = 10.0$ .  $U^*$  cuts are determined from the frequency equation (4.5) using contours of  $C_{EA}$ . Note that cuts are discontinuous across vortex formation mode boundaries.

taken during a single experimental run, shown in Figure 4.9. The timing of vortex shedding is quite similar for the two cases even though the  $2P_O$  mode shows a much weaker secondary vortex. Thus the phase of the vortex force (see time trace for  $C_{VORT}$  in Figure 4.9) is similar for the two cases; however, the magnitude of the vortex force is much lower for the  $2P_O$  mode than for the  $2P$  mode. Therefore, when we superpose the potential force (which will be the same for both modes since the motion is the same) onto the vortex force to yield the total force ( $C_{TOT}$ ), we find almost a  $180^\circ$  switch in phase angle for the  $2P_O$  mode. The  $2P_O$  mode then delivers a positive energy transfer into the body motion, while the  $2P$  mode generates negative energy transfer.

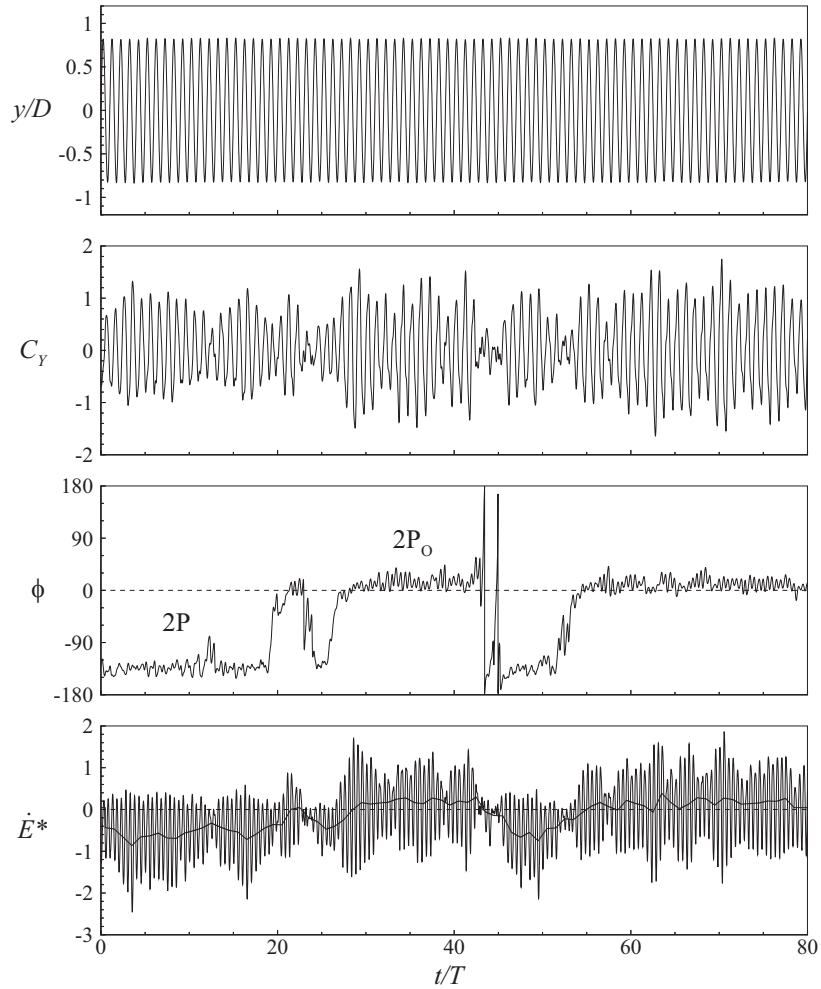


Figure 4.8: Force and energy transfer time traces in the  $2P_O$ – $2P$  overlap region ( $A^* = 0.80$ ,  $\lambda^* = 5.6$ ). The mode switching is most apparent in the phase angle,  $\phi$ . The instantaneous rate of energy transfer,  $\dot{E}^*$ , has large fluctuations, but cycle averages (shown as a thicker line) show that the  $2P_O$  yields a net positive fluid excitation, while the  $2P$  mode yields negative excitation.

For high amplitudes ( $A^* = 0.80$ ), as in the example above, the  $2P$  mode of vortex formation yields negative excitation, and thus cannot sustain free vibration. However, at amplitudes below about 0.6, the fluid excitation for the  $2P$  mode becomes positive. One might ask how the wake vortex dynamics change to accomplish this? As the transverse amplitude is decreased within the  $2P$  region, the wake becomes narrower, as shown in Figure 4.10. In addition, the timing of

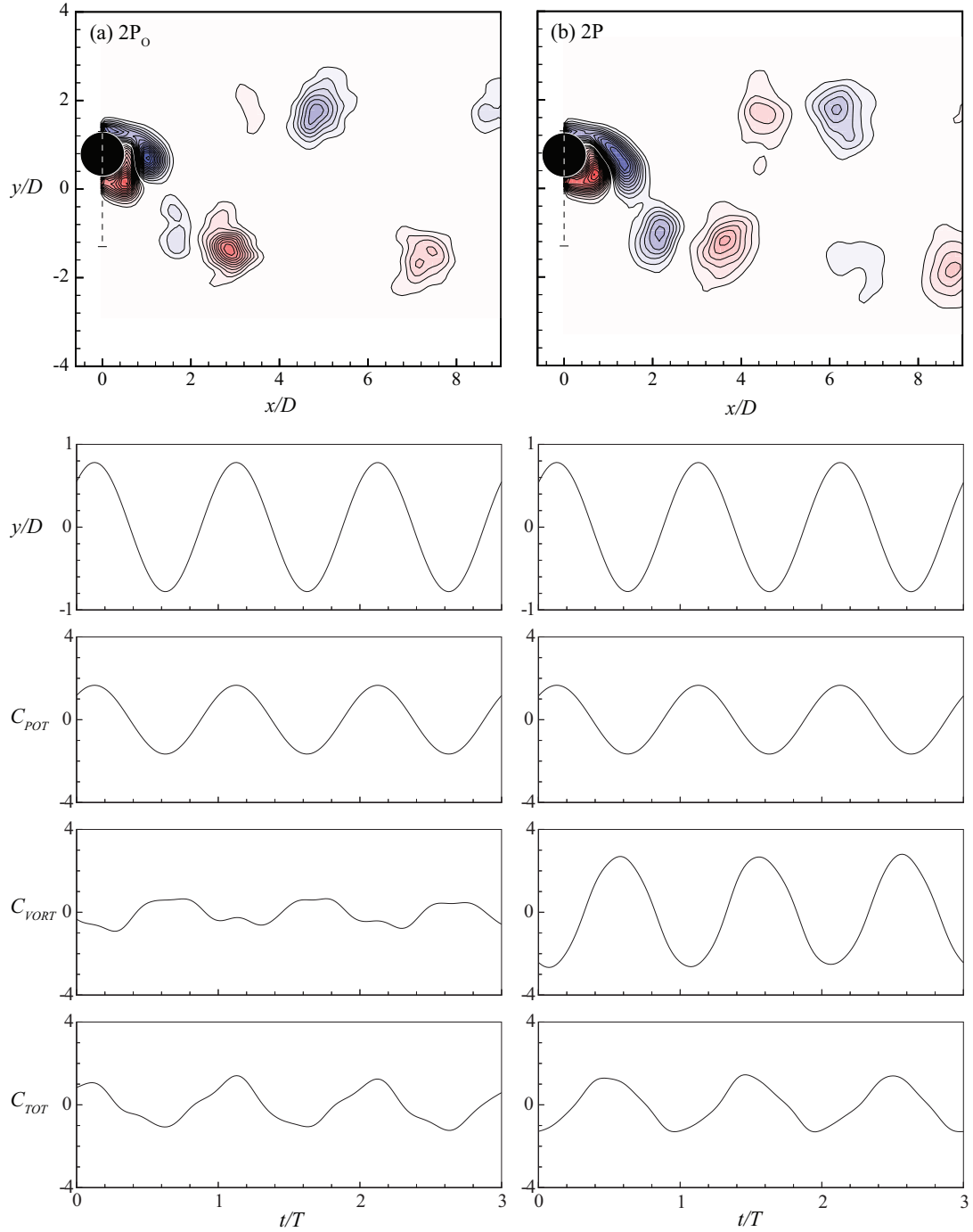


Figure 4.9: Vorticity fields and decomposed force time traces in the  $2P_0$ - $2P$  overlap region, for the same location as in Figure 4.8 ( $A^* = 0.80$ ,  $\lambda^* = 5.6$ ). The vorticity field shows a similar timing in vortex shedding, but with a much weaker secondary vortex strength in the  $2P_0$  case. The smaller magnitude of the vortex force in the  $2P_0$  case leads to a switch in phase of the total force. Vorticity contour levels shown are:  $\omega D/U = \pm 0.4, \pm 0.8, \pm 1.2, \dots$

vortex shedding shifts slightly. Even this small change in timing, as the amplitude ( $A^*$ ) falls below 0.6, is sufficient to alter the vortex phase to cause a switch from negative to positive excitation; in essence, there is no dramatic change in the vortex formation pattern, as energy transfer becomes positive.

## 4.5 Prediction of a free vibration response

The availability of our high resolution force contours now enables us to predict the response of a freely vibrating cylinder, using equations (4.4 - 4.5). We are required to set the system parameters  $\{m^*, \zeta, U^*\}$ , and then to solve for the response parameters  $\{A^*, f^*\}$ . We have measured the fluid forcing quantities:  $\{C_Y \sin \phi, C_{EA}\}$  as functions of  $A^*$  and  $\lambda^*$ , or equivalently as a function of  $A^*$  and  $f^*$ , if one fixes the normalised velocity,  $U^*$ . Thus we can simply solve numerically for amplitude ( $A^*$ ) and frequency ( $f^*$ ), and build up an entire response plot at a given  $m^*$  and  $\zeta$ , as one varies  $U^*$ .

A simpler way to understand this process is to combine the frequency equation (4.5) and amplitude equation (4.4), to give an equation with only the combined mass-damping on the left hand side:

$$(m^* + C_A)\zeta = \frac{C_Y \sin \phi}{4\pi^3 A^*} \lambda^{*2} \sqrt{\frac{m^* + C_A}{m^* + C_{EA}}}, \quad (4.12)$$

where we have also used  $U^*/f^* = \lambda^*$ . Now, for a given mass ratio, we can plot contours of the conglomeration of non-dimensional variables on right hand side of equation (4.12). Each contour will then represent a predicted free vibration response at a particular value of the combined mass-damping,  $(m^* + C_A)\zeta$ . The solution for a system at zero-damping will always follow the zero-excitation

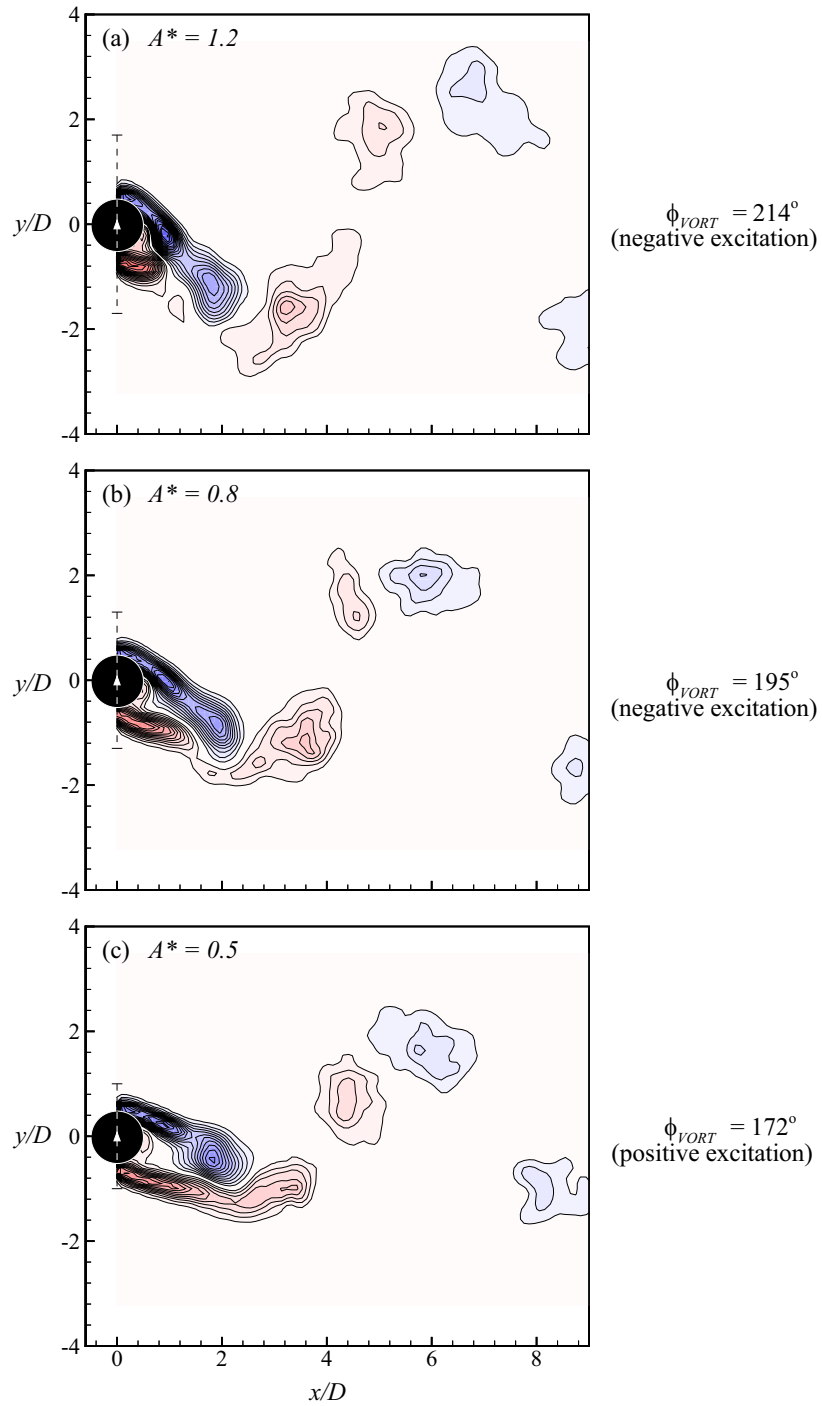


Figure 4.10: Vorticity fields for decreasing amplitude in the 2P region ( $\lambda^* = 8.0$ ). The vortex formation mode does not change, however the timing of vortex shedding becomes slightly later as amplitude decreases, causing a switch from negative to positive excitation. Vorticity contour levels shown are:  $\omega D/U = \pm 0.4, \pm 0.8, \pm 1.2, \dots$

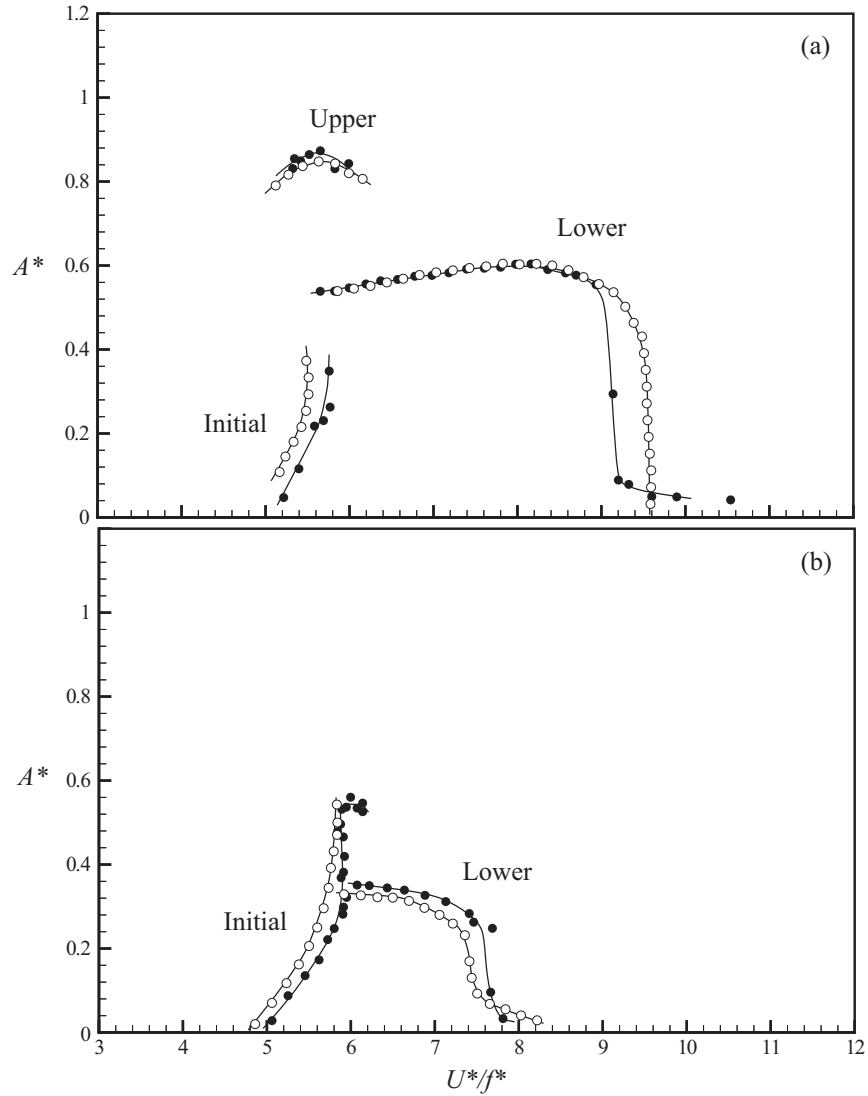


Figure 4.11: Measured and predicted amplitude response for a free vibration system at low mass-damping,  $(m^* + C_A)\zeta = 0$  (a), and high mass-damping,  $(m^* + C_A)\zeta = 0.340$  (b).  $\bullet$  measured free vibration response from Govardhan & Williamson (2006),  $\circ$  predicted response from the present controlled vibration data. In both cases  $m^* = 10.49$ .  $Re = 4,000$  for the controlled vibration case;  $Re = 4,000$  at peak amplitude for the free vibration case.

contour of  $C_Y \sin \phi = 0$ . (Note that for a high enough mass ratio, the frequency ratio,  $f^*$ , will be close to 1, and contours of  $C_{EA}$  are not actually needed.)

With this approach, we are readily able to use our controlled vibration data

to predict the response of a freely vibrating cylinder, in the examples of Figure 4.11. We find close agreement with measured free vibration amplitude response (taken from Govardhan & Williamson, 2006), for both high and low mass-damping. To obtain the complete predicted response plot, we look for solutions in each of the fluid forcing regimes identified in Figures 4.5 and 4.6. For the low mass-damping case, where we find a three branch response, the initial branch lies in the 2S region, the upper branch in the  $2P_O$  region, and the lower branch in the 2P region. For the high mass-damping case, there are two branches: an initial branch in the 2S region and lower branch in the 2P region. The 2S- $2P_O$  and  $2P_O$ -2P overlap regions can lead to some interesting behavior as we discuss later in §4.6.

The agreement between predicted and measured free vibration response shown here is much closer than has been found in previous studies, and is only possible because of the high resolution of our force data, and the careful matching of the experimental arrangement between the controlled and free vibration cases. The Reynolds number at peak response was also matched to be equal to 4,000 for the two cases (noting that for the controlled vibration prediction,  $Re = 4,000$  throughout the response plot). This match of Reynolds number is important, because the peak amplitude in the upper branch depends on  $Re$ , as explained in Govardhan & Williamson (2006), and discussed briefly below.

In addition to the fluid force contours at  $Re = 4,000$ , we have generated complete contour plots at  $Re = 12,000$ , and show for brevity only one of these plots (for excitation energy,  $C_Y \sin \phi$ ), within Appendix B. We have been able to predict complete curves of peak amplitude versus mass-damping from the two Reynolds numbers, using the idea of the “modified Griffin” plot put forward in

Govardhan & Williamson (2006). The agreement with the predictions from the controlled vibration contour plots with the free vibration data is good. We are also able to search for the peak amplitude,  $A_{PEAK}^*$ , which is found when one has zero damping, taken from the point where the curve for zero excitation energy ( $C_Y \sin \phi = 0$ ) reaches a maximum for each Reynolds number. A comparison of this predicted peak amplitude,  $A_{PEAK}^*$ , with the extensive compilation of peak amplitude from free vibration data, shows good agreement.

## 4.6 Introducing “energy portraits” to understand mode transitions

In the previous section we demonstrated the potential for accurate response prediction, using our contour plots of force. In this section, we study the transitions that occur between the different response branches, and stability of equilibrium amplitude solutions, using the concept of an “energy portrait”.

### 4.6.1 Introduction of the concept of an “energy portrait”

We define an “energy portrait” as a plot of the energy of excitation ( $E_{IN}^*$ ), and the energy dissipated to structural damping ( $E_{OUT}^*$ ), as a function of amplitude ( $A^*$ ), while keeping normalized velocity ( $U^*$ ) fixed. We use these energy portraits to determine the stability of equilibrium amplitude solutions, and to understand the mode transitions that occur between branches in free vibration. It is relevant in this section to refer often to Figure 4.5, where we plot normalised energy of excitation ( $C_Y \sin \phi$ ), and where the fluid force regimes, and shape of

the contours, are quite key to the energy portraits. (One should note that plots of fluid force excitation ( $C_Y \sin \phi$ ) as a function of amplitude were presented as early as Griffin (1980), and as noted by Bearman (1984) in his review, Griffin's plot could be used to show that the excitation, after reaching a maximum, decreased such that there was no excitation beyond an amplitude of  $1.0D - 1.5D$ .) This suggested a limiting displacement for free vibrations.

To demonstrate the usefulness of the concept of the energy portraits, we exhibit one possible shape which may occur for fluid excitation contours in the amplitude-wavelength plane, in Figure 4.12(a). This particular variation of excitation energy would lead to an 'S' shaped curve for  $E_{IN}^*$  in the energy portrait of Figure 4.12(b). The energy lost due to damping,  $E_{OUT}^*$ , will intersect the origin, and have a slope proportional to the specific value of mass-damping  $(m^* + C_A)\zeta$ . (One may note that the precise shape of the  $E_{OUT}^*$  curve, as well as the shape of the  $U^* = \text{constant}$  line in the plane of amplitude-wavelength, both depend on the frequency ratio,  $f^*$ . In general, the  $U^*$  cut will be nearly vertical (in a), and the  $E_{OUT}^*$  curve will be nearly straight (in b). Both lines become more straight as one increases the mass ratio, and  $f^* \sim 1.0$ ).

Steady state response solutions are found where the energy into the system equals the energy out of the system. In our example of lower damping, in Figure 4.12(b), there is one equilibrium point, and hence one possible free vibration amplitude. In our example of higher damping, in Figure 4.12(c), there exist three equilibrium points, in other words three response amplitudes. However, *only two of these response amplitudes are stable*. The central equilibrium solution is unstable: for example, if a perturbation increases the amplitude slightly, the energy into the system would be greater than the energy out of the system;

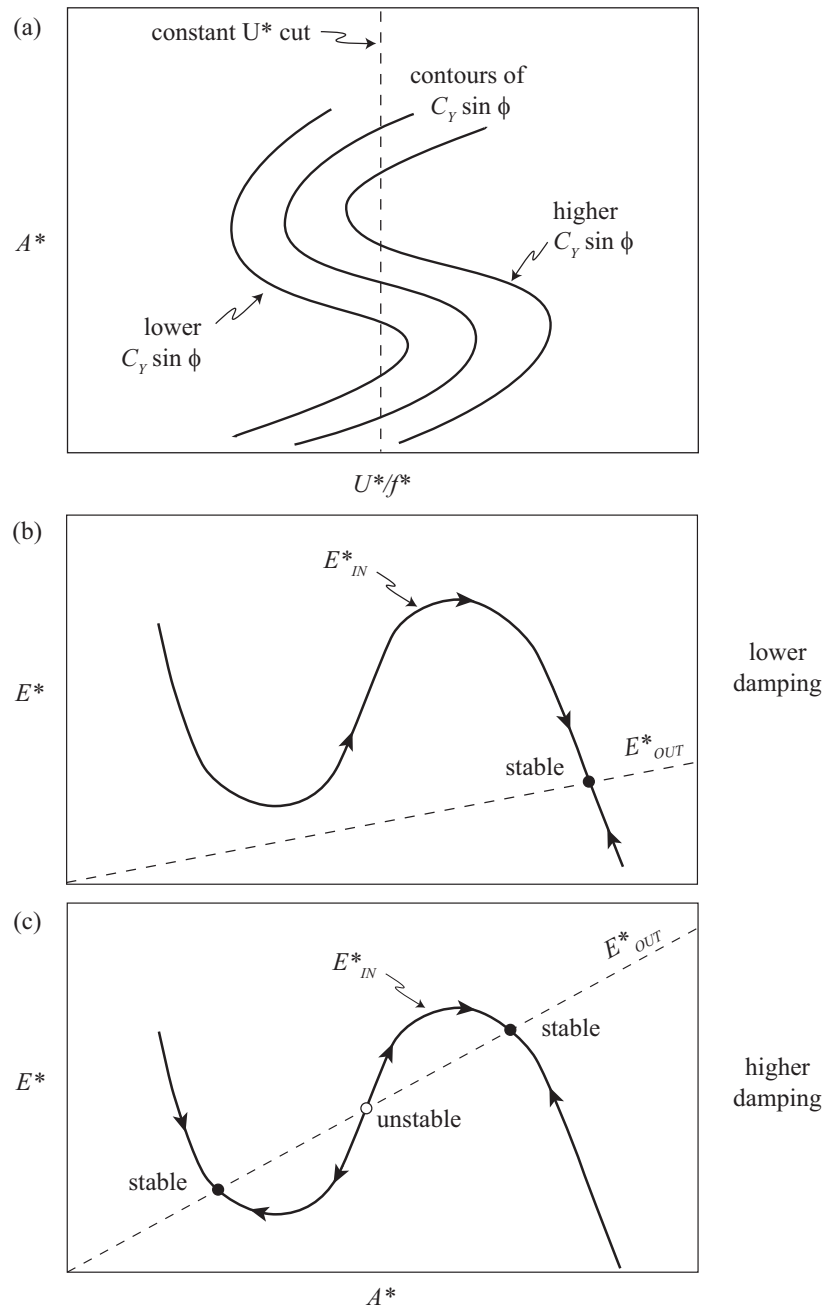


Figure 4.12: Schematic plots of an “energy portrait”. We take a cut of constant normalized velocity through contours of fluid excitation (a) and plot the energy balance ( $E_{IN}^*$  and  $E_{OUT}^*$ ) as a function of normalized amplitude (b) and (c). At the equilibrium points, the energy transferred from the fluid to the cylinder is equal to the energy lost to damping. Arrows indicate direction of movement for non-equilibrium states.

the amplitude would continue to increase, ultimately reaching the upper stable solution. Stability and instability of equilibrium solutions in the energy portrait can be defined by the slope of the energy curves, at the equilibrium points, as follows:

$$\text{Stable: } dE^*/dA^* < 0,$$

$$\text{Unstable: } dE^*/dA^* > 0,$$

where  $E^*$  is the net energy transfer into body motion:  $E^* = E_{IN}^* - E_{OUT}^*$ . Free vibration would occur at the stable equilibrium points. In our example, there are two stable free vibration amplitudes, and would correspond to two different branches of response.

Let us now apply the concept of the “energy portrait” to our controlled vibration data at  $Re = 4,000$ . We consider a typical mass ratio for systems in water,  $m^* = 10$ , for which the constant  $U^*$  lines (or “cuts”), in the amplitude-wavelength plane, will be nearly vertical. We start with a simple case, a cut in this plane for which  $U^* = 7.0$ . (This cut may be seen in the amplitude-wavelength plane, in Figure 4.7). For our chosen values of mass-damping,  $(m^* + C_A)\zeta$ , in Figure 4.13, there is only one equilibrium solution (a stable solution). As the mass-damping increases, the equilibrium amplitude (i.e. the predicted free vibration amplitude) will decrease. At sufficiently high mass-damping, no solution will exist, in this example.

We shall now employ the energy portrait concept in a more involved case. Let us consider a cut for which  $U^* = 5.1$  in the amplitude-wavelength plane, which we might expect will lead to an initial and upper branch of free vibration. In this case, the energy into the system follows an ‘S’ curve, as shown in Figure

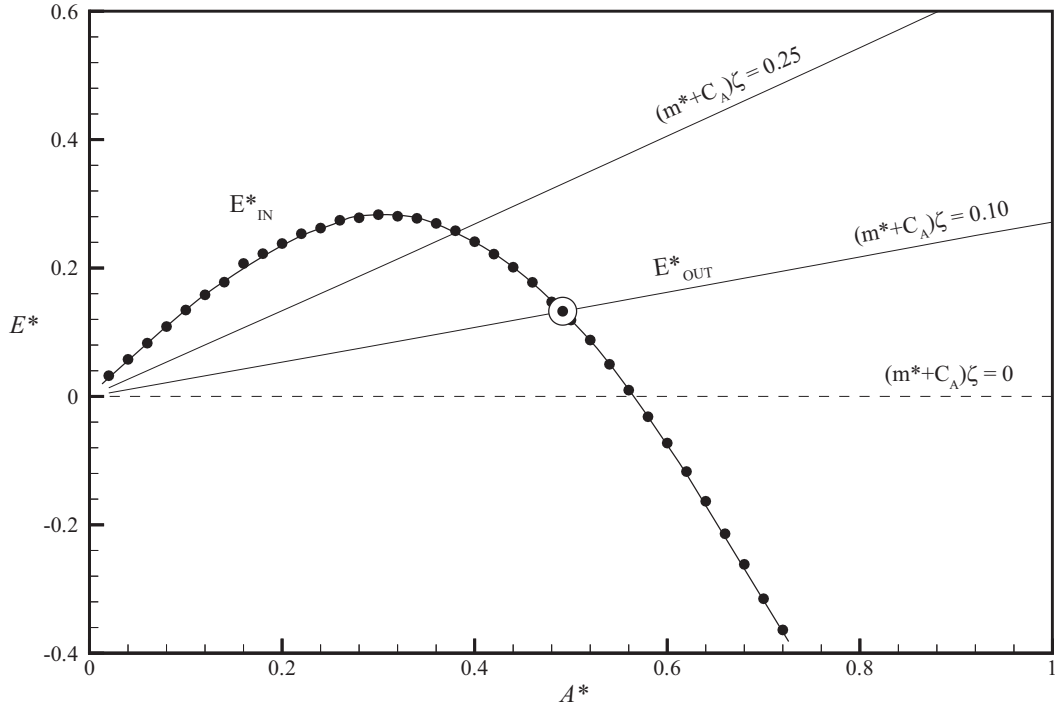


Figure 4.13: Energy portrait for  $m^* = 10$ ,  $U^* = 7.0$  (lower branch). The amplitude of the equilibrium point ( $\odot$ ) decreases as the mass-damping increases.

4.14, similar to the example in Figure 4.12, discussed above. The two stable equilibria at low and high amplitude will correspond to the initial branch and upper branch of free vibration, respectively. Of course, the unstable equilibrium will not appear in a free vibration response. All three solutions here represent the 2S mode of vortex formation, so this is an unusual case where both the initial branch and the upper branch would in fact show a 2S mode of vortex formation. This unusual case has not been demonstrated in free vibration experiments in the literature, as yet. We see from the energy portrait that under conditions of high mass-damping [ $(m^* + C_A)\zeta = 0.15$ ], only one stable equilibrium exists, corresponding to an initial response branch in free vibration. This is consistent with experimental measurements from free vibration results where the upper branch disappears, for sufficiently high mass-damping.

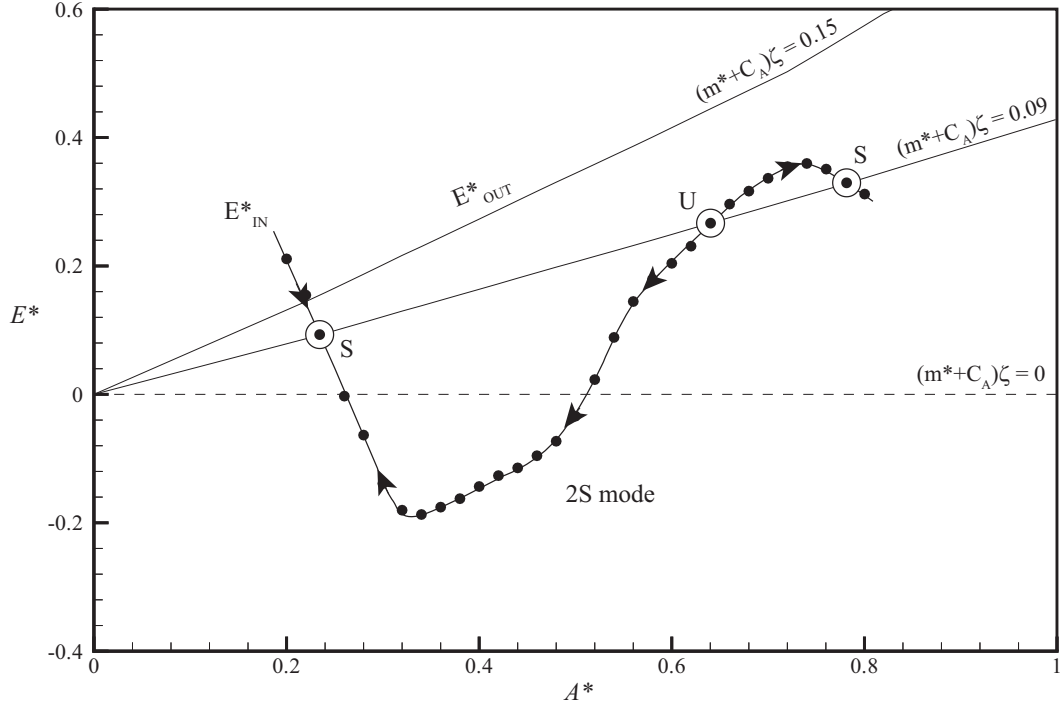


Figure 4.14: Energy portrait for  $m^* = 10$ ,  $U^* = 5.1$  (initial and upper branch). For low values of mass-damping there are two stable equilibrium points (indicated by 'S') and one unstable equilibrium point (indicated by 'U'). The stable equilibria correspond to the initial branch and upper branch of a free vibration response.

From the excitation force contours in Figure 4.5, we note there exists a region where the 2S and the  $2P_0$  regimes overlap, such that the fluid excitation will not be continuous across this transition. The cut for  $U^* = 5.1$  passes through this overlap region (a similar cut,  $U^* = 5.0$ , can be seen in Figure 4.7). Therefore the energy portrait will show a small range of amplitudes where two possibilities exist for  $E_{IN}^*$ , depending on the mode of vortex shedding (2S or  $2P_0$ ). In Figure 4.15, we now include this second branch of excitation energy, corresponding to the  $2P_0$  mode. ( $E_{OUT}^*$  will also be very slightly different for the two modes, but for simplicity we have kept an average value in this overlap regime.) For the higher mass-damping chosen here [ $(m^* + C_A)\zeta = 0.09$ ], three solutions are

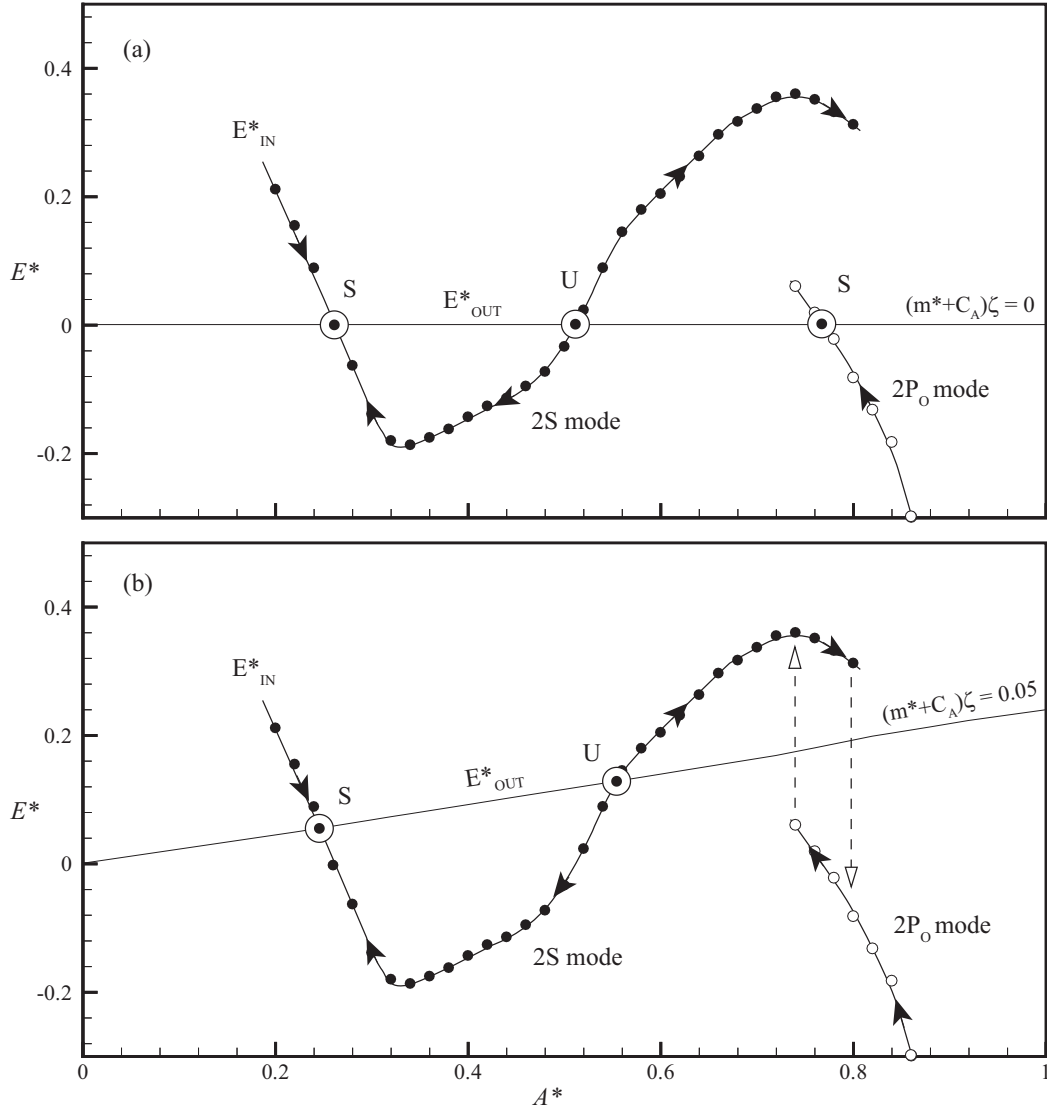


Figure 4.15: Energy portrait for  $m^* = 10$ ,  $U^* = 5.1$  showing distinct values of fluid excitation ( $E_{IN}^*$ ) for the 2S ( $\bullet$ ), and 2P<sub>0</sub> ( $\circ$ ) vortex formation modes. For low mass-damping (a) there are three equilibria ( $\odot$ ). For moderate mass-damping (b), there is no stable equilibrium point at the upper branch amplitude. Instead, the amplitude will vary between about  $A^* = 0.74$  and  $A^* = 0.8$ .

found as shown earlier in Figure 4.14. For our lowest selected mass-damping here [ $(m^* + C_A)\zeta = 0$ ], the high amplitude stable solution would exhibit the 2P<sub>0</sub> wake mode, in Figure 4.15(a), yielding an upper branch, as observed typically in free vibration experiments.

A particularly interesting case occurs if one has an intermediate mass-damping in Figure 4.15(b), since there is no equilibrium point to give a steady upper branch amplitude. If the system has a high amplitude above 0.6 or so, and we have the 2S mode of vortex formation, the energy into the system will be greater than the energy lost to damping, and the amplitude will increase until the system enters the  $2P_0$  regime. The fluid excitation will drop, but it will now fall below the energy dissipated to damping, causing the amplitude to decrease, until the vortex mode jumps back to the 2S mode. In this manner, the cycle will repeat. Thus the normalized amplitude will fluctuate in an unsteady manner, remaining between about 0.72 and 0.8. This type of behavior is actually observed in the free vibration case, where the upper branch often shows oscillations that are less steady than found in the initial or lower branches (Khalak & Williamson, 1996).

#### 4.6.2 Hysteresis between the Initial $\leftrightarrow$ Upper branches

In the free vibration response of Govardhan & Williamson (2006), as shown in Figure 4.11, there exists a hysteretic mode transition between the initial and upper response branches, around  $U^* = 5.5$ . This hysteresis, for such a low-mass damping system, can readily be understood, if we employ a set of energy portraits over a small range of normalized velocity, as shown in Figure 4.16. For simplicity we will consider a system with zero damping so that all the equilibria will lie on the horizontal axis. (Also we will take an average of the fluid excitation in the region where the 2S and  $2P_0$  modes overlap, simply to clarify the phenomena, and avoid the small cyclic oscillations we saw in Figure 4.15(b).) Depending on the normalized velocity, there may be one stable equilib-

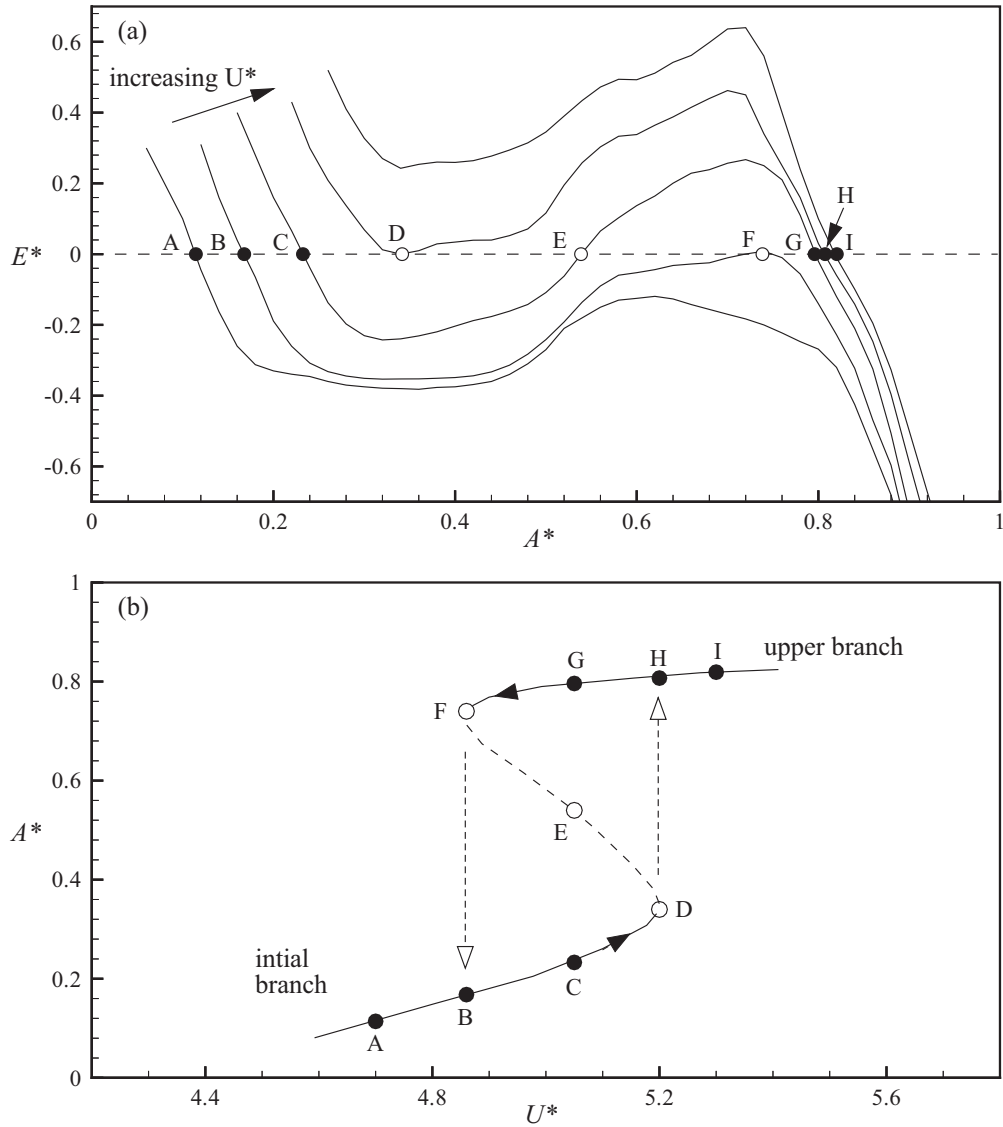


Figure 4.16: Energy portraits (a) and amplitude response (b) for the hysteresis mode transition between the initial and upper branches.  $E_{IN}^*$  curves are shown for  $U^* = 4.70, 4.86, 5.05, 5.20,$  and  $5.30$ ,  $\bullet$  stable equilibria,  $\circ$  unstable equilibria.

rium solution, or two stable solutions plus one unstable solution. The location of all these equilibrium solutions on a free vibration amplitude response plot are shown in Figure 4.16(b).

We commence with a low velocity  $U^* = 4.70$ , where only one solution exists, corresponding to the initial branch, shown as point A in Figure 4.16(b). The

reader should look back and forth between (a) and (b) as we discuss the hysteresis, as follows. As we increase  $U^*$  to 4.86 and upwards to 5.05, a second stable equilibrium point will appear on the upper branch (point G). Nevertheless, the system will remain on the initial branch (point C). Once the normalized velocity is increased to 5.20, the initial branch equilibrium will disappear in a *saddle-node bifurcation* (point D), and the amplitude will jump to the upper branch (point H). With further increase in  $U^*$ , the solution simply shifts along the upper branch (to point I and beyond). However, if the normalized velocity is decreased, the solution will remain on the upper branch, until that equilibrium disappears in another saddle-node bifurcation at  $U^* = 4.86$  (point F). The amplitude will then drop to the initial branch (point B), thus completing the hysteresis loop. In summary, the progression of points for increasing  $U^*$  is A-B-C-D-jump to H-I. For decreasing  $U^*$ , we have I-H-G-F-drop to B-A.

In the case of a free vibration system with high mass-damping, there are only two branches of response: an initial branch and a lower branch, as shown also in Figure 4.11, with a hysteresis mode transition between them. From the contours presented here, such a hysteresis would not be predicted. However, Bishop & Hassan (1964) showed from their controlled vibration “amplitude cuts” that the location of the jump in magnitude and phase of fluid forcing (which we now know is due to a change in vortex formation mode from 2S to 2P) depended on whether the frequency of vibration was increasing or decreasing. In our case we do not dynamically vary the frequency so we can not observe any hysteresis in the force contours. We expect that the precise location of the 2S-2P boundary will shift very slightly if the frequency (or wavelength) is dynamically increased or decreased, and that this shift in the boundary is what causes the hysteresis between the initial and lower branches of a high mass-damping response.

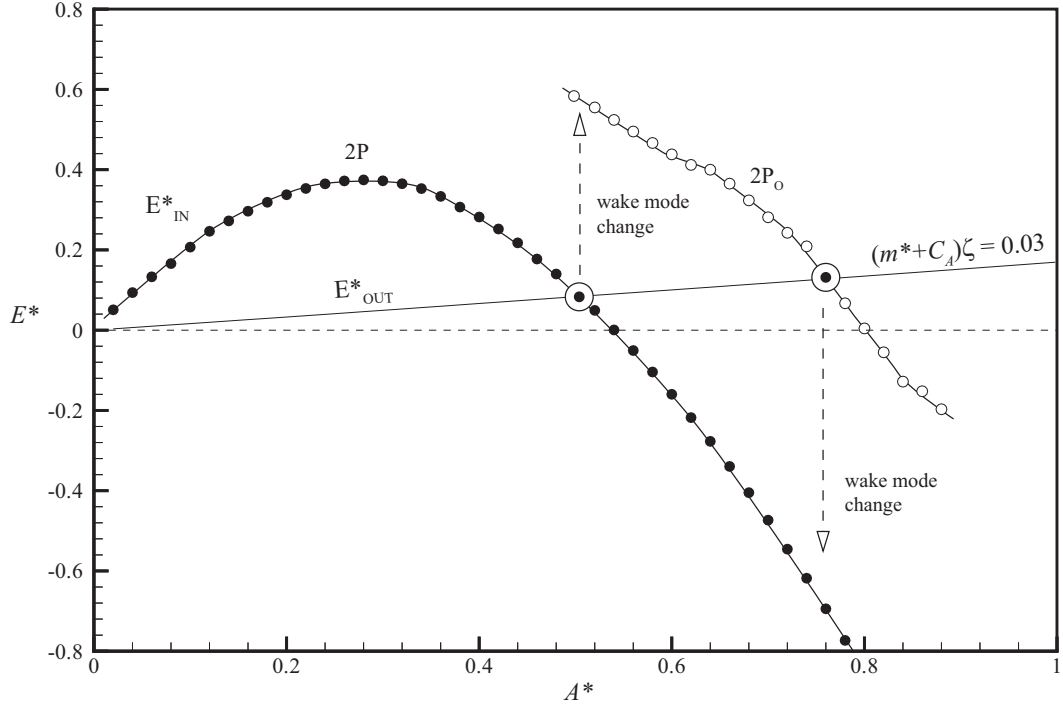


Figure 4.17: Energy portrait for  $m^* = 10$ ,  $U^* = 6.3$  (upper and lower branches), showing distinct values of fluid excitation ( $E_{IN}^*$ ) for the 2P ( $\bullet$ ), and  $2P_0$  ( $\circ$ ) vortex formation modes. Stable equilibria ( $\odot$ ) exist for each vortex formation mode, corresponding to the upper branch ( $2P_0$ ) and lower branch (2P). A change in the mode causes a jump in the fluid excitation, and therefore a change in amplitude.

#### 4.6.3 Intermittent switching between Upper $\leftrightarrow$ Lower branches

In the free vibration of Figure 4.11(a), there exists an intermittent switching between the upper and lower branches at velocities  $U^* \sim 6$ . If we look at the energy portrait for a normalized velocity cut ( $U^* = 6.3$ ) passing through the  $2P_0$ -2P overlap region, there will be two excitation energy  $E_{IN}^*$  curves, one for the each mode of vortex shedding, as shown in Figure 4.17. (There will also be two  $E_{OUT}^*$  curves, because the value of  $C_{EA}$  and thus  $f^*$  is slightly different for the two modes. This difference is extremely small (less than 1%) so we show an averaged line for simplicity.)

For low mass-damping, as indicated in Figure 4.17, if the vortex shedding mode is  $2P_O$ , then there will be one stable equilibrium at the upper branch amplitude (around  $A^* = 0.8$ ). However, this equilibrium will only persist if the vortex formation mode continues to be  $2P_O$ . If the wake switches to a  $2P$  mode, the fluid excitation will drop. This will cause the energy into the system to be less than the energy dissipated by damping, and therefore the amplitude will decrease until a new stable equilibrium for the  $2P$  mode is reached, corresponding to a lower branch amplitude (around  $A^* = 0.5$ ). Later in time, the vortex formation mode could possibly switch back to  $2P_O$ , causing the amplitude to increase back toward the upper branch amplitude. In this way, the amplitude could switch intermittently between the upper and lower branches, sometimes staying at one amplitude or the other for several cycles. This corresponds to what is actually observed in free vibration systems, for example in Govardhan & Williamson (2000).

We emphasize that the switching phenomenon described here is fundamentally different from the unsteady behavior which can occur in the  $2S$ - $2P_O$  overlap region described in §6.1 and shown in Figure 4.15(b). In the  $2S$ - $2P_O$  overlap region the variation in amplitude is much smaller and no steady motion is possible for either vortex formation mode. In the  $2P_O$ - $2P$  overlap region, the difference in amplitude is quite dramatic (appearing as a jump between an upper branch and lower branch), and we find steady amplitude motion can occur, so long as the vortex wake mode remains the same.

## 4.7 Defining the regime where free vibration is possible

The evaluation of fluid forcing, throughout the amplitude-wavelength plane, enables us to determine the regimes where free vibration can occur, of course under the assumption that such motion is approximately sinusoidal. The classical understanding, presented in Figure 4.18(a), is that the region of possible free vibration is the intersection of the positive excitation region, and the synchronized wake region. However, we have found, in this study, that there exist conditions where, even though fluid excitation is positive and the equations of motion are satisfied, the equilibrium solutions are unstable. We therefore remove the area in the amplitude-wavelength plane, where these solutions are unstable, to yield our regime of possible free vibration, in Figure 4.18(b).

We may further point out that vortex-induced motion can occur in the desynchronized region, if there is some positive fluid excitation at the oscillation frequency. The fluid forcing in the desynchronized region has a large component at the (higher) natural vortex shedding frequency, but in fact it also exhibits a smaller force component at the oscillation frequency, as discussed in more detail in Chapter 3 (Morse & Williamson, 2009*b*). Thus, one might expect that free vibration in this region would have distinctly non-sinusoidal motion. However, since the effect of fluid forcing on vibration amplitude is greatly diminished for frequencies away from the oscillation frequency, the higher frequency forcing component can have a negligible effect on the overall body dynamics. Therefore, in our search for the regime of possible free vibration, we add in the region of positive excitation within the desynchronised regime, in Figure 4.18(c). Finally, we may present the overall regime of possible free vibration in (d), which satisfies the requirements, that, not only the fluid excitation is positive, but also

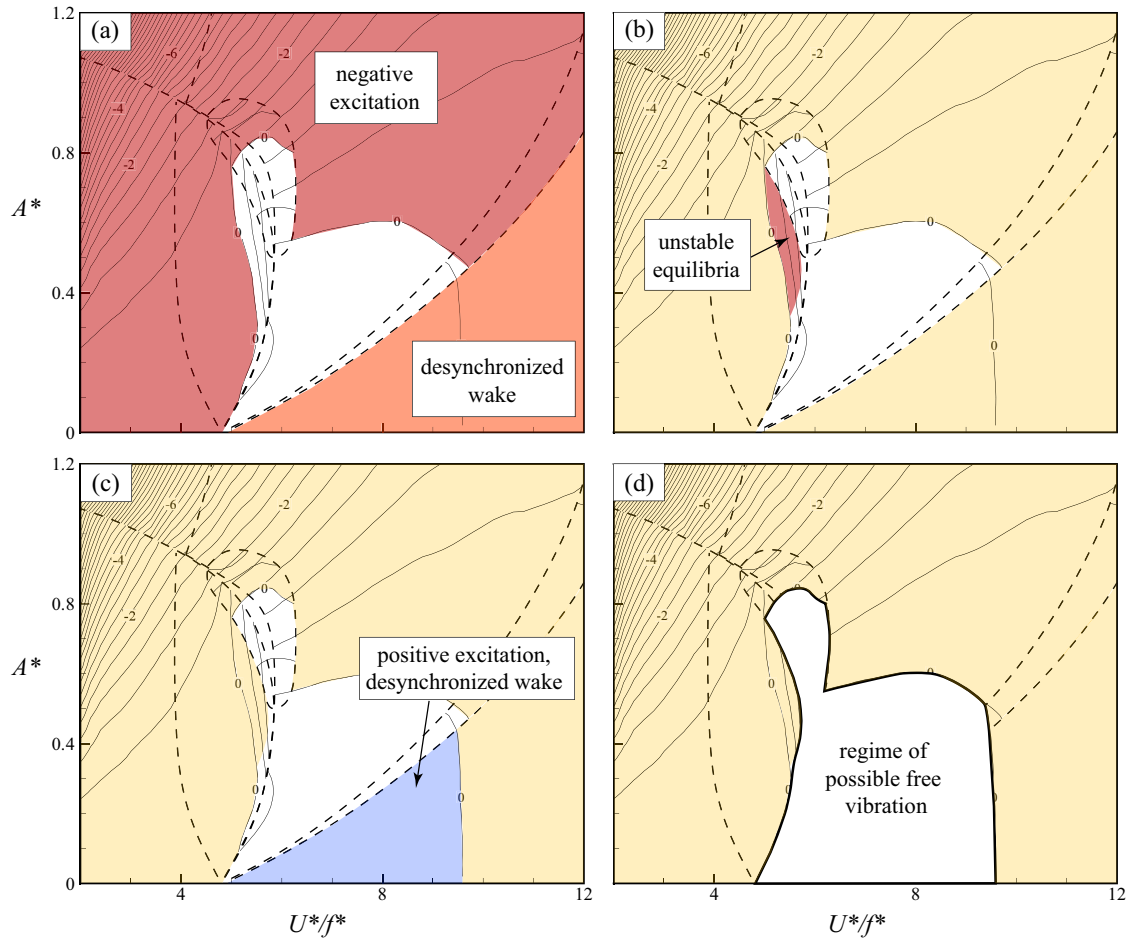


Figure 4.18: Map of where free vibration can occur in the amplitude-velocity plane. (a) Region where the wake is desynchronized from the cylinder motion and region where the fluid excitation is negative. (b) Region where the equilibria are unstable. (c) Region where positive excitation exists, even with a desynchronized wake. (d) Regime of possible free vibration: fluid excitation is positive, and the solutions to the equation of motion are stable.

the amplitude solutions are stable.

## 4.8 Conclusions

In this study, we present new measurements of fluid force on a cylinder that oscillates under controlled vibration, transverse to a flow. We present these new results in the form of high resolution force contour plots within the plane of normalized amplitude and wavelength ( $A^*, \lambda^*$ ), for Reynolds numbers:  $Re = 4,000$  and  $Re = 12,000$ . We identify distinct boundaries, and fluid force regimes, in the amplitude-wavelength plane, based solely on the force measurements. Indeed, we find good agreement between the shapes of the regimes evaluated from force measurements in the present work, and the regimes of vortex formation modes identified from flow visualization in the Williamson-Roshko (1988) map of regimes. By measuring the wake vorticity, we find vortex formation modes that correspond well with those in the Williamson-Roshko map, namely the 2S and 2P modes, as well as the asymmetric P+S mode.

The present high resolution contour plots have enabled us to discover a new high-amplitude regime, in the amplitude-wavelength plane, which overlaps the boundary between the 2S and 2P regimes. Vorticity measurements identify the new vortex formation mode to be similar to the 2P mode, but where the second vortex of each pair is much weaker than the first vortex, in what we define as the '2P<sub>OVERLAP</sub>' or '2P<sub>O</sub>' mode. During an experiment, the vortex formation mode and fluid force can switch intermittently between the 2P<sub>O</sub> and 2P modes, even when the amplitude and frequency are kept constant. The switch in vortex formation mode can cause a large jump in the fluid excitation which would lead to a jump in amplitude for a free vibration response, as found in direct measurements on elastically mounted bodies.

Employing the force contour data, we are able to predict the response of a freely vibrating cylinder. This prediction agrees well with direct measurements from free vibration experiments, for the three-branch response of a low mass-damping system, and for the two-branch response of a system with high mass-damping. We are also able to accurately recreate the “modified Griffin plot” of peak amplitude versus mass-damping at both  $Re = 4,000$  and  $Re = 12,000$  (shown in Appendix B), and our data also agrees well with the plot of peak amplitude as a function of  $Re$ , compiled in the recent work of Govardhan & Williamson (2006).

In order to study the stability of equilibrium amplitude solutions, and to better understand the mode transitions between solution branches of the free vibration response, we introduce the concept of an “energy portrait”. We define such an energy portrait as a plot of the excitation energy into the system and the energy out of the system dissipated by damping, as a function of amplitude, as we keep normalised flow velocity constant. The energy portrait allows us to identify equilibrium points, where there is a balance of energy transfer into the system ( $E_{IN}^*$ ) and out of the system ( $E_{OUT}^*$ ), and to determine the stability of these equilibrium points, as follows:

$$\text{Stable: } dE^*/dA^* < 0$$

$$\text{Unstable: } dE^*/dA^* > 0$$

where  $E^*$  is the net energy ( $E_{IN}^* - E_{OUT}^*$ ) transferred into the body motion.

In the vicinity of the transition between the initial and upper response branch found in free vibration, for low mass-damping, the fluid excitation follows an ‘S’ like shape, leading to multiple equilibria in the energy portrait. We

are able to explain the existence of hysteresis, found in free vibration, on the basis of a set of energy portraits, where we identify saddle node bifurcations, and where we may identify stable and unstable solutions. On the other hand, the transition from the upper branch to lower branch of free vibration response involves an intermittent switching between the modes. We may explain this phenomenon by considering the overlap of two mode regimes in the amplitude-wavelength plane. The vortex formation is able to switch intermittently as a function of time, and induces jumps between two stable amplitude solutions, one corresponding with the  $2P_O$  mode, having a higher excitation energy, and the other corresponding with the  $2P$  mode of vortex formation, with lower excitation energy. In essence, the hysteresis between modes occurs due to the shape of the fluid excitation contours in the amplitude-wavelength plane, while the intermittent switching transition occurs because there is an overlap of mode regimes in this plane.

As a final point, we may clearly define the region in the amplitude-wavelength plane which would admit free vibration. The requirements for free vibration have generally been assumed to be a synchronized wake and a positive fluid excitation. However, through our energy portraits, we identify a regime for unstable equilibria where steady free vibration is not possible, which must therefore be removed from the region of possible free vibration. We should also note that vortex-induced vibration can occur if there is an area of positive excitation even within the regime of the desynchronised wake. Therefore, our complete regime for free vibration in the amplitude-wavelength plane satisfies two principal criteria; namely, the existence of net positive fluid excitation, and stability of the equilibrium amplitude solutions.

## CHAPTER 5

# Steady, unsteady, and transient vortex-induced vibration predicted using controlled motion data

MORSE, T. L. & WILLIAMSON, C. H. K. (2009)

In preparation for *Journal of Fluid Mechanics*.

In this study, we represent transient and unsteady dynamics of a cylinder undergoing vortex-induced vibration, by employing measurements of the fluid forces for a body controlled to vibrate sinusoidally, transverse to a free stream. We generate very high-resolution contour plots of fluid force in the plane of normalized amplitude and wavelength of controlled oscillation. These contours can be used with an equation of motion to predict the *steady state* response of an elastically mounted body. The principal motivation with the present study is to extend this approach to the case where a freely vibrating cylinder exhibits *transient* or *unsteady* vibration, through the use of a simple quasi-steady model. In the model, we use equations which define how the amplitude and frequency will change in time, although the instantaneous forces are taken to be those measured under steady state conditions (the quasi-steady approximation), employing our high resolution contour plots.

The resolution of our force contours has enabled us to define accurately mode regime boundaries in the amplitude-wavelength plane, where there are jump changes in the fluid force, found here for the first time from controlled vibration studies. On account of these boundaries, we can define the different branches of response. In particular, we are able to characterize the nature of

the transition which occurs between the upper and lower amplitude response branches. This regime of vibration is of practical significance as it represents conditions under which peak resonant response is found in these systems. For higher mass ratios ( $m^* > 10$ ), our approach predicts that there will be an intermittent switching between branches, as the vortex formation mode switches between the classical 2P mode, and a “2P<sub>OVERLAP</sub>” mode. Interestingly, for low mass ratios ( $m^* \sim 1$ ), there exists a whole regime of normalized flow velocities, *where steady state vibration cannot occur*. In other words, the classical approach, using controlled vibration force measurements, is unable to predict free vibration response. However, if one employs the quasi-steady model, we discover that the cylinder can indeed oscillate, but only with non-periodic fluctuations in amplitude and frequency. The character of the amplitude response from the model is close to what is found in free vibration experiments. For very low mass ratios ( $m^* < 0.36$  in this study) this regime of unsteady vibration response will extend all the way to infinite normalized velocity.

## 5.1 Introduction

Vortex-induced vibration is important in many practical engineering applications. This phenomenon can lead to fatigue and failure of such structures as oil riser tubes, chimneys and bridges, among others. There are a large number of fundamental studies on the subject, as well as several review articles, for example: Sarpkaya (1979), Bearman (1984), Parkinson (1989), and more recently Williamson & Govardhan (2004). Prior studies have investigated a selection of different flow configurations, including rigid cylinders moving with multiple degrees of freedom, pivoted cylinders, or flexible cables. In this study, we

choose to focus on the most conceptually simple case of vortex-induced vibration, that of an elastically mounted rigid cylinder constrained to move transverse to a flow. Such an arrangement is a paradigm in that it has been found to yield phenomena that are exhibited in the more complex configurations.

In many previous vortex-induced vibration studies, the focus has been on the amplitude and frequency response of the body, when it has reached a state of steady vibration, as a function of the incoming flow velocity. Khalak & Williamson (1999) showed that for a rigid cylinder with only transverse motion and having a low combined mass-damping parameter, the amplitude of vibration exhibits three branches of response as the incoming flow velocity is increased: an initial branch, a high amplitude upper branch, and a lower branch, which may be seen in Figure 5.1. Over much of the response regime, the motion of the body is well represented by a sinusoidal function. However, in the present study, we focus also on the behavior of a cylinder as it exhibits *transient or unsteady dynamics*, in the transition regions between the different branches of response. These transition regions are significant, because the peak amplitude of vibration will often occur in an unsteady intermittent switching region between the upper and lower response branches, as found by Govardhan & Williamson (2006) in their recent study of peak amplitude response.

In the case of a controlled body, which is translated along a sinusoidal trajectory, Williamson & Roshko (1988) observed a set of different vortex formation modes, existing within certain regimes in a plot of normalized amplitude and wavelength of the body motion. Among the vortex formation modes they found were a '2S' mode, representing two single vortices formed per cycle, a '2P' mode, meaning two pair of vortices formed per cycle, and an asymmetric

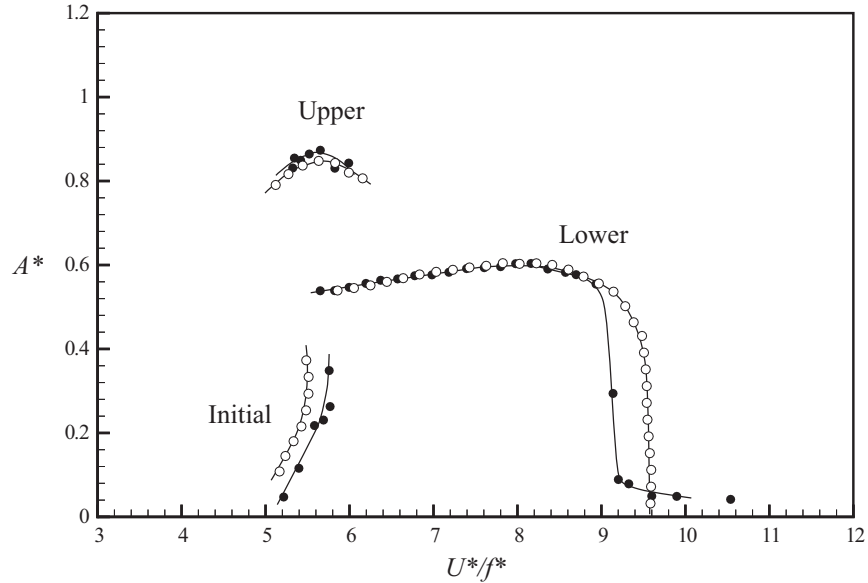


Figure 5.1: Comparison between steady state predicted response and directly measured free vibration response ( $m^* = 10.49$ ,  $\zeta = 0$ ).  $\bullet$  measured free vibration response from Govardhan & Williamson (2006),  $Re = 4,000$  at peak amplitude.  $\circ$  predicted response from the present controlled vibration data,  $Re = 4,000$  throughout.

'P+S' mode, comprising a pair of vortices and a single vortex in each cycle. On-  
goren & Rockwell (1988*b*) observed some comparable vortex formation modes,  
in the case of a body oscillating in-line with the flow. The 2S, 2P and P+S modes  
are illustrated schematically in Figure 5.2. The regimes of these modes within  
the amplitude-wavelength plane are shown later in Figure 5.3, which is in effect  
a more accurate representation of the Williamson & Roshko map of regimes, in  
this case compiled using force measurements at a single Reynolds number value  
throughout the plane, rather than using flow visualization. In Chapter 3 (Morse  
& Williamson, 2009*b*) we identified a new mode of vortex formation, which is  
important because it is responsible for peak amplitudes of response in these  
flows; namely the  $2P_{\circ}$  mode, also illustrated in Figure 5.2. This mode comprises  
two pairs of vortices in each cycle, but where the second vortex of each pair is

distinctly smaller than the first vortex. It is defined as the “ $2P_{\text{OVERLAP}}$ ” mode since its regime in the amplitude-wavelength plane overlaps other regimes, as shown in Figure 5.3 later.

Previous studies have observed different types of behavior for the transition from the high amplitude upper branch to the lower branch of response. Khalak & Williamson (1999) observed a range of normalized velocity where the amplitude would switch intermittently between an upper branch and lower branch level; these response branches are shown in Figure 5.1. In other free vibration studies, rather than a jump from the upper to lower branch, the amplitude variation was found to be more continuous (for example Vikestad, 1998; Bearman & Branković, 2004; Hover *et al.*, 2004).

Govardhan & Williamson (2000) characterized the switching behavior for a system of moderate mass ratio ( $m^* = 8.6$ ), and also for a system of very low mass ratio ( $m^* = 1.2$ ), where  $m^* = \text{oscillating mass} / \text{mass of fluid displaced}$ . They found that for higher body mass ( $m^* = 8.6$ ), the system would spend several cycles of vibration on one amplitude level, until there is an intermittent switch of both vortex mode and amplitude branch, causing the system to vibrate at a new clearly discernable amplitude level. However, for the  $m^* = 1.2$  case, they observed rapid variations in amplitude (and frequency), which led them to suggest that a similar intermittent switching is present, but that it is possibly faster in this case. In the latter case, two distinct amplitude levels are not discernable. Therefore, in a response plot of maximum amplitude or mean amplitude, the transition from the upper branch to the lower branch would appear to be a continuous variation in amplitude.

Hover *et al.* (2004) also looked at the effect of mass ratio on the upper-

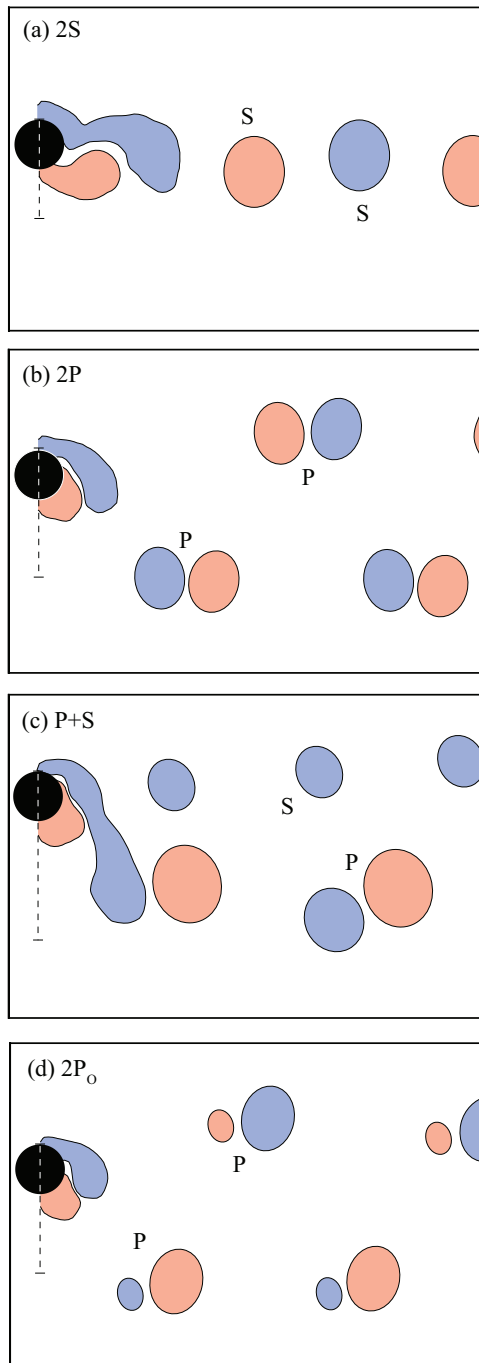


Figure 5.2: Representation of each of the main vortex formation modes:  $\{2S, 2P, P+S, 2P_0\}$ . The  $2P$  and  $2P_0$  modes show a similar pattern, with two vortices shed per cycle of vibration, except that in the  $2P_0$  case the secondary vortex is much weaker than the primary vortex.

lower transition region. They measured the correlation of fluid forces at opposite spanwise ends of a cylinder undergoing free vibration with  $m^* = 3.0$ , and showed that the correlation is quite high through most of the amplitude response plot, as one varies flow velocity, except in the region of the upper-lower branch transition. Employing hot wire measurements along the span, they showed that the wake is quite three-dimensional in this transition region. Interestingly, they found that for higher mass ratio ( $m^* = 10$ ) the force correlation becomes high throughout the entire response, again suggesting a mass ratio effect on the nature of the upper-lower transition. Lucor, Foo & Karniadakis (2005) computed the flow for a cylinder undergoing transverse vibration with  $m^* = 2.0$ , and also found that near the transition from the upper to lower branch there was a drop in the spanwise force correlation, and their computations showed the wake primary vorticity to be distinctly three-dimensional.

Our goal, in this study, is to gain further understanding of vortex-induced vibration when the amplitude or frequency varies either in a transient or an unsteady manner, and we shall study both the cylinder dynamics and the wake vortex dynamics. We are especially interested in the transition region between the upper and lower branches of response. Our approach will be to use controlled vibration force measurements, where the cylinder is prescribed to move with a sinusoidal motion, and we measure the fluid forces that act on the cylinder over a wide range of normalized amplitude and frequency. Controlled vibration of a cylinder has been employed by a number of investigators, including Sarpkaya (1977), Staubli (1983), Gopalkrishnan (1993), Hover *et al.* (1998), Carberry *et al.* (2005). Staubli and also Hover *et al.* have utilized their data sets to predict free vibration response plots.

In §5.2, we describe the details of our experimental method which has allowed us to obtain very high-resolution contour plots of fluid forcing in the plane of normalized amplitude and wavelength. In Chapter 3 (Morse & Williamson, 2009*b*), we used these contours to identify a set of regimes of vortex formation which correspond well with the map of vortex formation modes obtained by Williamson & Roshko (1988) from flow visualization. These contours were also used to predict *steady state* behavior of a freely vibrating cylinder. We include an example comparison between prediction and direct free vibration measurement here in Figure 5.1, where we find close agreement between steady state solutions, using an equation of motion for a free vibration system, described in §5.3.1 and §5.3.2.

In this study, we extend our use of the finely resolved force contours, obtained for purely sinusoidal oscillations, to the case where amplitude or frequency may vary in time. For this purpose, we develop a simple quasi-steady model, in §5.3.3. In the model, we use equations which define how the amplitude and frequency will change in time. However, for the instantaneous forces, we use those measured under steady state conditions (the quasi-steady approximation), employing our high-resolution contour plots.

We use this simple model to predict transient behavior, as the system approaches a final steady state solution, in §5.4. In §5.5, we apply the quasi-steady model to a system of low mass, and identify a *large regime of flow velocities for which the cylinder cannot vibrate in steady state motion*; the model shows that it may only oscillate with an unsteady behavior. We are thus able to characterize the nature of the upper branch to lower branch transition at high, moderate, and low mass ratio, using this approach, in close agreement with what is found

from direct measurements of free vibration. This is followed by our conclusions in §5.6.

## 5.2 Experimental Details

The present experiments are conducted in the Cornell-ONR Water Channel, which has a cross-section of 38.1 cm x 50.8 cm. The turbulence level in the test section of the water channel is less than 0.9%. A cylinder of diameter 3.81 cm and length 38.1 cm is suspended vertically in the water channel and forced to oscillate transverse to the flow using a computer-controlled motor attached to a transverse lead screw. The controlled vibration system is automated and may be run unattended, allowing the acquisition of large sets of data. The flow speed is kept constant, to yield  $Re = 4,000$  throughout the data set. A fixed end plate is placed 2 mm below the bottom of the cylinder (but not in contact with the cylinder) to encourage two-dimensional vortex shedding, following the study of Khalak & Williamson (1996). We measure fluid forces on the cylinder with a two-axis force balance utilizing LVDTs (linear variable differential transducers) over a wide range of normalized amplitude ( $A^* = A/D = \text{amplitude/diameter}$ ) and wavelength ( $\lambda^* = \lambda/D = \text{wavelength/diameter}$ ). We vary  $A^*$  from 0.02 to 1.6, with a resolution of 0.02, and vary  $\lambda^*$  from 2 to 16, with a resolution of 0.2, yielding a total of 5680 individual runs. For each run, the fluid force magnitude ( $F_1$ ) and phase angle ( $\phi$ ) at the fundamental (body oscillation) frequency is calculated using a Fourier series analysis. Relevant fluid forcing quantities, which will be introduced in the next section (for example,  $C_Y \sin \phi$  and  $C_{EA}$ ) are obtained using just the force component at the body oscillation frequency, which in general represents almost the entire force signal content. Since the prescribed

motion is perfectly sinusoidal, the fundamental is the only frequency component of the fluid force which makes a net contribution to the energy transfer from fluid to body motion.

In order to determine vorticity using DPIV (digital particle image velocimetry), the flow is seeded with 14-micron silver coated glass spheres, which are illuminated by a sheet of laser light from a 50 mJ Nd:Yag pulsed laser. Pairs of particle images are acquired using a Jai CV-M2CL CCD camera (1600 x 1200 pixels), and analyzed using cross-correlation of sub-images. We use a two-step windowing process (with window shifting) to obtain particle displacements between image pairs. Vorticity fields calculated from the image pairs are phase averaged over approximately 10 cycles. Further details on the force and PIV measurements may be found in Chapter 3 (Morse & Williamson, 2009*b*).

### **5.3 Equations of motion and introduction of a quasi-steady model**

In order to predict the dynamics of a freely vibrating cylinder from controlled vibration force measurements (both for steady state and transient behavior), we need to use the equation of motion for vortex-induced vibration in the transverse ( $y$ ) direction (normal to the flow):

$$m\ddot{y} + c\dot{y} + ky = F(t), \quad (5.1)$$

where  $m$  is the oscillating mass;  $c$  is the structural damping;  $k$  is the spring constant; and  $F(t)$  is the fluid force in the transverse direction.

### 5.3.1 Steady state equations of motion for free vibration

When the body has reached steady state vibration, and the motion is synchronized with the periodic vortex formation mode, the force and displacement are generally well predicted by sinusoidal functions:

$$y(t) = A \sin \omega t, \quad (5.2)$$

$$F(t) = F_1 \sin (\omega t + \phi), \quad (5.3)$$

where  $\omega = 2\pi f$  and  $\phi$  = the phase angle between the fluid force and the body displacement. The phase angle ( $\phi$ ) is an important quantity, as it determines the direction of energy transfer between the fluid and the body motion; it must be between 0 and 180° for the fluid excitation to be positive, and hence for free vibration to occur. Our selected set of non-dimensional parameters in this problem is presented in Table 5.1. In particular, the principal parameters defining the body motion are the normalized amplitude ( $A^*$ ) and the frequency ratio ( $f^*$ ), in a flow of normalized velocity  $U^*$ .

If we substitute (5.2) and (5.3) into the equation of motion above (5.1), we can obtain the “amplitude equation”:

$$A^* = \frac{1}{4\pi^3} \frac{C_Y \sin \phi}{(m^* + C_A) \zeta} \left( \frac{U^*}{f^*} \right)^2 f^*, \quad (5.4)$$

which includes the force coefficient in phase with the body velocity ( $C_Y \sin \phi$ ), equivalent to a normalized energy transferred from the fluid to the cylinder, which is also called the fluid excitation. We may similarly obtain the “frequency equation”:

$$f^* = \sqrt{\frac{m^* + C_A}{m^* + C_{EA}}}, \quad (5.5)$$

where  $C_A$  is the potential flow added-mass coefficient ( $C_A = 1.0$  for a circular cylinder), and  $C_{EA}$  is an “effective” added-mass coefficient that includes an

Table 5.1: Non-dimensional groups. In the groups below,  $U$  is the free-stream velocity,  $\lambda$  is the oscillation wavelength,  $f$  is the oscillation frequency,  $f_N$  is the natural frequency in water,  $D$  is the cylinder diameter,  $L$  is the submerged cylinder length,  $\nu$  is the fluid kinematic viscosity,  $\rho$  is the fluid density, and  $F_Y$  is the transverse fluid force. The added mass,  $m_A$ , is given by  $m_A = C_A m_d$ , where  $m_d$  is the displaced fluid mass and  $C_A$  is the potential added-mass coefficient ( $C_A = 1.0$  for a circular cylinder).

Mass ratio	$m^*$	$\frac{m}{\pi\rho D^2 L/4}$
Damping ratio	$\zeta$	$\frac{c}{2\sqrt{k(m+m_A)}}$
Normalized velocity	$U^*$	$\frac{U}{f_N D}$
Normalized wavelength	$\lambda^*$	$\frac{\lambda}{D} = \frac{U}{fD}$
Normalized amplitude	$A^*$	$\frac{A}{D}$
Frequency ratio	$f^*$	$\frac{f}{f_N}$
Transverse force coefficient	$C_Y$	$\frac{F_Y}{\frac{1}{2}\rho U^2 D L}$
Reynolds number	$Re$	$\frac{\rho U D}{\mu}$

apparent effect due to the total transverse fluid force in phase with the body acceleration ( $C_Y \cos \phi$ ):

$$C_{EA} = \frac{1}{2\pi^3} \frac{C_Y \cos \phi}{A^*} \left( \frac{U^*}{f^*} \right)^2, \quad (5.6)$$

The amplitude and frequency equations derived above must hold if the cylinder is oscillating with steady state (sinusoidal) vibration. Over much of a free vibration response plot, as in Figure 5.1, the body motion and fluid forcing are quite sinusoidal and the above equations are sufficient to accurately predict

the amplitude and frequency of motion. A principal interest in this study is to extend free vibration prediction to cases where the amplitude and frequency vary. In order to make such predictions, we employ a quasi-steady assumption, described below in §5.3.3.

### 5.3.2 Contours of fluid forcing

From our high resolution controlled vibration force measurements, we present, in Figure 5.3, contour plots of the fluid forcing quantities  $C_Y \sin \phi$  and  $C_{EA}$ , in a plot of normalized amplitude ( $A^*$ ) and normalized wavelength ( $\lambda^*$ ) which represent the sinusoidal trajectory for the cylinder relative to the fluid. The normalized wavelength is equivalent to the flow velocity normalized by the oscillation frequency ( $\lambda^* = U^*/f^* = U/fD$ ). The fluid excitation plot showing contours of  $C_Y \sin \phi$  in Figure 5.3(a) was presented first in Chapter 3 (Morse & Williamson, 2009b).

In certain regions of the parameter space, we find jumps in the character of the fluid forcing, and thus are able to identify boundaries separating different fluid forcing regimes, which correspond to boundaries separating different vortex shedding modes in the Williamson & Roshko (1988) map of regimes. Vorticity measurements confirm the modes of vortex formation in each regime, including the 2S, 2P, and P+S modes, introduced in §5.1, as well as a regime where the vortex formation is not synchronized with the cylinder oscillation.

We also identify regions where two vortex formation regimes overlap, as may be seen in the contours of Figure 5.3. In these regions the wake may switch intermittently between two distinct modes even as the cylinder is vibrating with

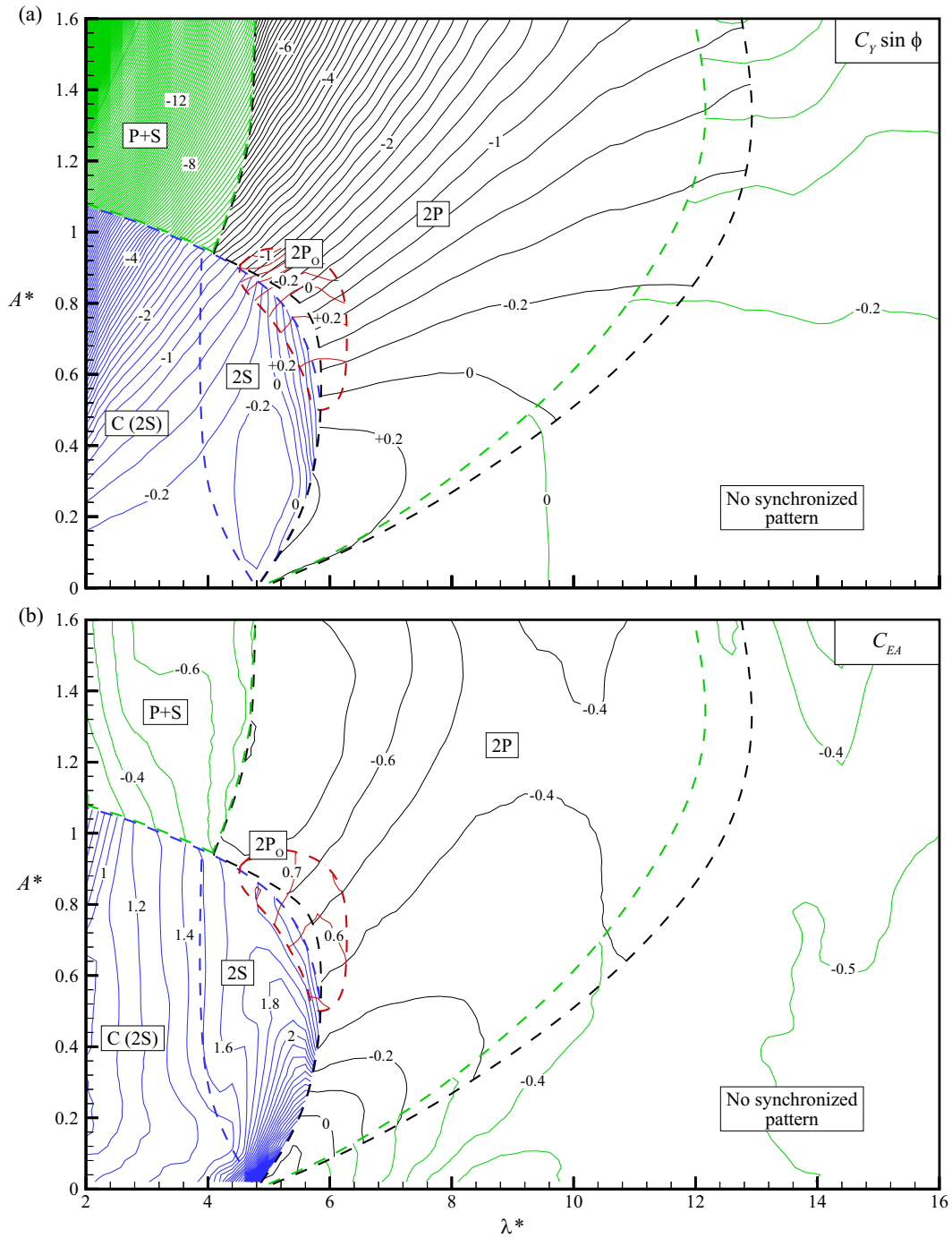


Figure 5.3: Contours of fluid forcing from controlled sinusoidal vibration: (a)  $C_Y \sin \phi$  with contour interval of 0.2; and (b)  $C_{EA}$  with contour interval of 0.1. Boundaries between modes are indicated by dashed lines; contours overlap in regions where multiple vortex shedding modes are possible.

constant amplitude and frequency, as shown in Chapter 3 (Morse & Williamson, 2009*b*). In the principal overlap region, we identify a ‘ $2P_O$ ’ (or  $2P_{\text{OVERLAP}}$ ) mode of vortex formation where two pairs of vortices are shed per cycle of oscillation (similar to the classical 2P mode) but where the secondary vortex is much weaker than the primary vortex in each pair, as described briefly in §5.1 (see the sketch in Figure 5.2d). The existence of an overlapping mode is significant, because it is associated with the maximum amplitude where positive excitation occurs. It will thus be the mode yielding the peak resonant amplitude in free vibration. We shall also see that the overlap of the  $2P_O$  mode with the 2S and 2P regimes leads to some interesting unsteady body dynamics, which are discussed in §5.4 and §5.5. A comprehensive characterization of the different changes found as one crosses the regime boundaries, shown in Figure 5.3, including time traces and spectra for the different forcing regimes, may be found in Chapter 3 (Morse & Williamson, 2009*b*).

From the force contours in Figure 5.3, we can predict the steady state (sinusoidal) response (amplitude,  $A^*$ , and frequency,  $f^*$ ) of a freely vibrating cylinder for a given set of system parameters  $\{m^*, \zeta, U^*\}$ . We simply find the point (or points) in the amplitude-wavelength plane where both the amplitude equation (5.4) and frequency equation (5.5) are satisfied. By varying the normalized velocity ( $U^*$ ) we can build up an entire response plot. As an introduction to the present results, we show in Figure 5.1 that the steady state response of a freely vibrating cylinder can be accurately predicted, reproduced from Chapter 4 (Morse & Williamson, 2009*c*). The initial branch will have a 2S vortex formation mode, the upper branch a  $2P_O$  mode, and the lower branch a 2P mode.

### 5.3.3 Quasi-steady model for free vibration response

In the present work, we would like to extend our prediction of freely vibrating cylinder dynamics to transient or unsteady behavior. To do this, we will need to introduce a quasi-steady assumption. Specifically, we assume that as the amplitude or frequency of oscillation is varying, the instantaneous fluid forcing (magnitude and phase) is given by our controlled vibration force contours for purely sinusoidal motion at the instantaneous value of the amplitude and frequency. Naturally, we expect that this assumption will be more accurate for slower variations in amplitude or frequency.

Our goal is to implement this quasi-steady assumption in a model that is both simple and useful. Therefore we will not attempt to determine the cylinder dynamics in terms of  $y(t)$  but rather we will assume the motion takes on a sinusoidal form, but with varying amplitude and frequency. Therefore we will be solving for  $A^*(\tau)$  and  $f^*(\tau)$ , where  $\tau = t/T$  or time/period of oscillation, and the solution will be advanced in fractions of the oscillation period. We know that as the system approaches a steady state solution (constant amplitude and frequency) the model should reduce to the steady state amplitude and frequency equations determined above (5.4),(5.5).

We use the form of the amplitude equation to define an “effective damping”,  $\zeta_{eff}$ , which includes the structural damping as well as the effect of the fluid excitation,  $(C_Y \sin \phi)$  as follows:

$$\zeta_{eff} = \zeta - \frac{C_Y \sin \phi}{4\pi^3 (m^* + C_A) A^*} \left( \frac{U^*}{f^*} \right)^2 f^*, \quad (5.7)$$

Similarly, we define an “effective mass”,  $m_{eff}^*$ , which includes the structural mass as well as an effective added mass due to the fluid forcing in phase with

acceleration ( $C_Y \cos \phi$ ) as follows:

$$m_{eff}^* = m^* + \frac{1}{2\pi^3} \frac{C_Y \cos \phi}{A^*} \left( \frac{U^*}{f^*} \right)^2 = m^* + C_{EA}, \quad (5.8)$$

We then assume that the system behaves like a simple spring-mass-damper system except that the mass ( $m_{eff}^*$ ) and the damping ( $\zeta_{eff}$ ) can dynamically vary depending on the instantaneous amplitude or frequency. The effective damping will determine if the amplitude increases or decreases as follows:

$$\frac{dA^*}{d\tau} = (-2\pi\zeta_{eff}f^*) A^*, \quad (5.9)$$

which is the well-known equation for amplitude decay in damped harmonic vibration. The effective mass will affect the frequency of oscillation as follows:

$$f = \frac{1}{2\pi} \sqrt{\frac{k}{m_{eff}}}, \quad (5.10)$$

We normalize this frequency by the natural frequency in still water ( $f_N$ ) to yield:

$$f^* = \sqrt{\frac{m^* + C_A}{m_{eff}^*}}, \quad (5.11)$$

To implement the model, we first need to define the system parameters:  $\{m^*, \zeta, U^*\}$  and initial values for  $A^*$  and  $f^*$ . Then we look up the values of  $(C_Y \sin \phi)$  and  $C_{EA}$  from the contours in Figure 5.3. At this point, we use equation (5.9) to determine the change in amplitude over one time step, and advance  $A^*$ . Similarly, we use equation (5.11) to find the new value of frequency  $f^*$  at the end of the time step. We let the time step,  $\Delta\tau$ , be variable so that the amplitude or frequency does not change by too great an amount (more than say 5%) in one iteration.

In most cases that we consider, the frequency changes associated with transient situations will be small. However, one should note that, based on the

method described above, the frequency would change instantaneously, and thus the rate of variation in frequency toward the steady state solution would depend on the value of the time step. To avoid this, we adjust our model by making the approximation that it will take 1 cycle of oscillation for the frequency to change, and thus for time steps less than 1 cycle, the frequency will make a fractional change toward the value given by equation (5.11).

A complication with implementing the model is that at some points in the amplitude-wavelength plane there are two possibilities for the fluid forcing, as two modes of vortex formation are possible, shown as overlapping contours in Figure 5.3. Of course this overlap phenomenon (between the  $2S$  and  $2P_O$  modes, and between the  $2P_O$  and  $2P$  modes) is what leads to some of the interesting behavior observed in vortex-induced vibration systems, such as the intermittent switching between the upper and lower branches of response, as we explain in §5.4.2. We will therefore handle the overlap regions in two different ways, as described in the following sections.

## **5.4 Transient behavior for moderate and high mass ratio systems**

For a vortex-induced vibration system, the equilibrium solution (i.e. the amplitude and frequency for steady state vibration), will be the intersection of the curves along which the amplitude equation (5.4) is satisfied, and the curve along which the frequency equation (5.5) is satisfied. The curves will generally not be continuous, showing jumps when the vortex formation mode changes. In this section, we use the quasi-steady model to determine how the equilibrium solu-

tions are approached.

#### 5.4.1 Approaching a lower branch equilibrium

We begin with a simple starting case: a system having moderate mass ratio,  $m^* = 10.0$ , and very low damping,  $\zeta = 0.001$ , at normalized velocity,  $U^* = 8.0$ . For this case, there is an equilibrium solution in the lower branch of a free vibration response, as shown by the bull's eye in Figure 5.4(a). We choose to look for solutions in the  $(A^*, U^*/f^*)$  space, since that is the parameter space for our controlled vibration contours. This is equivalent to the  $(A^*, f^*)$  space since we are fixing the value of the normalized velocity,  $U^*$ .

Employing our quasi-steady model, we give the system arbitrary initial conditions and observe how the system approaches the equilibrium solution. As can be seen in Figure 5.4(b), for this example, it happens to take longer for a low amplitude initial condition to reach the equilibrium solution, than for a high amplitude initial condition. This is because the contour levels of fluid excitation ( $C_Y \sin \phi$ ) are closer together for the higher amplitude approach to the equilibrium solution (there is a steeper gradient of excitation versus amplitude). In summary, the technique appears to work well in such examples.

#### 5.4.2 Intermittent switching between upper and lower branch equilibria

One of our main goals in developing our quasi-steady model is to predict the cylinder dynamics in the upper to lower branch transition region of a free vibration response. In Figure 5.5(a), a system with  $U^* = 6.3$  will have two equilibrium solutions, depending on the mode of vortex formation. For the  $2P_0$  mode, the

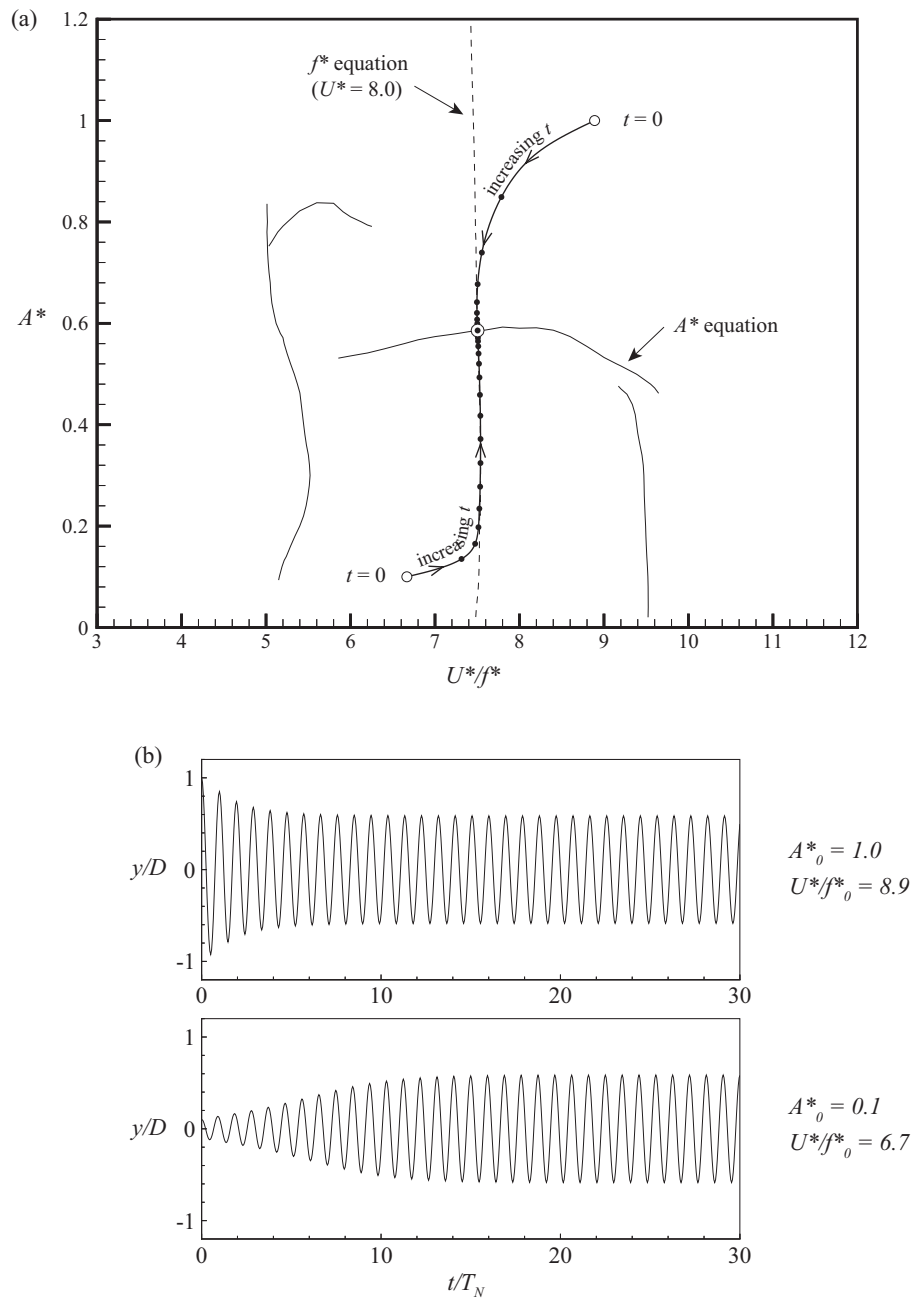


Figure 5.4: Prediction of transient behavior for an equilibrium solution in the lower branch,  $m^* = 10$ ,  $\zeta = 0.001$ ,  $U^* = 8.0$ . In (a) we show how the equilibrium solution  $\bullet$  is approached for arbitrary initial conditions  $\circ$ .  $\bullet$  indicates location after each cycle of oscillation. In (b) we show time traces for the two initial conditions investigated.

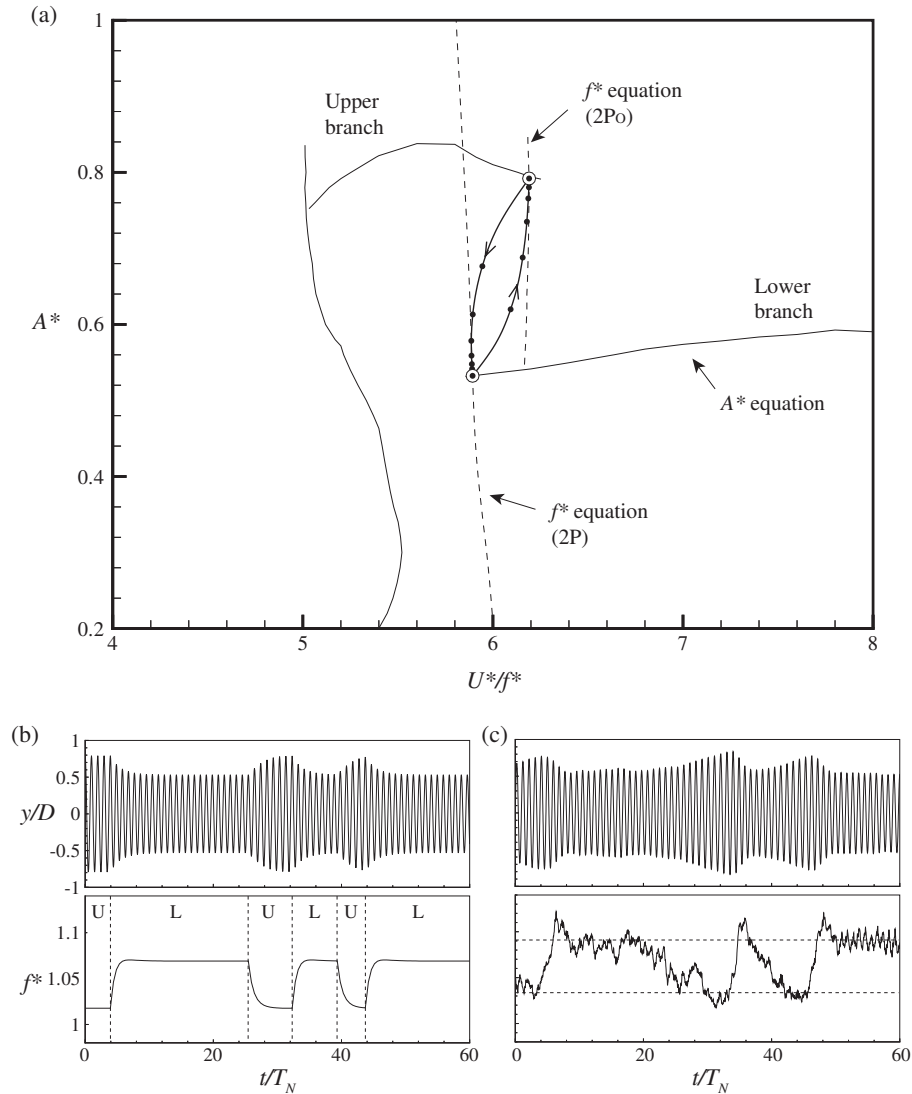


Figure 5.5: Prediction of intermittent switching transient behavior,  $m^* = 10$ ,  $\zeta = 0.001$ ,  $U^* = 6.3$ . (a) We use the quasi-steady model to determine the dynamics of the cylinder as it moves between an equilibrium point  $\odot$  in the 2P and 2P<sub>0</sub> regimes (lower branch and upper branch). In (b) we show a predicted time trace, which we compare with an actual free vibration intermittent switching time trace at  $m^* = 8.63$  from Govardhan & Williamson (2000) in (c)

equilibrium solution will lie in the upper branch; for the pure 2P mode, the equilibrium solution will lie in the lower branch.

In order to observe the switching behavior, we run the quasi-steady model

twice. In the first case we give the system the initial conditions corresponding to the upper branch equilibrium (see bull's eye for the  $2P_O$  mode in Figure 5.5a), but we use the force contours for the  $2P$  mode. The  $2P$  mode yields negative fluid excitation at the higher upper branch amplitude, so it cannot sustain free vibration there; the amplitude must drop to the lower branch level, where the fluid excitation is positive. We then perform the reverse, selecting the lower branch initial conditions, but using the  $2P_O$  mode forces, and observe how the amplitude increases to the upper branch. For a freely vibrating cylinder, we expect the switch in vortex formation mode will happen randomly. Here we arbitrarily decide when the vortex formation mode switches, and build up an intermittent switching time trace, shown in Figure 5.5(b), which we compare to an actual intermittent switching time trace from Govardhan & Williamson (2000), in Figure 5.5(c). In choosing moments in time where we switch modes, we are guided by the experimental data in (c), in this particular case.

We are interested in the number of cycles required for the amplitude to make a transition. We see that a typical experimental drop in amplitude from the upper to the lower branch is well represented by our quasi-steady model predictions. However, the experimental rise in amplitude from the lower to upper branch appears to take a few cycles longer than our predictions. We attribute this to the stipulation in our model that the vortex formation mode changes instantaneously. For a real system, there may be several cycles of oscillation over which the vortex formation mode changes from  $2P$  to  $2P_O$ , before the system can start to more rapidly increase amplitude.

We can make an estimate of how fast the vortex formation mode switches, by observing time traces of the phase angle from our controlled vibration force

measurements, in Figure 5.6. The 2P mode will have a phase angle of around  $180^\circ$  while the  $2P_0$  mode will have a phase angle of around  $0^\circ$  (see Chapter 2 for a detailed description of the force characteristics for each mode). For lower amplitudes, the switch in phase takes several cycles of vibration, whereas at higher amplitudes, the switch occurs nearly instantaneously, as may be observed in Figure 5.6. Therefore, at low amplitudes, when the vortex formation mode switches from 2P to  $2P_0$ , we expect several additional cycles of oscillation are required for the vortex formation mode to change. Our model does not include such an effect.

## 5.5 Unsteady behavior for very low mass ratio systems

We now turn to another case where the quasi-steady model proves to be quite revealing: that of a very low mass ratio system. In §5.3, we showed how we may predict the response of a freely vibrating cylinder at moderate mass ratio,  $m^* = 10$ . One of the well-known results from previous vortex-induced vibration studies is that, as the mass ratio decreases, there is a widening of the range of normalized velocity ( $U^*$ ) over which vibration occurs (observed originally by Ramberg & Griffin, 1981). We are in a position to predict this result employing our controlled vibration data.

### 5.5.1 The effect of reducing mass ratio on the upper branch to lower branch transition

At moderate mass ratio,  $m^* = 15$ , (and zero damping) we use our controlled vibration data to predict the steady state response of a free vibration system. The

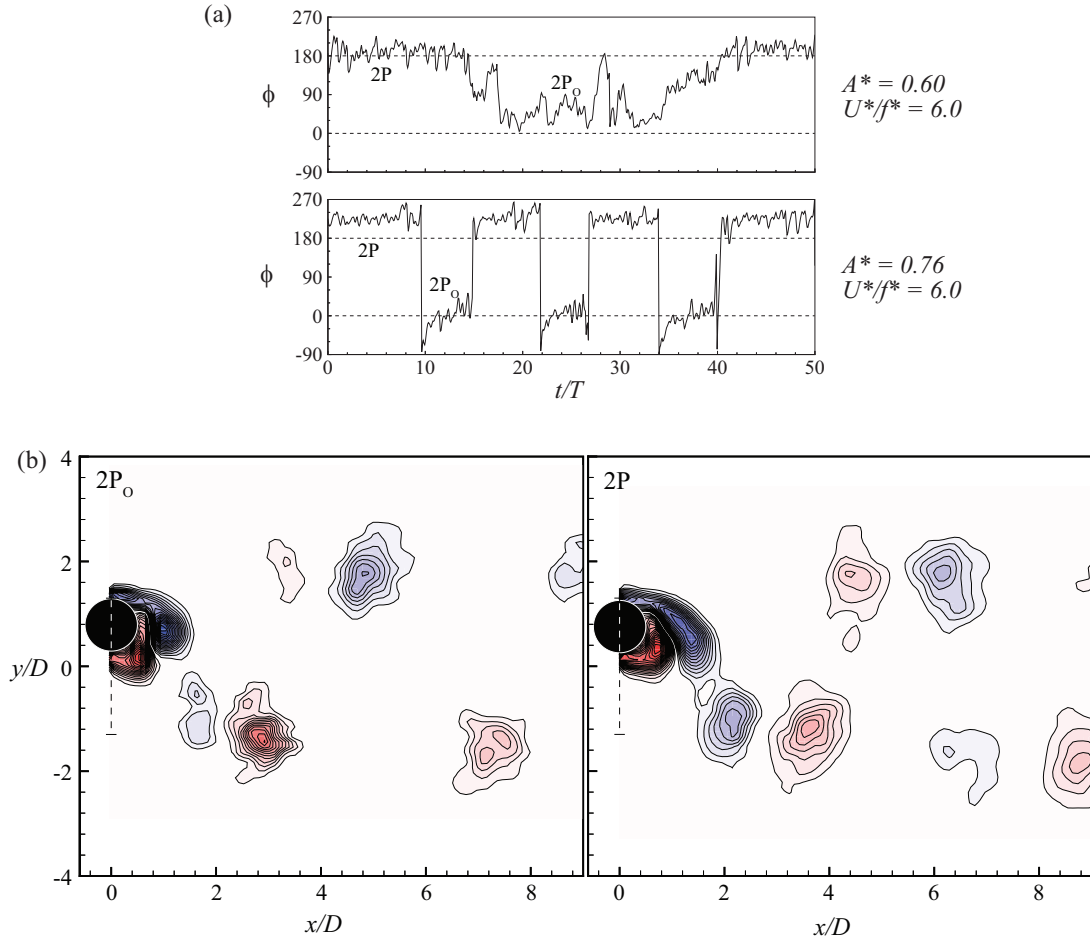


Figure 5.6: Phase switching and vortex formation modes in the  $2P-2P_0$  overlap regime. (a) The phase between cylinder motion and fluid force, showing more rapid transitions between modes for the higher amplitude case than for the lower amplitude case. (b) Vorticity fields for the  $2P$  and  $2P_0$  vortex formation modes, both obtained at  $A^* = 0.8$ ,  $U^*/f^* = 5.6$ . Contour levels shown are:  $\omega D/U = \pm 0.4, \pm 0.8, \pm 1.2, \dots$

regime of response extends up to  $U^* \approx 10$ , as shown in Figure 5.7(a). Also, there is a small range of normalized velocity for which two steady state solutions exist (thus two possible amplitudes of vibration) in the region between the upper and lower response branches, close to  $U^* = 6$ . In §5.4.2 we indicated how this is associated with intermittent switching between the branches. As we decrease mass ratio, we find a certain special value ( $m^* = 7.7$ ) where the upper and lower

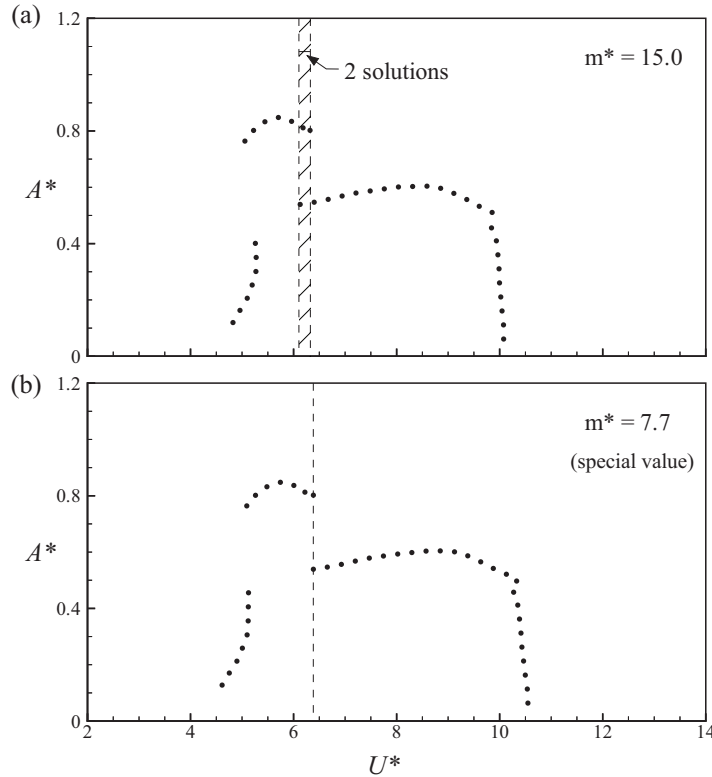


Figure 5.7: Predicted amplitude response for moderate mass ratio systems. (a) At  $m^* = 15.0$  there is a small band of normalized velocity ( $U^*$ ) in the upper to lower branch transition region where two steady state solutions exist. (b) As  $m^*$  is decreased to a special value of 7.7, there is no upper branch - lower branch overlap.

branches no longer overlap, and there is one value of amplitude for each value of normalized velocity, as shown in Figure 5.7(b).

As we decrease mass ratio even further to  $m^* = 1.0$  (still with zero damping) we find a further widening of the regime of velocity ( $U^*$ ) for which vibration occurs, as shown in Figure 5.8. However, we encounter a seemingly intractable problem: we find large regimes of velocity ( $U^* = 7$  to 11 in Figure 5.8) where there is no steady state solution to the equations of motion, i.e. *no points for which both the amplitude and frequency equations are satisfied*. This would seem to suggest that vortex-induced vibration cannot occur in these regions, in direct

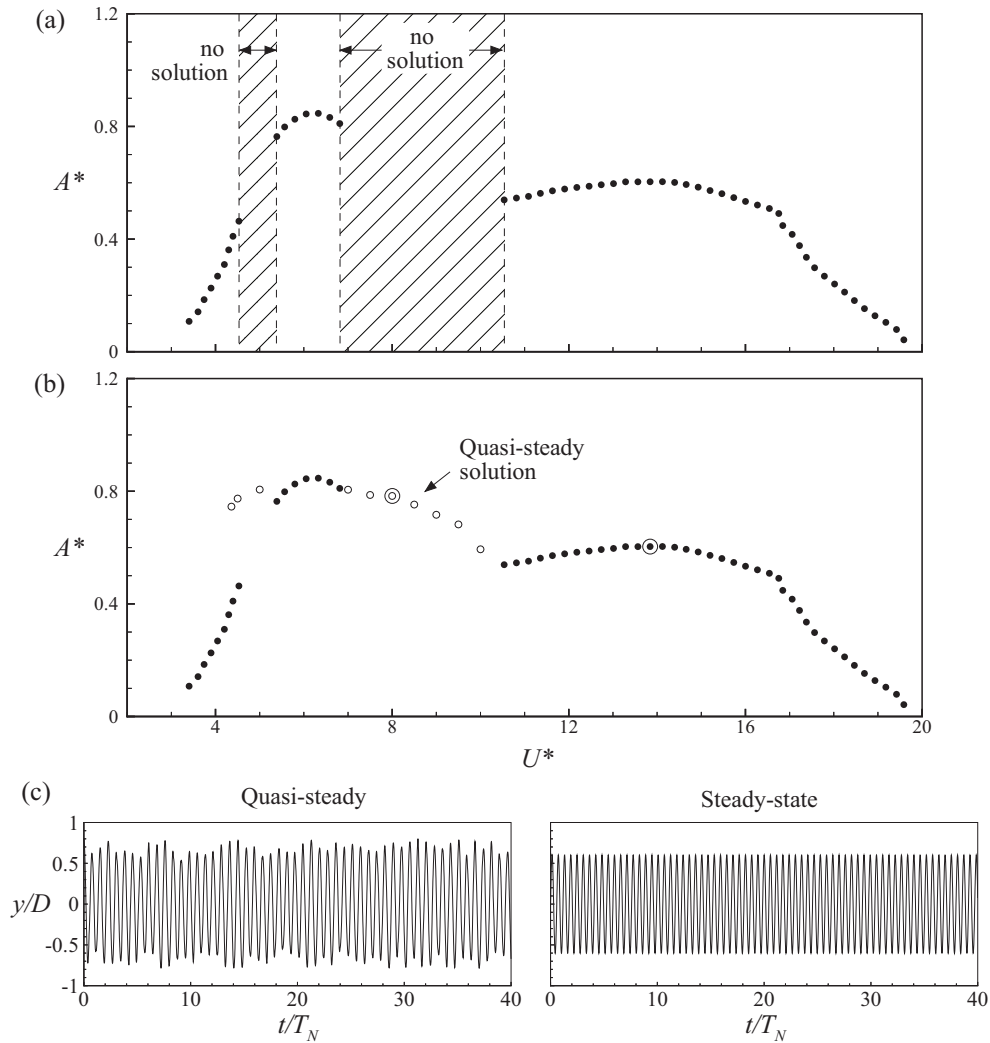


Figure 5.8: Predicted amplitude response character for a very low mass ratio system,  $m^* = 1.0$ . (a) We find large gaps in the predicted response ( $\bullet$ ) where no steady state solution exists. (b) We use our quasi-steady model to predict unsteady behavior ( $\circ$ ) in these gaps. (c) Predicted time traces for unsteady system dynamics (at location:  $\odot$ ) and for steady state vibration (at location:  $\bullet$ ).

contradiction with published free vibration results.

In the transition region between the upper and lower branch, free vibration response is generally not precisely sinusoidal, and exhibits variations in amplitude and frequency, as found by Govardhan & Williamson (2000). This would suggest that our controlled vibration force measurements, (from purely sinu-

soidal motion) would not be easily applicable. However, even in this case, we shall apply, in an approximate manner, our quasi-steady model, to determine the peak amplitudes.

In running the model, we encounter situations where the solution may reside within the  $2P-2P_O$  overlap region. We then need to determine which mode of vortex formation the system takes on, as a function of time. Based on what one finds typically in free vibration experiments, we will assume that there is a 10% chance, within each cycle of motion of the body, that the mode will switch between  $2P$  and  $2P_O$ . Obviously, one has to make some assumption here, and it is clear that this is a somewhat arbitrary stipulation. However, it turns out from the model results that the value chosen for the probability of mode switch has very little influence on the response plot that we construct below, in Figure 5.8(b).

When we run our quasi-steady model, we find that the amplitude and frequency fluctuate, as shown in Figure 5.8(c). Computing the average amplitude of the top 10% of the peaks, which is the parameter used by Hover *et al.* (1998) and Govardhan & Williamson (2006), we find that the predicted amplitude in this unsteady region fits well with the rest of our predicted response plot, as shown in Figure 5.8(b).

If we compare our complete predicted response plot (combining the steady state solutions with the non-steady solutions) with directly measured free vibration response (for very low mass ratios around 1.0) from Govardhan & Williamson (2000), we find good qualitative agreement, both in the amplitude response and the frequency response, as shown in Figure 5.9. We note that the slightly higher amplitudes of the upper branch from the free vibration experi-

ments are due to the effects of the higher Reynolds number in this case, consistent with the results of Govardhan & Williamson (2006). In summary, the quasi-steady model appears to compare well with direct free vibration measurements. The model, employed at very low mass ratios, exhibits a regime of unsteady vibration, which contrasts with the character of intermittent mode jumps between bistable steady state solutions associated with higher mass ratios.

### 5.5.2 Regime of unsteady response solutions in the $A^* - U^*$ plane

In the example described above, we focused on the case of a system at zero damping. If we consider higher values of the damping, we may define an entire region in the  $(U^*, A^*)$  plane where no steady state solution is possible, as shown in Figure 5.10. This map will be unique for each value of the mass ratio. The extent of the regime without steady solutions will grow as the mass ratio is reduced.

We may briefly explain how the “void”, where there exist no steady state solutions, can occur. In the plot of amplitude versus wavelength ( $A^* - \lambda^*$ ), mode regime boundaries are carefully defined from force measurements. A sketch of a representative boundary in Figure 5.11(a) indicates that the value of  $C_{EA}$  jumps in value as it crosses the boundary, just as it does for the boundary between the 2S and 2P modes in Figure 5.3(b). If, on the other hand, one now replots the boundary in the plane of amplitude versus normalized velocity ( $A^*$  versus  $U^*$ ) then one must multiply all  $\lambda^*$  values (or  $U^*/f^*$  values) in Figure 5.11(a) by the relevant normalized frequency ( $f^*$ ), to construct the new plot in Figure 5.11(b). (For a given mass ratio,  $m^*$ , equation 5.5 will yield this frequency,  $f^*$ ). Our problem arises because the frequency ( $f^*$ ) involves  $C_{EA}$ , and therefore has

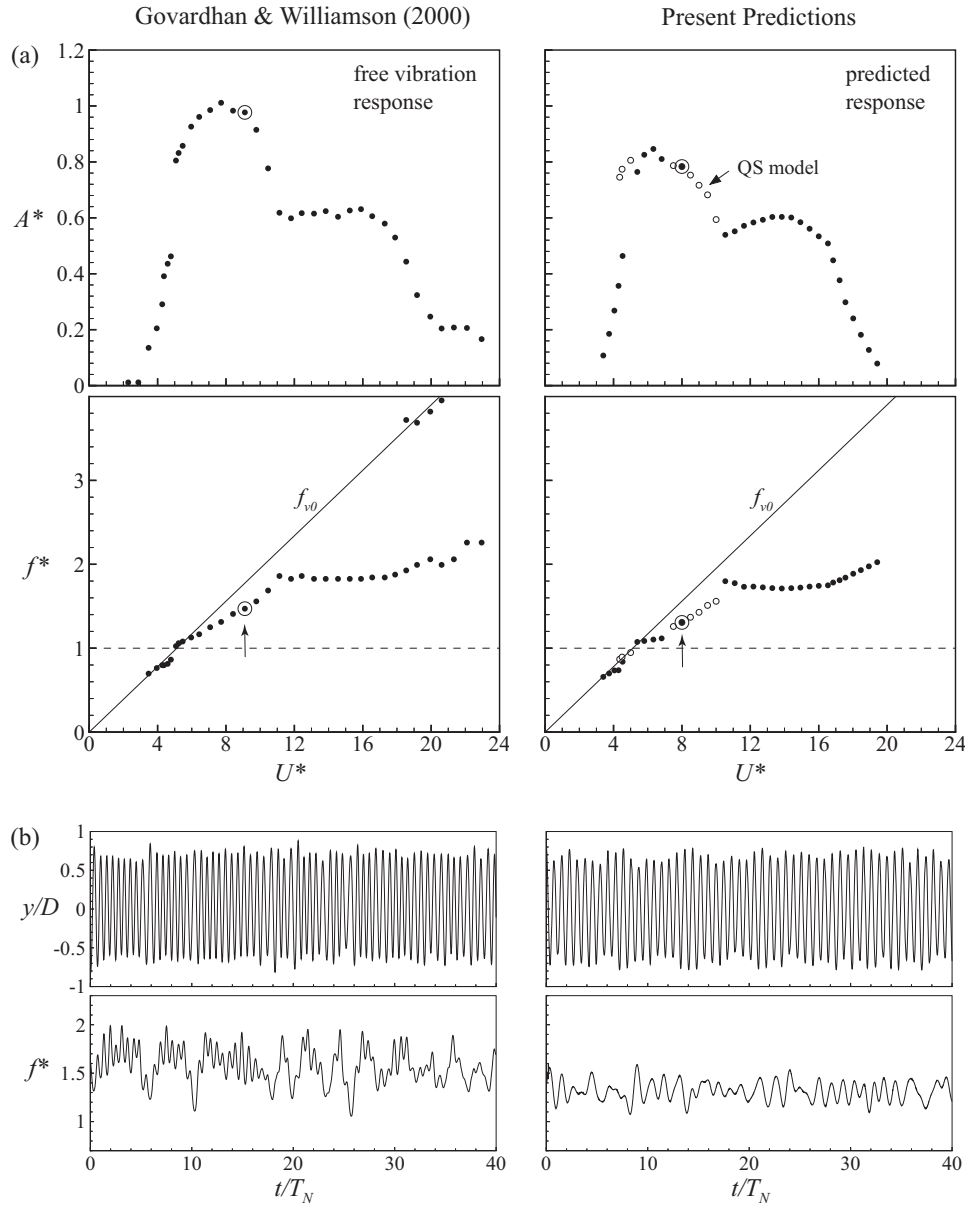


Figure 5.9: Comparison between measured free vibration amplitude and frequency response at  $m^* = 1.19$  and predictions from controlled vibration at  $m^* = 1.0$ . We also show time traces (b) at selected locations ( $\odot$ ) for each case. Measured free vibration response is from Govardhan & Williamson (2000).

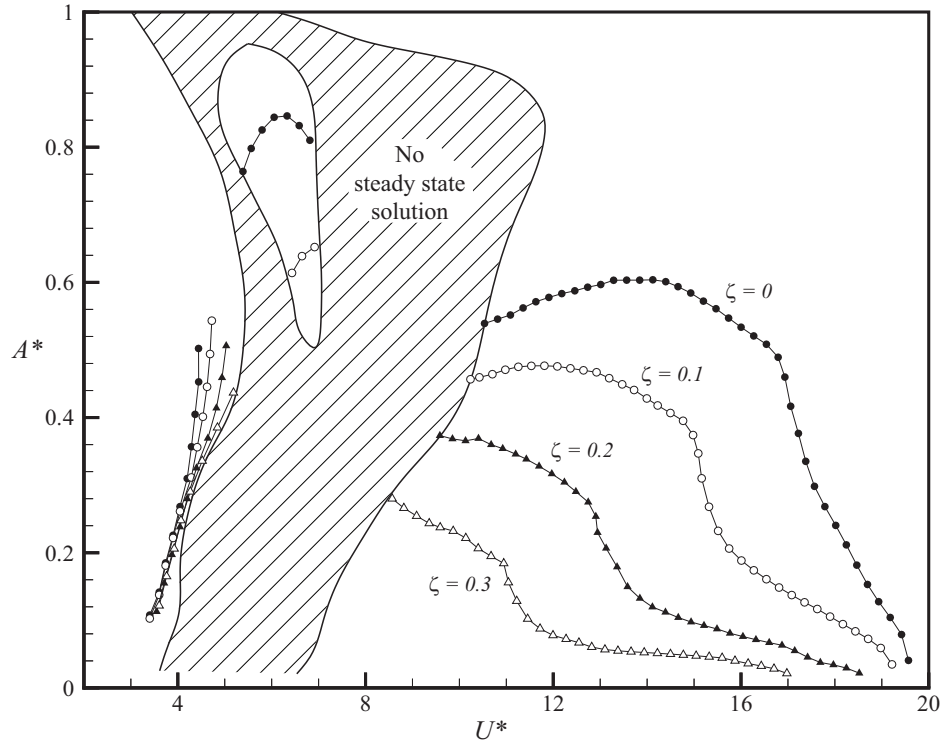


Figure 5.10: Map of steady and unsteady solutions in the  $A^*-U^*$  plane for  $m^* = 1.0$ . Where there is no steady state solution, the system can only oscillate with unsteady vibration.

a jump change in value across the regime boundary. Thus the regime boundary on the left for the 2S mode in (a) will get pulled to the left by the lower value of  $f^*$  on this side, while the 2P boundary in (a) gets pulled to the right by the higher value of  $f^*$ . In this way, a void appears in between these two mode regimes, 2S and 2P in Figure 5.11(b), where no steady state solutions are found. As mass ( $m^*$ ) becomes smaller so this difference in frequency ( $f^*$ ) across the boundary gets larger, and the void grows, ultimately extending to infinite  $U^*$ , if the mass falls below a “critical” value described in the next section.

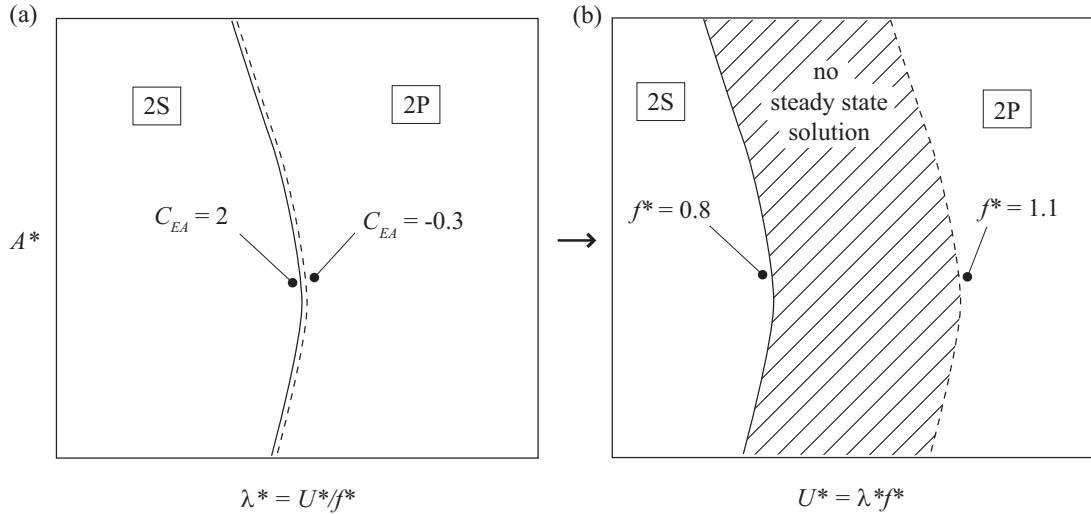


Figure 5.11: Schematic plot showing how a void with no steady state solution occurs. The boundary between the 2S and 2P modes in the  $A^* - U^*/f^*$  plane (a) is stretched apart in the  $A^* - U^*$  plane (b) due to different values of  $C_{EA}$  (and thus different values of  $f^*$ ) on opposite sides of the boundary. This leaves a void in the  $A^* - U^*$  plane where no steady state solution occurs.

### 5.5.3 Frequency response at very low mass ratio

We can also study the effect of very low mass ratio on the frequency response. For our brief discussion here, we focus on a system with zero damping. In the upper branch, the frequency ratio ( $f^*$ ) is typically slightly higher than 1.0, as in Figure 5.9. In the lower branch, the frequency is typically nearly constant over a wide range of normalized velocity; the value of this frequency increases, as mass ratio is diminished, as predicted from equation (5.5). The roughly constant value of  $f^*$  in the lower branch occurs because  $C_{EA}$  is nearly constant throughout the lower branch, as may be seen in the  $C_{EA}$  contours of Figure 5.3. In between the upper and lower branches, only an unsteady vibration response exists for low mass ratio, and the frequency is found to increase approximately linearly with normalized velocity, as we found in Figure 5.9. The effect of mass ratio on the frequency response is found in Figure 5.12, where one can immedi-

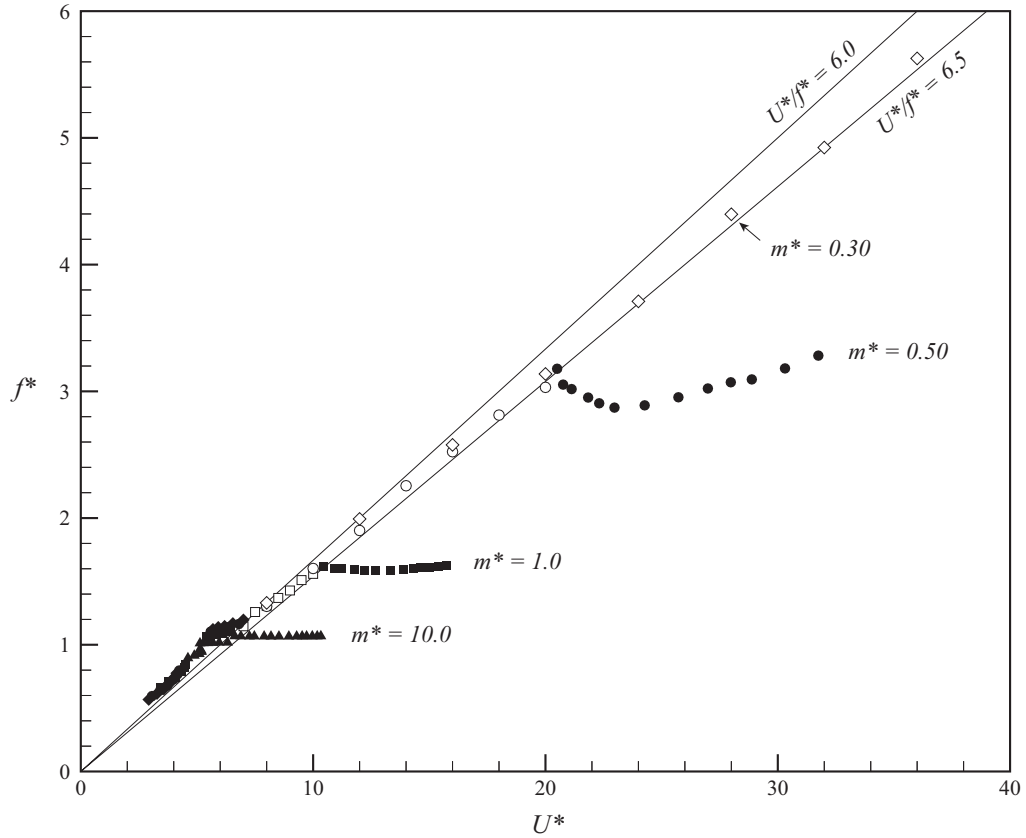


Figure 5.12: Predicted frequency response at different values of mass ratio. Solid symbols indicate steady state behavior, open symbols indicate unsteady behavior. As mass ratio decreases, the range of normalized velocity ( $U^*$ ) become wider, extending to infinite values for  $m^* < 0.36$ .

ately see the similar types of response that we saw earlier in Figure 5.9, except that the unsteady vibration regime grows dramatically as the mass is reduced to  $m^* = 0.5$  and below.

At this point, we should like to describe what happens at very low mass ratios,  $m^* < 1$ . We first need to introduce the concept of a critical mass. From the frequency equation (5.5), we see that the effective added mass ( $C_{EA}$ ) can play an important role in determining the frequency ratio ( $f^* = f/f_N$ ). Govardhan & Williamson (2000) found that throughout the lower response branch in free

vibration, the effective added mass was given approximately by  $C_{EA} = -0.54$ , so that the frequency ratio is given by:

$$f^* = \sqrt{\frac{m^* + C_A}{m^* - 0.54}}, \quad (5.12)$$

Therefore as the mass ratio ( $m^*$ ) is reduced, the frequency ratio ( $f^*$ ) in the lower branch can become large. Furthermore, when the mass ratio falls below a critical value of  $m_{crit}^* = 0.54$ , the lower branch will never be reached, and ceases to exist. The upper branch will then persist indefinitely, up to infinite normalized velocity ( $U^* \rightarrow \infty$ ), giving an infinitely wide regime of resonance. In Chapter 6 (Morse & Williamson, 2009a), we show the influence of Reynolds number on the value of the critical mass, and for  $Re = 4,000$ , its value is  $m_{crit}^* = 0.36$ .

For extremely low mass, below the critical mass ratio,  $m^* < 36\%$ , the lower branch ceases to exist. In this case, the regime of large amplitude vibrations will extend from the end of the upper branch ( $U^* \approx 7$ ) all the way to infinite normalized velocity. The example in Figure 5.12, for  $m^* = 0.30$ , shows the unsteady vibration frequency response increasing throughout the range of plotted  $U^*$  at least up to 40, but in fact this trend will persist to infinite  $U^*$ , since  $m^* < m_{crit}^*$  in this case.

The present quasi-steady model somewhat changes our interpretation of what happens when the mass ratio falls below the critical value (36% in this case). Govardhan & Williamson (2000, 2002) described the critical mass phenomenon as involving an extension of the *upper branch* to infinite  $U^*$ . In fact, based on the study here, we see that, rather than the upper branch extending to infinite  $U^*$ , it is the *unsteady vibration response* (which is a state *between* upper and lower branches) that is found to extend to infinite normalized velocity.

## 5.6 Conclusions

In this study we have defined the fluid forces acting on a cylinder under controlled transverse vibration in a flow. Our high-resolution contour plots have been discussed before in Chapters 3 and 4 (Morse & Williamson, 2009 $b,c$ ) where extensive steady state vibrations have been studied, along with the details of the vortex formation modes. In this study, we also make use of the accurate determination of mode regime boundaries in the plane of amplitude-wavelength, which have been defined for the first time in such controlled vibration experiments. (Previous studies show a reasonably smooth variation of forces throughout the amplitude-wavelength plane.) The definition of the regime boundaries in our studies has enabled us to predict, for the first time, not only the general shape of amplitude response plots, but also to show the existence of all the principal response branches found in free vibration experiments. However, the focus in this study is to the development of a quasi-steady approach that can indicate what happens in cases of *transient or unsteady vibration*.

Cases of unsteady vibration arise when the response exhibits a transition between different response branches, which may seem like an unusual situation, but in fact it is quite common in free vibration systems, and is significant because *these unsteady vibrations represent the conditions giving the peak amplitude of response in low-mass systems*. In essence, we find that significant portions of the response plot, especially for the low mass ratios, are actually non-periodic. Such a regime in a response plot, which we refer to as a “void”, surprisingly does not admit steady state solutions, although we know from free vibration that large vibrations can exist. The system cannot satisfy both the amplitude and frequency equations, defined in this study, at the same time. The key to

understanding this phenomenon of a predicted “void” is observing how the fluid forces make a distinct jump across the mode regime boundaries in the amplitude-wavelength plane. In an approximate manner, we attempt here to represent the system within these voids, using the quasi-steady model, and the resulting amplitude response predictions are surprisingly similar to what is found in high-amplitude free vibration experiments for very low mass ratios. The predicted response frequency variation is almost linearly increasing in the upper-lower branch transition, but becomes more constant when the response is firmly in the lower branch, which is also close to what is found in free vibration. For extremely low mass ratios, below a critical value ( $m^* < 0.36$  in this case), the unsteady response regime stretches up to infinite normalized flow velocity,  $U^* \rightarrow \infty$ . In other words, the regime *without* the presence of steady state solutions is the one which extends to infinite flow velocities, rather than the upper branch steady state solutions, as supposed in Govardhan & Williamson (2002).

Our model can also represent the intermittent switching of modes, for higher mass ratios, that are found in free vibration. For moderate mass ratios ( $m^*$  of order 10), there exists a range of normalized velocity,  $U^*$ , for which there are two steady state solutions to the equations of motion (corresponding to the upper and lower response branches). In this case, the response will switch intermittently between them depending on which vortex formation mode is selected by the flow (the 2P or 2P<sub>O</sub> modes).

An unanswered question is what are the wake vortex dynamics in the transition region at low mass ratio? Of course we do not expect that the entire wake is switching rapidly between a 2P and 2P<sub>O</sub> vortex formation mode. Lucor *et al.* (2005) found that the wake was quite three dimensional in the upper to lower

branch transition region, in their case for  $m^* = 2.0$ . What seems plausible is that the wake shows different vortex dynamics at different points along the cylinder span in the transition region yielding a net fluid forcing which is in between the forcing for the  $2P$  and  $2P_O$  modes. In contrast, for the intermittent switching behavior at higher mass ratio, we suggest that the wake is largely two-dimensional for much of the time, when the response is seated for long periods on one branch or the other, between the intermittent mode switching.

## CHAPTER 6

# The effect of Reynolds number on the critical mass phenomenon in vortex-induced vibration

MORSE, T. L. & WILLIAMSON, C. H. K. (2009)

Submitted to *Physics of Fluids*.

In this study, we investigate the critical mass phenomenon in vortex-induced vibration over a wide range of Reynolds numbers ( $Re = 4,000 - 30,000$ ). We consider an elastically mounted cylinder that is able to vibrate transverse to a fluid flow. If we remove the restoring spring ( $k = 0$ ), then above a certain critical mass ratio ( $m^* = \text{oscillating body mass} / \text{displaced fluid mass}$ ), the cylinder will experience almost no motion, despite its unrestrained freedom to move transverse to the flow. However, when the mass ratio is decreased below a special critical value, without altering anything else in the system, we see a catastrophic increase in amplitude, and the body settles into a large amplitude periodic vibration. This corresponds to a change from a desynchronized wake to a 2P mode of vortex formation, where two pairs of vortices are formed per cycle of motion. Since a system with no restoring force represents a case of infinite normalized velocity ( $U^* \rightarrow \infty$ ), the observation of high amplitude motion indicates that the regime of  $U^*$  giving resonant vibration extends to infinity, for sufficiently small mass ratio. In this work, we measure the critical mass directly from experiments with no spring stiffness, and we show also how the critical mass may be accurately predicted from force measurements from controlled vibration experiments, or from free vibration measurements of elastically mounted cylinders.

Critical mass gradually increases with Reynolds number ( $Re$ ) from a value of 0.36 to 0.54, over the regime  $Re = 4,000 - 30,000$ . The fact that the critical mass is a function of Reynolds numbers should be expected, because it depends on the vortex-induced forces, which are influenced by gradual changes in vortex formation as  $Re$  increases. The evaluation of critical mass in this configuration, and indeed in other diverse vortex-induced vibration (VIV) systems, is important because it can predict the regime of normalised velocities that will yield large amplitude vibration, and which one may wish to avoid in practice. The fact that critical mass, at moderate Reynolds numbers, in several diverse VIV systems, including cylinders in one or two degrees of freedom, pivoted bodies, cantilevers, and tethered spheres, are all within a small range 0.36 - 0.6, remains an interesting question.

## 6.1 Introduction

Vortex-induced vibration (VIV) is an important problem in many fields of engineering. One of the most common issues with riser tubes bringing oil to the surface from the seabed, is the tendency for such structures to vibrate due to vortex-induced motion over the long length of the tube. VIV is also a problem in civil engineering, affecting dynamics of structures such as bridges, chimneys, and buildings, among other applications. The range of problems caused by vortex-induced vibration has led to a large number of experimental and computational studies on the subject, including several review articles, for example: Bearman (1984), Sarpkaya (1979), Parkinson (1989), and more recently Williamson & Gowardhan (2004). Classically, it has been assumed that resonant large amplitude vibration will only occur when the frequency of vortex formation for the non-

oscillating body, and thus the frequency of fluid forcing, is close to the natural frequency of the structure ( $f_{vo} \approx f_N$ ). This occurs when the normalized velocity ( $U^*$ ) is about 5, when  $U^* = U/f_N D$  becomes roughly equal to the inverse of the Strouhal number  $1/S$  ( $U$  = free stream velocity,  $f_N$  = natural frequency in still water,  $D$  = diameter). In the present study, we shall see that vortex-induced vibration may occur over an immense regime of frequencies ( $f$ ), up to several hundred times the natural frequency, and indeed as  $f/f_N \rightarrow \infty$ . The regime of normalised velocities over which there is large-amplitude resonant response may also extend to infinity. This is far from the general view one has of classical resonance. In this work, we seek to determine how the value of critical mass, below which the phenomenon of an infinitely wide regime of resonance occurs, is influenced by Reynolds number.

In this study, we focus on the conceptually simple case of an elastically mounted cylinder, constrained to move only transverse to a flow. Khalak & Williamson (1999) showed that for low combined mass-damping, such a system will have three branches of response when normalized amplitude ( $A^* = A/D$ ) is plotted against normalized velocity ( $U^*$ ): an initial response branch, an upper branch, and a lower branch. (An example of the three branch response may be found later in Figure 6.2.) They found that for a system with a relatively high mass ratio of 10 ( $m^* = \text{oscillating mass}/\text{displaced fluid mass}$ ), the high amplitude upper branch exists for  $U^*$  between about 4.5 and 5.5, which corresponds with the vortex formation frequency ( $f_{vo}$ ) being close to the natural frequency of the structure,  $f_{vo} \approx f_N$ , mentioned above. However, as the mass ratio is decreased to  $m^* = 1.19$ , the upper branch persists to  $U^* = 10.5$ , double the expected regime of  $U^*$  for resonant conditions. Govardhan & Williamson (2000) pushed mass ratio even lower to 0.52 and found that high amplitude vibration ( $A^* \sim 1$ )

persisted to the upper flow speed limits of their flow facility (up to  $U^* = 22$ ), with no signs of diminishing. At this point, the frequency of vibration reaches four times the natural frequency of the system ( $f = 4f_N$ ), which is clearly a departure from classical resonance.

In order to understand why the frequency of large-amplitude vibration can become so much higher than the natural frequency, it is useful at this point to introduce an equation of motion for a system undergoing vortex-induced vibration in the transverse y-direction:

$$m\ddot{y} + c\dot{y} + ky = F(t), \quad (6.1)$$

where  $m$  is the oscillating mass;  $c$  is the structural damping;  $k$  is the spring constant; and  $F(t)$  is the fluid force in the transverse direction. When the body oscillation is synchronized with the periodic vortex wake mode, the force and displacement are generally well approximated by sinusoidal functions:

$$y(t) = A \sin(\omega t), \quad (6.2)$$

$$F(t) = F_1 \sin(\omega t + \phi), \quad (6.3)$$

where  $\omega = 2\pi f$  and  $\phi$  = the phase angle between the fluid force and the body displacement. If we substitute (6.2) and (6.3) into the equation of motion (6.1), following the approach of Khalak & Williamson (1999), we can obtain an “amplitude equation”:

$$A^* = \frac{1}{4\pi^3} \frac{C_Y \sin \phi}{(m^* + C_A) \zeta} \left( \frac{U^*}{f^*} \right)^2 f^*, \quad (6.4)$$

and a “frequency equation”:

$$f^* = \sqrt{\frac{m^* + C_A}{m^* + C_{EA}}}, \quad (6.5)$$

where  $C_Y$  = the transverse force coefficient =  $F_Y / \frac{1}{2} \rho U^2 D L$  ( $\rho$  = fluid density,  $L$  = submerged length);  $C_A$  = the potential added mass coefficient (= 1.0 for a circular

cylinder); and  $\zeta =$  the damping ratio  $= c/2\sqrt{k(m + m_A)}$  ( $m_A =$  the added mass  $= C_A \times$  the mass of fluid displaced).  $C_{EA}$  is the effective added mass coefficient, related to the force in phase with acceleration as follows:

$$C_{EA} = \frac{1}{2\pi^3} \frac{C_Y \cos \phi}{A^*} \left( \frac{U^*}{f^*} \right)^2, \quad (6.6)$$

From (6.5), we see that the effective added mass ( $C_{EA}$ ) can play an important role in determining the frequency ratio ( $f^* = f/f_N$ ). Govardhan & Williamson (2000) found that throughout the lower response branch in free vibration, the effective added mass was given approximately by  $C_{EA} = -0.54$ , so that the frequency ratio is given by:

$$f^* = \sqrt{\frac{m^* + C_A}{m^* - 0.54}}, \quad (6.7)$$

Therefore as the mass ratio ( $m^*$ ) is reduced, the frequency ratio ( $f^*$ ) in the lower branch can become large. Furthermore, when the mass ratio falls below a critical value of  $m_{crit}^* = 0.54$ , the lower branch will never be reached, and ceases to exist. The upper branch will then persist indefinitely, up to infinite normalized velocity ( $U^* \rightarrow \infty$ ), giving an infinitely wide regime of resonance.

To confirm the existence of this regime of resonance, Govardhan & Williamson (2002), for  $Re = 22,000$ , measured the dynamics of a freely vibrating cylinder operating at *infinite* normalized velocity,  $U^* = U/f_N D \rightarrow \infty$ , which could be achieved by removing the springs from their experimental arrangement, giving the system a natural frequency,  $f_N = 0$ . They found that if the mass ratio of the structure fell below a certain critical value, the system would suddenly exhibit large amplitude vibrations, proving the existence of an infinite regime of resonance. The value they found for  $m_{crit}^*$  was 0.542, which is the same value predicted from the elastically mounted experiments of Govardhan

& Williamson (2000), at the same Reynolds number.

Our motivation for the present study is triggered from some controlled vibration measurements, where we prescribe the motion of the cylinder to be a sine wave relative to the fluid, defined by a normalised amplitude and wavelength. (The experiments were actually achieved by transverse vibrations of a body in the flow of a water channel). Using controlled vibration, we compile very high resolution fluid force contours, leading to accurate prediction of the response for a freely vibrating cylinder, as presented in Ref. 8. Such force contours may also be used to predict the critical mass in a VIV system. In the case of the controlled experiments conducted at  $Re = 4,000$ , we found  $m_{crit}^* = 0.36$ . Initially, this was a disconcerting result for us, since almost all of our previous experiments yielded the value close to 0.54. It remains a question why we find a distinctly different value for the critical mass here, from controlled vibration, as opposed to the value found from free vibration. Could this be a function of the fact there is some fundamental difference between forced and free vibration experiments? This disparity is the principal trigger for this study, and essentially we will find that controlled and free vibration experiments are quite consistent; it is the dependance of the critical mass on Reynolds number that will explain the differences.

The free vibration experiments from Govardhan & Williamson (2002), were conducted at  $Re = 22,000$ , whereas the controlled vibration was compiled for  $Re = 4,000$ . Reynolds number is known to have a significant effect on the peak amplitude of response, as shown by Govardhan & Williamson (2005a) and Klamo, Leonard & Roshko (2005), and characterized in more detail by Govardhan & Williamson (2006), so we might therefore expect a possible effect of Reynolds

number on the deduced value of critical mass.

From numerical simulations at low Reynolds numbers, where the vortex formation is laminar, Govardhan & Williamson (2002) used some of the results from simulations by Shiels, Leonard & Roshko (2001), to determine a critical mass of 0.25 at  $Re = 100$ . Ryan, Thompson & Hourigan (2005) also used numerical simulations in the laminar regime  $Re = 50-200$ , and found critical mass values in the range,  $Re = 0.1 - 0.5$ . In the present study, we focus on a range of  $Re$  from 4,000 to 32,000, where vortex formation is quite different. This is part of a regime of wake vortex dynamics for a stationary cylinder from  $Re = 1,000 - 100,000$ , where the evolving vortices are turbulent, and one finds the drag and Strouhal number are only slowly varying with Reynolds number. (Roshko, 1993; Williamson, 1996)

In the present study, we have set up our cylinder free to move only transverse to the free stream in a water channel. As described briefly in §6.2, the cylinder is mounted to a carriage, which is usually restrained by springs. However, the principal free vibration experiments, in §6.3, are those for which we have removed the springs, to yield an infinite normalised velocity  $U^*$ . Under these conditions we can vary the mass of the oscillating structure to yield the critical mass, below which the body will suddenly start to vibrate vigorously. By varying Reynolds number, we determine its influence on critical mass. Vorticity measurements demonstrate the vortex formation modes responsible for enabling the body to vibrate at large amplitude, throughout the variation of Reynolds number studied here. In §6.4, we describe how one may predict the value of critical mass from either free or controlled vibration data, and determine its variation with Reynolds number. These results are found to be in good

agreement with the experiments where we have no restoring force, and where the normalised velocity is infinite. Conclusions from this work are presented in §6.5.

## 6.2 Experimental Details

The present experiments are conducted using a hydroelastic facility, in conjunction with the Cornell-ONR Water Channel, both of which are described in detail by Khalak & Williamson (1996, 1999). The hydroelastic facility is comprised of a vertical cylinder suspended from a carriage, which rides normal to the flow on air bearings mounted above the water channel, providing very low structural damping. In the present case no springs are used ( $k = 0$ ), so the motion of the body is not restrained transverse to the flow. The cylinder has a diameter of 7 cm and submerged length 44.5 cm. Flow speed is varied from 11.4 cm/s to 38.6 cm/s, yielding  $Re$  from 8,000 to 27,000. The water channel has a cross section of 38.1 cm by 50.8 cm, and the turbulence level in the test section of the water channel is less than 0.9%. The displacement of the cylinder is measured using a non-contact magnetostrictive sensor.

In addition to the free vibration experiments, we present force data from controlled vibration, using the same flow facility. The cylinder is suspended vertically from a carriage on a transverse lead screw, which is driven by a computer controlled motor to give sinusoidal oscillation. We measure fluid forces on the body with a two-axis force balance utilizing LVDTs (linear variable distance transducers) over a wide range of normalized amplitude,  $A^*$ , and wavelength,  $\lambda^* = \lambda/D$ , (noting that  $\lambda^*$  is equivalent to  $U^*/f^*$  or  $U/fD$ ). Controlled vibration

experiments are conducted at  $Re = 4,000$  (using a 3.81 cm diameter and 38.1 cm length cylinder), and at  $Re = 12,000$  (using a 6 cm diameter and 42 cm length cylinder). These measurements are conducted at high resolution (intervals of 0.02 for  $A^*$  and 0.2 for  $U^*/f^*$ ).

In order to measure velocity and vorticity in the flow, using DPIV, the flow is seeded with 14-micron silver coated glass spheres, which are illuminated by a sheet of laser light from a 50 mJ Nd:Yag pulsed laser. Pairs of particle images are acquired using a Jai CV-M2CL CCD camera (1600 x 1200 pixels), and analyzed using cross-correlation of sub-images. We use a two-step windowing process (with window shifting) to obtain particle displacements between image pairs.

### 6.3 Vortex-induced vibration at infinite normalized velocity

The intention here is to set up a system which represents a body operating at infinite normalised velocity  $U^*$ , and to determine for what value of the mass the system will suddenly commence large amplitude vibration. As mentioned earlier, this is achieved by having the cylinder free to move transverse to the flow, on air bearings, and to remove the restraint of springs. Under such conditions, Govardhan & Williamson (2002) observed a sudden jump in the amplitude of vibration as the mass ratio was decreased below a critical mass ratio,  $m_{crit}^* = 0.542$ , in their case for  $Re = 22,000$ , as shown in Figure 6.1(a). In the present case, we show from a similar experiment at  $Re = 12,000$ , in Figure 6.1(b) the existence of a sharp jump in amplitude at  $m_{crit}^* = 0.505$ , so already one may determine some effect of Reynolds number. These and other data points (from 5 different  $Re$ ) for critical mass are plotted in Figure 6.5 later, as the solid symbols,

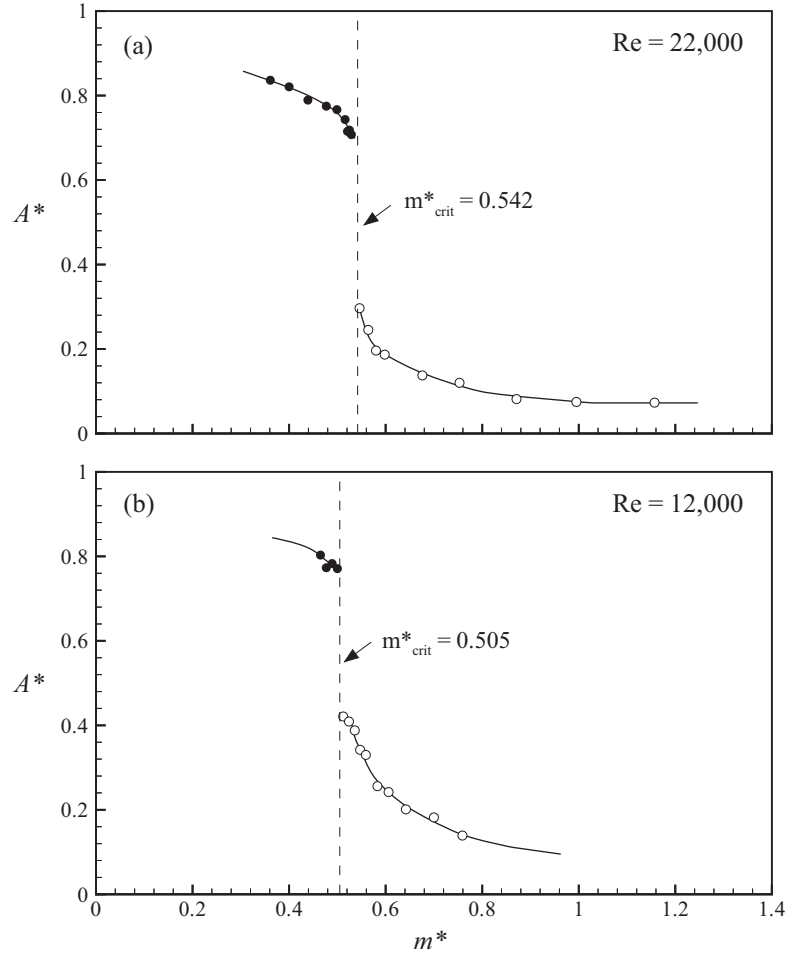


Figure 6.1: Existence of a critical mass ratio. We plot amplitude of vibration ( $A^*$ ) as mass ratio ( $m^*$ ) is varied for a system with no restoring force, giving infinite normalized velocity. (a)  $Re = 22,000$  from Govardhan & Williamson (2002), (b)  $Re = 12,000$ , present results.  $\bullet$  :  $m^* < m^*_{crit}$ ;  $\circ$  :  $m^* > m^*_{crit}$ .

indicating clearly the effect of Reynolds number.

In addition to the jump in amplitude of response, there is also a sudden change in the oscillation frequency, as the mass ratio is decreased below the critical value. This may be seen in a plot of amplitude ( $A^*$ ) versus wavelength ( $U^*/f^*$ ) in Figure 6.2. The response curve in this plot is computed using the fluid force data from controlled vibrations. In this case, we have a contour of  $C_Y \sin \phi$ , which is the coefficient of force in phase with the body's velocity; it

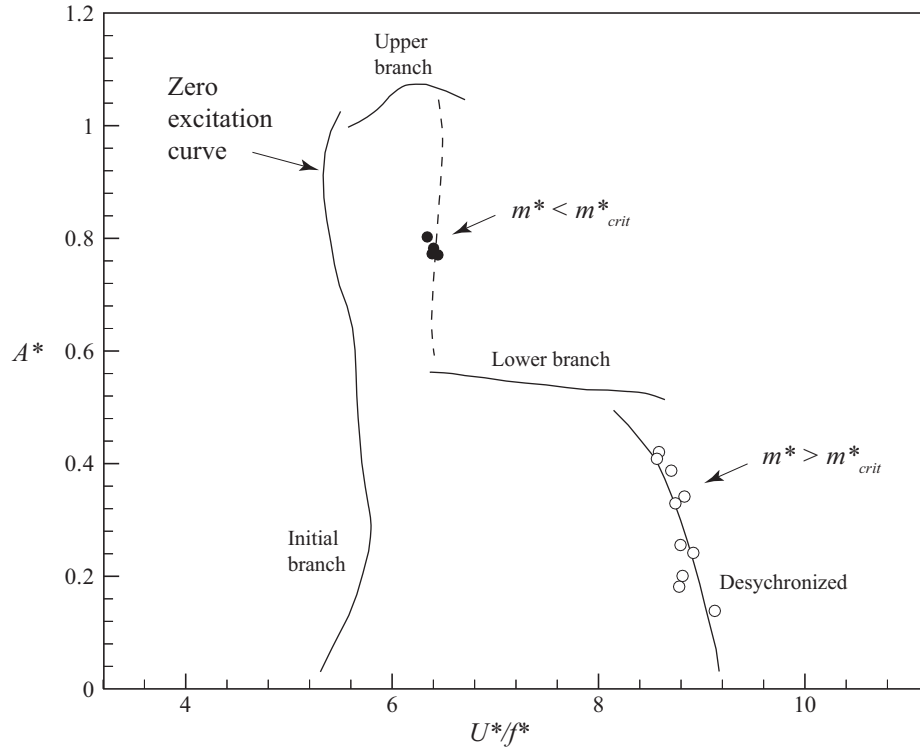


Figure 6.2: Locations of the operating point in the normalized amplitude-velocity plane for  $Re = 12,000$ . (—) Zero excitation contour from controlled vibration data. • mass ratios below  $m_{crit}^*$  lie in the upper to lower branch transition region, ○ mass ratios above  $m_{crit}^*$  lie in the desynchronized regime.

is the normalised fluid excitation, or energy transfer from fluid to body motion, which under steady state conditions, must equal the normalised energy lost to damping per cycle (see equation 6.4). Our response plot in Figure 6.2 comes from the contour of zero excitation ( $C_Y \sin \phi = 0$ ), so this represents the predicted free vibration response for zero damping. To return to the change in frequency mentioned above, this is observed in Figure 6.2 where there is a sudden change in the value of  $U^*/f^*$  (from the open symbols to the solid symbols), as the body commences large amplitude vibration, in a location which we call the “operating point”. For  $m^* < m_{crit}^*$ , the operating point falls in a region in between the upper and lower branches of response. In this region, we find the

vortex formation mode to be the 2P mode, an example of which is shown in Figure 6.3(a), representing two vortex pairs formed per cycle of motion, following the nomenclature of Williamson & Roshko (1988). For  $m^* > m_{crit}^*$ , the operating point falls in the region where the wake is desynchronized from the body oscillation, an example of which is shown in Figure 6.3(b). The critical mass thus defines not only a sharp jump in amplitude and frequency, but also a distinct change in vortex formation mode.

## 6.4 Influence of Reynolds number on prediction of critical mass

We would like to determine the critical mass from free vibration plots, and show, for example, a representative schematic of such a plot in Figure 6.4. In this example, we again consider a response in the amplitude-wavelength plane for zero damping (so that  $C_Y \sin \phi = 0$ ), at Reynolds number of 4,000. We now impose the condition of zero spring stiffness,  $k = 0$ , which places us at infinite normalised velocity,  $U^* \rightarrow \infty$ , and we have from the frequency equation (6.5) that:

$$m^* = -C_{EA} \quad (6.8)$$

At the operating point in the amplitude-wavelength plane of Figure 6.4, both the frequency equation (6.8) and the amplitude equation, which in this case is:

$$C_Y \sin \phi = 0 \quad (6.9)$$

must be satisfied. Thus for a system with no springs and zero damping, the operating point, for a given mass  $m^*$  and Reynolds number, will be the inter-

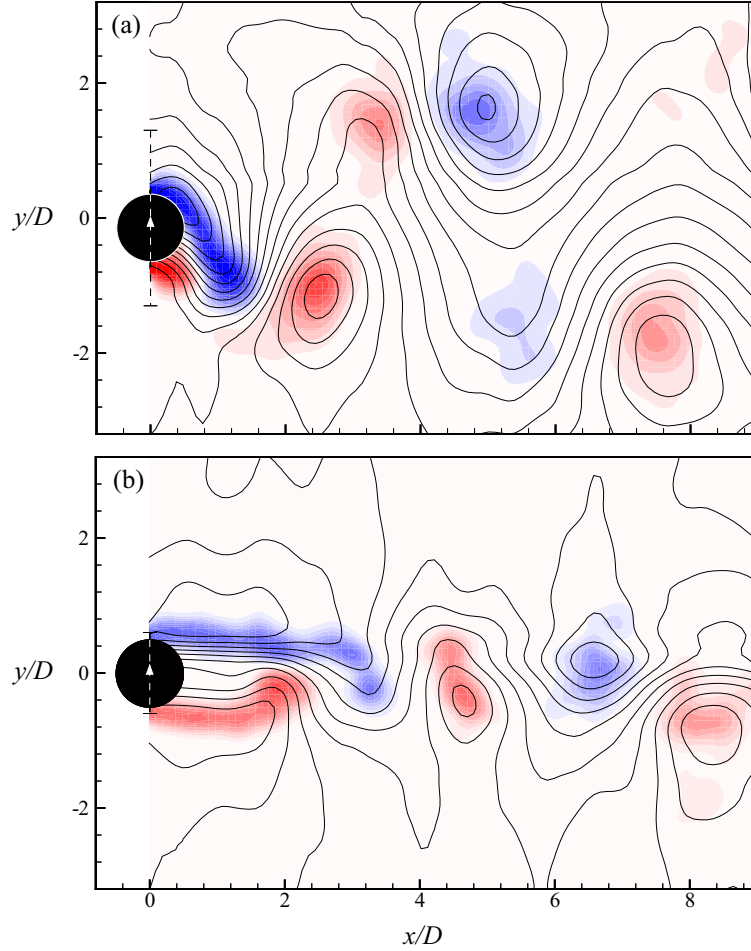


Figure 6.3: Streamlines and vorticity contours from DPIV for the 2P vortex formation mode (a):  $A^* = 0.8, U^*/f^* = 5.6$  (phase-averaged over 10 cycles of vibration) and for a desynchronized wake (b):  $A^* = 0.1, U^*/f^* = 8.0$  (not phase-averaged) at  $Re = 4,000$ . Streamlines are shown for a frame of reference moving to the right with the free stream velocity. Vorticity contour levels shown are:  $\omega D/U = \pm 0.4, \pm 0.8, \pm 1.2, \dots$

section of the zero excitation contour ( $C_Y \sin \phi = 0$ ) and the  $m^* = -C_{EA}$  contour, shown schematically in Figure 6.4.

When we are operating at infinite  $U^*$ , we wish to search for the maximum mass ratio  $m^*$ , beyond which the large amplitude motions cease. This will be the critical mass. Along the amplitude response curves in Figure 6.4, we determine the measured value of  $C_{EA}$ . From equation (6.8), we simply look for the maximum

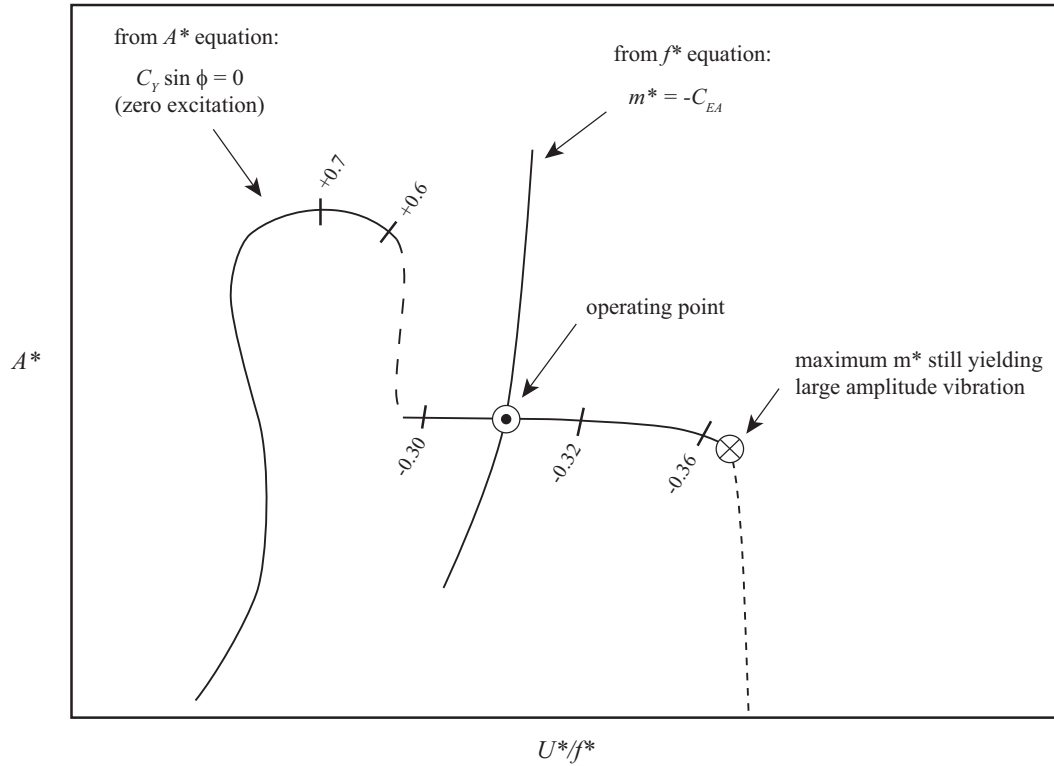


Figure 6.4: Schematic diagram showing how the operating point is determined. The system will oscillate at the point where both the  $A^*$ -equation and the  $f^*$ -equation are satisfied. If no such point exists, the system will not oscillate. (---) indicates the upper to lower transition region, (-.-) indicates the desynchronized regime. We also show values of  $C_{EA}$  at various points along the zero excitation contour.

value of  $[-C_{EA}]$ , which we write as  $[-C_{EA}]_{max}$ . In other words, any mass below this value would correspond to some point in the response plot having large amplitude vibration. We should note that  $[-C_{EA}]$  or  $m^*$  increases as  $U^*$  increases, along the zero excitation contour in Figure 6.4, so we are seeking  $[-C_{EA}]_{max}$  or  $m^*_{crit}$  at the right hand end of the lower branch of response. This corresponds with the point labelled by the cross.

One further side point to note here is that the experiments at infinite normalised velocity (condition of no springs), in Figure 6.2, yield the large amplitude response between upper and lower response branches (the solid symbols),

rather than giving such an experimental response at the right hand end of the lower branch. This happens because, for  $Re = 12,000$ , along the lower branch, the value of  $C_{EA}$  changes only a tiny amount, and the experiments were not fine enough to pick up points intermediate to the solid symbols and the end of the lower branch.

The results of applying the ideas above to determine critical mass are shown in Figure 6.5, along with the earlier data found by experiments without springs. Data using controlled vibration experiments are shown as the open circles, and data from several previous studies, at very low damping, are shown as the triangles and squares. We use this approach for experimental data, at very low damping, from Govardhan & Williamson (2000); Hover, Tvedt & Triantafyllou (2001); Branković & Bearman (2006); and Hover, Techet & Triantafyllou (1998). We see a good agreement from all the types of data and approaches, yielding a consistent trend amongst all the data; the critical mass ratio increases gradually from 0.36 to 0.54, as  $Re$  increases from 4,000 to 30,000.

This fact that the critical mass approximately reaches a constant level of 0.54 at around  $Re = 16,000$ , explains why so many of our early studies, in a range of Reynolds numbers from 15,000 - 22,000, yielded a critical mass of 0.54. It also suggests that our observation that critical mass is 0.36 from the controlled vibration approach, while being quite different from the value 0.54 in free vibration, is not some intrinsic difference brought on by using these two different approaches, but rather it is simply an effect of different Reynolds numbers.

Evaluation of the critical mass is also useful to find the regime of velocity,  $U^*$ , over which there is large amplitude response. For a system of low mass-damping, the right hand end of the lower branch lies at  $U^*/f^* \approx 9.5$ . Thus  $U^*$

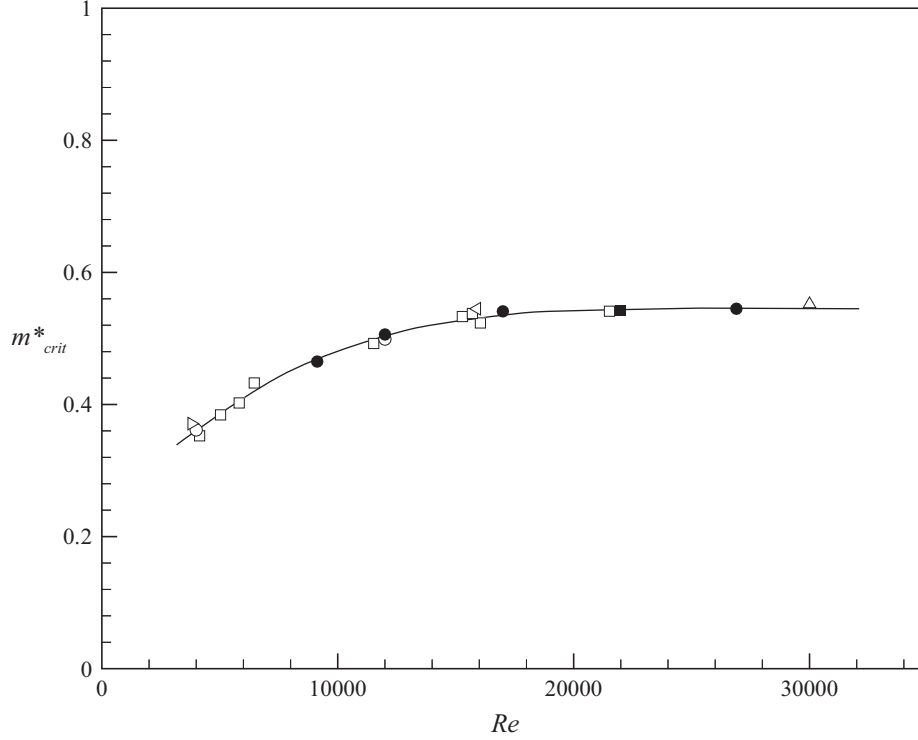


Figure 6.5: Critical mass as a function of  $Re$ . Values of  $m^*_{crit}$  are obtained from experiments at infinite normalized velocity: ● present results, ■ from Govardhan & Williamson (2002). Predictions of the critical mass are found using  $C_{EA}$  in the lower branch from controlled vibration: ○ present results, and from free vibration: □ Govardhan & Williamson (2000), and unpublished data taken at the same time. We also show data: △ Hover *et al.* (2001), ◁ Branković & Bearman (2006), ▷ Hover *et al.* (1998)

for the end of synchronization is governed by:

$$U^*_{end} \approx 9.5 \sqrt{\frac{m^* + C_A}{m^* - m^*_{crit}}} \quad (6.10)$$

and is shown for different values of  $Re$  in Figure 6.6. To quote typical values, for moderate Reynolds numbers,  $Re \sim 30,000$ , one would wish to avoid lightly damped structures of order  $m^* = 1$ , where one would expect large amplitude vibration even up to  $U^* \sim 20$ . Of course lighter structures, of relative density close to 54%, and for velocities above  $U^* = 3$ , will not be able to escape large vibrations, at any flow speed.

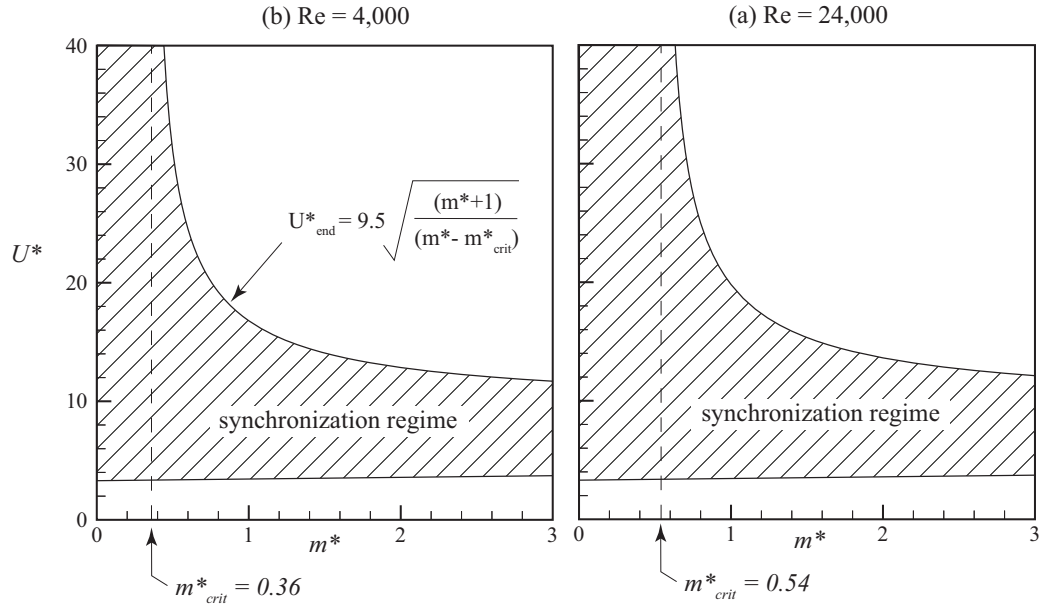


Figure 6.6: The regime of normalized velocity ( $U^*$ ) where a synchronized response can occur for  $Re = 4,000$  (a) and  $Re = 24,000$  (b). The end of synchronization will depend on the value of  $m^*$ , and on  $m^*_{crit}$  which depends on  $Re$ , as shown in Figure 6.5.

## 6.5 Conclusions

The discovery that, for moderate structural mass of a vibrating structure, there exists a critical mass below which a body can resonate over an unlimited regime of normalised velocities ( $U^* \rightarrow \infty$ ), is significant for practical applications. Such bodies may vibrate at frequencies several hundred times the natural frequency of the structure in the fluid, and so this phenomenon is clearly quite distinct from classical resonance, where one expects the vibrating frequency at resonance to be close to the natural frequency. We are interested, in this study, in designing investigations which may quantify both the critical mass for a given VIV configuration, and in determining the regime of flow speeds giving large amplitude vibrations. This work in this study was triggered by the fact that there appeared to be distinct differences in the predicted critical mass coming from

the controlled vibration approach to VIV, as compared to results coming from free vibration experiments. Some conclusions in previous works suggested that one must expect differences in VIV results to arise because there are intrinsic differences between these two approaches. However, we show here that it is the Reynolds number that influences the value of  $m_{crit}^*$ , rather than the approach. Indeed, there is a very good agreement between the predictions of critical mass from controlled vibration, and the direct measurements from free vibration experiments.

Our approaches involve experiments where a cylinder is confined to transverse vibration at extremely low damping, but where the spring restraints are removed, yielding effectively an infinite normalised velocity. In other words, if, under these conditions, one finds a mass below which there is a catastrophic jump to periodic large amplitude motion, then this indicates that the regime of resonant vibrations has reached infinite normalised flow speed, for masses below that value. In essence, one has found the critical mass. We also determine this mass from controlled vibration studies, and from experiments of selected previous studies with very light damping, where one may compute the effective added mass, and deduce the critical mass. The critical mass is clearly influenced by Reynolds number, rising from 0.36 at  $Re = 4,000$  to 0.54 at  $Re = 16,000$ , and continuing to be close to 0.54 as Reynolds numbers rise to 30,000. The plateau beyond  $Re = 16,000$ , and the fact that most of our previous experiments (Govardhan & Williamson, 2000, 2002) were for  $Re$  greater than this value, explains why we had assumed 0.54 to be the value to use. Over this regime of  $Re = 4,000 - 30,000$ , we have found the vortex formation regime to switch from a desynchronised mode, at higher  $m^*$ , to the 2P mode, whereby two vortex pairs are formed per cycle, for  $m^*$  below the critical mass. By careful exploitation of dif-

ferent approaches and different studies, we now present the effect of Reynolds number on the critical mass, over this regime of  $Re$ .

The significance in finding this influence of Reynolds number on critical mass lies in the fact that this parameter defines the regime of velocities that one might consider avoiding when employing light structures, or those in a marine environment, where typically  $m^* < 10$ . The evaluation of critical mass in several studies, including one degree of freedom vibrating cylinders (Govardhan & Williamson, 2002), two degree of freedom configurations (Jauvtis & Williamson, 2004), pivoted columns (Flemming & Williamson, 2005), tethered spheres (Govardhan & Williamson, 2005b), have all yielded critical mass between 0.5 - 1.0. It is obviously of interest to answer a fundamental question which remains: why must one expect such a value for critical mass in such systems? We are presently addressing this questions.

## CHAPTER 7

# The effect of end conditions on the vortex-induced vibration of cylinders

MORSE, T. L., GOVARDHAN, R. N. & WILLIAMSON, C. H. K. (2009)

To appear in *Journal of Fluids and Structures*.

In the present investigation we study the effect of end conditions on the vortex-induced vibration of an elastically mounted rigid cylinder. This work was triggered by some initial controlled vibration experiments which showed that spanwise end conditions can have a large effect on measured fluid forces on a cylinder, and this suggested that some of the disparity amongst previous free vibration studies may possibly be attributed to differences in end conditions. In the principal experiments here, we are concerned with a vertical cylinder piercing the clean free surface of a water channel, and attached to a carriage system mounted atop the channel. The upper end of the submerged cylinder is thus the free surface, while the lower end is manipulated to yield three different conditions, namely: an attached endplate; an unattached endplate fixed to the channel floor (with a variable gap between cylinder and plate); and a condition of no endplate at all. Interestingly, we find that the free vibration response for the attached and unattached endplate cases were nearly identical. One expectation was that the case *without* an endplate would lead to a flow around the end of the body, modifying the vortex dynamics, and thereby reducing the correlation of the induced fluid forces on the body. Surprisingly, over the entire response plot, *the vibration amplitude is markedly higher in the absence of an endplate*, with the exception of the peak amplitude, which remains nearly unchanged. Unexpectedly,

the vibrations become much more steady at flow velocities in the vicinity of the peak response, if the endplate is removed. In a further set of experiments, we undertake controlled vibration, where we vary the gap between cylinder and endplate. We discover a large discontinuous jump in the magnitude of fluid excitation, when the gap exceeds 15% of a diameter. For larger gaps, the fluid excitation becomes independent of the gap size, effectively equivalent to having no plate at all. This study is consistent with some of the disparity between the character of vibration response plots in previous studies, if one takes into account the particular end conditions chosen in those studies.

## 7.1 Introduction

Vortex-induced vibration is an important problem in many fields of engineering. It affects the dynamics of riser tubes bringing oil from the seabed to the surface, as well as civil engineering structures such as bridges, chimneys, and buildings, and is cause for concern in many other practical applications. The range of problems caused by vortex-induced vibration has led to a large number of experimental and computational studies on the subject, including several review articles, for example: Sarpkaya (1979), Griffin & Ramberg (1982), Bearman (1984), Parkinson (1989), and more recently Williamson & Govardhan (2004).

In studies of vortex-induced vibration, the case of an elastically mounted rigid cylinder, constrained to move transverse to an incoming flow, is often used as a paradigm for understanding more diverse experimental arrangements. The present study of the effects of spanwise end conditions on free vibration response has actually been triggered by some recent experiments (shown in Chap-

ter 2 Morse & Williamson, 2006), where we set out to conduct controlled vibrations of a body, and to make accurate comparisons with free vibration studies, involving measurements of fluid force, and predictions of amplitude. Our own free-vibration arrangement comprises a vertical cylinder, attached below an air-bearing carriage system sitting atop a water channel. The lower end of the submerged portion of the cylinder vibrates transversely above an endplate that is fixed to the channel floor. (It is noted briefly that we were careful to ensure “clean” free surface conditions, removing any dust film that may be present, and enabling the vortex lines to pass through the surface consistent with vortex formation parallel to the body). At the outset, we were discouraged to find significant disparity between forces measured from our controlled experiments versus those measured for free vibration, under the same conditions of amplitude and frequency (see Figure 7.1). It soon became apparent that the key to the large differences in fluid forces was due to the sensitivity of the flow around the body to small differences in the gap dimension between cylinder and endplate. Such effects are clearly seen in the force fluctuations exhibited in Figure 7.1, showing marked differences for different gap sizes (different values of  $g^* = \text{gap} / \text{diameter}$ ). On the other hand, if one ensures *precisely* the same experimental arrangements between the free and controlled vibration cases, one not only observes the fluid forces to be nearly identical, but one also finds highly accurate response prediction (as shown in Chapter 4, Morse & Williamson, 2009c). On the basis of these preliminary results, we can therefore expect differences in experimental end condition arrangements between different researchers to affect the free vibration response, as well as the fluid forcing from vortex dynamics.

A further interesting fact will emerge from the comparison of force fluctuations in Figure 7.1. Upon inspection of these fluctuations, one would suspect

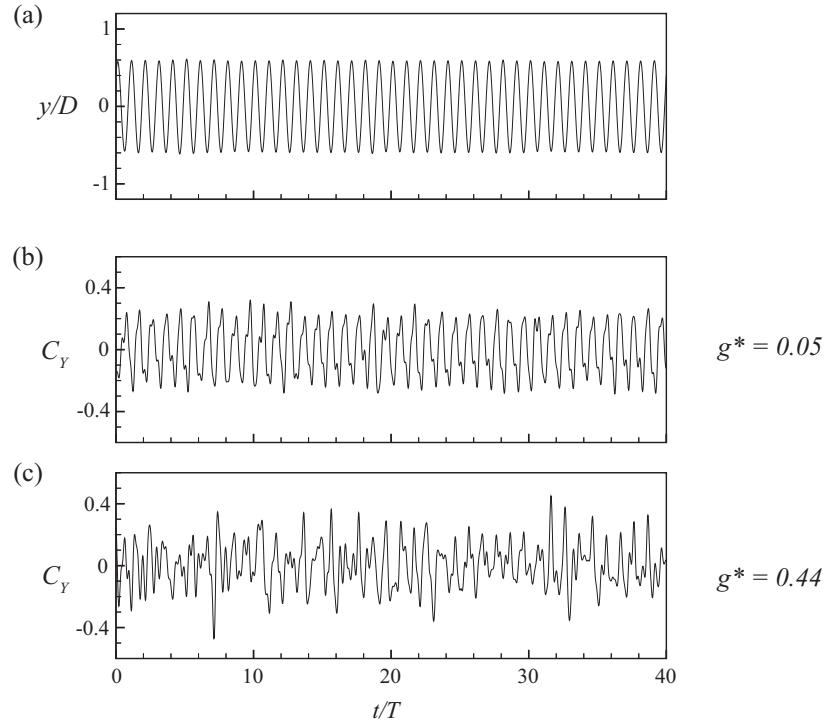


Figure 7.1: Effects of the gap size ( $g^*$ ) on the transverse force measurements ( $C_Y$ ). Despite the fact that we matched closely the transverse displacement,  $y/D$  ( $A^* = 0.60, U^*/f^* = 7.55$ ), the free vibration forces in (b) differ substantially from the controlled vibration forces in (c). We deduce that these differences are due the sensitivity of the flow to gap size. We define the gap size ( $g^*$ ) as the gap between the bottom of the cylinder and an unattached endplate, divided by the cylinder diameter.

that the more organized periodic forces for the small gap ( $g^* = 0.05$ ) would provide a larger energy transfer from fluid to body motion, than would be found at the larger gap ( $g^* = 0.44$ ), where the forces are less periodic. (One would naturally expect the vortex formation to be disrupted due to the flow around the ends.) In fact, the converse is true! The larger gap in (c) yields greater energy transfer, and the system would, if elastically mounted, increase its displacement amplitude; in essence, the larger gap would yield a larger vibration amplitude. This counter-intuitive result has been part of the stimulus for this study. One of the keys to understanding this result, is the fact that increasing the gap also

modifies the phase between fluid force and body motion ( $\phi$ ) such that the energy of excitation increases.

We are concerned, in this study, primarily with low values of mass and damping for a vibrating structure, and therefore focus on experiments conducted in water facilities; namely, water channels and towing tanks. We mention here some of the variety of end conditions employed in previous experiments in water facilities. Research groups in Norway have primarily used towing tanks, with horizontal cylinders supported by struts from an elastic structure above the tank, with circular endplates attached to the cylinder ends (Anand & Torum, 1985; Moe & Overvik, 1982; Vikestad *et al.*, 2000). The group at MIT (for example, Hover *et al.*, 1998) have also been using a horizontal cylinder with attached endplates in their towing tank experiments. In their case, they have developed an ingenious technique involving representation of the mass, damping and stiffness on a computer, while the fluid force is actually measured from their cylinder in the tank. This *Virtual Cable Testing Apparatus* allows them to run “virtual” free vibration experiments. In the experiments of Sarpkaya (1995), he has also used a horizontal cylinder suspended by struts, but in his case the endplates were fixed to the tunnel walls with a small gap separating them from the cylinder.

Vertical cylinders have also been used, beginning with recent studies by Khalak & Williamson (1996), who used a vertical cylinder (in a water channel) that was suspended from a carriage mounted on air bearings. They used an unattached endplate fixed to the channel floor. Jauvtis & Williamson (2004) set up a pendulum for two degree-of-freedom experiments, with a cylinder suspended beneath it in a water channel, again using an unattached endplate,

whereas Owen, Bearman & Szewczyk (2001) for their pendulum arrangement, employed endplates fixed to the cylinder. Branković & Bearman (2006) have also conducted vertical cylinder experiments, but without endplates at all, leaving a small gap between the body and the channel floor (and allowing the possibility for the channel boundary layer to influence the end conditions). Klamo, Leonard & Roshko (2006) also used a free end without endplates. In summary, these experimental arrangements indicate the variety of approaches to treating the end conditions, and *it must be expected that there will also be a variety of responses, due to the different end conditions, even if all other flow parameters are kept constant*. The expectation of such differences is part of the stimulus of this study.

Much attention has been paid to the effect on free vibration response of varying experimental parameters such as mass and damping, and more recently, Reynolds numbers (see Govardhan & Williamson, 2005a, 2006; Klamo *et al.*, 2005). Reynolds number is defined by  $Re = UD/\nu$ , where  $U$  is free stream velocity,  $D$  is diameter, and  $\nu$  is the kinematic viscosity. However, the effects of end conditions on free vibration response have been largely overlooked, and there has been no systematic study in the literature concerning the effects on response coming from different types of spanwise end configurations.

In the case of fixed cylinders in a flow, the end boundary conditions can have an important effect on the flow over both short cylinders (Slaouti & Gerard, 1981), and over long cylinders even hundreds of diameters in length (Williamson, 1988, 1989, 1996). The vortex dynamics in the laminar regime ( $Re < 190$ ), and for moderate  $Re \sim 5,000$  (Prasad & Williamson, 1997), are affected by end conditions. It is also well known that the length-diameter ratio (Szepessy & Bearman, 1992), and the end conditions, can affect the pressure distribution

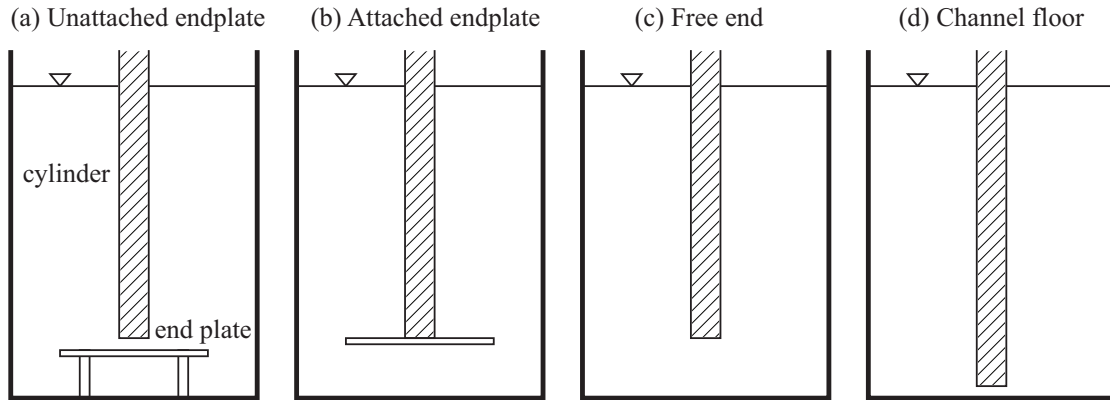


Figure 7.2: Schematic diagram of some typical end conditions: (a) unattached endplate, with a small gap between the endplate and the bottom of the cylinder (b) attached endplate, (c) free end, (d) cylinder end close to the channel floor.

along the span (Stansby, 1974). One might suspect that body oscillations would reduce such effects, because vibration increases correlation lengths and vortex formation coherence along the span. However, Hover *et al.* (2004) have measured the correlation between fluid forces measured at both ends of a cylinder undergoing vortex-induced motion, and found that it drops significantly for oscillation frequencies below the natural vortex shedding frequency. Our present results will also show that a variation of end conditions has the most effect on response when the oscillation frequency is below the natural shedding frequency (in which case the normalized velocity exceeds the value corresponding to the peak amplitude response).

In the present work, we will principally be concerned with the effects of three different end boundary conditions, as illustrated later in Figure 7.2: the case of an unattached endplate (where we may vary the gap between cylinder and plate); an attached endplate; and the case of no endplate. As these boundary conditions are modified, we keep all other parameters, such as the cylinder dimensions, mass, damping and Reynolds number the same. We will also be

primarily interested in experiments at high amplitude, under conditions of low mass and damping. In this case, previous studies have shown the existence of three branches of response (Khalak & Williamson, 1999), as illustrated in Figure 7.3 (the solid symbols), namely the initial branch (marked by the letter I), the upper branch (U), and the lower branch (L). There are therefore two mode transitions in this case. The first transition between the initial-upper branch is hysteretic, while the second one between the upper-lower branch involves an intermittent switching of modes. The transitions and their relationship with vortex dynamics modes and fluid forces were studied in detail by Govardhan & Williamson (2000). With respect to the present study, we wish to know how the end boundary conditions might affect the character of these response branches, their peak amplitudes, their regime of synchronization, and the possible changes to the mode transitions.

We shall describe the experimental approaches in §7.2. The influence of end conditions on free vibration response are studied in §7.3, while the effects of end conditions on forces measured in controlled vibration are included in §7.4. Brief comparisons with previous investigations, where various different end conditions are employed, are presented in §7.5, followed by the conclusions in §7.6.

## **7.2 Experimental details**

Our free vibration experiments are conducted using a hydroelastic facility described in detail in Khalak & Williamson (1996). The cylinder is suspended vertically from a carriage above the test section of the Cornell-ONR Water Channel. The carriage is attached to shafts which ride through air bearings. This system

constrains the cylinder to move only transverse to the free stream flow, while ensuring very low structural damping. Springs of varying stiffness can be attached to the carriage to adjust the system elasticity, and mass can be added to the carriage to vary the system mass ratio. The test section of the water channel has a cross section of 38.1 cm x 50.8 cm. The flow speed is varied in the range 10-32 cm/s, and the turbulence level in the test section is measured to be less than 0.9%. The cylinder diameter is 5.08 cm, and has a submerged depth of 40.6 cm, giving an aspect ratio ( $L/D$ ) of 8, and a Reynolds number regime,  $Re = 5,000 - 16,000$  over a range of flow speeds. The transverse displacement is measured using a non-contact (magnetostrictive) position transducer. The reported amplitude is the average of the top 10% of the individual amplitude peaks, evaluated in the manner described by Hover *et al.* (1998). In our case, we measure this amplitude over a complete displacement time trace of several hundred cycles.

For our controlled vibration measurements, we use precisely the same cylinder, but in this case it is suspended from a transverse lead screw system, driven by a computer-controlled motor. A two-axis force balance, utilizing linear variable displacement transducers (LVDTs), was used to measure the lift and drag forces on the body. The inertial forces due to the oscillating structural mass are subtracted from the total measured force, to yield the fluid forces on the cylinder. Instantaneous phase measurements are obtained through use of the Hilbert transform (see Khalak & Williamson, 1999).

Our three end condition arrangements were exhibited earlier in Figure 7.2. For the unattached endplate case, we can vary the gap, such that  $g^* = 0.02 - 0.5$ , where the smallest gap corresponds to close to 1 mm. The endplate is rectangular (50.8 cm x 36.8 cm wide) with rounded corners. The attached endplate is

circular with a diameter of 20.3 cm (four times the cylinder diameter). In the case without an endplate, the bottom of the cylinder is about 7 cm from the channel floor.

In this study, we will need to define the energy transfer between fluid and body motion, and present the relevant non-dimensional groups. We introduce here an equation of motion often used to represent the vortex-induced vibration of a cylinder in the transverse  $y$ -direction (perpendicular to the free stream) as follows:

$$m\ddot{y} + c\dot{y} + ky = F(t), \quad (7.1)$$

where  $m$  = system mass;  $c$  = structural damping;  $k$  = spring stiffness; and  $F(t)$  = fluid force in the transverse direction. When the body motion is synchronized with the vortex shedding, reasonable approximations to the force and motion are often given as:

$$y = A \sin(\omega t), \quad (7.2)$$

$$F(t) = F_1 \sin(\omega t + \phi), \quad (7.3)$$

where  $\omega = 2\pi f$ ;  $f$  = oscillation frequency. The phase angle ( $\phi$ ), between fluid force and body displacement, is crucial in determining the energy transfer from fluid to body motion, and hence in influencing the amplitude of oscillation. We select a set of relevant non-dimensional parameters in this problem, which are presented in Table 7.1.

The response amplitude and frequency may be derived in a straightforward manner, along the lines of Khalak & Williamson (1999), as follows:

$$A^* = \frac{1}{4\pi^3} \frac{C_Y \sin \phi}{(m^* + C_A) \zeta} \left( \frac{U^*}{f^*} \right)^2 f^*, \quad (7.4)$$

$$f^* = \sqrt{\frac{m^* + C_A}{m^* + C_{EA}}}, \quad (7.5)$$

Table 7.1: Non-dimensional groups. In the groups below,  $U$  is the free-stream velocity,  $f$  is the oscillation frequency,  $f_N$  is the natural frequency in water,  $D$  is the cylinder diameter,  $L$  is the submerged length,  $\rho$  is the fluid density,  $\nu$  is the fluid kinematic viscosity, and  $g$  is the gap between the endplate and the cylinder. The added mass,  $m_A$  is given by  $m_A = C_A m_d$ , where  $m_d$  is the displaced fluid mass and  $C_A$  is the potential added mass coefficient ( $C_A = 1.0$  for a circular cylinder).

Mass ratio	$m^*$	$\frac{m}{\pi\rho D^2 L/4}$
Damping ratio	$\zeta$	$\frac{c}{2\sqrt{k(m+m_A)}}$
Velocity ratio	$U^*$	$\frac{U}{f_N D}$
Amplitude ratio	$A^*$	$\frac{A}{D}$
Frequency ratio	$f^*$	$\frac{f}{f_N}$
Transverse force coefficient	$C_Y$	$\frac{F}{\frac{1}{2}\rho U^2 DL}$
Gap ratio	$g^*$	$\frac{g}{D}$
Reynolds number	Re	$\frac{UD}{\nu}$

where  $C_A$  is the potential flow added mass coefficient ( $C_A = 1.0$  for a circular cylinder), and  $C_{EA}$  is an “effective” added mass coefficient that includes an apparent effect due to the total transverse force in phase with body acceleration ( $C_Y \cos \phi$ ):

$$C_{EA} = \frac{1}{2\pi^3} \frac{C_Y \cos \phi}{A^*} \left( \frac{U^*}{f^*} \right)^2, \quad (7.6)$$

where these non-dimensional groups  $\{A^*, U^*, f^*, C_Y, m^*\}$  are defined in Table 7.1.

The amplitude equation (7.4) above shows the importance of the normalized

fluid excitation ( $C_Y \sin \phi$ ) in determining the amplitude of vibration. For a system in steady state, the fluid excitation is balanced by the energy lost due to structural damping. Thus  $C_Y \sin \phi$  will always be positive, and quite small for a system of low mass-damping. In controlled vibration experiments, the fluid excitation is often measured for a cylinder moving with a prescribed amplitude and frequency, and the above equations are used to make predictions about the free vibration response from these measurements.

### 7.3 Effect of end conditions on free vibration response

In this work we focus on systems with low mass-damping, with a mass ratio of  $m^* = 9.3$ , and a mass-damping of  $(m^* + C_A)\zeta = 0.014$ . We measure the free vibration response of the system, for varying end conditions, keeping all other aspects of the experimental arrangement the same.

#### 7.3.1 Comparison between unattached endplate and no endplate

We are interested here in the classic case where there is an unattached endplate (with  $g^* = 0.04$ ), and we shall compare this condition with having no endplate at all. Employing the endplate, our response shows the typical three branches: initial, upper, and lower (denoted with I, U, and L in Figure 7.3). Without an endplate, two points can be made immediately from Figure 7.3. Firstly, the amplitude decreases continuously, without clear evidence of an upper and lower branch. A consistent trend is found for the frequency response, in that the frequency,  $f^*$  increases gradually, without the characteristic jump in frequency associated with upper and lower response branches. Secondly, despite these dis-

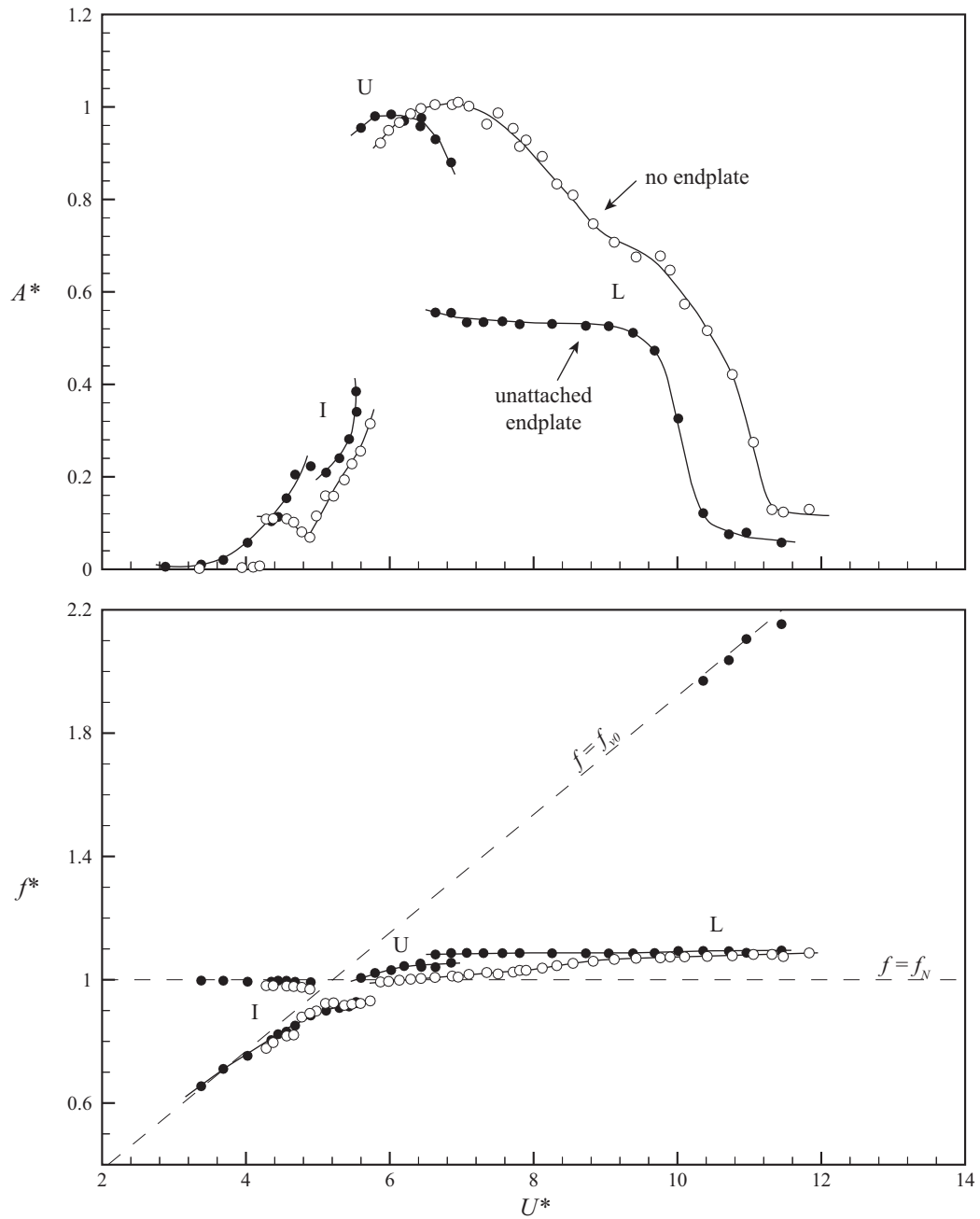


Figure 7.3: Response amplitude ( $A^*$ ) and frequency ( $f^*$ ) as a function of the normalized fluid velocity ( $U^*$ ). Comparison between the unattached endplate case, ( $g^* = 0.04$ ) (●), and the case without an endplate (○). By removing the endplate, the amplitude diminishes continuously from its peak value, without evidence of a distinct upper and lower branch.  $m^* = 9.3$ ,  $(m^* + C_A)\zeta = 0.014$ ,  $\text{Re} = 5,000 - 16,000$ .

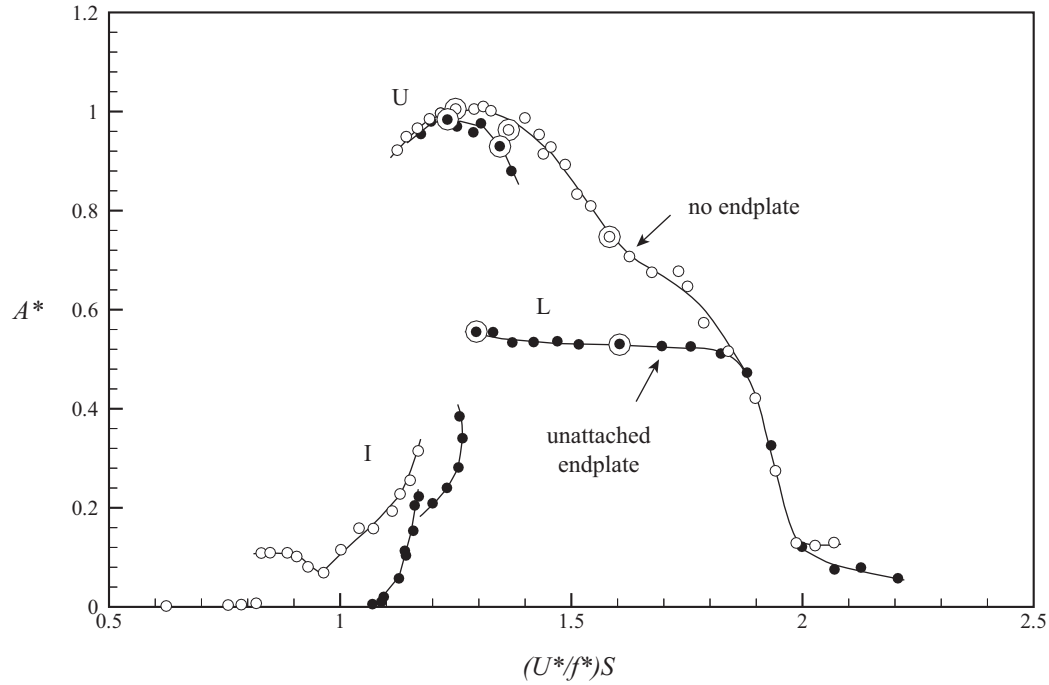


Figure 7.4: Response amplitude ( $A^*$ ) as a function of the normalized fluid velocity ( $(U^*/f^*)S$ ). Comparison between the unattached endplate case, ( $g^* = 0.04$ ) ( $\bullet$ ), and the case without an endplate ( $\circ$ ). The bull's eyes indicate locations of displacement time traces shown in Figure 7.5.

tinct changes in the shape of the amplitude and frequency response, the peak amplitude remains almost precisely the same.

One might note that there is a horizontal shift between the response plots in Figure 7.3, suggesting that some renormalization in the horizontal axis might be considered. A useful normalized velocity is given as  $(U^*/f^*)S$ , where  $S = f_{vo}D/U = \text{Strouhal Number}$  for the non-oscillating body. This is equivalent to the parameter which relates the two most basic frequencies in the problem:  $f_{vo}/f$ , where  $f_{vo} = \text{vortex shedding frequency for the non-oscillating body}$ , and  $f = \text{body oscillation frequency}$ . Because of slight differences in the Strouhal number in the two sets of experiments (see also, Khalak & Williamson, 1996), the renormalized plot appears to line up reasonably in Figure 7.4, in that the peak

amplitudes, and the drop off in response at high  $U^*$ , occur at quite similar velocities. However, there is one major deduction to be made from this plot: over the entire plot, the amplitude level for the case without an endplate is higher, except right at the peak amplitude, where response is essentially the same. Without an endplate, one would expect the vortex shedding to be disrupted by the flow around the end of the span, and for the shedding to be less correlated along the span, with smaller lift forces, and reduced response. One might therefore interpret the higher response in Figure 7.4, when the endplate is removed, as counter-intuitive.

Concerning the upper-lower branch transition, we characterize the response now by observing briefly some typical time traces of body displacement, in Figure 7.5. For the unattached endplate, in the upper branch (Figure 7.5a), the cylinder response shows some significant variation in amplitude, as has typically been found in previous studies (for example, Khalak & Williamson, 1996). At higher normalized velocity  $(U^*/f^*)S = 1.35$ , in the regime of upper-to-lower branch transition, the cylinder response shows an intermittent switching between a higher, but somewhat unsteady amplitude of the upper branch, and a lower but more steady amplitude of the lower branch. At still higher normalized velocity  $(U^*/f^*)S = 1.60$ , in the lower branch, the response becomes quite periodic.

However, by removing the endplate, we were surprised to find that the unsteady amplitude envelope, normally associated with the upper branch, is replaced by a remarkably steady vibration amplitude, shown clearly as  $(U^*/f^*)S$  is increased through 1.25-1.58. Not only is the amplitude level increased generally, without the endplate, as we saw earlier, but the vibrations become much

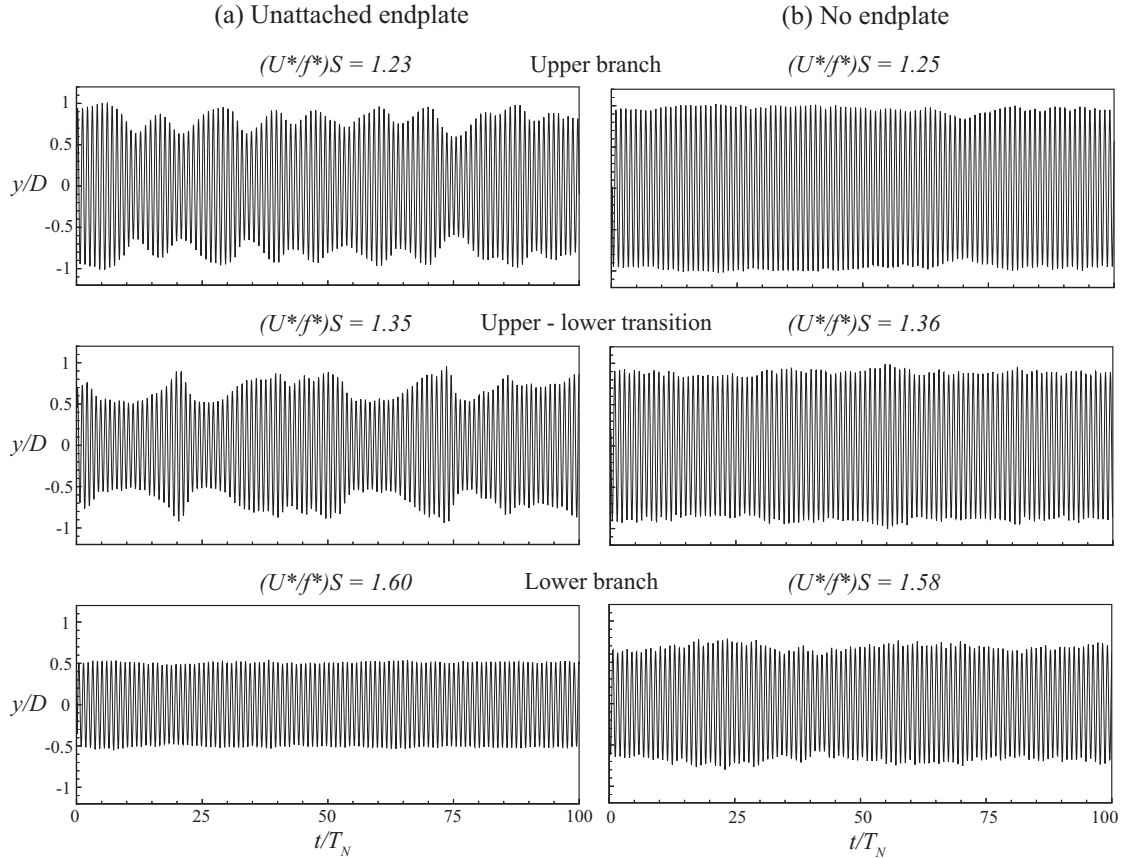


Figure 7.5: Comparison of displacement time traces between the cylinder with an unattached endplate, ( $g^* = 0.04$ ) (a), and a cylinder with no endplate (b). The chosen normalized velocities,  $(U^*/f^*)S$  correspond with the bull's eyes in Figure 7.4. The intermittent switching between the upper and lower branch for the unattached endplate case is replaced by a much more periodic vibration when the endplate is removed.

more steady if the endplate is removed, and the fluid is allowed to flow around the end.

### 7.3.2 Comparison between unattached endplate and attached endplate

In this section we investigate the case where the endplate is attached to the end of the cylinder, since it is a configuration commonly used in previous research

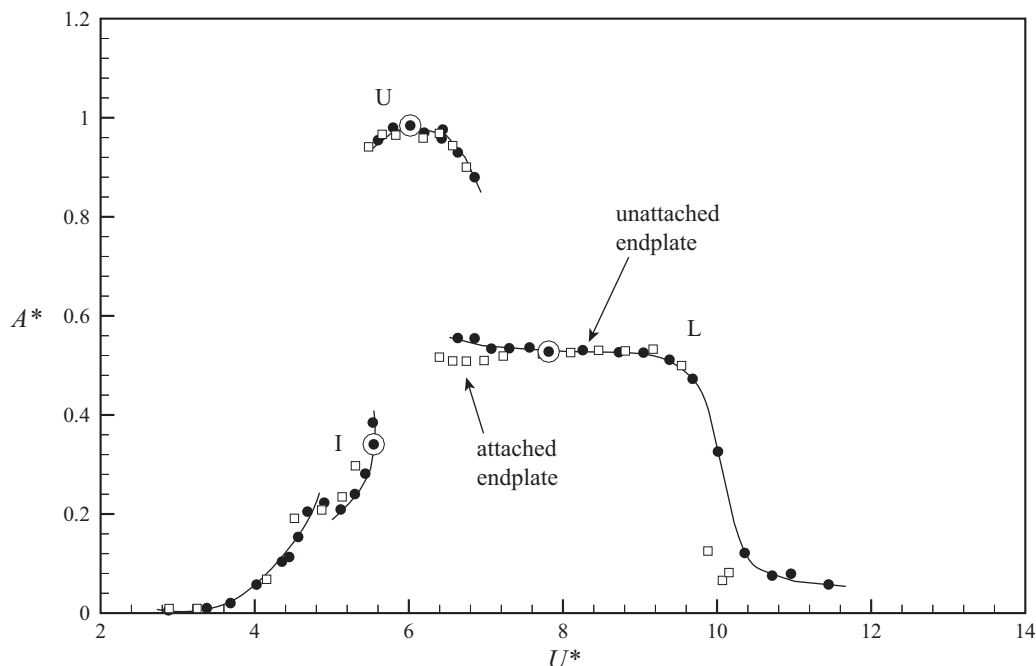


Figure 7.6: Response amplitude ( $A^*$ ) as a function of the normalized fluid velocity ( $U^*$ ). Comparison between the unattached endplate case, ( $g^* = 0.04$ ) ( $\bullet$ ), and attached endplate case ( $\square$ ). The responses are nearly identical for the two cases. Although not shown, the frequency data for the attached endplate case also agrees remarkably well with the unattached endplate case, shown in Figure 7.3. The bull's eyes indicate the cases chosen to exhibit time traces of force in Figures 7.7-7.8.  $m^* = 9.3$ ,  $(m^* + C_A)\zeta = 0.014$ ,  $\text{Re} = 5,000 - 16,000$ .

studies. Our expectation in this case was that there would be distinct differences compared with the case of the unattached endplate. However, there is a strong similarity in both amplitude and frequency response, as shown in Figure 7.6. Furthermore, although not shown here, the time traces of cylinder motion for the two cases were virtually indistinguishable. To emphasize this agreement, it is worth mentioning that the two data sets shown in Figure 7.6 were taken eight years apart; the unattached endplate response was from a set of data taken in 1998 (along with the data that was eventually published in Govardhan & Williamson, 2000), while the attached endplate response was taken in 2006.

Our initial suspicion was that the extra fluid forces on the attached endplate, moving through the fluid with the cylinder, would have some effect to reduce the system response, by adding some “effective” damping. However, we deduce from the results here that any small forces on the endplate must be insignificant compared to the forcing due to the vortex shedding, and secondly that the vortex formation is effectively the same in the presence of an endplate, whether it is moving with the body or fixed with the respect to the laboratory. Finally, on a practical note, we prefer to use the unattached endplate, because changing the test body will not entail each time the addition of a custom endplate, whose surface must be scrutinized to be parallel to the fluid flow.

#### **7.4 Study of end conditions through controlled vibration**

The whole investigation in this study was actually stimulated by the wish to extensively measure fluid forces on a body that is controlled to vibrate in a sinusoidal transverse vibration, at extremely high resolution. This required very small increments of amplitude and frequency (Chapter 3 Morse & Williamson, 2009*b*). Obviously, with such an investment of effort to capture force contour plots, it was imperative to study very precisely the correct experimental conditions, from the outset. It was important to ensure we used the correct end boundary conditions for the oscillating cylinder. Our chosen experimental arrangement for the controlled vibrations is exactly the same as used for the free vibration experiments in §7.3, except the motion was controlled to be strictly sinusoidal. We conducted experiments to match the values of  $A^*$ ,  $U^*/f^*$ , and  $Re$  from the free vibration response (case of an unattached endplate). These particular points in the initial, upper, and lower branches are shown by the bull’s eye

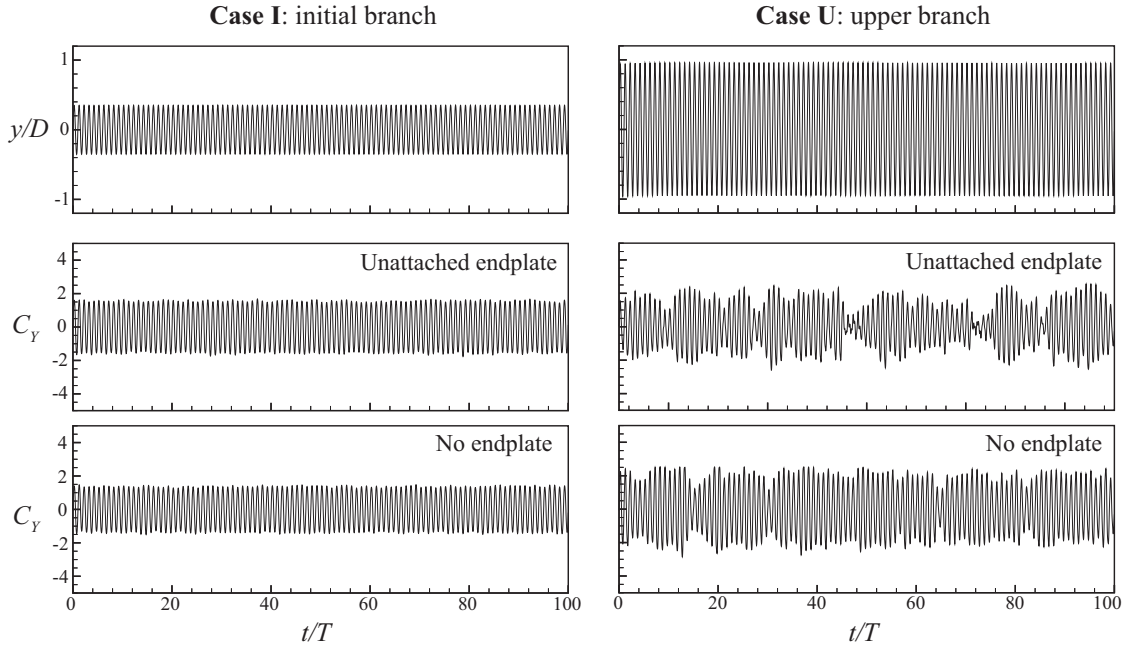


Figure 7.7: Time traces of transverse force ( $C_Y$ ) for an unattached endplate ( $g^* = 0.04$ ), and for no endplate in the initial and upper branches of response. For both end conditions the motion of the cylinder ( $y/D$ ) is controlled to be sinusoidal with  $U^*/f^* = 6.0$ ,  $A^* = 0.34$  in the initial branch, and with  $U^*/f^* = 5.8$ ,  $A^* = 0.98$  in the upper branch.

symbols in Figure 7.6. For each chosen point, we run the controlled vibration either with an unattached endplate or without an endplate, and compare the measured forces.

In the initial branch, the fluid forcing is quite similar for both end conditions, as shown in Figure 7.7. However, as expected, the forces start to exhibit some differences when one studies the upper branch; the maximum level of transverse force is approximately the same for each end condition, but there is more intermittency for the unattached endplate case. This is consistent with the free vibration experiments, where the upper branch is much steadier without an endplate. Nevertheless, prior to any experiments, one would have suspected the endplate would bring more periodicity.

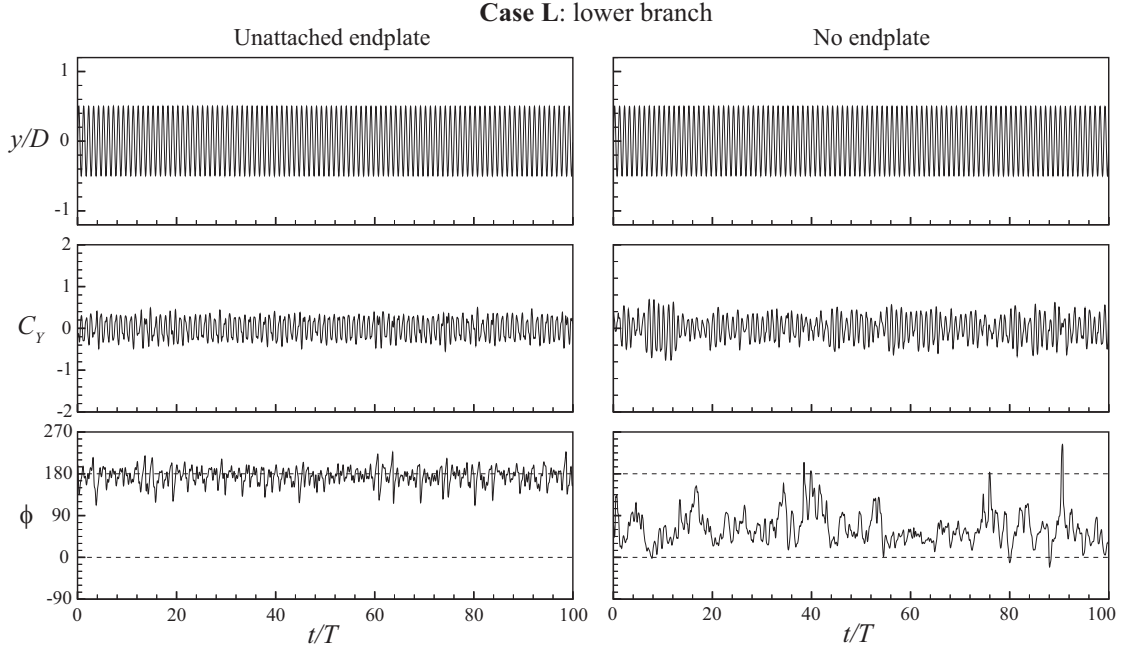


Figure 7.8: Time traces of transverse force ( $C_Y$ ) and phase angle ( $\phi$ ) for an unattached endplate ( $g^* = 0.04$ ), and for no endplate. In both cases the motion of the cylinder ( $y/D$ ) is controlled to be sinusoidal with  $U^*/f^* = 7.2$  and  $A^* = 0.53$ , corresponding to the lower branch.

In the lower branch, there are considerable differences between the two end conditions. For the case with an endplate in Figure 7.8, the fluid force amplitude  $C_Y(t)$  is quite steady. The phase angle,  $\phi$  is just below  $180^\circ$ , yielding a small positive excitation per cycle ( $C_Y \sin \phi$ ) if we were considering free vibration. Without an endplate, the fluid forcing is much less steady, which would lead to the expectation that the response amplitude (if one had free vibration) would drop. However, we find that the phase angle has a mean value of  $63^\circ$ , even though it varies considerably, which would yield a much higher fluid excitation ( $C_Y \sin \phi$ ). In essence, if the cylinder was freely oscillating at the amplitude used here ( $A^* = 0.53$ ) and the endplate was removed, the energy into the system would then be much higher than the energy lost due to damping and the amplitude would increase. This is consistent with results from the free vibration experiments,

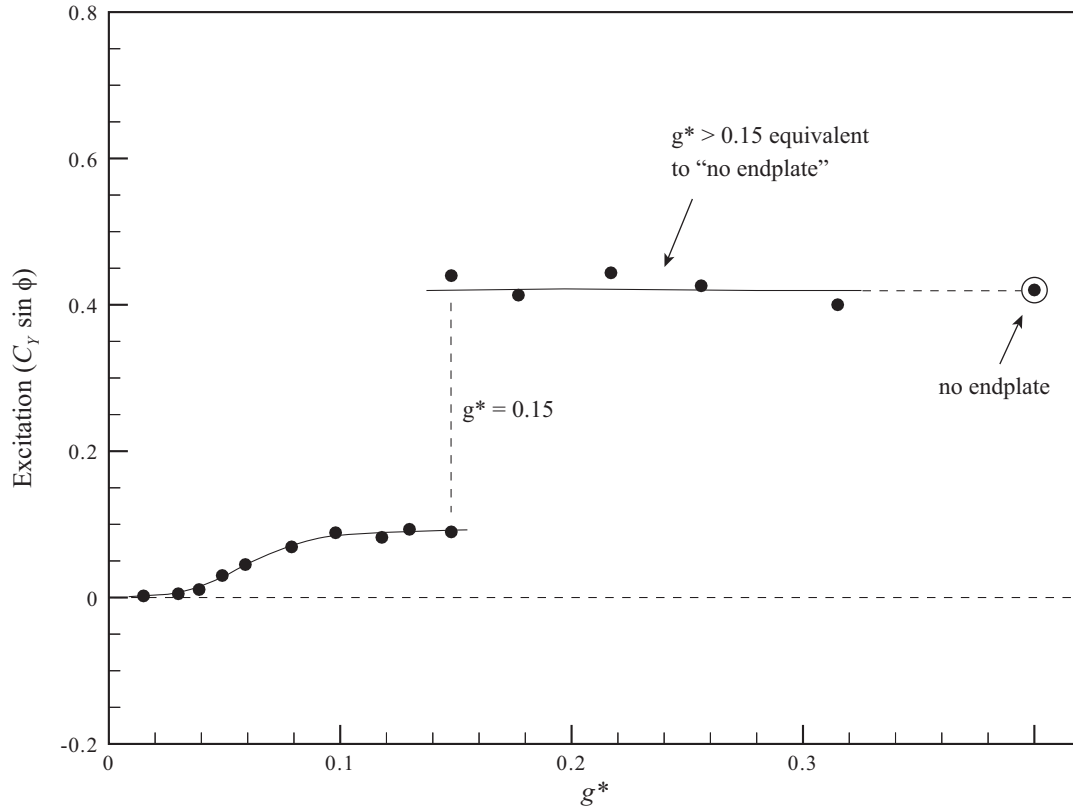


Figure 7.9: The effect of endplate gap ( $g^*$ ) on the fluid excitation ( $C_Y \sin \phi$ ) for a cylinder with an unattached endplate. When the gap ratio is greater than 0.15, the fluid forcing is equivalent to the no endplate case. (At all points the motion of the cylinder is controlled to be sinusoidal with  $U^*/f^* = 7.2$  and  $A^* = 0.53$ , corresponding to the lower branch.)

where the absence of an endplate led to higher amplitudes.

In §7.1, for controlled vibrations using an unattached endplate, we showed from our early study that the fluid forces were significantly influenced by the gap between the bottom of the cylinder and the endplate (Figure 7.1). Of course, one expects that with sufficient gap, the system would respond as though there were no endplate. We study now the effect of varying the endplate gap in the lower response branch, where the effect of end conditions is most pronounced. The variation in fluid excitation ( $C_Y \sin \phi$ ) with gap ratio is shown in Figure 7.9.

For small gap ratios, where the gap is 10-15% of a diameter ( $g^* = 0.1 - 0.15$ ), the excitation is roughly 0.1. However, for larger gaps, where  $g^*$  exceeds 15%, there is a large jump in the fluid excitation up to roughly 0.4, which corresponds well with the case without an endplate (included as the bull's eye in Figure 7.9). This critical gap ratio ( $g^* = 0.15$ ) is a useful result which suggests, for example, that with a 2.5 cm cylinder an endplate gap greater than 4 mm is the equivalent to having no endplate at all.

## **7.5 Comparison with previous investigations employing different end conditions**

A summary of the characteristic low mass-damping free vibration responses for each of the end conditions in this study are presented for clarity in Figure 7.10. One may compare the present results with free vibration responses taken from selected previous investigations, in Figure 7.11. Cases where attached endplates are used (Moe & Overvik, 1982; Owen *et al.*, 2001) exhibit good correspondence with our cases of unattached and attached endplates, showing three distinct response branches. On the other hand, Klamo (2007) did not use endplates in his experimental arrangement. His smallest gap with  $g^* = 0.4$  should yield similar results to our case without an endplate, based on the results of our gap study (Figure 7.9), and indeed the comparison of the character of the response plot is good. The response plot shows a gradual decrease in amplitude from the peak, rather than a distinct upper and lower branch. This type of response can be found in several other previous studies in the literature, and it remains possible that such responses are influenced by the end conditions, as shown in

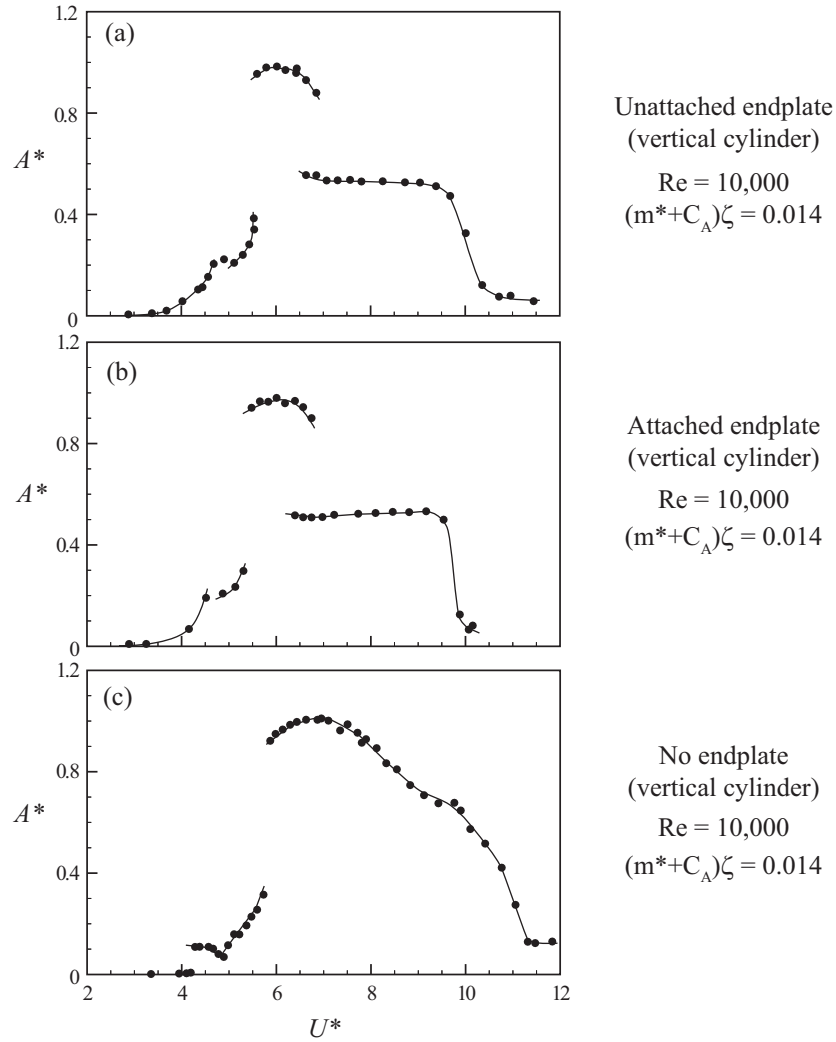


Figure 7.10: A summary of the amplitude responses for each of the end conditions studied here: (a) unattached endplate, (b) attached endplate, (c) no endplate.

the present work.

In studies that did not employ endplates, the investigators generally took care in placing the bottom of the cylinder close to the channel floor (for example, Branković & Bearman, 2006). If the gap ratio is small enough ( $g^* < 0.15$ ) we might expect that this end condition will yield a response that is similar to the case of an unattached endplate, as the two end conditions are quite similar.

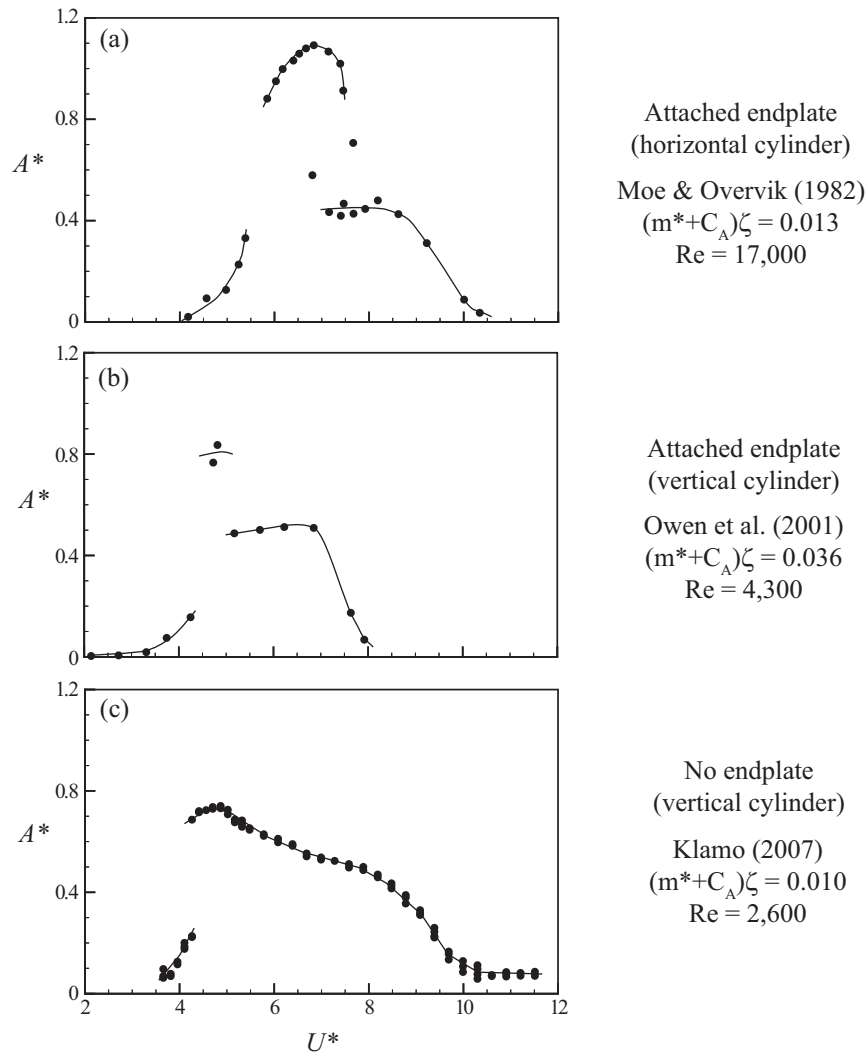


Figure 7.11: Comparison among several previous vortex-induced vibration studies of the amplitude ( $A^*$ ) response as a function of normalized velocity ( $U^*$ ): (a) Moe & Overvik (1982), (b) Owen *et al.* (2001), (c) Klamo (2007).

However, the experiment relies on the properties of the boundary layer on the channel floor which would depend on the channel construction (for example, the streamwise length of the boundary layer, or the existence of seams joining sections of the facility). Thus the boundary layer could be quite unsteady, and would certainly vary from one facility to the next, making comparisons difficult.

## 7.6 Conclusions

In this study, we investigate the effect of end conditions on the transverse vortex-induced vibration response of a circular cylinder with low mass-damping. While we are able to vary the conditions at the lower end of a vertical cylinder in our water channel, all other aspects of the experimental arrangement are kept constant.

The case of an attached endplate, and the case of an unattached endplate, show nearly identical free vibration responses, although having an unattached endplate is simpler to arrange accurately, on a practical basis. However, the condition without an endplate shows significant differences. We expected, prior to this study, that removing an endplate would lead to increased fluid flow around the end of the cylinder, a reduction in spanwise vortex shedding correlation and fluid force correlation, and thereby to a reduced response amplitude. Quite contrary to this expectation, the absence of an endplate leads to significantly higher levels of excitation, leading to higher amplitudes over the entire amplitude response plot, except where both sets of data reach the same maximum amplitude. The increased excitation ( $C_Y \sin \phi$ ) is principally due to a shift in the phase of the fluid force (relative to body motion). Essentially, the case without an endplate yields roughly the same peak amplitude response when compared to both cases with the endplates. The general character of the response is modified if the endplate is removed; the response amplitude diminishes continuously as velocity is increased beyond the value for peak amplitude, and there is no apparent jump between upper branch and lower branch modes.

Under conditions of controlled vibration, we also study the effect of varying

the gap between an endplate and the bottom of the cylinder. For gaps larger than 15% of a diameter, we find a jump increase in the fluid excitation. Under these conditions, the force and response dynamics become equivalent to removing the endplate altogether. For smaller gaps,  $g^* < 15\%$ , one is effectively investigating the case of an attached or unattached endplate.

The character of response plots, in previous studies, correspond reasonably well with the character of the different responses found here, if one compares cases with similar end conditions. There are, of course, other aspects of the experimental arrangement besides end conditions, such as Reynolds numbers, turbulence levels, techniques of measurement, more degrees of freedom, and spanwise variations, that would lead to differences in the response character, but we suggest that end conditions should be taken into account as influencing quite significantly the character of a response plot. It is, however, interesting that the peak amplitude response is not strongly influenced by the end conditions, at least based on the present results.

## APPENDIX A

### Additional fluid forcing contours

In §3.3 we showed contours of  $C_Y \sin \phi$  and  $C_Y \cos \phi$ . Here we present contour plots of the total force,  $C_Y$ , and vortex force,  $C_V$ , in Figure A.1, as well as the total phase,  $\phi$ , and vortex phase,  $\phi_V$ , in Figure A.2. The different regimes of vortex shedding are perhaps most easily characterized by the phase angle in Figure A.2. When transitioning from the 2S mode to the 2P<sub>O</sub> mode, there is no strong jump in total phase, however there is a large jump of about 180° in the vortex phase. When transitioning from the 2P<sub>O</sub> mode to the 2P mode, the large jump occurs in the total phase, with only a small change in the vortex phase (since the basic vortex shedding mode is not varying).

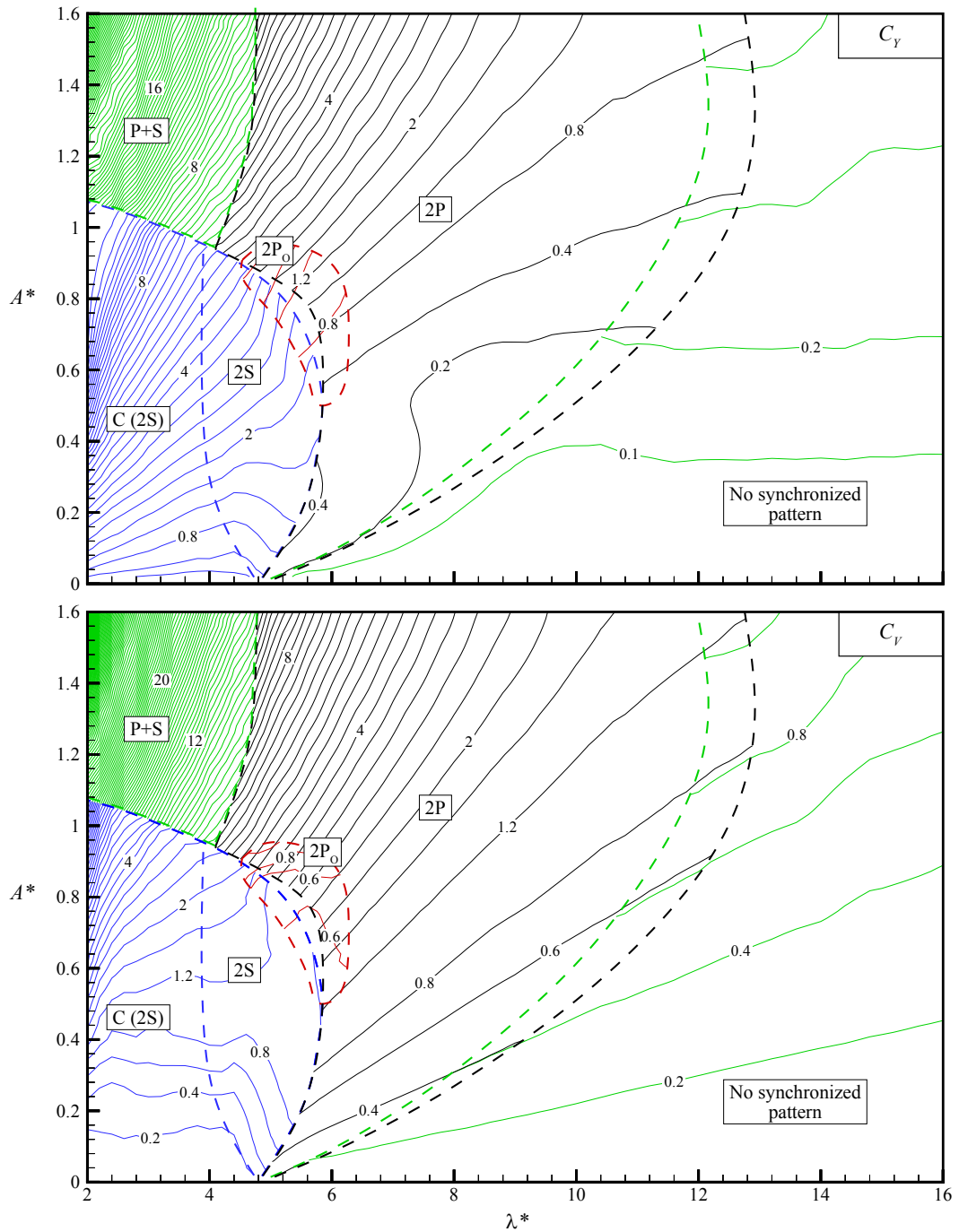


Figure A.1: Contours of the magnitude of the total force,  $C_Y$ , and the vortex force,  $C_V$  at  $Re = 4,000$ . Boundaries between modes are indicated by dashed lines. Contour interval in both cases is 0.4 with additional contours for very low forcing.

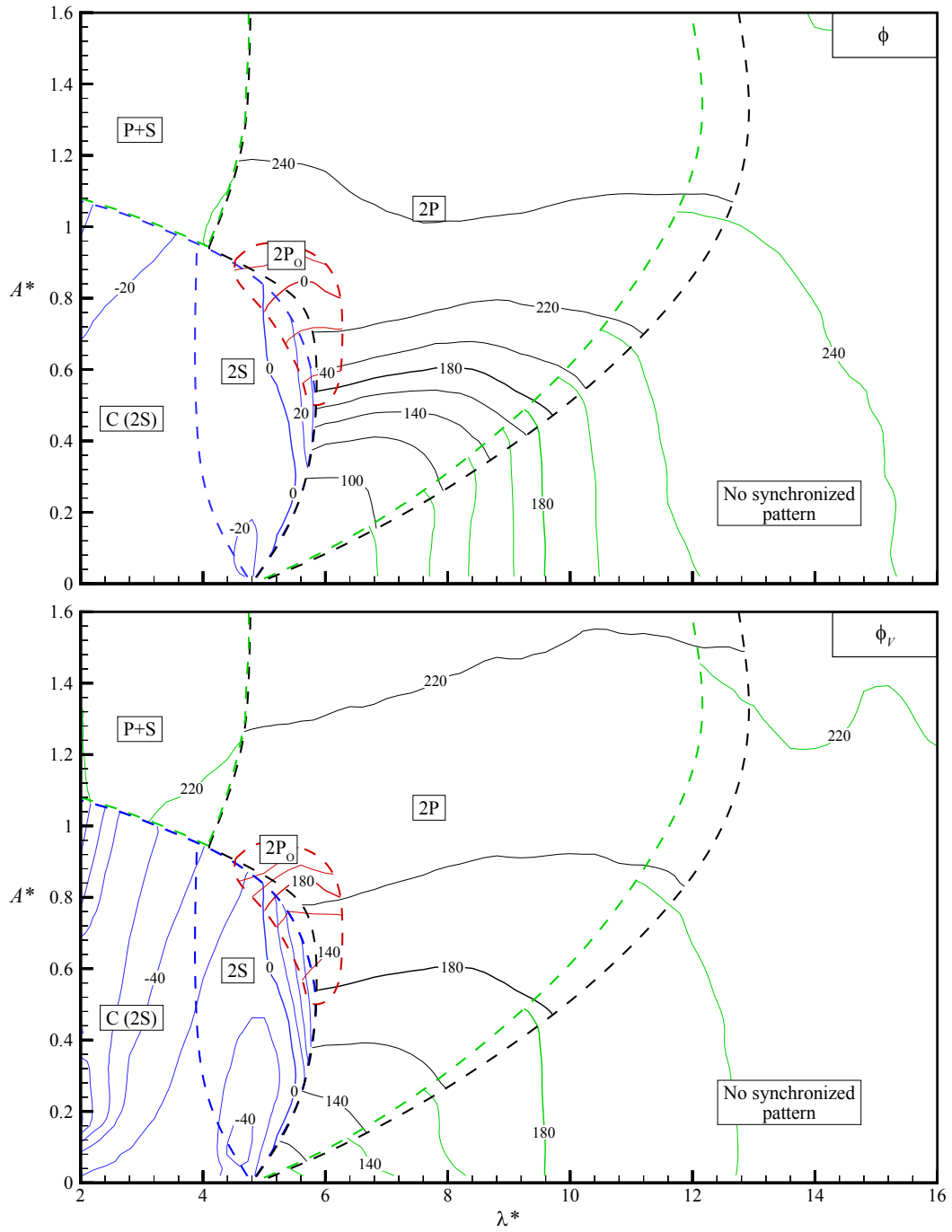


Figure A.2: Contours of the total phase,  $\phi$ , and the vortex phase,  $\phi_V$ , at  $\text{Re} = 4,000$ . Boundaries between modes are indicated by dashed lines. Contour interval in both cases is  $20^\circ$ .

## APPENDIX B

### **The effect of Reynolds number on fluid force contours and prediction of the modified “Griffin plot”**

A basic question one might ask is how dependant are the fluid forcing contours in the amplitude-wavelength plane on the value of Reynolds number used for the plot. We have conducted another complete set of experiments to obtain force contours at  $Re = 12,000$ . We present as an example, in Figure B.1, contours of the fluid excitation ( $C_Y \sin \phi$ ). Interestingly, the same fluid forcing regimes are found for the  $Re = 12,000$  case as we found here for  $Re = 4,000$ , including the  $2P_O$  mode. The general shape of the fluid excitation contours is also quite similar, suggesting that the same general conclusions made in the present study remain valid over a whole range of Reynolds number. One should note that we are not in a position to observe the P+S regime, because the high amplitude, low wavelength (high frequency) region of the amplitude-wavelength plot (top left corner) exceed the limits of our facilities at this  $Re$ . The major effect of increased  $Re$  appears to be a vertical stretching of the 2S and  $2P_O$  regimes. The zero excitation contour in the  $2P_O$  regime has a distinctly higher amplitude. This means that one expects a higher peak amplitude response for very small (or zero) damping, as Reynolds number is increased. On the other hand, the location of the zero excitation contour for the 2P region, in the amplitude-wavelength plane, remains virtually unchanged as Reynolds number is increased.

It is interesting that, in fact, our controlled vibration contours at  $Re = 4,000$  and  $12,000$  can also be used to predict the peak amplitude vibration response as

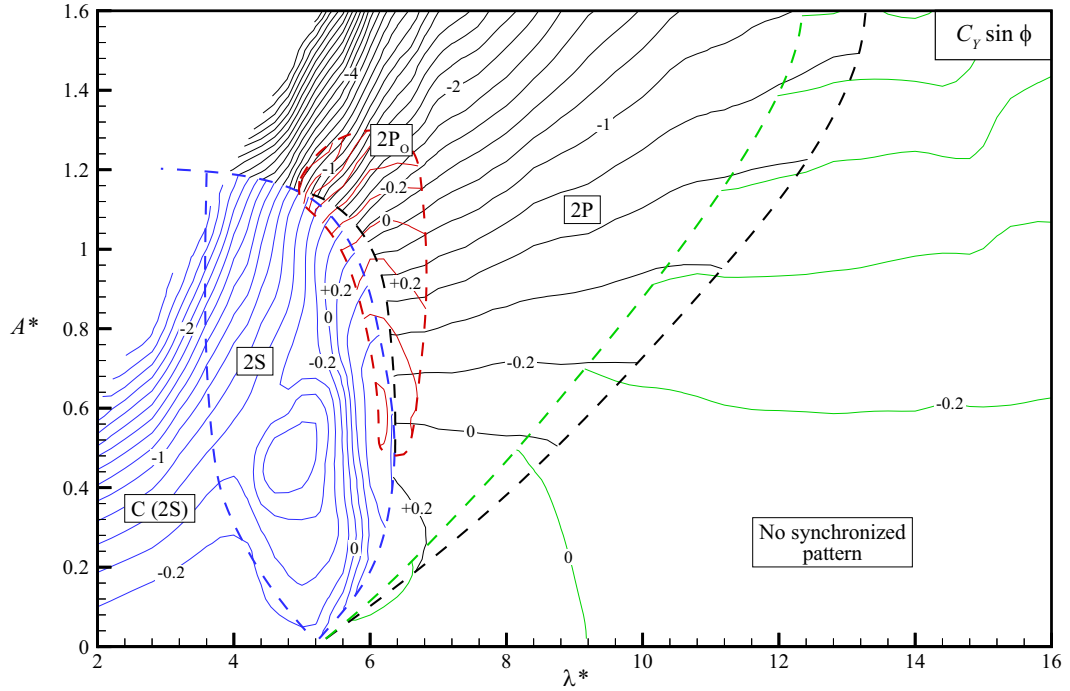


Figure B.1: Contours of the force in phase with velocity,  $C_Y \sin \phi$  (normalized “fluid excitation”), for  $Re = 12,000$ . Boundaries between modes are indicated by dashed lines. We could not obtain data in the upper left corner due to the limits of our facilities. Contour interval is 0.2

a function of mass-damping, in what is called a “modified Griffin” plot. Such a plot, which was presented by Govardhan & Williamson (2006), shows the effect mass-damping, as well as Reynolds number, on the peak amplitude response in free vibration, and involves a collapse of such extensive data into a single curve. Here we choose to plot the two Reynolds numbers separately to indicate the effect of Reynolds number more directly. We can compute these data as curves in Figure B.2(a), using the approach of §4.5.

For both Reynolds numbers, the controlled vibration contours yield good agreement with the empirical formula, taking into account mass-damping as well as Reynolds number, deduced by Govardhan & Williamson:

$$A^* = (1 - 1.2\alpha + 0.30\alpha^2) \log(0.41Re^{0.36}). \quad (\text{B.1})$$

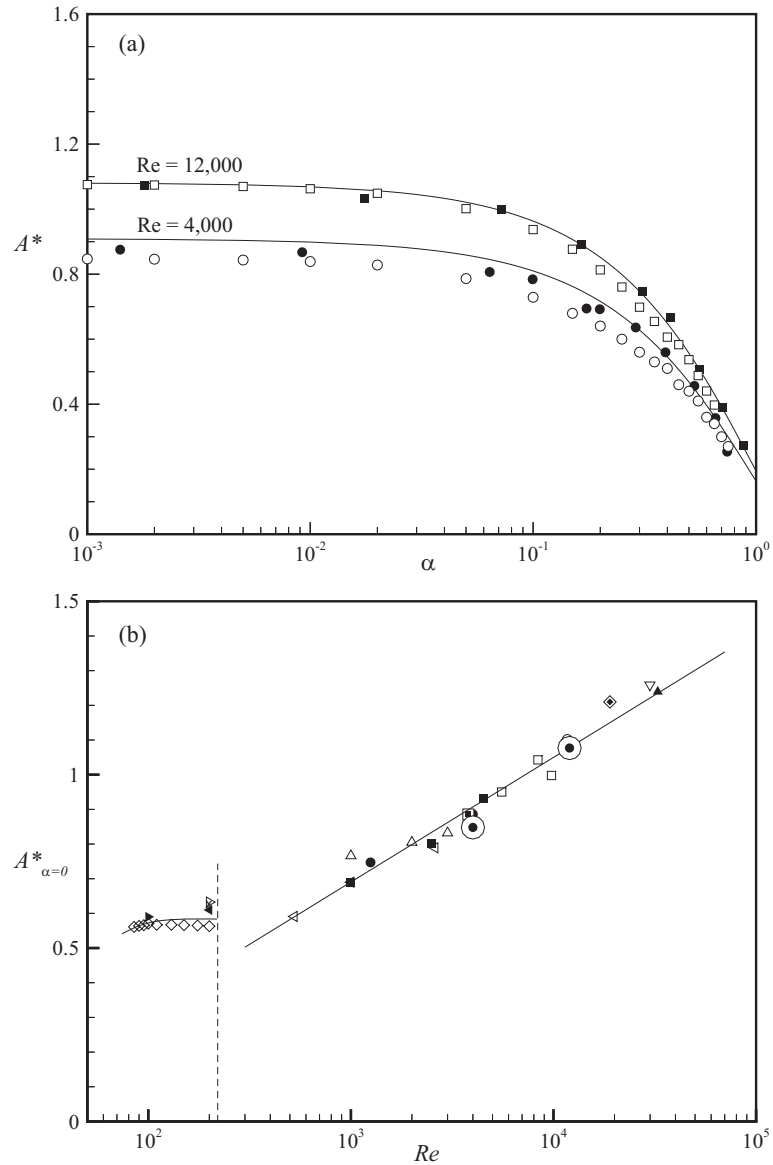


Figure B.2: (a) The “Griffin” plot of peak amplitude vs. mass-damping,  $\alpha$ .  $\bullet$   $Re = 4,000$ ,  $\blacksquare$   $Re = 12,000$ , free vibration results from Govardhan & Williamson (2006).  $\circ$   $Re = 4,000$ ,  $\square$   $Re = 12,000$  predicted peak amplitude from present controlled vibration data. The lines indicate the best-fit for a range of experiments, deduced by Govardhan & Williamson (2006):  $A^* = (1 - 1.2\alpha + 0.30\alpha^2) \log(0.41Re^{0.36})$ . (b) Peak amplitude at zero mass-damping vs.  $Re$  for a wide range of experiments, taken from Govardhan & Williamson (2006), symbols are given in Table 3 of that paper (not reproduced here).  $\odot$  our present predictions from controlled vibration.

The predicted peak amplitude is slightly lower than the measured free vibration amplitude for the  $Re = 4,000$  case, but the shape of the trend is well predicted. The agreement with free vibration peak amplitude data at  $Re = 12,000$  appears to be good. We also find the location, in our amplitude-wavelength plane, where the excitation energy ( $C_Y \sin \phi$ ) is zero, for both  $Re=4,000$  and  $12,000$ . These values predict the peak response amplitude, which could be found in free vibration, if the damping is brought to zero. A subsequent inclusion of our data onto the plot of peak response (for zero damping) as a function of Reynolds number, compiled for free vibration experiments by Govardhan & Williamson:

$$A_{PEAK}^* = \log(0.41Re^{0.36}), \quad (\text{B.2})$$

is shown in Figure B.2(b), indicating good agreement.

## APPENDIX C

### **Complete vorticity fields for each major vortex formation mode**

In the previous sections we showed several snapshots of the vorticity fields at particular phases of oscillation to illustrate the different modes of vortex formation and how they relate to the character of the fluid forcing. For completeness, here we show complete vorticity fields at four phases of oscillation for each of the major vortex formation modes at  $Re = 4,000$ :  $\{2S, P+S, 2P_O, 2P\}$  (Figures C.1 – C.6).

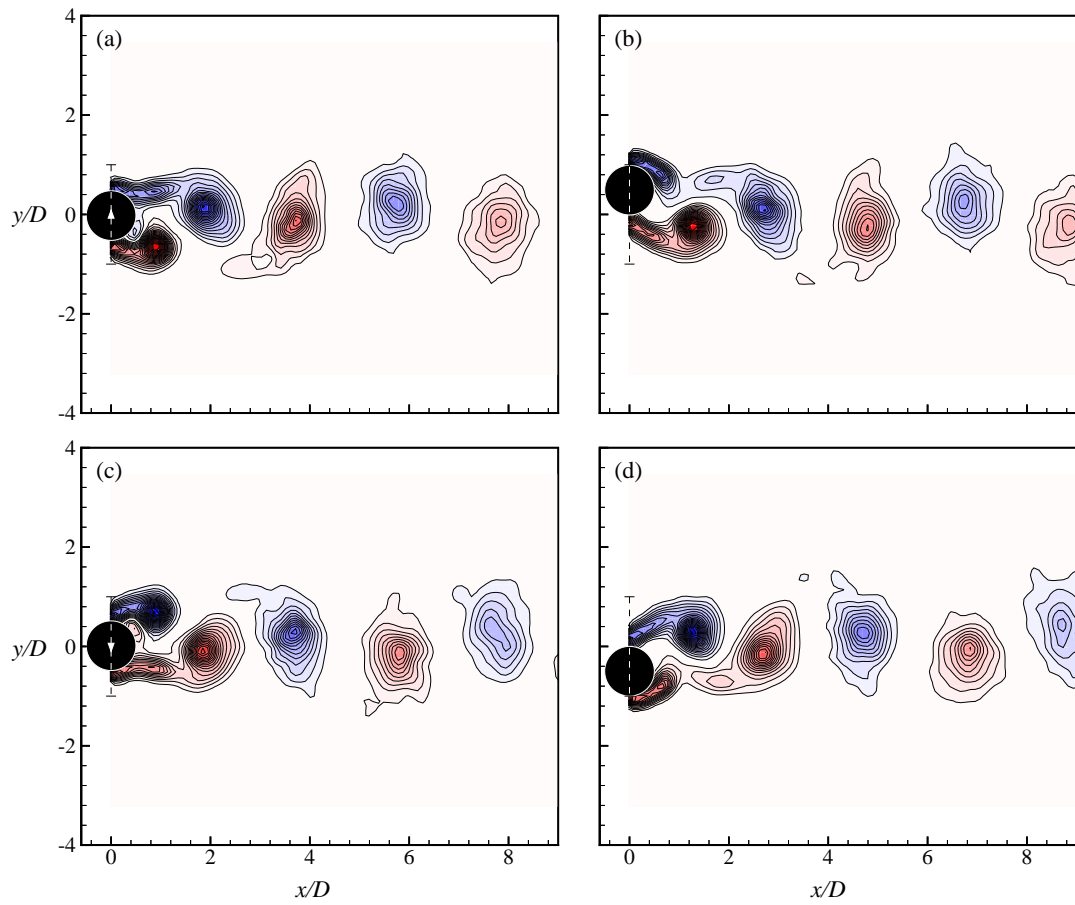


Figure C.1: Vorticity fields for the 2S mode of vortex formation ( $A^* = 0.5$ ,  $\lambda^* = 5.0$ ), phase-averaged over 20 cycles of oscillation. Contour levels shown are:  $\omega D/U = \pm 0.4, \pm 0.8, \pm 1.2, \dots$

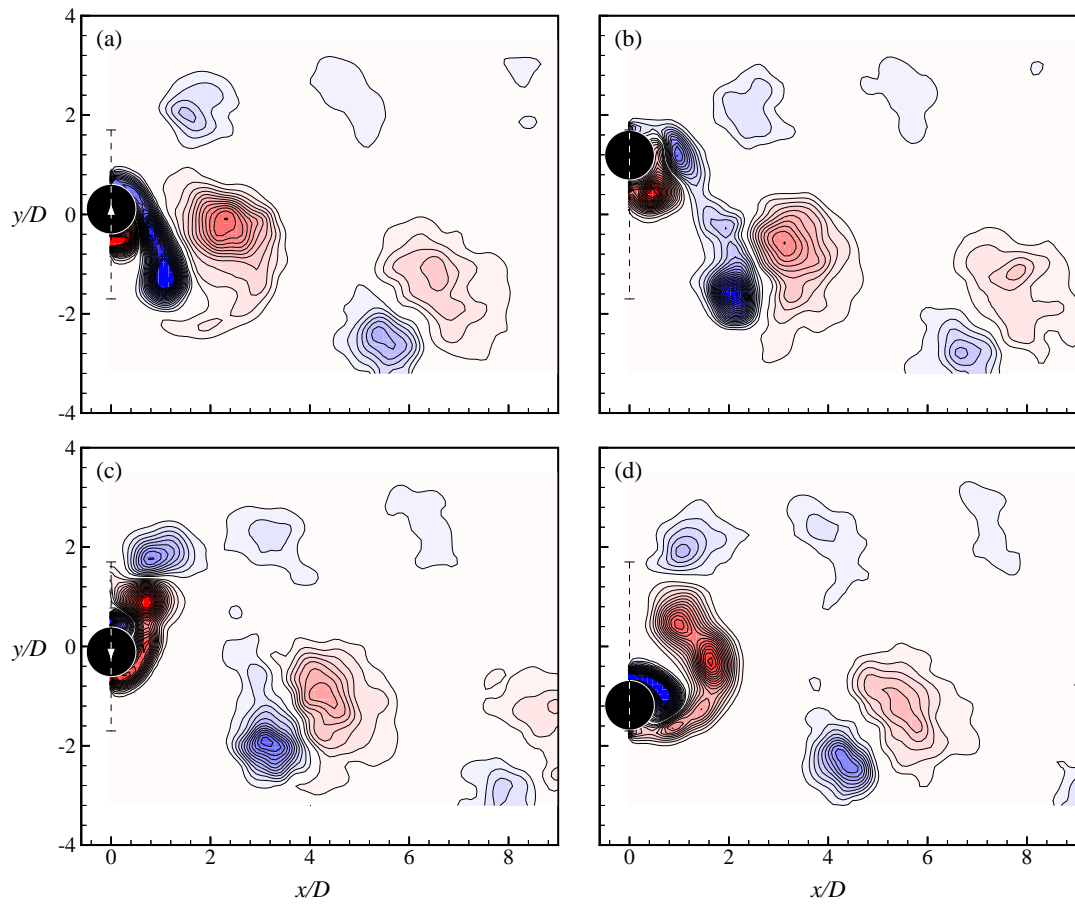


Figure C.2: Vorticity fields for the P+S mode of vortex formation ( $A^* = 1.2$ ,  $\lambda^* = 4.0$ ), phase-averaged over 20 cycles of oscillation. Contour levels shown are:  $\omega D/U = \pm 0.4, \pm 0.8, \pm 1.2, \dots$

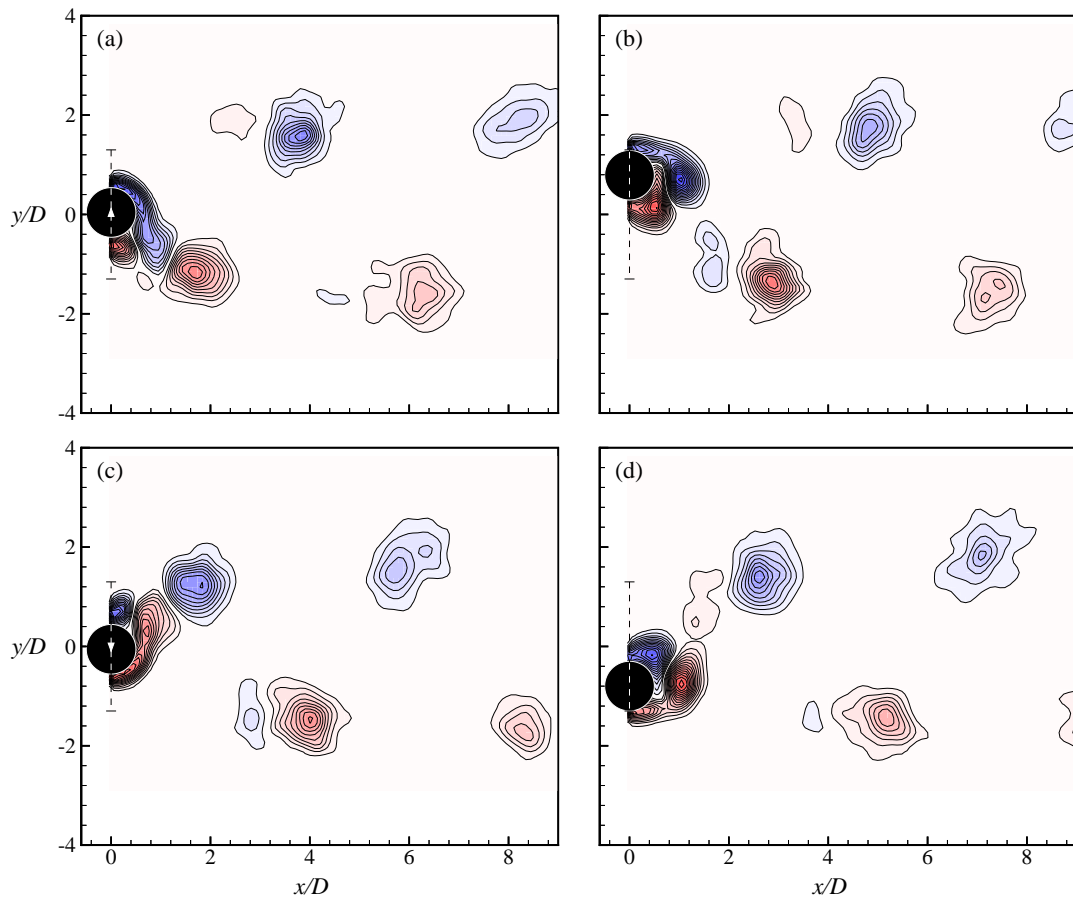


Figure C.3: Vorticity fields for the  $2P_O$  mode of vortex formation in the  $2P_O$ - $2P$  overlap region ( $A^* = 0.8, \lambda^* = 5.6$ ), phase-averaged over 10 cycles of oscillation. Contour levels shown are:  $\omega D/U = \pm 0.4, \pm 0.8, \pm 1.2, \dots$

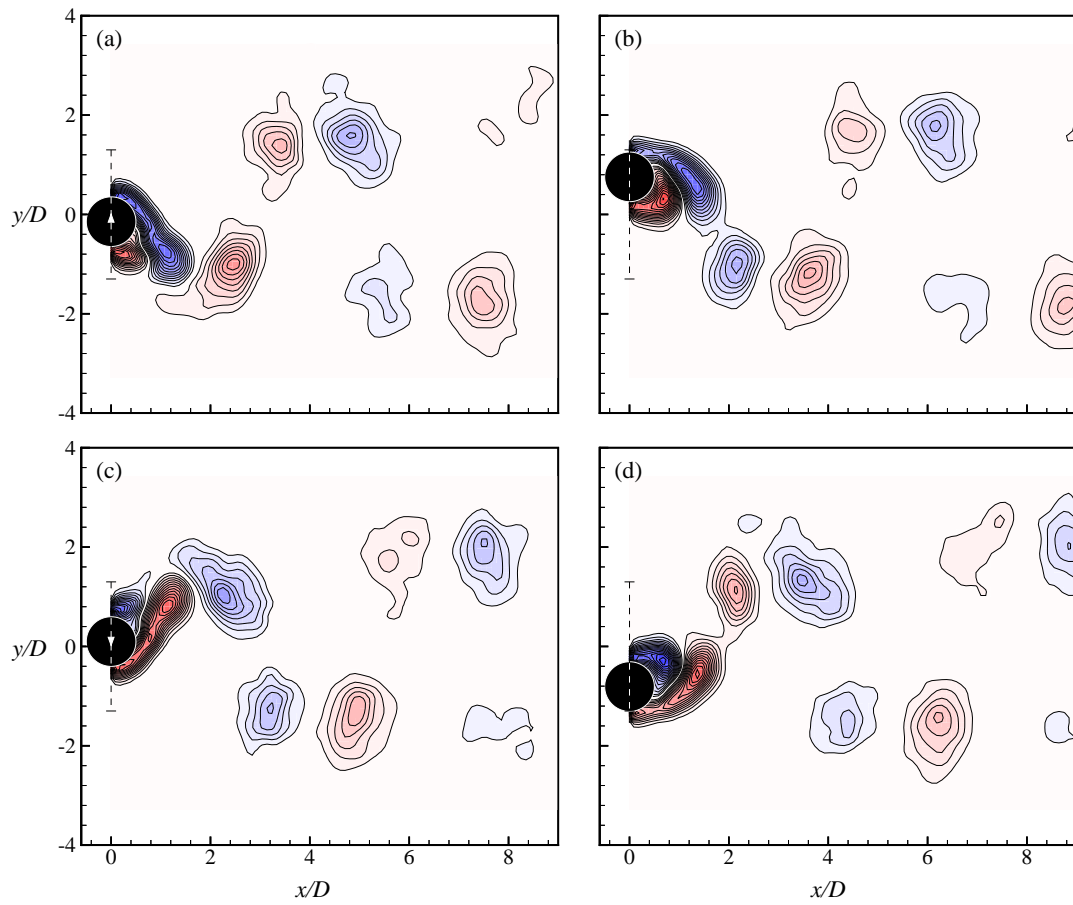


Figure C.4: Vorticity fields for the 2P mode of vortex formation in the  $2P_O$ -2P overlap region ( $A^* = 0.8$ ,  $\lambda^* = 5.6$ ), phase-averaged over 10 cycles of oscillation. Contour levels shown are:  $\omega D/U = \pm 0.4, \pm 0.8, \pm 1.2, \dots$

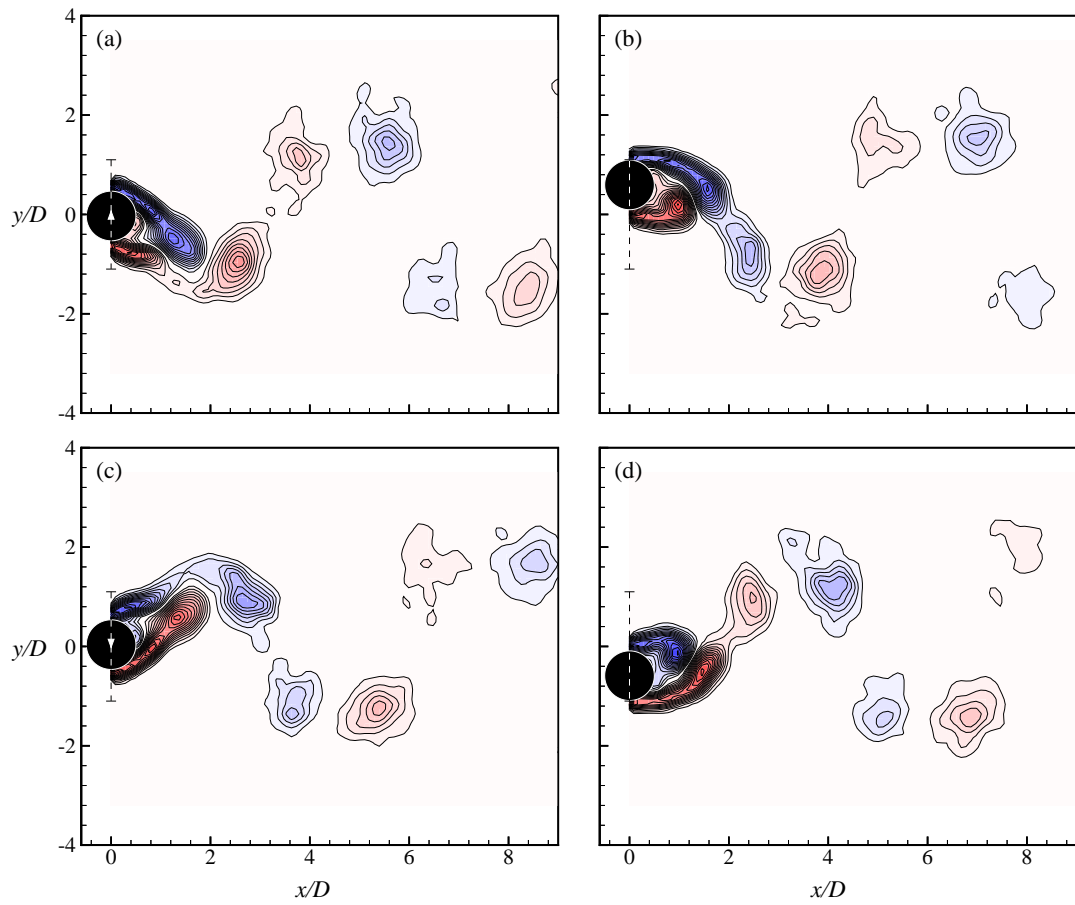


Figure C.5: Vorticity fields for the 2P mode of vortex formation ( $A^* = 0.6$ ,  $\lambda^* = 6.4$ ), phase-averaged over 20 cycles of oscillation. Contour levels shown are:  $\omega D/U = \pm 0.4, \pm 0.8, \pm 1.2, \dots$

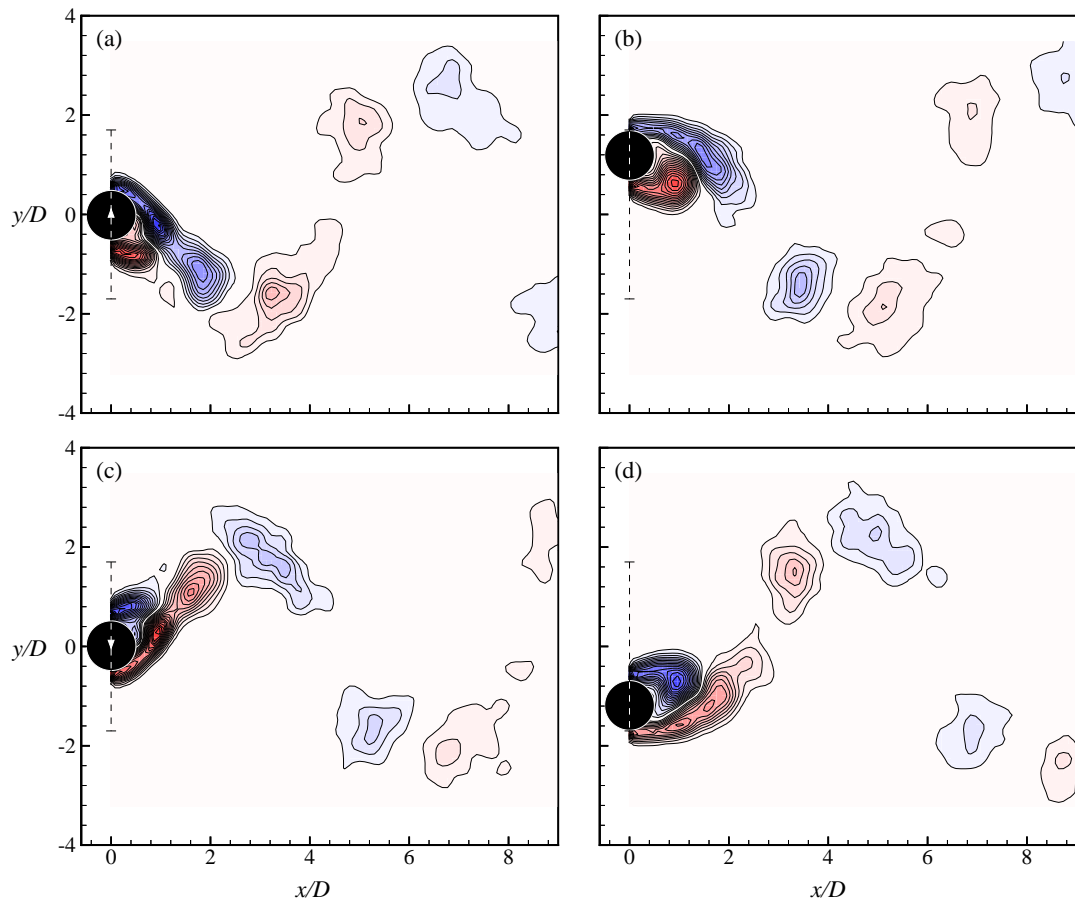


Figure C.6: Vorticity fields for the 2P mode of vortex formation ( $A^* = 1.2$ ,  $\lambda^* = 8.0$ ), phase-averaged over 20 cycles of oscillation. Contour levels shown are:  $\omega D/U = \pm 0.4, \pm 0.8, \pm 1.2, \dots$

## APPENDIX D

### **The effect of fluid forcing at frequencies above the fundamental oscillation frequency**

Our analysis throughout this study has assumed that the fluid force is well represented by a sinusoidal function. Thus we could extract the component of force at the fundamental (body oscillation) frequency and use it effectively to predict a free vibration response.

In most cases, the force is in fact quite sinusoidal. However, in the region where the wake is desynchronized from the cylinder oscillation, the force is distinctly not sinusoidal, having one component at the body oscillation frequency, and a generally larger component at the vortex shedding frequency, as shown in Figure D.1. At first glance, we would expect that because of the strongly non-sinusoidal nature of the forcing, the free vibration motion would also not be sinusoidal in this regime. Thus, we would not expect our sinusoidal controlled vibration data to be successful in predicting the response.

However, if we look at an actual free vibration time trace at the high normalized velocity end of response, in the desynchronized regime, shown in Figure D.2, we see that although the fluid forcing includes components at multiple frequencies, the cylinder motion is quite sinusoidal, having only one dominant frequency. Indeed we can see that the large peaks in the force spectra at the higher frequencies have only a very weak effect on the displacement spectra, yielding only very small bumps. This phenomena can be understood by looking at the equation of motion in the correct manner.

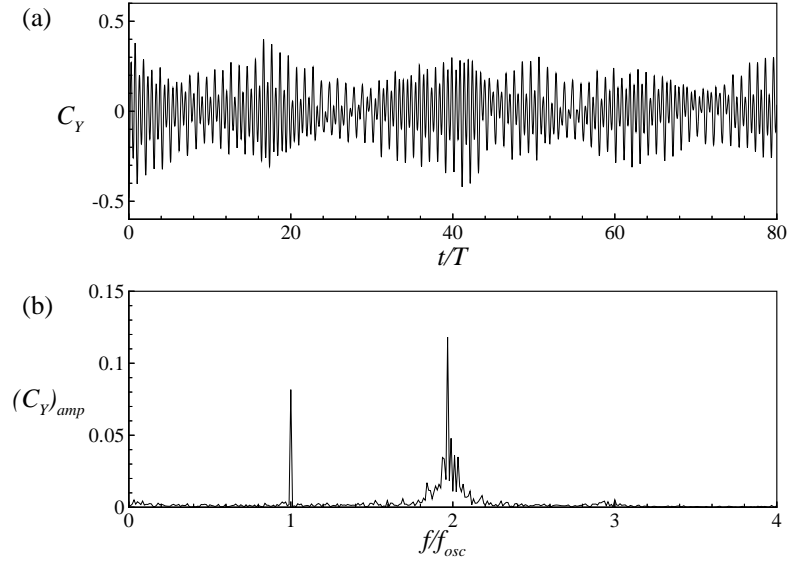


Figure D.1: Time trace (a) and spectrum (b) of the fluid force for a controlled vibration run at  $A^* = 0.3$ ,  $\lambda^* = 9.4$ . The fluid forcing shows components at the body oscillation frequency and the vortex shedding frequency

As shown previously in §4.5, by assuming a sinusoidal form of the equation of motion, we can obtain the amplitude and frequency equations, reproduced here:

$$A^* = \frac{1}{4\pi^3} \frac{C_Y \sin \phi}{(m^* + C_A) \zeta} \left( \frac{U^*}{f^*} \right)^2 f^*, \quad (\text{D.1})$$

$$f^* = \sqrt{\frac{m^* + C_A}{m^* + C_{EA}}}, \quad (\text{D.2})$$

These equations are useful for understanding the relationship between the structural parameters, the fluid forces, and the body motion. However, if we want to predict the force time trace or spectra from the displacement time trace or spectra (or vice versa) the following formulation is more useful:

$$\tan \phi = \frac{2(m^* + C_A) \zeta f^*}{m^* (1 - f^{*2}) + C_A} \quad (\text{D.3})$$

$$A^* = C_Y \frac{U^{*2}/2\pi^3}{\sqrt{(2(m^* + C_A) \zeta f^*)^2 + (m^* (1 - f^{*2}) + C_A)^2}} \quad (\text{D.4})$$

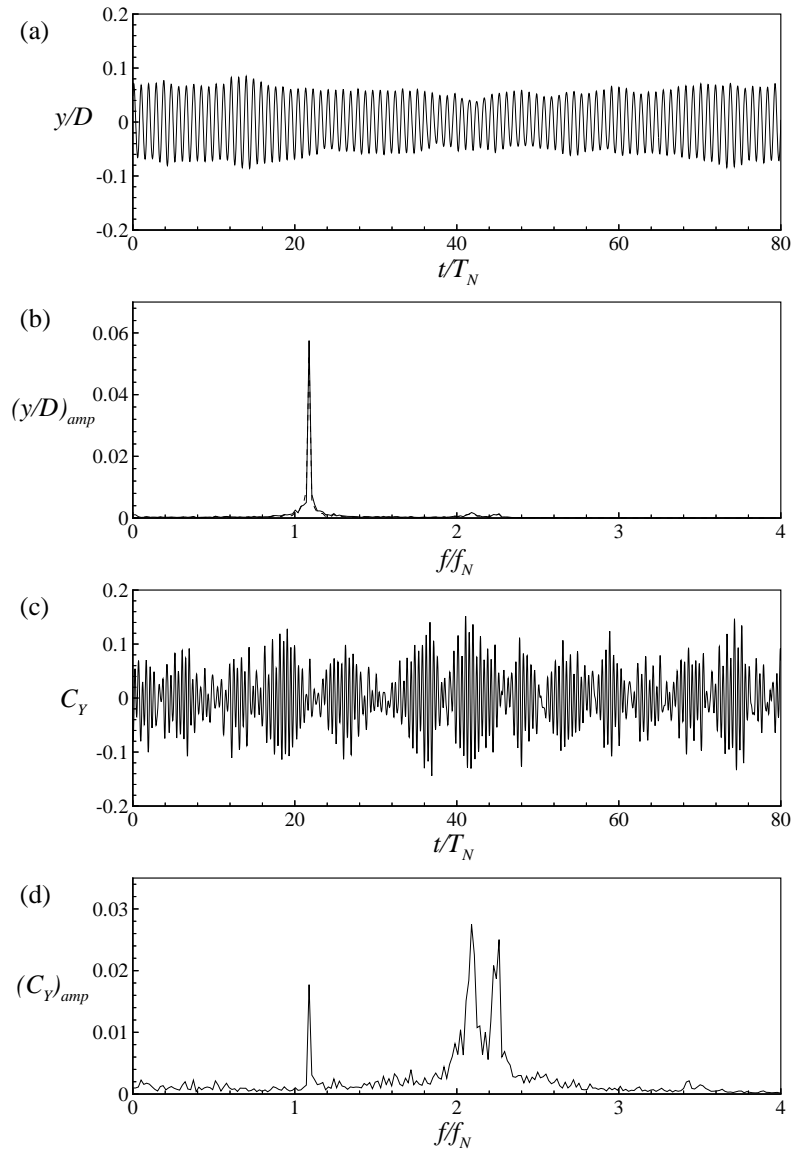


Figure D.2: Time trace and spectra of the displacement and fluid force for a free vibration run in the desynchronized regime,  $U^* = 10.54$ . In (b) we show the measured displacement spectrum (—) as well as a predicted displacement spectrum, obtained from the force spectrum and equation (D.4) (- -), which is nearly indistinguishable from the measured spectrum.

Note that these same equations can be found in standard vibrations textbooks, we have simply non-dimensionalized them appropriately for vortex-induced vibration.

Since the system obeys a linear equation of motion, the different components of a multi-frequency response are independent and can be analyzed separately. Thus, equations (D.3) and (D.4) hold for each component of the force and displacement:  $\{A_N^*, f_N^*, C_{YN}, \phi_N\}$ . As an example, we use equation (D.4) to calculate the displacement spectra from the force spectra for the free vibration run shown in Figure D.2. We find that this predicted spectra is nearly identical to the measured spectra, indicating that these equations can be applied successfully (i.e. the system behaves linearly and the data was carefully collected).

We also can see from equation (D.4) that the parameter  $f^*$  has a large effect on the degree to which fluid forcing is transmitted to the cylinder motion: the further  $f^*$  is from 1 (i.e. the further the forcing frequency is from the natural frequency), the lower the effect on displacement. This is of course a standard result from basic vibration analysis but it explains why the components of the fluid forcing at higher frequencies have a strongly reduced effect on the cylinder motion.

Now we would like to apply a similar analysis to the controlled vibration data. We will use the controlled vibration run shown in Figure D.1 at  $A^* = 0.30$ ,  $\lambda^*$  or  $U^*/f^* = 9.40$ .

The first step is to calculate the structural parameters that would yield a sinusoidal free vibration response that is in equilibrium with the the fluid forcing at the oscillation frequency. If we assume a system with mass ratio,  $m^* = 10$ , we

find, using equations (D.1) and (D.2) that the damping ratio,  $\zeta$  must be 0.0052 and the normalized velocity,  $U^*$  must be 10.03. These are the system parameters which will yield sinusoidal vibration at  $A^* = 0.30$ ,  $U^*/f^* = 9.40$  (if we take only the force component at the oscillation frequency).

Now we will add in the effect of the fluid forcing at the higher vortex shedding frequency. To do this we use equations (D.3) and (D.4) to determine the amplitude and phase of the cylinder displacement due to the component of fluid forcing at the vortex shedding frequency. If we now add this component of the cylinder motion to the original sinusoidal motion at  $A^* = 0.30$ ,  $U^*/f^* = 9.40$ , we obtain the free vibration motion that is in steady state equilibrium with the fluid forcing.

Of course the fluid forcing shown in Figure D.1 was obtained for purely sinusoidal motion. Now that we have added in a second component, can we expect the motion to yield the same fluid forcing? If we compare the displacement in the two cases, with and without the added component at the vortex shedding frequency, shown in Figure D.3, we see that they are nearly identical. Thus adding the vortex shedding frequency component would not be expected to change the fluid forcing.

We will now try a second example, at  $m^* = 0.5$ . At this mass ratio, for the fluid forcing shown in Figure D.1 to yield motion at  $A^* = 0.30$ ,  $U^*/f^* = 9.40$ , we find that the damping ratio,  $\zeta$  must be 0.364 and the normalized velocity,  $U^*$  must be 35.3. If we now add the effect at the vortex shedding frequency using the same procedure described above for  $m^* = 10$ , we find that the higher frequency force now does have a significant effect on the predicted cylinder motion, as shown in Figure D.4.

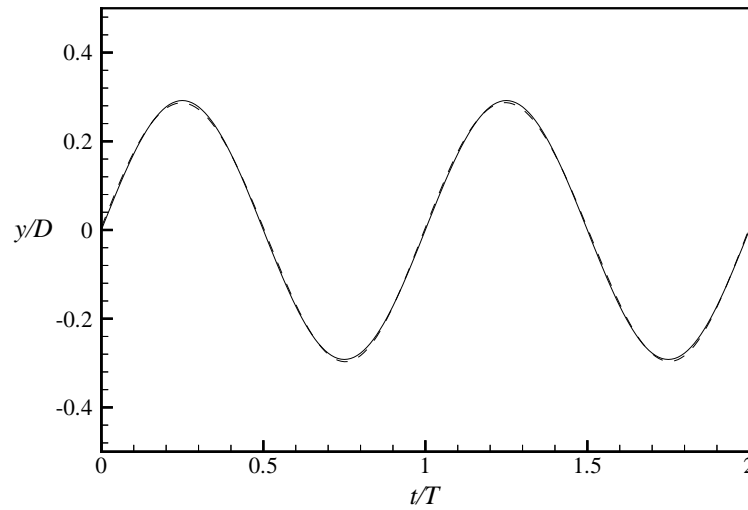


Figure D.3: Comparison between the cylinder displacement for perfectly sinusoidal motion (—) and the cylinder displacement which includes the component at the vortex shedding frequency (- - -) for  $m^* = 10.0$

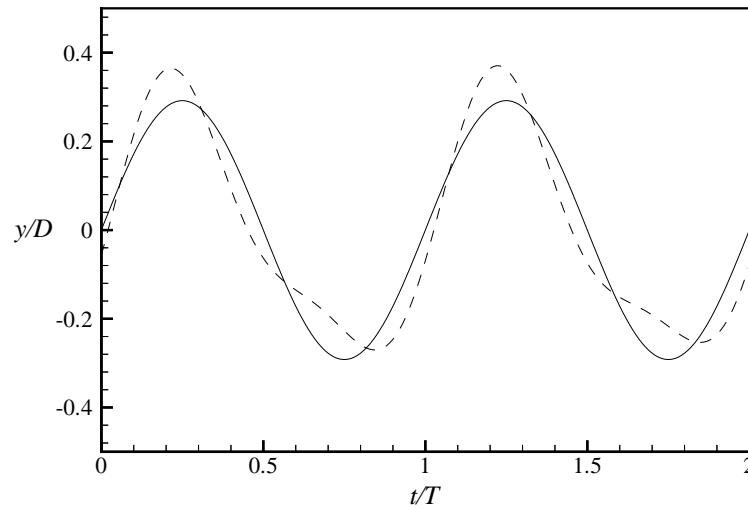


Figure D.4: Comparison between the cylinder displacement for perfectly sinusoidal motion (—) and the cylinder displacement which includes the component at the vortex shedding frequency (- - -) for  $m^* = 0.5$

We conclude that (very very nearly) sinusoidal free vibration can occur when the wake is desynchronized as long as the contribution to the displacement from the fluid force at the dominant oscillation frequency is much greater than the contribution from the fluid force at the vortex shedding frequency, as determined by the relation given in equation (D.4). This will generally be true for higher mass ratio, but not for lower mass ratio.

## APPENDIX E

### Publications from this work

#### E.1 Journal Publications

MORSE, T. L. & WILLIAMSON, C. H. K. 2006 Employing controlled vibrations to predict fluid forces on a cylinder undergoing vortex-induced vibration. *J. Fluids Struct.* **22**, 877-884.

MORSE, T. L., GOVARDHAN, R. N. & WILLIAMSON, C. H. K. 2009 The effect of end conditions on the vortex-induced vibration of cylinders. *J. Fluids Struct.* To appear.

MORSE, T. L. & WILLIAMSON, C. H. K. 2009 Fluid forcing, wake modes, and transitions for a cylinder undergoing controlled oscillations. *J. Fluids Struct.* To appear.

MORSE, T. L. & WILLIAMSON, C. H. K. 2009 Prediction of vortex-induced vibration response by employing controlled motion. *J. Fluid Mech.* Submitted.

MORSE, T. L. & WILLIAMSON, C. H. K. 2009 Steady, unsteady, and transient vortex-induced vibration predicted using controlled motion data. *J. Fluid Mech.* In preparation.

MORSE, T. L. & WILLIAMSON, C. H. K. 2009 The effect of  $Re$  on the critical mass phenomenon in vortex-induced vibration. *Phys. Fluids* Submitted.

## E.2 Conference Publications

- MORSE, T. L. & WILLIAMSON, C. H. K. 2004 Forces on a Cylinder with Periodic Transverse Motion in a Free Stream. *Bull. Am. Phys. Soc.* **49**
- MORSE, T. L. & WILLIAMSON, C. H. K. 2005 Employing controlled vibrations to predict fluid forces on a freely vibrating cylinder. *Proc. 4th Conf. on Bluff Body Wakes and Vortex-Induced Vibration (BBVIV-4) Santorini, Greece.*
- MORSE, T. L. & WILLIAMSON, C. H. K. 2005 Predicting the response of a cylinder undergoing vortex-induced vibration using controlled vibrations. *Bull. Am. Phys. Soc.* **50**.
- MORSE, T. L. & WILLIAMSON, C. H. K. 2006 Understanding mode transitions in vortex-induced vibrations of a circular cylinders using controlled vibration. *Bull. Am. Phys. Soc.* **51**.
- MORSE, T. L. & WILLIAMSON, C. H. K. 2007 An investigation of wake mode transitions and amplitude jumps in vortex-induced vibration using controlled vibration. *Bull. Am. Phys. Soc.* **52**.
- MORSE, T. L. & WILLIAMSON, C. H. K. 2007 Understanding mode transitions in vortex-induced vibration using controlled vibration. *Proc. 5th Conf. on Bluff Body Wakes and Vortex-Induced Vibration (BBVIV-5) Costa do Sauípe, Brazil.*
- MORSE, T. L. & WILLIAMSON, C. H. K. 2008 Understanding mode transitions in vortex-induced vibration using controlled motion. *9th International Conference on Flow-Induced Vibrations (FIV2008) Prague, Czech Republic.*

## REFERENCES

- ANAND, N. M. & TORUM, A. 1985 Free span vibration of submerged pipelines in steady flow and waves. In *Proc. Intl. Symp. Separated Flow Around Marine Struct.*, pp. 155–199. Trondheim, Norway.
- BEARMAN, P. W. 1984 Vortex shedding from oscillating bluff bodies. *Ann. Rev. Fluid Mech.* **16**, 195–222.
- BEARMAN, P. W. & BRANKOVIĆ, M. 2004 Experimental studies of passive control of vortex-induced vibration. *European Journal of Mechanics B-Fluids* **23**, 9–15.
- BISHOP, R. E. D. & HASSAN, A. Y. 1964 The lift and drag forces on a circular cylinder oscillating in a flowing fluid. *Proc. Roy. Soc. London Ser. A* **227**, 51–75.
- BLEVINS, R. D. 1990 *Flow-Induced Vibrations*. New York: Van Nostrand Reinhold.
- BRANKOVIĆ, M. & BEARMAN, P. W. 2006 Measurements of transverse forces on circular cylinders undergoing vortex-induced vibration. *J. Fluids Struct.* **22**, 829–836.
- BRIKA, D. & LANEVILLE, A. 1993 Vortex-induced vibrations of a long flexible circular cylinder. *J. Fluid Mech.* **250**, 481–508.
- CARBERRY, J., GOVARDHAN, R., SHERIDAN, J., ROCKWELL, D. & WILLIAMSON, C. H. K. 2004 Wake states and response branches of forced and freely oscillating cylinders. *European Journal of Mechanics B-Fluids* **23**, 89–97.
- CARBERRY, J., SHERIDAN, J. & ROCKWELL, D. 2001 Forces and wake modes of an oscillating cylinder. *J. Fluids Struct.* **15**, 523–532.

- CARBERRY, J., SHERIDAN, J. & ROCKWELL, D. 2003 Controlled oscillations of a cylinder: a new wake state. *J. Fluids Struct.* **17**, 337–343.
- CARBERRY, J., SHERIDAN, J. & ROCKWELL, D. 2005 Controlled oscillations of a cylinder: forces and wake modes. *J. Fluid Mech.* **538**, 31–89.
- FENG, C. C. 1968 The measurement of vortex-induced effects in flow past stationary and oscillating circular and D-section cylinders. Master's thesis, University of British Columbia, Vancouver, BC, Canada.
- FLEMMING, F. & WILLIAMSON, C. H. K. 2005 Vortex-induced vibrations of a pivoted cylinder. *J. Fluid Mech.* **522**, 215–252.
- GOPALKRISHNAN, R. 1993 Vortex-induced forces on oscillating bluff cylinders. PhD thesis, MIT, Cambridge, MA, USA.
- GOVARDHAN, R. & WILLIAMSON, C. H. K. 2000 Modes of vortex formation and frequency response of a freely vibrating cylinder. *J. Fluid Mech.* **420**, 85–130.
- GOVARDHAN, R. & WILLIAMSON, C. H. K. 2002 Resonance forever: Existence of a critical mass and an infinite regime of resonance in vortex-induced vibration. *J. Fluid Mech.* **473**, 147–166.
- GOVARDHAN, R. N. & WILLIAMSON, C. H. K. 2005a Revealing the effect of Reynolds number on vortex-induced vibrations using controlled negative and positive damping. In *Proc. 4th Conf. on Bluff Body Wakes and Vortex-Induced Vibration (BBVIV-4)*. Santorini, Greece.
- GOVARDHAN, R. N. & WILLIAMSON, C. H. K. 2005b Vortex-induced vibrations of a sphere. *J. Fluid Mech.* **531**, 11–47.

- GOVARDHAN, R. N. & WILLIAMSON, C. H. K. 2006 Defining the 'modified Griffin plot' in vortex-induced vibration: revealing the effect of Reynolds number using controlled damping. *J. Fluid Mech.* **561**, 147–180.
- GRIFFIN, O. M. 1980 Vortex-excited cross-flow vibrations of a single cylindrical tube. *Trans. ASME: J. Pres. Vessel Techn.* **102**, 158–166.
- GRIFFIN, O. M. & RAMBERG, S. E. 1982 Some recent studies of vortex shedding with application to marine tubulars and risers. *ASME: J. Energy Resource Technol.* **104**, 2–13.
- GU, W., CHYU, C. & ROCKWELL, D. 1994 Imaging of vortex formation from an oscillating cylinder. *Phys. Fluids* **6**, 3677–3682.
- HOVER, F. S., DAVIS, J. T. & TRIANTAFYLLOU, M. S. 2004 Three-dimensionality of mode transition in vortex-induced vibrations of a circular cylinder. *European Journal of Mechanics B-Fluids* **23**, 29–40.
- HOVER, F. S., TECHET, A. H. & TRIANTAFYLLOU, M. S. 1998 Forces on oscillating uniform and tapered cylinders in crossflow. *J. Fluid Mech.* **363**, 97–114.
- HOVER, F. S., TVEDT, H. & TRIANTAFYLLOU, M. S. 2001 Vortex-induced vibrations of a cylinder with tripping wires. *J. Fluid Mech.* **448**, 175–195.
- JAUVTIS, N. & WILLIAMSON, C. H. K. 2004 The effect of two degrees of freedom on vortex-induced vibration at low mass and damping. *J. Fluid Mech.* **509**, 23–62.
- KHALAK, A. & WILLIAMSON, C. H. K. 1996 Dynamics of a hydroelastic cylinder with very low mass and damping. *J. Fluids Struct.* **10**, 455–472.

- KHALAK, A. & WILLIAMSON, C. H. K. 1999 Motions, forces and mode transitions in vortex-induced vibrations at low mass-damping. *J. Fluids Struct.* **13**, 813–851.
- KLAMO, J. T. 2007 Effects of damping and Reynolds number on vortex-induced vibrations. PhD thesis, Caltech.
- KLAMO, J. T., LEONARD, A. & ROSHKO, A. 2005 On the maximum amplitude for a freely vibrating cylinder in cross-flow. *J. Fluids Struct.* **21**, 429–434.
- KLAMO, J. T., LEONARD, A. & ROSHKO, A. 2006 The effects of damping on the amplitude and frequency response of a freely vibrating cylinder in cross-flow. *J. Fluids Struct.* **22**, 845–856.
- LIGHTHILL, J. 1986 Wave loading on offshore structures. *J. Fluid Mech.* **173**, 667–681.
- LUCOR, D., FOO, J. & KARNIADAKIS, G. E. 2005 Vortex mode selection of a rigid cylinder subject to viv at low mass=damping. *J. Fluids Struct.* **20**, 483–503.
- MERCIER, J. A. 1973 Large amplitude oscillations of a circular cylinder in a low speed stream. PhD thesis, Stevens Inst. Tech., Hoboken, NJ, USA.
- MOE, G. & OVERVIK, T. 1982 Current-induced motions of multiple risers. In *Proc. BOSS-82, Behaviour of Offshore Struct.* (ed. C. Chryssostomides & J. J. Connor), pp. 618–639. Hemisphere.
- MORSE, T. L. & WILLIAMSON, C. H. K. 2006 Employing controlled vibrations to predict fluid forces on a cylinder undergoing vortex-induced vibration. *J. Fluids Struct.* **22**, 877–884.

- MORSE, T. L. & WILLIAMSON, C. H. K. 2009a The effect of  $Re$  on the critical mass phenomenon in vortex-induced vibration. *Phys. Fluids* Submitted.
- MORSE, T. L. & WILLIAMSON, C. H. K. 2009b Fluid forcing, wake modes, and transitions for a cylinder undergoing controlled oscillation. *J. Fluids Struct.* To appear.
- MORSE, T. L. & WILLIAMSON, C. H. K. 2009c Prediction of vortex-induced vibration response by employing controlled motion. *J. Fluid Mech.* Submitted.
- NAUDASCHER, E. & ROCKWELL, D. 1994 *Flow-Induced Vibrations: An Engineering Guide*. Rotterdam, Netherlands: Balkema.
- ONGOREN, A. & ROCKWELL, D. 1988a Flow structure from an oscillating cylinder. Part 1. Mechanisms of phase shift and recovery in the near wake. *J. Fluid Mech.* **191**, 197–223.
- ONGOREN, A. & ROCKWELL, D. 1988b Flow structure from an oscillating cylinder. Part 2. Mode competition in the near wake. *J. Fluid Mech.* **191**, 225–245.
- OWEN, J. C., BEARMAN, P. W. & SZEWCZYK, A. A. 2001 Passive control of VIV with drag reduction. *J. Fluids Struct.* **15**, 597–605.
- PARKINSON, G. 1989 Phenomena and modelling of flow-induced vibrations of bluff bodies. *Progr. Aerospace Sci.* **26**, 169–224.
- POTTEBAUM, T. S. 2003 The relationship between near-wake structure and heat transfer for an oscillating circular cylinder in cross-flow. PhD thesis, Caltech, Pasadena, CA, USA.
- PRASAD, A. & WILLIAMSON, C. H. K. 1997 Three dimensional effects in turbulent bluff-body wakes. *J. Fluid Mech.* **343**, 235–264.

- RAMBERG, S. E. & GRIFFIN, O. M. 1981 *Hydroelastic response of marine cables and risers*, pp. 1223–1245. Trondheim, Norway: Norwegian Institute of Technology.
- ROSHKO, A. 1993 Perspectives on bluff-body aerodynamics. *J. Wind Eng. Ind. Aero.* **49**, 79–100.
- RYAN, K., THOMPSON, M. C. & HOURIGAN, K. 2005 Variation in the critical mass ratio of a freely oscillating cylinder as a function of Reynolds number. *Phys. Fluids* **17**, 038106.
- SARPKAYA, T. 1977 Transverse oscillations of a circular cylinder in uniform flow, Part I. *Tech. Rep.* NPS-69SL77071. Nav. Postgrad. Sch., Monterey, CA, USA.
- SARPKAYA, T. 1979 Vortex-induced oscillations. *Trans. ASME: J. Appl. Mech.* **46**, 241–258.
- SARPKAYA, T. 1995 Hydrodynamic damping, flow-induced oscillations, and bi-harmonic response. *Trans. ASME: J. Offshore Mech. Arctic Engng.* **117**, 232–238.
- SHIELS, D., LEONARD, A. & ROSHKO, A. 2001 Flow-induced vibration of a circular cylinder at limiting structural parameters. *J. Fluids Struct.* **15**, 3–21.
- SLAOUTI, A. & GERRARD, J. H. 1981 An experimental investigation of the end effects on the wake of a circular-cylinder towed through water at low Reynolds numbers. *J. Fluid Mech.* **122**, 297–314.
- STANSBY, P. K. 1974 Effects of end plates on base pressure coefficient of a circular cylinder. *Aeronautical Journal* **78**, 36–37.

- STAUBLI, T. 1983 Calculation of the vibration of an elastically mounted cylinder using experimental data from forced vibration. *ASME J. Fluids Eng.* **105**, 225–229.
- SUMER, B. M. & FREDSOE, J. 1997 *Hydrodynamics around Cylindrical Structures*. Singapore: World Scientific.
- SZEPESSY, S. & BEARMAN, P. W. 1992 Aspect ratio and end plate effects on vortex shedding from a circular cylinder. *J. Fluid Mech.* **234**, 191–217.
- VIKESTAD, K. 1998 Multi-frequency response of a cylinder subjected to vortex shedding and support motions. PhD thesis, Norwegian University of Science and Technology.
- VIKESTAD, K., VANDIVER, J. K. & LARSEN, C. M. 2000 Added mass and oscillation frequency for a circular cylinder subjected to vortex-induced vibrations and external disturbance. *J. Fluids Struct.* **14**, 1071–1088.
- WILLIAMSON, C. H. K. 1988 Defining a universal and continuous Strouhal-Reynolds number relationship for the laminar vortex shedding of a circular cylinder. *Phys. Fluids* **31**, 2742–2744.
- WILLIAMSON, C. H. K. 1989 Oblique and parallel modes of vortex shedding in the wake of a circular cylinder at low Reynolds numbers. *J. Fluid Mech.* **206**, 579–627.
- WILLIAMSON, C. H. K. 1996 Vortex dynamics in the wake. *Ann. Rev. Fluid Mech.* **28**, 477–539.
- WILLIAMSON, C. H. K. & GOVARDHAN, R. 2004 Vortex-induced vibrations. *Ann. Rev. Fluid Mech.* **36**, 413–455.

WILLIAMSON, C. H. K. & ROSHKO, A. 1988 Vortex formation in the wake of an oscillating cylinder. *J. Fluids Struct.* **2**, 355–381.